

FABRICATION, FUNCTIONALISATION AND CHARACTERISATION OF EPITAXIAL GRAPHENE DEVICES

By

V. Karthik Nagareddy

School of Electrical and Electronic Engineering

Newcastle University, United Kingdom

A THESIS SUBMITTED TO THE FACULTY OF SCIENCE, AGRICULTURE AND
ENGINEERING FOR THE DEGREE OF DOCTOR OF PHILOSOPHY

April 2014



Dedicated to
My parents and brother

Declaration

I certify that all material in this thesis which is not my own work has been identified and that no material has previously been submitted and approved for the award of a degree by this or any other university.

V. Karthik Nagareddy

April 2014

Acknowledgements

I would like to express my sincere gratitude to many people who helped me during the period of my PhD studies. Foremost, I am very grateful to Dr. Alton Horsfall for giving me the opportunity to pursue PhD under his supervision. His extremely supportive and encouraging nature has given me immense confidence in successfully completing this project. Special thanks to Dr. Jon Goss and Prof. Nick Wright for their constant guidance and support throughout my PhD work.

A big thank you to our collaborators at U.S. Naval Research Laboratory (NRL). In particular, I am grateful to Dr. Kurt Gaskill for giving me the opportunity to do a six-week internship at NRL. It was a great pleasure and a wonderful experience working with some of the eminent scientists in the field of graphene research.

During my stay at NRL, there were several people who helped me in successfully completing this short internship. Especially, I would like to give my sincere appreciations to Dr. Virginia Wheeler and Dr. Luke Nyakiti for growing epitaxial graphene samples used in this thesis and to Dr. Sandra Hernandez for functionalisation and XPS characterisation of these samples. A special acknowledgement is due to Dr. Scott Walton, Dr. Charles Eddy, Dr. Rachael Myers-Ward, Dr. Nelson Garces and Anindya Nath.

I am also grateful to Prof. Peter Cumpson and Dr. Anders Barlow at Newcastle University for performing XPS measurements on the samples investigated in this thesis. A special thank you is also due to HK for devoting his time in performing low-frequency noise measurements on some of the devices fabricated in this work.

I would like to thank the EPSRC and BAE systems for providing financial support through the DHPA scheme for the duration of my PhD. I would also like to acknowledge the School of Electrical and Electronic Engineering at Newcastle for providing necessary resources to efficiently perform my PhD work. Sincere thanks to Dr. Konstantin Vasilevsky for helping me with the cleanroom related processing.

A heart felt thank you to all my colleagues in the research group, including Amit, Ben, Lucy, Rupert, Simon, Leonie, Hassan, Graeme, HK, Sandip, Omid, Dan and Neal for the endless enjoyable discussions. Finally, I would like to thank my parents for their constant encouragement and endless support throughout my life.

Abstract

Graphene has attracted considerable attention in recent years due to its remarkable material properties and its potential for applications in next-generation nanoelectronics. In particular, the high specific surface area, extremely high electrical conductivity and exceptionally low electrical noise make graphene an ideal material for surface-sensitive applications such as chemical sensing, biological sensing and DNA sequencing. The surface cleanliness of graphene devices is critical for these applications, along with low contact resistance at metal/graphene interfaces. In addition, having pristine surface is also essential to carry out controlled functionalisation of graphene to target its chemical reactions with designated analyte species.

However, it was found that conventional lithography processing techniques used for graphene device fabrication significantly contaminates the graphene surface with resist residues, which cannot be removed by any known organic solvents. The presence of such chemical contamination degrades the intrinsic properties of graphene and also significantly affects the performance of graphene based electronic devices. In this thesis, two methods were developed to address this issue, where, for the first method, rapid thermal annealing of graphene devices was performed in N_2/H_2 atmosphere, whilst for the second method, a metal sacrificial layer was used to prevent graphene from coming into direct with photoresist during the lithography process. Chemical, electrical, structural and surface morphological analysis showed that clean graphene surfaces can be achieved by both these methods, which allowed the intrinsic properties of graphene to be measured.

In addition to surface contamination, the performance of graphene devices is also limited by contact resistance associated with the metal-graphene interface, where an unique challenge arise as charge carriers are injected from a three-dimensional metal film into a two-dimensional graphene sheet. The quantitative analysis of the data demonstrates that highly reactive metals such as Ti destroys the graphene lattice and results in high contact resistance, whereas metals with higher work functions and lower lattice mismatch to graphene (such as Ni) was found to result in significantly lower contact resistance. The work function, binding energy, diffusion energy and the lattice mismatch of the deposited metals were used to explain the electrical and structural characteristics of different types of metal/graphene interfaces.

ABSTRACT

In order to enhance the chemical reactivity of graphene surfaces, controlled functionalisation of epitaxial graphene films using electron-beam generated oxygen plasma has been demonstrated at room temperature. It was found that oxygen functionalisation not only introduces different oxygen functional groups onto the graphene surface, but also results in strain relaxation, in which the intrinsic compressive strain present in epitaxial graphene film decreased progressively with the increasing plasma pressure. A detailed study on the effect of e-beam plasma treatment on the chemical, electrical, structural and morphological characteristics of epitaxial graphene films have been investigated from initial to advanced oxidation stages.

Finally, the effectiveness of oxygen functionalised graphene as a chemical sensor for detecting a wide range of polar chemical vapours in the ambient atmosphere has been demonstrated. The sensing characteristics of oxygen functionalised graphene devices showed ultra-fast response (10 s) and recovery times (100 s) to different chemical vapours, whilst unfunctionalised graphene sensors showed considerably weaker sensitivity and extremely slow recovery time in the range of ~ 1.5 to 2 hours. A strong correlation between the dipole moment of the chemical and the magnitude of the response was observed, in which oxygen functionalised sensors displayed a twofold increase in the sensitivity over un-functionalised sensors with the increasing dipole moment from 2.0 D to 4.1 D. The sensing properties of graphene and the effect of oxygen functionalization on sensor responses were critically examined in an effort to provide a detailed understanding on the graphene sensing mechanism and provide a pathway for future advancements in the graphene sensor research.

Contents

Declaration	iii
Acknowledgements	iv
Abstract	v
List of publications	xi
List of conference presentations	xii
List of figures	xiv
List of tables	xxv
Acronyms	xxvi
Notations	xxviii
Chapter 1	1
1.1 Allotropes of carbon	1
1.2 Graphitic materials	2
1.2.1 Graphite.....	2
1.2.2 Fullerene and carbon nanotubes.....	2
1.2.3 Graphene: The non-existing material.....	4
1.3 Motivation and objectives.....	5
1.4 Thesis outline.....	8
Chapter 2	10
2.1 Introduction.....	10
2.2 Graphene properties.....	11

2.3	Electronic structure of graphene.....	11
2.4	Synthesis of graphene	13
2.4.1	Mechanical exfoliation	13
2.4.2	CVD growth on metals.....	14
2.4.3	Epitaxial growth on SiC	16
2.5	SiC as a template for the graphene growth.....	16
2.5.1	SiC crystal structure.....	17
2.5.2	SiC surface preparation and graphene growth	18
2.5.3	Effect of SiC polytype on the graphene growth	22
2.5.4	Other growth methods on SiC	23
2.6	Importance of metal contacts on graphene	24
2.7	Significance of graphene functionalisation	28
2.7.1	Oxidation of graphene	31
2.8	Graphene as a chemical sensor	34
2.8.1	Influence of resist contamination on the graphene sensor response	38
2.8.2	Impact of oxygen functional groups on the sensor response	39
2.9	Summary	40
	Chapter 3	41
3.1	Epitaxial graphene growth process.....	41
3.1.1	Substrate preparation.....	41
3.1.2	Graphene growth.....	43
3.2	Oxygen plasma functionalisation process.....	44
3.3	Fabrication of graphene devices.....	46
3.3.1	Direct photolithography	46
3.3.2	Reverse photolithography	48
3.3.3	Metal deposition	48
3.3.4	Rapid thermal annealing	48
3.4	Microscopic and spectroscopic characterisation	49

3.4.1	Atomic force microscopy	49
3.4.2	X-ray photoelectron spectroscopy	52
3.4.3	Raman spectroscopy	55
3.5	Electrical characterisation	65
3.5.1	Transmission line model measurements	65
3.5.2	Van der Pauw and Hall measurements	67
3.5.3	Low-frequency noise measurements	69
3.6	Summary	71
Chapter 4		73
4.1	Introduction	73
4.2	Experimental details	76
4.3	Results and Discussion	77
4.3.1	High temperature measurements of metal-graphene interfaces	77
4.3.2	Cleaning graphene surfaces using rapid thermal annealing	82
4.3.3	Electrical characteristics of graphene fabricated using aluminium sacrificial layer approach	95
4.4	Summary	109
Chapter 5		110
5.1	Introduction	110
5.2	Experimental details	113
5.2.1	Graphene growth and functionalisation	113
5.2.2	Surface characterisation	113
5.3	Results and Discussion	114
5.3.1	XPS Analysis - identifying chemical moieties on the graphene surface	114
5.3.2	AFM Analysis - examining surface morphological changes	125
5.3.3	Raman Analysis - monitoring structural characteristics	127
5.3.4	Hall measurements	137
5.4	Summary	140

Chapter 6	141
6.1 Introduction.....	141
6.2 Experimental details.....	142
6.3 Results and Discussion	144
6.3.1 XPS analysis.....	144
6.3.2 Raman analysis.....	148
6.3.3 Hall measurements.....	155
6.3.4 TLM measurements.....	158
6.3.5 Low-frequency noise measurements	161
6.4 Summary.....	166
Chapter 7	168
7.1 Introduction.....	168
7.2 Experimental details.....	170
7.3 Results and Discussion	172
7.3.1 UFEG sensor response: I-V measurements	174
7.3.2 UFEG sensor response: Low-frequency noise measurements.....	179
7.3.3 Sensing polar chemicals using OFEG sensors	182
7.3.4 OFEG sensor response: I-V measurements	184
7.3.5 Effect of dipole moment on the sensor response.....	187
7.3.6 OFEG sensor response: Low-frequency noise measurements.....	189
7.4 Summary.....	192
Chapter 8	194
8.1 Future outlook.....	196
References	198

List of publications

1. S.C. Hernández, V.D. Wheeler, M.S. Osofsky, G.G. Jernigan, **V.K. Nagareddy**, A. Nath, E.H. Lock, L.O. Nyakiti, R.L. Myers-Ward, K. Sridhra, A.B. Horsfall, C.R. Eddy, Jr. D.K. Gaskill, and S.G. Walton, “Plasma-based chemical modification of epitaxial graphene with oxygen functionalities,” *Surface and Coatings Technology*, vol. 241 p. 8-12, (2014).
2. **V.K. Nagareddy**, H.K. Chan, S.C. Hernández, V.D. Wheeler, L.O. Nyakiti, C.R. Eddy, R.L. Myers-Ward, J.P. Goss, N.G. Wright, S.G. Walton, D.K. Gaskill, and A.B. Horsfall “Improved chemical detection and ultra-fast recovery using oxygen functionalised epitaxial graphene sensors,” *IEEE Sensors Journal*, vol. 13, p. 2810-2817, (2013)
3. **V.K. Nagareddy**, H.K. Chan, S.C. Hernández, V.D. Wheeler, L.O. Nyakiti, R.L. Myers-Ward, C.R. Eddy, Jr, J.P. Goss, N.G. Wright, S.G. Walton, D.K. Gaskill, and A.B. Horsfall, “Detection of polar chemical vapors using epitaxial graphene grown on SiC (0001),” *Applied Physics Letters*, vol. 102, p. 173103, (2013).
4. **V.K. Nagareddy**, S.C. Hernández, V.D. Wheeler, L.O. Nyakiti, R.L. Myers-Ward, C.R. Eddy, Jr, J.P. Goss, N.G. Wright, S.G. Walton, D.K. Gaskill, and A.B. Horsfall, “High temperature stability of oxygen functionalised epitaxial graphene/metal contact interfaces,” *Materials Science Forum*, vols. 740-742, p. 145-148, (2013).
5. **V.K. Nagareddy**, S.C. Hernández, V.D. Wheeler, L.O. Nyakiti, R.L. Myers-Ward, C.R. Eddy, Jr, J.P. Goss, N.G. Wright, S.G. Walton, D.K. Gaskill, and A.B. Horsfall, “Oxygen functionalised epitaxial graphene sensors for enhanced polar organic chemical vapour detection,” *Proceedings of IEEE Sensors Conference*, Taipei, p. 1-4, (2012).
6. **V.K. Nagareddy**, D.K. Gaskill, J.L. Tedesco, R.L. Myers-Ward, C.R. Eddy, Jr, J.P. Goss, N.G. Wright and A.B. Horsfall, “Temperature dependent chemical sensitivity of epitaxial graphene,” *Materials Science Forum*, vols. 717-720, p. 691-694, (2012).
7. **V.K. Nagareddy**, I.P. Nikitina, D.K. Gaskill, J.L. Tedesco, R.L. Myers-Ward, C.R. Eddy, J.P. Goss, N.G. Wright and A.B. Horsfall, “High temperature measurements of metal contacts on epitaxial graphene,” *Applied Physics Letters*, vol. 99, p. 073506, (2011).

8. J.P. Goss, P.R. Briddon, **V.K. Nagareddy**, N.G. Wright, A.B. Horsfall, J.D. Caldwell, D.K. Gaskill and G.G. Jernigan, “Influence of intercalated silicon on the transport properties of graphene,” *Materials Science Forum*, vols. 679-680, p. 793-796, (2011).
9. **V.K. Nagareddy**, V.D. Wheeler, L.O. Nyakiti, R.L. Myers-Ward, C.R. Eddy, J.P. Goss, N.G. Wright, D.K. Gaskill, and A.B. Horsfall, “Effect of high temperature annealing on the chemical, electrical and structural properties of epitaxial graphene,” In preparation.
10. **V.K. Nagareddy**, S.C. Hernández, H.K. Chan, V.D. Wheeler, L.O. Nyakiti, R.L. Myers-Ward, C.R. Eddy, Jr, J.P. Goss, N.G. Wright, S.G. Walton, D.K. Gaskill, and A.B. Horsfall, “Effect of surface oxidation on the electrical and $1/f$ noise characteristics of epitaxial graphene/metal contact interfaces,” In preparation.
11. **V.K. Nagareddy**, S.C. Hernández, V.D. Wheeler, L.O. Nyakiti, R.L. Myers-Ward, C.R. Eddy, Jr, J.P. Goss, N.G. Wright, S.G. Walton, D.K. Gaskill, and A.B. Horsfall, “Oxygen functionalisation induced intrinsic strain relaxation of epitaxial graphene films grown on SiC (0001),” In preparation.
12. **V.K. Nagareddy**, V.D. Wheeler, L.O. Nyakiti, R.L. Myers-Ward, C.R. Eddy, Jr, J.P. Goss, N.G. Wright, D.K. Gaskill, and A.B. Horsfall, “Achieving ultra-clean graphene surfaces using sacrificial layer for electronic device applications,” In preparation.

List of conference presentations

1. D.K. Gaskill, H.K. Chan, V.D. Wheeler, **V.K. Nagareddy**, L.O. Nyakiti, A. Nath, R.L. Myers-Ward, Z.R. Robinson, N.Y. Graces, M.V. Rao, J.P. Goss, N.G. Wright, C.R. Eddy, Jr, A.B. Horsfall, “Low-frequency noise in Al₂O₃ and HfO₂ epitaxial graphene FETs” *MRS Spring Meeting*, San Francisco, California, Apr 21-25, (2014), Oral presentation.
2. D.K. Gaskill, H.K. Chan, V.D. Wheeler, **V.K. Nagareddy**, L.O. Nyakiti, A. Nath, R.L. Myers-Ward, Z.R. Robinson, N.Y. Graces, M.V. Rao, J.P. Goss, N.G. Wright, C.R. Eddy, Jr, and A.B. Horsfall, “The low-frequency noise spectrum in gated epitaxial graphene field-effect-transistors” *APS March Meeting*, Denver, Mar 3–7, (2014), Oral presentation.
3. H.K. Chan, V.D. Wheeler, **V.K. Nagareddy**, L.O. Nyakiti, A. Nath, R.L. Myers-Ward, Z.R. Robinson, N.Y. Graces, M.V. Rao, J.P. Goss, N.G. Wright, C.R. Eddy, Jr, D.K.

LIST OF CONFERENCE PRESENTATIONS

- Gaskill and A.B. Horsfall, “Ultra-low $1/f$ Noise in top gated epitaxial graphene field-effect-transistors,” *44th IEEE Semiconductor Interface Specialists Conference*, Arlington, Virginia, Dec 5–7, (2013), Poster presentation.
4. H.K. Chan, V.D. Wheeler, **V.K. Nagareddy**, L.O. Nyakiti, A.Nath, R.L. Myers-Ward, Z.R. Robinson, N.Y.Graces, M.V. Rao, J.P. Goss, N.G. Wright, C.R. Eddy, Jr, A.B. Horsfall and D.K. Gaskill, “ $1/f$ noise in epitaxial graphene field effect transistors using Al_2O_3 and HfO_2 high-k dielectrics,” *AVS 60th International Symposium and Exhibition*, Long beach, California, Oct 27–Nov 1, (2013), Oral presentation.
 5. **V.K. Nagareddy**, S.C. Hernández, H.K. Chan, V.D. Wheeler, L.O. Nyakiti, R.L. Myers-Ward, C.R. Eddy, Jr, J.P. Goss, N.G. Wright, S.G. Walton, D.K. Gaskill, A.B. Horsfall, “Electrical and structural characterisation of O-functionalised epitaxial graphene and metal contact interfaces,” *Graphene Week*, Chemnitz, Jun 2-7, (2012), Poster presentation.
 6. **V.K. Nagareddy**, S.C. Hernández, V.D. Wheeler, L.O. Nyakiti, R.L. Myers-Ward, C.R. Eddy, Jr, J.P. Goss, N.G. Wright, S.G. Walton, D.K. Gaskill, and A.B. Horsfall, “Oxygen functionalised epitaxial graphene sensors for enhanced polar organic chemical vapour detection,” *IEEE Sensors 2012*, Taipei, October 28-31 (2012), Oral presentation.
 7. D.K. Gaskill, L.O. Nyakiti, V.D. Wheeler, **V.K. Nagareddy**, A. Nath, R.L. Myers-Ward, N.Y. Graces, S.C. Hernández, S.G. Walton, M.V. Rao, A.B. Horsfall, C.R. Eddy, Jr, and J.S. Moon, “Ingredients for low noise epitaxial graphene applications,” *AVS 59th International Symposium and Exhibition*, Tampa, Florida, October 28-Nov 2, (2012), Oral presentation.
 8. **V.K. Nagareddy**, S.C. Hernández, V.D. Wheeler, L.O. Nyakiti, R.L. Myers-Ward, C.R. Eddy, Jr, J.P. Goss, N.G. Wright, S.G. Walton, D.K. Gaskill, and A.B. Horsfall, “Oxygen functionalization of epitaxial graphene films grown on SiC (0001) using electron-beam generated plasmas,” *Graphene Conference: From research to applications*, London, October 15-16, (2012), Poster presentation.
 9. V.D. Wheeler, N.Y. Graces, L.O. Nyakiti, R.L. Myers-Ward, G.G. Jernigan, A. Nath, **V.K. Nagareddy**, S.C. Hernández, S.G. Walton, C.R. Eddy, Jr, and D.K. Gaskill, “Overcoming processing problems to achieve high quality epitaxial graphene devices,” *Electronic Materials Conference*, Pennsylvania, June 20-22, (2012), Oral presentation.

List of figures

Figure 1.1: Schematic representation of different carbon allotropes, showing their dimensionality and hybridisation [9].	3
Figure 1.2: Graphene the mother of all graphitic carbon allotropes of different dimensionalities [11].	4
Figure 2.1: (a) Illustration of the hexagonal lattice structure of graphene showing unit cell with two carbon atoms A and B. (b) Electronic band structure of graphene obtained from theoretical calculations [9].	12
Figure 2.2: Evolution of the band structure of graphene with the increasing thickness [52].	13
Figure 2.3: (a) Digital image of mechanical exfoliation and transfer process of graphene flakes. (b) Optical microscopic image of a graphene flake showing different contrasts for monolayer, bilayer and multilayer graphene [54].	14
Figure 2.4: (a) Schematic of the CVD growth process on Cu foils. (b) SEM images showing the evolution of individual graphene domains to form a continuous film (c) illustration of roll-to-roll production of CVD graphene (d) a prototype of a graphene based touch screen display [23,58,59].	15
Figure 2.5: (a) Tetrahedral bonding in SiC (b) Hexagonal SiC as a basic building block of the SiC crystal structure. Crystal structures of (c) 3C-SiC (d) 4H-SiC and (e) 6H-SiC [9].	17
Figure 2.6: (a) as-receive SiC substrate showing polishing damage on the surface (b) Formation of smooth steps after H ₂ etching (c) Swiss-cheese like pattern of the graphene surface after UHV growth (d) Increased SiC step terrace width after graphene growth in Ar (e) and (f) LEEM images of corresponding UHV and Ar grown graphene film morphology, respectively [71,72].	19
Figure 2.7: (top) Images showing the interface layer, monolayer, bilayer and tri-layer graphene films on 6H-SiC (0001) substrate. (bottom) Corresponding TEM images [69].	20
Figure 2.8: (a) Leighton image of epitaxial graphene grown on 72 mm diameter 6H-SiC (0001) wafer and (b) Processed epitaxial graphene wafer into MOSFETs [73].	21
Figure 2.9: AFM topography image of as-grown graphene on the (a) Si-face of the 6H-SiC and (b) C-face of the 6H-SiC	22
Figure 2.10: (a),(b) and (c) AFM topography images of different SiC polytypes. (d),(e) and (f) are the corresponding LEEM images showing the graphene thickness uniformity [76,77].	23

LIST OF FIGURES

Figure 2.11: Schematic illustration of the interface at (a) metal-semiconductor (b) metal-metal and (c) metal-graphene interfaces [80].	24
Figure 2.12: (top) Effect of metals (a) Ag (b) Cu and (c) Au on the Dirac point of graphene (middle) Corresponding band structure of graphene when in contact with these metal films [82,83]. (bottom) Effect of metal films on the electrical conductivity and the carrier mobility	26
Figure 2.13: (a) Evolution of the high resolution XPS C1s spectra of graphene with the increasing (a) Ti and (b) Pd metal films [85]	27
Figure 2.14: Transformation of sp^2 hybridisation to sp^3 hybridisation upon functionalising graphene with reactive chemical species [105]	29
Figure 2.15: Evolution of the band structures of (a) SLG and (b) BLG with O-functional groups [109]	30
Figure 2.16: Contact angle measurements of (a) SiC substrate (b) epitaxial graphene on SiC (c) oxygen plasma treated epitaxial graphene and (d) after annealing plasma treated graphene [92]	31
Figure 2.17: XPS C1s spectra of (a) as-synthesised GO (b) thermally reduced GO in UHV at 200°C (c), (d), (e) and (f) reduction of oxygen functional groups with the increasing annealing temperature to up to 1000°C [115]	32
Figure 2.18: (a) Evolution of the Raman spectra of single layer graphene upon oxygen functionalisation with varying functionalisation times. (b) The corresponding electrical characteristics of the functionalised graphene [117]	33
Figure 2.19: STM topography image of epitaxial graphene (a) before and (b) after oxygen functionalisation (c) STM protrusions showing the epoxy functional groups (d) Schematic illustration of the epoxy functional group bonded to the graphene surface (e) and (f) functionalisation and the annealing induced recovery of the graphene [119].	34
Figure 2.20: (a) Response of exfoliated graphene sensor to electron donating and electron withdrawing gas species and (b) Monitoring the single molecule detection of NO ₂ during adsorption and desorption from the graphene surface [93]	36
Figure 2.21: (a) Electrical response of multi-layer epitaxial graphene sensor to NO ₂ gas at different temperatures and (b) Response of single layer graphene to the same gas species [28].	37
Figure 2.22: (a) 1/f noise deviation and appearance of bulges after exposure of different chemical vapours and (b) More pronounced effects of 1/f noise bulges showing different characteristics frequencies for different chemical species [134].	37

LIST OF FIGURES

Figure 2.23: Effect of photoresist contamination on the chemical sensing responses of exfoliated graphene sensor for (a) water vapour exposure (b) nonanal (c) octanoic acid and (d) trimethylamine vapours, respectively [36].	38
Figure 2.24: (a) Effect of oxygen functional groups on the enhancement of the sensor response and (b) rGO sensor response to different molecular gases at different concentrations [135,136].	39
Figure 3.1: Overview of the experimental set-up used for growing epitaxial graphene films on SiC substrates. (a) AXITRON CVD reactor system (b) Rotatory shaft used for placing the samples and also for spinning during the growth (c) Sample used in this thesis before graphene growth (d) Feed through of gases available for the graphene growth. (e) Growth chamber showing loading of samples and (f) SiC samples during the graphene growth.	42
Figure 3.2: Graph showing different temperature cycles and ambient environments used during the graphene growth process.	43
Figure 3.3: AFM topography images showing the surface of SiC after H ₂ and graphene growth. Scale bar represents 2 μm .	43
Figure 3.4: (a) Schematic view of the e-beam plasma reactor used for oxygen functionalisation process. (b) Schematic illustration of the plasma during the exposure and (c) Real time digital image of the sheet like plasma produced during the functionalisation process [145,147].	45
Figure 3.5: Schematic illustration of process steps followed for the fabrication of graphene devices.	47
Figure 3.6: (a) Typical Van der Waals force curve used for repulsive and attractive forces of contact and non-contact mode AFM (b) AFM illustration showing the laser beam deflected signal from the cantilever collected by a photodetector and typical raster like scanning performed during the topography measurement [149].	50
Figure 3.7: (a) AFM surface topography of epitaxial graphene grown on 6H-SiC substrate taken in non-contact mode. Scale bars represent 600 nm. (b) Corresponding phase image of the sample revealing different contrast brightness at step terraces and step edges, indicating variation in thickness at these regions. (c) The Height profile of the topography image shown in (a).	51
Figure 3.8: (a) Illustration of photoelectron emission process in XPS and (b) Schematic of an XPS experimental set-up for analysing samples [9].	52
Figure 3.9: A typical XPS wide energy scan of an as-grown epitaxial graphene sample showing Si, C and O as main elements present on the surface.	53

LIST OF FIGURES

Figure 3.10: High-resolution XPS C1s spectra of as-grown epitaxial graphene showing Si-C, C-C and the interface layer, respectively.....	54
Figure 3.11: Schematic view of a typical Raman spectroscopy set-up. (b) Energy level diagram showing stokes, anti-stokes and Rayleigh scattering and (c) Phonon spectrum of graphene [9].	56
Figure 3.12: (a) Raman spectrum of a pristine graphene showing characteristic G and 2D peaks and (b) Raman spectrum of a disordered graphene with an intense D and D' peaks [151].	57
Figure 3.13: (a) First order G-band process (b) and (d) Intervally and intra-valley one-phonon second order double resonance process for D-band and D' bands respectively (C) two-phonon second order double resonance and (e) triple resonance process for 2D-peak [151].	58
Figure 3.14: Raman peak fitting procedure using Lorentzian functions for identifying (a) single layer, (b) bi-layer and (c) tri-layer graphene films [153].	58
Figure 3.15: (a) Evolution of defect density from $L_D=24$ nm to $L_D=2$ nm in an ion-bombarded graphene flake ad (b) Intensity of I_D/I_G ratio of the defective graphene as a function of increasing defect density in the graphene [154].	59
Figure 3.16: (a) Evolution of G and 2D peaks of the graphene with n and p-doping. (b) and (C) shows the shift in the position of G and 2D peaks as a function of carrier concentration [156].	60
Figure 3.17: (a) Effect of doping on the intensities of G and 2D peaks and (b) Influence of doping on the I_{2D}/I_G ratio of Raman spectrum [156,157].	61
Figure 3.18: Sketch of Raman peak positions of graphene for tensile and compressive strains.	62
Figure 3.19: (a) Evolution of G and 2D peaks under uni-axial strain. Peak splitting of the G-peak can be seen here. (c) and (d) decrease in peak positions on graphene with the increasing strain [156].	63
Figure 3.20: (a) Raman spectra of graphene on SiC and free-standing graphene. (b) and (c) Change in intensity and the peak positions of G and 2D peaks respectively [159].	63
Figure 3.21: (left) As-taken Raman spectra of before and after graphene growth on 6H-SiC substrate. (right) 2D-peak fitting with single Lorentzian function.	65
Figure 3.22: (a) Optical microscopic image of a typical TLM test structure fabricated in this work. (b) TLM plot of total resistance as a function of channel length.	66

LIST OF FIGURES

Figure 3.23: (a) Optical microscopic image of a fabricated Van der Pauw device (Hall cross) used in this thesis and (b) the sketch of an as-grown graphene sample measured in another Van der Pauw configuration.	67
Figure 3.24: (left) Typical Hall bar structure (right) Hall bar pattern fabricated in this work.	68
Figure 3.25: Extracted mobility and carrier densities of as-grown blanket epitaxial graphene samples used this thesis.	69
Figure 3.26: Different noise types present in a low-frequency noise spectrum.....	69
Figure 3.27: Block diagram of a typical low-frequency noise measurement set-up.	70
Figure 3.28: Typical $1/f$ noise spectrum observed in graphene.....	71
Figure 4.1: (left) schematic cross section of a two-terminal graphene device showing the transfer of injected carrier from the metal into the graphene channel. (right) An equivalent circuit for the contact resistance as a series resistor network.	74
Figure 4.2: a) AFM topography image of an as-grown epitaxial graphene in vacuum. Scale bar is $10\ \mu\text{m}$ and b) Raman spectrum of the as-grown graphene film.....	77
Figure 4.3: Conventional lithography process steps followed for the graphene device fabrication.....	78
Figure 4.4: (a) I-V characteristics of Cr/Au and Ti/Au metal contacts (b) TLM plot of total resistance against varying channel lengths for Cr/Au and Ti/Au contacts at 20°C and 400°C	79
Figure 4.5: (a) Raman 2D-peak taken from the (a) Ti/Au contact location, which showed bi-layer graphene and (b) Cr/Au contact regions, showing tri-layer graphene.....	79
Figure 4.6: (a) Temperature dependence of sheet resistance extracted from TLM method and b) comparison of contact resistance between Cr/Au and Ti/Au contacts as a function of temperature.....	80
Figure 4.7: (a) Effect of ambient annealing on R_c of Ti/Au contacts, which resulted in considerable improvement in the room temperature performance of the contacts. (b) GAXRD spectrum of the samples after annealing.	81
Figure 4.8: (a) Raman spectrum of as-grown graphene film in Ar atmosphere, showing characteristics G and 2D peaks. (b) Optical microscopic image of different types of fabricated devices on the epitaxial graphene.	83
Figure 4.9: (a) Effect of annealing environment on the device electrical resistance (b) I-V characteristics of devices annealed in different annealing environments, showing ohmic behaviour.	84

LIST OF FIGURES

Figure 4.10: TLM plots of samples annealed in a) ambient air, b) vacuum and c) N ₂ /H ₂ atmosphere.	85
Figure 4.11: (a) Extracted sheet resistance values from (a) TLM and (b) Van-der-Pauw test structures before and after annealing in different annealing environmental conditions.	86
Figure 4.12: Influence of different annealing environments on the contact resistance.	87
Figure 4.13: AFM topography images of the graphene surface at different annealing temperatures and the corresponding height profile images. All scale bars in the figures are 2µm.	88
Figure 4.14: RMS surface roughness of epitaxial graphene as a function of temperature at different annealing environments.	89
Figure 4.15: Surface chemistry of graphene surface for a) as-grown, b) as-fabricated, c) N ₂ /H ₂ annealed at 200°C, d) 300°C, e) 350°C and f) 400°C.	91
Figure 4.16: Structures of chemical compounds present in a typical novolac photoresist: a) DNQ or Diazonaphthoquinone b) 1-methoxy-2-propyl acetate and c) novolac resin.	93
Figure 4.17: The impact of a) vacuum annealing and b) N ₂ /H ₂ annealing the graphene mobility.	94
Figure 4.18: Lithography process steps followed for the graphene device fabrication using Al(O _x) based sacrificial layer approach.	97
Figure 4.19: AFM topography and line profile images (a) as-grown graphene surface 10×10 µm (left) and 3×3 µm area (right). b) Just after lithography and before the metal deposition. Scale bars in the images (a) and (e) are 2 µm, whilst its 600 nm for the images (b) and (f) ...	99
Figure 4.20: Process flow used for examining the surface cleanliness of graphene using conventional direct lithography and sacrificial layer approach.	100
Figure 4.21: AFM topography image of the graphene channel region, showing clean and contaminated areas after photoresist removal. Clean region was initially covered with Al(O _x) layer prior to photoresist spinning, whilst other half the sample was left as-is. The corresponding height profiles show that thickness of resist residues were found to be as high as 10 nm. Scale bar is 4 µm.	100
Figure 4.22: C1s spectra of (left) as-grown and (right) Sacrificial layer treated epitaxial graphene.	101
Figure 4.23: (a) Effect of different processing conditions on the device electrical resistance. (b) TLM plot of N ₂ /H ₂ annealed and Al(O _x) sacrificial layer fabricated structures.	102

LIST OF FIGURES

Figure 4.24: (a) TLM plot of Ti/Au and Ni/Au contacts showing the variation in total resistance (b) Sheet resistance of Al(OX) layer processed sample extracted using TLM and Hall measurements.....	104
Figure 4.25: Evaluation of contact resistance of metal-graphene interfaces for a wide range of metallisation schemes. Note, all these metals were capped with 175 nm Au layer.....	104
Figure 5.1: a) XPS survey spectra of graphene before and after HF treatment and b) deconvoluted high resolution XPS Si2p spectra after HF treatment showing Si-C, O-Si-C and SiOx peaks.....	115
Figure 5.2: XPS Survey spectra of as-grown and as-functionalised epitaxial graphene samples at different operating pressures.	116
Figure 5.3: a) surface at% of oxygen and carbon derived from the XPS survey spectra with the increasing plasma pressure. b) Effect of plasma pressure on C/O ratios in functionalised graphene.....	117
Figure 5.4: High resolution C1s spectrum of an as-grown, HF treated sample showing deconvoluted peaks of SiC, graphene and interfacial layer respectively.....	118
Figure 5.5: High resolution XPS C1s deconvoluted spectra of as-functionalised graphene samples at a) 25 mTorr, b) 50 mTorr, c) 75 mTorr and d) 90 mTorr. Increasing the pressure leads to an increase in the concentration of oxygen functional groups.....	119
Figure 5.6: a) the relative contribution of C1s peak components estimated by dividing the area under each component by whole C1s peak area. b) Estimation of the distribution of O-functional groups on the graphene surface by dividing the area of area O-functional groups to the area of C-C peak.....	120
Figure 5.7: Deconvoluted XPS O1s spectra of as-functionalised samples at a) 25 mTorr b) 50 mTorr, c) 75 mTorr and d) 90 mTorr pressure.....	122
Figure 5.8: Concentration of oxygen functional groups on the graphene surface functionalised at different operation pressure.....	123
Figure 5.9: Deconvoluted Si2p spectra of functionalised samples at different operating pressures, showing negligible change to the O-Si-C or SiOx peaks.	125
Figure 5.11: RMS roughness of functionalised graphene with the increasing pressure. Solid line is guide to the eye only.	126
Figure 5.11: (top) AFM topographic images of the graphene surface before and after oxygen functionalisation. (bottom) corresponding surface roughness measured on the sample step terraces	126

LIST OF FIGURES

Figure 5.12: Raman spectra of graphene with characteristic G and 2D peaks. Inset shows the 2D-peak fitted with a single Lorentzian.	127
Figure 5.13: Evolution of Raman spectra of epitaxial graphene with the increasing plasma pressure.	129
Figure 5.14: a) The plot of an average size of nanocrystallites as a function of plasma pressure b) Correlation between the ratio of the integrated intensities of D and G peaks (I_D/I_G) vs $1/L_a$. Solid lines are guide to the eye only.	130
Figure 5.15: Illustration of a) structurally distorted region (red colour) and defect activated region (green colour) (b) Evolution of disorder and defect regions with the increasing defect density.	130
Figure 5.16: a) I_D/I_G ratio of all functionalised samples as a function of average defect distance. b) Estimated defect density at each functionalisation pressure. Solid lines are guide to the eye only.	131
Figure 5.17: Dependence of of a) integrated intensity ratio and b) FWHM of 2D and G peaks on the plasma pressure. Solid lines are guide to the eye only.	132
Figure 5.18: Change in the shape and intensity of 2D peak at different plasma pressures and the corresponding peak fitting using single Lorentzian function shown in solid lines.	133
Figure 5.19: a) G and 2D peak positions of graphene with the increasing plasma pressure. b) Relative shift of G and 2D peaks with respect to the as-grown graphene peak positions. Solid lines are guide to the eye only.	134
Figure 5.20: Relative shift of G (left) and 2D peak (right) positions as a function of induced strain by oxygen functional groups. Solid line indicates linear fits. The slopes of the fitting lines are also included.	136
Figure 5.21: Change in intrinsic strain in graphene as a function of plasma pressure. Solid lines are guide to the eye only.	Error! Bookmark not defined.
Figure 5.22: Schematic energy diagrams showing the effective hole doping of epitaxial graphene after O-functionalisation at 90 mTorr pressure.	138
Figure 5.23: a) Plot showing the change in carrier density and mobility as a function of plasma pressure. b) Decrease in conductivity of functionalised epitaxial graphene films with the increasing functionalisation pressure	139
Figure 6.1: Schematic cross section of process steps followed for samples functionalised using method-A (top) and method-B (bottom) approaches.	144
Fig. 6.2: High resolution XPS C1s spectra of epitaxial graphene taken before and after oxygen plasma functionalisation using methods A and B respectively.	145

LIST OF FIGURES

Figure 6.3: High resolution XPS O1s spectra of a) method-A and b) method-B sample....	148
Figure 6.4: Raman spectra of unfunctionalised graphene and O-functionalised graphene using method-A and method-B approaches	149
Figure 6.5: Raman spectra of method-B sample taken at patterned graphene edge before and after functionalisation, showing significant doping. Solid lines indicate Lorentzian fittings.	153
Figure 6.6: Raman spectra of method-B sample showing the magnitude of doping at basal plane areas and at patterned graphene edge sites. Solid lines indicate Lorentzian fittings...	154
Figure 6.7: Change in carrier mobility of unfunctionalised graphene, method-A and method-B functionalised graphene samples. Dashed lines indicate guide to the eye only.	156
Figure 6.8: Dependence of carrier mobility on the sheet carrier density of unfunctionalised and functionalised graphene samples.	157
Figure 6.9: Change in sheet resistivity of graphene before functionalisation and after functionalising using method-A and method-B approaches. Dashed lines indicate guide to the eye only.	158
Figure 6.10: a) I-V characteristics of method-A and method-B functionalised sample b) TLM plot corresponding method-A and method-B sample. Solid lines in (b) indicates TLM linear fits.	159
Figure 6.11: Low-frequency noise characteristics of unfunctionalised graphene, method-A and method-B functionalised graphene samples. Solid lines indicate logarithmic curve fittings.	161
Figure 6.12: a) Normalised noise amplitude of unfunctionalised, method-A and method-B functionalised samples b) Correlation between noise amplitude and the I_D/I_G ratio.....	164
Figure 6.13: Log scale plot of the noise amplitude normalised by resistance as a function of device channel length for method-A and method-B samples. Dashed lines indicate power-law fits.	165
Figure 6.14: Log scale plot of the noise amplitude normalised to device channel area as a function of device channel resistance for method-A and method-B samples. Dashed lines are guide to the eye only.....	166
Figure 7.1: (Left) schematic cross section of a two-terminal chemiresistor device and (Right) AFM topographic images of a Van der Pauw device test structure.....	170
Figure 7.2: a) AFM topographic image and b) the XPS C1s spectrum of the graphene after N_2/H_2 annealing for 60 min.....	172

LIST OF FIGURES

Figure 7.3: Raman spectrum of graphene showing G and 2D peaks. The 2D-peak was fitted (solid line) with a single Lorentzian function.....	173
Figure 7.4: Typical I-V characteristics of a chemiresistor before and after N ₂ /H ₂ anneal...	173
Figure 7.5: The chemical sensing behaviour of epitaxial graphene sensors to the saturated vapours of polar protic and polar aprotic chemicals in the ambient.	175
Figure 7.6: Elovich plots showing the relative resistance variation of the graphene sensor with linear fits to a) polar aprotic and b) polar protic vapour.	176
Figure 7.7: Relationship between the dipole moment of a chemical and the magnitude of UFEG sensor response.	178
Figure 7.8: Change in adsorbate induced charge carrier density with the increasing dipole moment of a chemical.....	179
Figure 7.9: Low-frequency noise spectra of graphene in air and during exposure to a) H ₂ O ₂ and b) ethylene glycol vapours.....	180
Figure 7.10: Change in noise amplitude and the Hooge parameter as a function of dipole moment of the chemical and the induced carrier density.	181
Figure 7.11: XPS C1s spectrum of oxygen functionalised graphene at 75 mTorr pressure.	182
Figure 7.12: Raman spectra of graphene before and after O-functionalisation at 75 mTorr	183
Figure 7.13: Change in I-V characteristics of an OFEG sensor exposed to polar protic and aprotic chemical vapours.	184
Figure 7.14: Sensing behaviour of an OFEG sensor to polar protic (EG) and polar aprotic (NMP and DMAC) chemical vapours.	185
Figure 7.15: Comparison between UFEG and OFEG chemiresistor sensor responses upon exposure to the vapours of a) DMAC and b) H ₂ O ₂	186
Figure 7.16: Change in resistance of OFEG chemiresistor sensors exposed to polar protic and aprotic chemical vapours.	187
Figure 7.17: Repeatability and long-term stability of OFEG sensors. a) Variation in resistance of several chemiresistors after exposure to different chemical vapours followed by recovery. b) Resistance of chemiresistors over 160 days taken after recovery. Solid line is guide to the eye only.	188
Figure 7.18: Low-frequency noise behaviour of a) unfunctionalised graphene and b) oxygen functionalised graphene in open air and under exposure to DMF vapour. Solid lines are logarithmic fits to the experimental data.	190

LIST OF FIGURES

- Figure 7.19: The noise spectra of O-functionalised graphene sample after de-oxygenation, i.e. removing O-functional groups from the graphene surface. 191
- Figure 7.20: Influence of metal contacts on the $1/f$ noise response of graphene devices. ...192

List of tables

Table 2.1: Comparison of material properties of 3C-SiC, 4H-SiC and 6H-SiC to those of Si and GaAs at room temperature ([67]).....	18
Table 4.1: Work function (WF), binding energy (B.E), Diffusion energy barrier (E_{Diff}), effective metal-graphene distance ($d_{\text{M-G}}$) and lattice mismatch of all metals used in this study.	105
Table 4.2: Comparison of the best reported contact resistance values in the literature using different pre or post fabrication treatment with the current study.....	108
Table 5.1: Comparison of conductivity values of rGO with the present work. Note, the thicknesses of the reported rGO films/flakes are usually from few layer to multi-layer....	139
Table 6.1: Differences in the relative concentration of O-functional groups present on the graphene surface after functionalisation at 75 mTorr pressure using method-A and method-B approaches.....	147
Table 6.2: Raman data for method-A functionalised sample.....	151
Table 6.3: Raman data of method-B functionalised sample taken from different areas of the sample.	154
Table 6.4: Room temperature Hall measurements of unfunctionalised, method-A and method-B functionalised graphene samples.	155
Table 6.5: Electrical characteristics of metal-oxygen functionalised graphene interfaces extracted from TLM measurements	160
Table 7.1: List of polar analytes used in this study, their molecular properties [308] and relative resistance response.	174

Acronyms

<i>Acronym</i>	<i>Expansion</i>
<i>CVD</i>	Chemical Vapour Deposition
<i>NMP</i>	N-methyl-2-pyrrolidone
<i>DMF</i>	Dimethylformamide
<i>IPA</i>	Isopropyl Alcohol/Isopropanol
<i>EG</i>	Ethylene glycol
<i>DMSO</i>	Dimethylsulphoxide
<i>DMAC</i>	Dimethylacetamide
<i>CNT</i>	Carbon Nanotube
<i>MWNT</i>	Multi-Walled Carbon Nanotube
<i>XPS</i>	X-ray Photoelectron Spectroscopy
<i>AFM</i>	Atomic Force Microscopy
<i>E-beam</i>	Electron-beam
<i>TLM</i>	Transmission Line Model
<i>SiC</i>	Silicon Carbide
<i>SLG</i>	Single Layer Graphene
<i>BLG</i>	Bi-Layer Graphene
<i>TLG</i>	Tri-Layer Graphene
<i>FLG</i>	Few-Layer Graphene
<i>MLG</i>	Multi-Layer Graphene
<i>GO</i>	Graphene Oxide
<i>rGO</i>	Reduced Graphene Oxide
<i>HOPG</i>	Highly Oriented Pyrolytic Graphite
<i>UHV</i>	Ultra High Vacuum
<i>IFL</i>	Interface Layer
<i>TEM</i>	Transmission Electron Microscopy
<i>SEM</i>	Scanning Electron Microscopy
<i>LEEM</i>	Low-Energy Electron Microscopy
<i>STM</i>	Scanning Tunnelling Microscopy
<i>TiC</i>	Titanium Carbide

ACRONYMS AND NOTATIONS

<i>DOS</i>	Density of States
<i>RIE</i>	Reactive-Ion-Etching
<i>RTP/RTA</i>	Rapid Thermal Processing/Rapid Thermal Annealing
<i>RMS</i>	Root-Mean-Square
<i>FWHM</i>	Full-Width at Half Maximum
<i>LNA</i>	Low-Noise Analyser
<i>FFT</i>	Fast-Fourier Transform
<i>MOSFET</i>	Metal Oxide Field Effect Transistor
<i>PMMA</i>	Poly (methyl methacrylate)
<i>GAXRD</i>	Glancing Angle X-ray Diffraction
<i>TMAH</i>	Tetramethylammonium hydroxide
<i>Al(O_x)</i>	Aluminium Oxide
<i>CMOS</i>	Complementary Metal-Oxide-Semiconductor
<i>DFT</i>	Density Functional Theory
<i>UFEG</i>	Unfunctionalised Epitaxial Graphene
<i>OFEG</i>	Oxygen functionalised Epitaxial Graphene
<i>MeOH</i>	Methanol
<i>BZ</i>	Benzaldehyde
<i>AA</i>	Acetic Anhydride
<i>NNPSD</i>	Normalised Noise Spectral Density
<i>MBE</i>	Molecular Beam Epitaxy
<i>DNQ</i>	Diazonaphthoquinone

Notations

<i>Notation</i>	<i>Definition</i>
E_F	Fermi Energy
E_D	Dirac Point
ρ_{sh}	Sheet resistivity
Φ_M	Metal work-function
χ	Electron affinity
μ_H	Hall mobility
Φ_G	Graphene work-function
R_{sh}	Sheet resistance
R_C	Contact resistance
A_N	Noise amplitude
α_H	Hooge parameter
λ	Scattering mean free path
λ_m	Metal-graphene coupling length
R_T	Total resistance
E_{Diff}	Diffusion energy barrier
d_{M-G}	Effective metal-graphene contact distance
L_a	Average size of nanocrystalline region
L_D	Average distance between two defect sites
n_D	Average defect density
$\omega_G^o, \omega_{2D}^o$	G and 2D peak positions of pristine graphene
$\omega_D, \omega_G, \omega_{2D}$	D-peak, G-peak and 2D-peak positions of as-grown graphene
$\Delta\omega_G, \Delta\omega_{2D}$	Shift in G and 2D peak positions with respect to pristine graphene
δ_G, δ_{2D}	Shift in G and 2D peak positions with respect to as-grown graphene
γ_G, γ_{2D}	Gruneisen parameter for G and 2D peaks, respectively
$\epsilon_G, \epsilon_{2D}$	Calculated strain for G and 2D peaks

Chapter 1

Introduction

1.1 Allotropes of carbon

Carbon is one of the most abundant elements in the universe and forms the basis of all organic structures, including the naturally occurring life on earth. It is present in over 95% of known chemical compounds overall and in terms of flexibility in bonding, it is unrivalled by any of the other elements of the periodic table, where, carbon atoms can bind to both electronegative and electropositive atoms and are able to form long chains or crystals [1, 2]. Even when the interaction with other elements is excluded, carbon atoms possess an extraordinary versatility in bonding among themselves, which results in a variety of interesting allotropes [1, 2]. The diversity of bonds that it can make is well demonstrated in two of the best-known carbon materials, graphite and diamond. Despite consisting of the same element these two materials are very different from each other in terms of chemical, electrical and mechanical properties. For instance, diamond is the stiffest and is one of the strongest known materials, while graphite is one of the softest. Diamond is transparent, whilst graphite is an opaque material. Diamond is electrically insulating, whereas, graphite is highly conducting. Such a disparity in properties, despite being made of the same element is a result of differences in the arrangement of carbon atoms in these materials. There are many other allotropes of carbon (i.e. the materials which are entirely made of carbon atoms) that were recently discovered, which differ from each other only by the way the carbon atoms are arranged [1, 2]. According to the hybridisation of the carbon atomic orbitals, these carbon allotropes can be divided into three categories. First, when all carbon atoms are bonded in sp^3 hybridisation, diamond structures are formed, whilst, sp^2 hybridisation results in graphitic materials. The third category of carbon allotropes is amorphous carbons, which consist of

mixtures of sp^2 and sp^3 hybridised carbon atoms. A schematic overview of different allotropes of carbon is shown in Figure 1.1. Both diamond and amorphous carbon are interesting materials, but they play no role in this thesis and hence are not given any further attention.

1.2 Graphitic materials

Graphitic materials are a special class of allotropes with sp^2 hybridised carbon atoms, which can take any dimension ranging from zero-dimensional fullerene to three-dimensional graphite. They are commonly referred to as graphitic materials, because graphite is the best and the longest known representative of this class.

1.2.1 Graphite

Graphite is a naturally occurring allotrope of carbon, which was discovered in early 1500's [1]. As shown in the Figure 1.1, the structure of graphite consists of planes of covalently bonded carbon atoms arranged in hexagonal rings stacked on top of each other. These hexagonal carbon planes are held together by weak Van der Waals forces, resulting in an in-plane bond strength that exceeds the interlayer bonding by several orders of magnitude. For instance, the in-plane bond length of carbon atoms is 1.42 Å, whilst it is 3.35 Å for interlayer carbon bonds [1]. This weak bonding between the adjacent carbon planes enable them to slide over each other, making graphite particularly useful for applications such as in pencil leads and as a lubricant [1]. It is also used in nuclear reactors to control the nuclear fission reaction speed and also as a battery electrode to store the charge [1, 3, 4].

1.2.2 Fullerene and carbon nanotubes

Fullerene (C_{60}) or buckminsterfullerene or buckyballs was discovered in 1985 by R.E. Smalley, R.F. Curl Jr., and H.W. Kroto and were later awarded the Nobel Prize in chemistry in 1996 [5, 6]. Fullerene is a zero-dimensional molecule with discrete quantum energy states, in which carbon atoms are arranged in the form of a hollow sphere containing hexagonal and pentagonal rings as shown in Figure 1.1. Here the carbon atoms are sp^2 hybridised, but unlike in graphite, they are not arranged in a plane. The geometrical arrangement of fullerene strains the sp^2 hybridised carbon atoms, resulting in the semiconducting or insulating behaviour of the molecule.

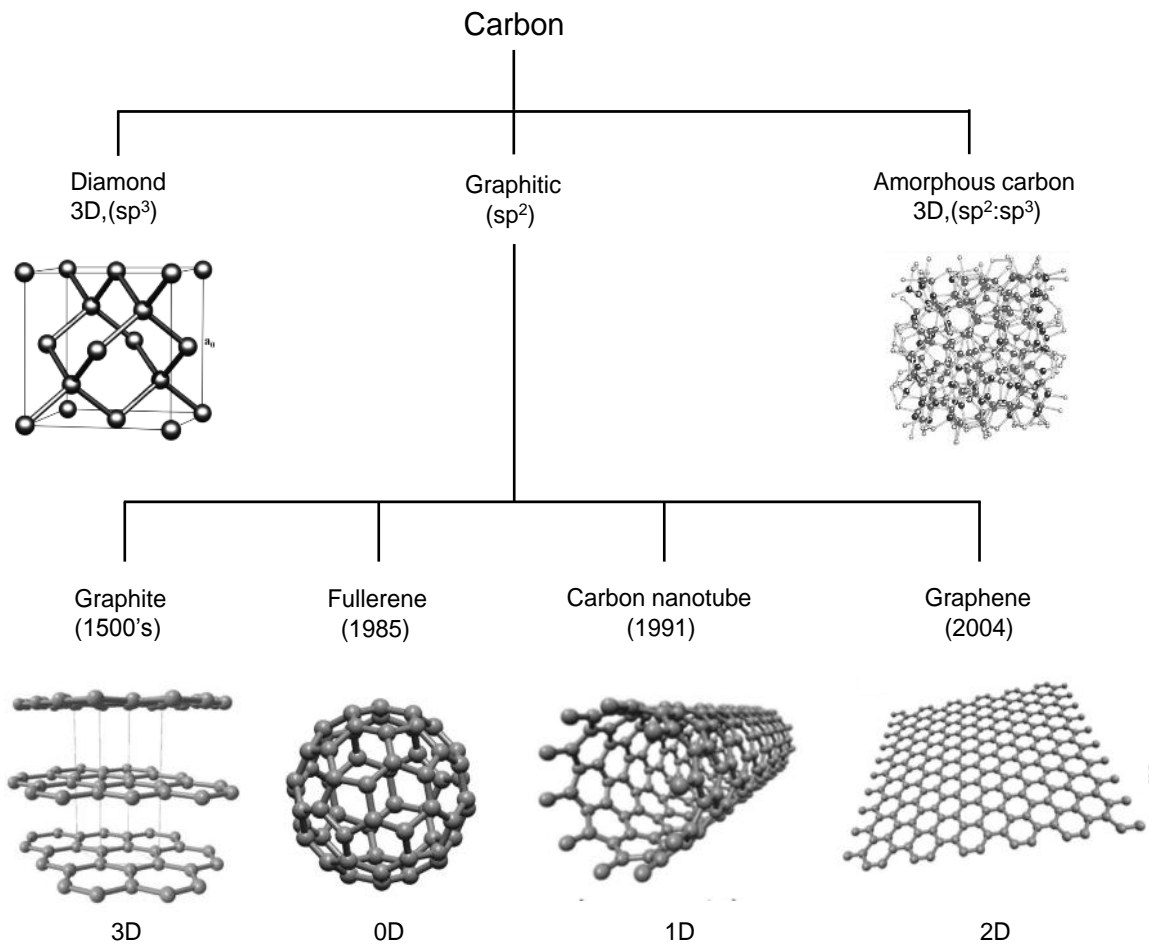


Figure 1.1: Schematic representation of different carbon allotropes, showing their dimensionality and hybridisation [9].

The other form of carbon allotrope is carbon nanotube (CNT), where the carbon atoms are bonded together in a hexagonal structure forming a hollow cylindrical shape as shown in Figure 1.1. Although the discovery of CNTs remains a contentious issue, Sumio Iijima is often credited with their official discovery in 1991 [7]. CNTs can be in the form of a single tube, referred to as single-walled nanotube (SWNT), or in the form of two or more concentric tubes positioned one inside the other, referred to as double-walled or multi-walled nanotubes (MWNTs), respectively. The quantum states in CNTs are restricted in such a way that electrons can only travel in one dimension, hence they can be thought of as one-dimensional materials [7-9].

1.2.3 Graphene: The non-existing material

The recently discovered allotrope of carbon is a two-dimensional material called *graphene*, where each carbon atom is bonded to three other carbon atoms to form a honeycomb like structure shown in Figure 1.1 [10]. Graphene has a number of unusual properties and plays an important role in understanding the properties of other carbon allotropes. For example, as represented in Figure 1.2, the three-dimensional material graphite can be obtained by stacking graphene sheets on top of each other, whereas, fullerenes can be created from graphene by curling it up with the introduction of pentagons in a systematic way. CNTs can be obtained by just rolling up a graphene layer(s) along a given direction [11].

Although graphene is the mother of all these allotropes, it is the last material to be discovered in the carbon family that gives access to all dimensions. This is because, it has been widely believed that single layers of graphene could not exist in a free standing state due to its two-dimensional structure. Peierls [12] and Landau [13] theoretically showed that the thermal fluctuations in low-dimensional crystals leads to such displacements of atoms that they become comparable to inter-atomic distances at any given temperature and therefore will be thermodynamically unstable and eventually curl up into carbon soot.

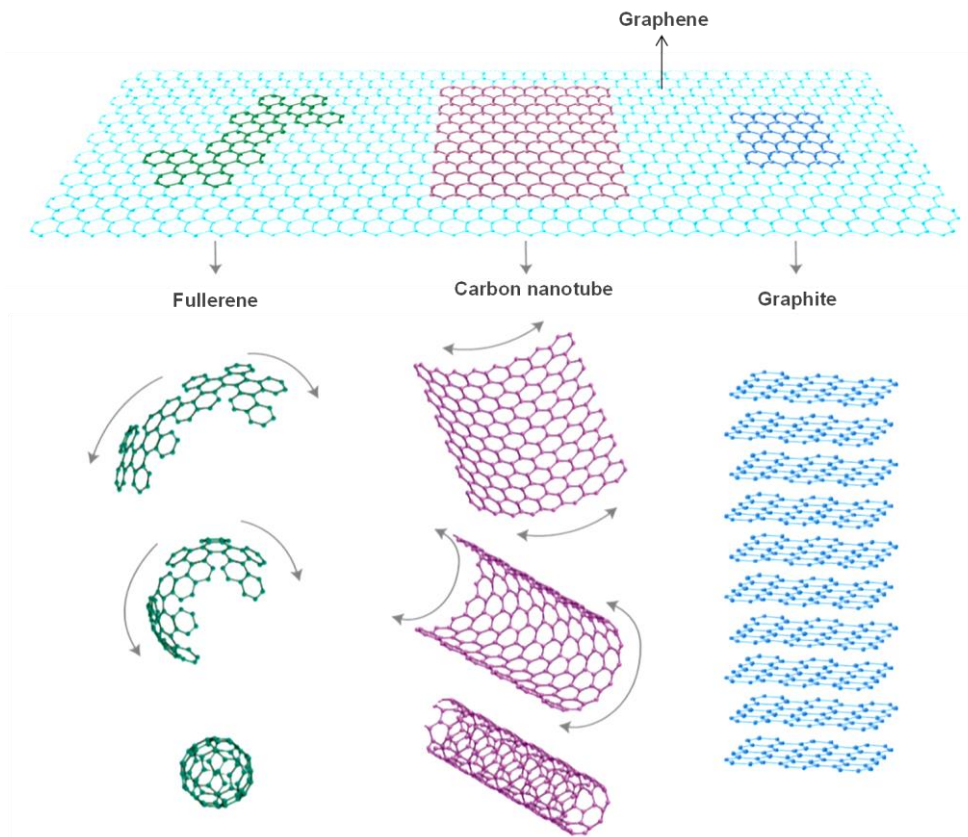


Figure 1.2: Graphene the mother of all graphitic carbon allotropes of different dimensionalities [11].

Experimental observations showing decreasing melting temperatures with the decreasing film thickness further provided strong support to this theory [14-16]. However, it came as a complete surprise to the scientific community when Geim and Novoselov *et al.* showed in 2004 that such single layer sheets can not only be isolated but can also be in a stable form at room temperature [10]. The apparent stability of graphene monolayers was later argued to be due to the soft crumpling in the third dimension (Figure 1.3 inset), which has been observed on a lateral scale of approximately 10 nm and is believed to suppress the thermal vibrations [17]. Nevertheless, the approach to produce graphene was based on an astonishingly simple method by repeatedly peeling of carbon layers from graphite until a single layer of carbon called *graphene* is achieved. Graphene is not only the first truly two-dimensional crystalline material to be discovered but also is the thinnest material, being one atom thick. This discovery had led to a Nobel Prize in physics, awarded to Geim and Novoselov in 2010 “for ground breaking experiments regarding the two-dimensional material graphene” [18]. Immediately, after this discovery, many other two-dimensional materials were discovered, including, molybdenum disulphide (MoS_2), boron nitride (BN), tungsten disulphide (WS_2), molybdenum diselenide (MoSe_2), tungsten diselenide (WSe_2) and many more [19]. However, despite their intriguing properties, none of these materials received the same level of attention or scientific interest as graphene did.

1.3 Motivation and objectives

Ever since the discovery of graphene in 2004, there has been an explosion of scientific research, resulting in an exponential rise in the number of research papers being published every year as shown in Figure 1.3. A brief timeline in the Figure 1.4 shows the important breakthroughs in the graphene research over the years. The primary reason for this sudden surge in interest in graphene is due to its exceptional material properties and the potential for applications in next-generation nanoelectronics [11, 20]. An overwhelming majority of studies on graphene was mainly performed on exfoliated graphene flakes. Although the exfoliated flakes are useful for investigating the fundamental properties of graphene and for demonstrating proof-of-concept devices, it is not compatible with the state-of-the-art Si fabrication process due to its low throughput and inability to produce large size graphene films. Alternatively, two large-scale methods were developed for industrial applications, which include, growth of graphene on metal foils/films using chemical vapour deposition, (CVD) technique and epitaxial graphene growth via thermal decomposition of SiC at high

temperatures (>1200°C) [21, 22]. Both these approaches have found their usefulness in different applications. For example, due to its low production cost and high throughput, CVD graphene films are currently being considered for developing touch screen displays

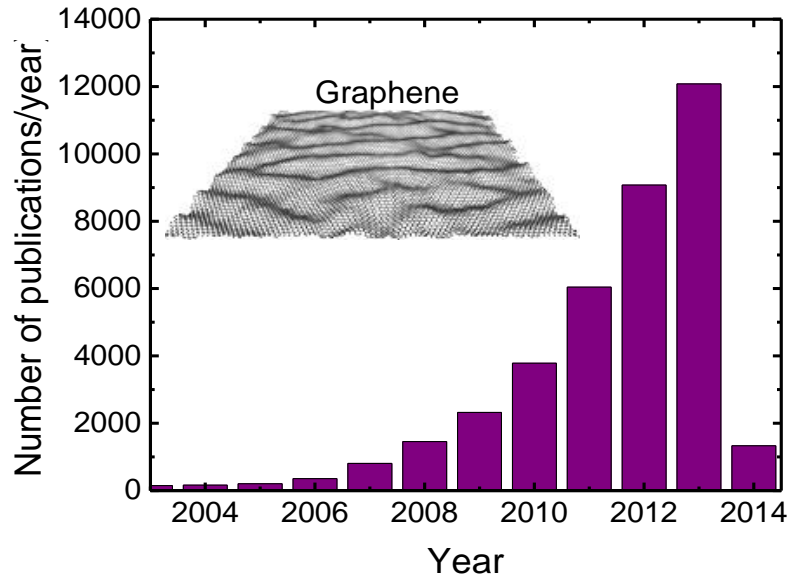


Figure 1.3: Exponential rise in the number of publications on the topic 'graphene'. Source: Thomson reuters web of knowledge (28th Feb 2014).

GRAPHENE TIMELINE

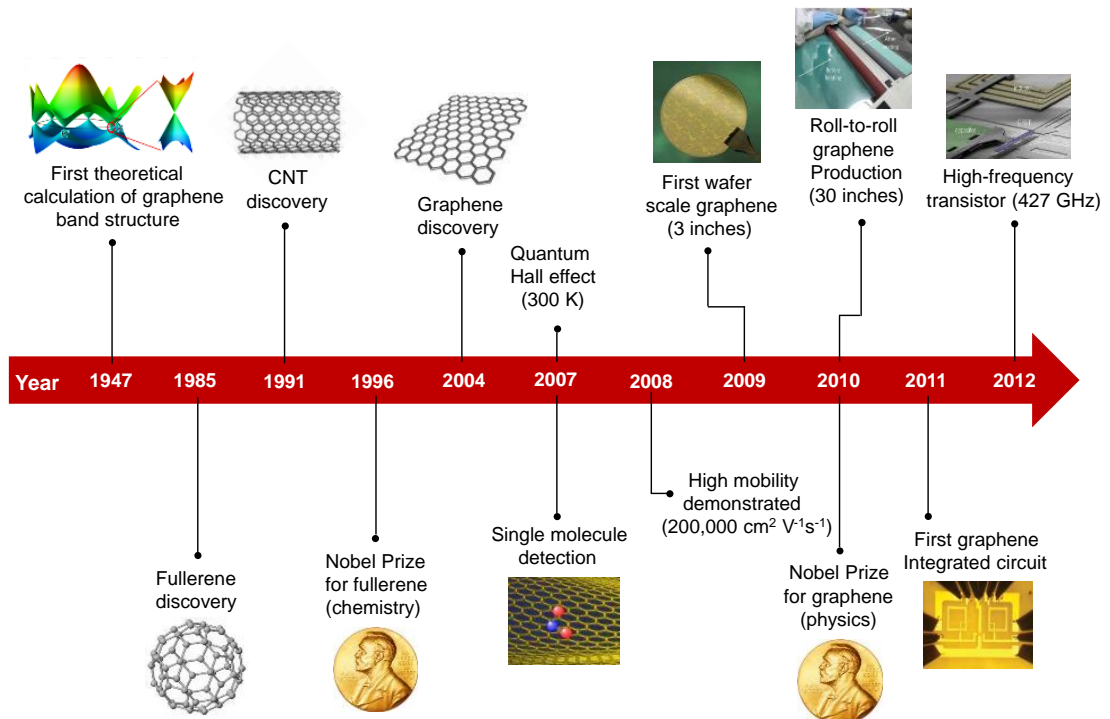


Figure 1.4: A brief timeline of the progress in graphene research over the years.

[23], transparent electrodes for solar cells [24] and memory devices [25] and for flexible electronic applications [23, 26]. In contrast, epitaxial graphene on SiC is intensely being researched for high-frequency electronics [27], chemical and biological sensors [28, 29], photonics and optoelectronic applications [30]. Among these, the chemical and biological sensing is particularly attractive because of the high specific surface area, exceptionally low electrical noise and highly sensitive electronic properties of graphene to surface chemical adsorbates. The performance of the sensor can further be improved by functionalising graphene with different reactive species, which facilitates the strong adsorption of a wide range of analyte molecules and enhances the sensitivity and selectivity of the sensor dramatically [31, 32]. One of the main advantages of graphene based sensors is their multi-functionality, i.e. a single graphene sensor device can be used for detecting the chemical environment as well as strain, pressure and the magnetic field, making it particularly useful for interactive consumer electronic applications [33].

Epitaxial graphene on SiC in particular is attractive for the fabrication of sensor devices, because, unlike CVD approach, graphene can be directly grown on semi-insulating SiC substrates [21], eliminating the need for transfer to other insulating materials. In addition, SiC has superior biocompatibility, in comparison to Si and is already being used as a base material for medical implants [34]. Therefore, epitaxial graphene directly grown on SiC could offer an attractive platform in developing advanced biomedical devices. Moreover, the fabrication of epitaxial graphene sensors is compatible with standard fabrication techniques and can also be easily integrated into the well-established SiC circuit technology.

However, before graphene can be used in practical sensor applications, there are several issues that need to be addressed. First, as graphene sensor devices require metal contacts to connect to other electronic device components, it is crucial to understand the effect of metal-graphene interfaces on the device electrical characteristics. It was shown that the choice of metal used as a contact electrode to the graphene can dramatically affect the operation of the device by increasing the metal-graphene interfacial contact resistance, thereby compromising the device performance [35]. Second, as graphene is sensitive to its surrounding environment, the performance of graphene based devices also strongly depends on device processing conditions. For example, it was shown that typical lithographic processing significantly contaminates the graphene surface and degrades the electronic properties by doping the graphene film and increasing the sheet resistance by several orders of magnitude [36, 37]. Since, graphene based sensors operate on the principle of changes in the electrical resistance

or conductance upon exposure to chemical vapours, maintaining low contact and sheet resistances are crucial for maximising the sensor response. In addition, clean and contamination free graphene surfaces are required to eliminate spurious sensing responses and also for efficient functionalisation of graphene [36]. Therefore, before fabricating epitaxial graphene based chemical sensors, these potential difficulties will have to be investigated and overcome. In this thesis, epitaxial graphene films grown on the Si-face of 6H-SiC substrates were used to understand the effect of processing conditions, influence of surface functionalisation on the chemical, electrical, structural and sensing properties of fabricated graphene devices.

1.4 Thesis outline

The thesis is structured into eight chapters, with the first chapter being this introduction. In chapter 2, a brief background on the electronic and structural properties of graphene is presented along with a review on different methods used for the graphene synthesis. In particular, a detailed discussion on the growth of epitaxial graphene films on SiC substrates is presented. The influence of metal contacts on the electrical properties of graphene devices and the significance of graphene surface functionalisation for the development of graphene based chemical sensors for practical applications is discussed in detail.

Chapter 3 highlights the experimental procedures used in this thesis. First, the epitaxial graphene growth procedure is discussed, followed by a brief description of the electron-beam plasma based oxygen functionalisation process. In addition, an overview of the process steps employed for fabricating transmission line model (TLM) structures, Van der Pauw test structures and Hall bar patterns are described. A detailed overview of different surface and electrical characterisation techniques used for analysing the chemical, electrical and structural properties of graphene is also discussed.

In chapter 4, the influence of metal contacts, the effect of photolithography processing and high-temperature annealing on the electrical characteristics of metal-graphene interfaces was investigated. In order to minimise lithography induced contamination, two methods were developed here, in which, for the first method, rapid thermal annealing of graphene devices was performed in N_2/H_2 atmosphere, whilst the second utilises a metal sacrificial layer to prevent graphene from coming into direct with photoresist during the lithography process. Chemical, electrical, structural and surface analysis showed that clean graphene surfaces can be achieved by both these methods, which allowed the intrinsic properties of

graphene to be measured. TLM results showed that Ti with significant lattice mismatch along with its highly reactive nature can destroy the graphene lattice and leads to high contact resistance, whereas, Ni was found to produce lowest contact resistance among all the metals investigated due to its lowest lattice mismatch with the graphene film.

Chapter 5 presents the oxygen functionalisation of epitaxial graphene films using electron-beam generated plasmas. XPS revealed the presence of different oxygen functional groups (eg. hydroxyl, epoxy, carbonyl and ether) on the graphene surface, whilst Raman spectroscopy showed the transformation of planar sp^2 symmetry of graphene to distorted sp^3 hybridisation as a result of plasma treatment. In addition, it was found that oxygen plasma treatment results in strain relaxation, in which the intrinsic compressive strain present in epitaxial graphene film decreases progressively with the increasing plasma pressure. Hall measurements showed p-type doping of O-functionalised graphene films with induced carrier densities of up to $5 \times 10^{14} \text{ cm}^{-2}$ obtained at the highest oxidation pressure (90 mTorr).

A systematic study on the effect of oxygen functionalisation on the electrical characteristics of epitaxial graphene-metal contact interfaces is presented in Chapter 6. Two functionalisation approaches were investigated, wherein, for the first approach, oxygen functionalisation was performed on as-grown blanket graphene films, followed by device fabrication (method-A) and for the second approach, device fabrication was performed first, followed by oxygen functionalisation (method-B). Hall, TLM and low-frequency noise characterisation demonstrated that functionalising graphene after device fabrication (i.e method-B) yields superior electrical properties with high mobility, low contact resistance, low sheet resistance and substantially lower noise characteristics without significantly degrading the structural characteristics of graphene.

Chapter 7 demonstrates the chemical sensing behaviour of unfunctionalised and oxygen functionalised graphene chemiresistor sensors to a wide range of polar chemical vapours in the ambient atmosphere. Specifically, the effect of chemical polarity and the significance of dipole moment on the sensing properties of graphene were studied using two-probe, Hall and $1/f$ noise measurements. It was found that oxygen functionalisation not only enhances the sensitivity of the sensor by two-fold, but also significantly improves the recovery time (30s-150s), in comparison to unfunctionalised graphene sensors (1h-2 h).

Finally, chapter 8 provides the key conclusions from the results presented in the thesis. In addition, a future outlook on the development of graphene chemical sensors and the strategies required for the commercialisation of graphene sensor technologies is outlined.

Chapter 2

Literature review

2.1 Introduction

Graphene has been attracting enormous scientific attention from physicists, chemists, material scientists and engineers due to its wide range of potential applications. Nevertheless, the term ‘graphene’ has been inconsistently used by many researchers in the literature [38], leading to some confusion in its fundamental definition. Graphene can be either defined by its electronic properties or by its physical properties. However, since the electronic properties of graphene can significantly change depending on the substrate it is lying on [39], or even by just exposing to the ambient atmosphere [40], it is highly recommended to use the physical properties when defining graphene. In this thesis, the following definitions were adopted: graphene or single layer graphene (SLG) or monolayer graphene all represent one sheet of sp^2 bonded carbon atoms, in which each carbon atom is covalently bonded to three nearest neighbouring atoms in the plane with a C-C distance of 0.142 nm to form a hexagonal lattice structure, as shown in the Figure 2.1(a). Bilayer graphene (BLG) and trilayer graphene (TLG) represent two and three individual sheets of graphene layers stacked on top of each other, respectively. Few layer graphene (FLG) indicates a stack of four to five graphene layers, whilst multilayer graphene (MLG) is a stack of six to ten graphene layers. Note, the term ‘pristine graphene’ in this thesis refers to the graphene which is in undoped, unstrained and unperturbed state.

2.2 Graphene properties

Despite the simplicity of the lattice structure, graphene exhibits some remarkable material properties, which exceed those obtained from any other material measured to-date. For example, the strong covalent bonds between the in-plane carbon atoms of the graphene sheet gives the material exceptional mechanical strength that despite being so thin, graphene is stronger than the hardest known substance diamond on the same thickness scale with an Young's modulus of 1TPa and an intrinsic strength of 130 GPa [41]. Despite its hardness, it is the only crystal that can be stretched elastically by 20% in one dimension without breaking [41]. In addition to the mechanical strength, graphene is highly transparent (97.7%) [42], yet it is so dense that not even Helium atom can pass through it [43]. The two-dimensional nature of graphene also makes it an ultimate surface material with the largest specific surface area as high as 2630 m²/g [44]. Furthermore, graphene possess extremely high thermal conductivity of up to 5000 W mK⁻¹ [45], in comparison to CNTs (3500 W mK⁻¹) or diamond (2500 W mK⁻¹), whilst the electrical resistivity of graphene (1.0×10⁻⁶ Ω-cm) is also better than the best known conducting materials such as Ag (1.59×10⁻⁶ Ω-cm) and Cu (1.68×10⁻⁶ Ω-cm) [46]. In fact, graphene is currently being explored for resistance standard measurements in metrology, where the graphene grown on SiC has already been demonstrated to deliver superior resistance accuracy than conventionally used GaAs based heterostructures [47]. In terms of carrier mobility, graphene is by far the best material with a room temperature mobility of over 200,000 cm² V⁻¹ s⁻¹ [48, 49], whilst the next closest material is InSb with a mobility of 77,000 cm² V⁻¹ s⁻¹ at room temperature [11].

2.3 Electronic structure of graphene

The fascinating properties of graphene, in particular the electronic properties of graphene actually arise from the honeycomb lattice structure and exhibits a basis with two carbon atoms A and B per unit cell (see Figure 2.1(a)). The carbon atom consists of four valence electrons, where three are bonded to three nearest neighbouring carbon atoms in the plane by strong σ (sigma) bonds. The electrons participating in these bonds do not participate in electron transport but provide the graphene sheet with exceptional mechanical strength. All of the unusual electronic properties of graphene arise from the fourth valence electron. This conduction electron oscillates up and down perpendicular to the graphene plane and produces a p_z orbital. As the bonding distance between the carbon atoms is very small, the

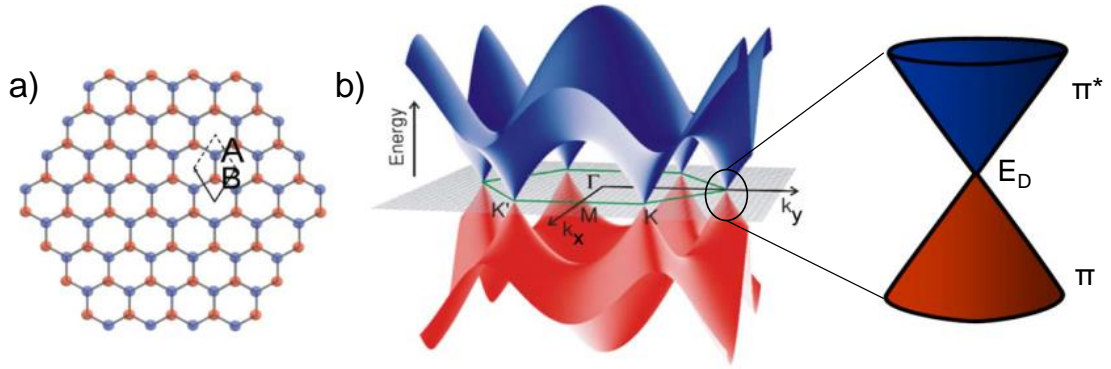


Figure 2.1: (a) Illustration of the hexagonal lattice structure of graphene showing unit cell with two carbon atoms A and B. (b) Electronic band structure of graphene obtained from theoretical calculations [9].

p_x orbital of one carbon atom overlaps with the p_x orbital of neighbouring carbon atom to form π -bonds that lead to delocalised electron π -bands. By using tight-binding calculations the electronic properties of graphene can be addressed by calculating the π -band structure, as shown in Figure 2.1(b). Note, although graphene was discovered in 2004, the electronic band structure was calculated as early as in 1947 by Wallace *et al.* [50]. The band structure calculations in Figure 2.1(b) shows an unusual structure, where the lower valance band (π) and the upper conduction band (π^*) meet each other at the K and K' points. This crossing point is called the Dirac point (E_D). For an undoped graphene, the position of Fermi energy (E_F) is exactly located at E_D , where the valance and conduction band overlap smoothly without repulsion or bandgap opening. As a consequence, graphene is usually described as a zero-bandgap semiconductor or more precisely as a semi-metal [51]. As highlighted in Figure 2.1(b), π -bands exhibit linear dispersion around E_D , with an energy $E = \hbar v_F |\mathbf{k}|$. Here, v_F is Fermi velocity in graphene, which is approximately 10^6 m/s, \hbar is Planck's constant, and \mathbf{k} is the wave vector measured from K [51]. A linear dispersion usually characterizes particles whose kinetic energy vastly exceeds their rest mass. Hence, electrons in graphene mimic the behaviour of photons or ultra-relativistic particles such as neutrinos with an energy-independent v_F that is 300 times smaller than the speed of light [51]. Due to the absence of bandgap, graphene exhibits an ambipolar behavior, where the charge carrier can be continuously tuned between electrons to holes with carrier concentrations as high as 10^{13} cm⁻². With the increase in graphene thickness, electronic properties also change dramatically. Figure 2.2 shows that evolution of band structure calculated using tight binding calculations for monolayer to few layer graphene [51, 52]. As can be seen, the bilayer graphene exhibits parabolic bands that touch at the Dirac point, exhibiting the semi-metallic behavior similar

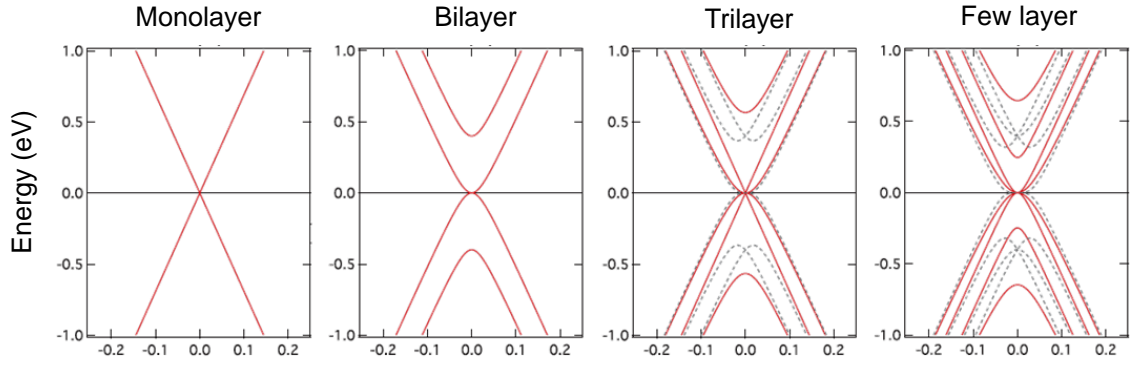


Figure 2.2: Evolution of the band structure of graphene with the increasing thickness [52].

to monolayer graphene. In the case of tri-layer and few layer graphene, the band structure not only depends on the number of layers but also on their stacking sequence. Each new layer adds two π -bands to the existing band structure, making it more complex and eventually reaching the band structure of graphite.

2.4 Synthesis of graphene

The development of graphene based electronics depends on the large scale availability of the material. There are several methods to produce graphene, including, mechanical exfoliation, liquid-phase exfoliation, laser ablation and photo-exfoliation, chemical vapour deposition (CVD) on metal substrates, epitaxial growth on SiC, molecular beam epitaxy (MBE) and metal-catalysed crystallisation of amorphous carbon [33, 53]. Nevertheless, much of the research attention has been focused on mechanical exfoliation, CVD graphene growth and the epitaxial graphene on SiC techniques.

2.4.1 Mechanical exfoliation

This technique is remarkably simple, which consists of repeated mechanical peeling of graphene layers from high quality graphite crystals such as highly ordered pyrolytic graphite (HOPG) using an adhesive tape as shown in Figure 2.3(a) [54]. These exfoliated graphene flakes are then transferred on to a SiO_2 surface for characterisation and device fabrication. It was shown that the thickness of these transferred graphene flakes can be easily identified from the variation in contrast of different layers in an optical microscope as shown in Figure 2.3(b), provided the thickness of SiO_2 is 300 nm. The largest flake sizes that can be achieved currently using this technique are in the order of millimetres [55] and hence, it is not suitable

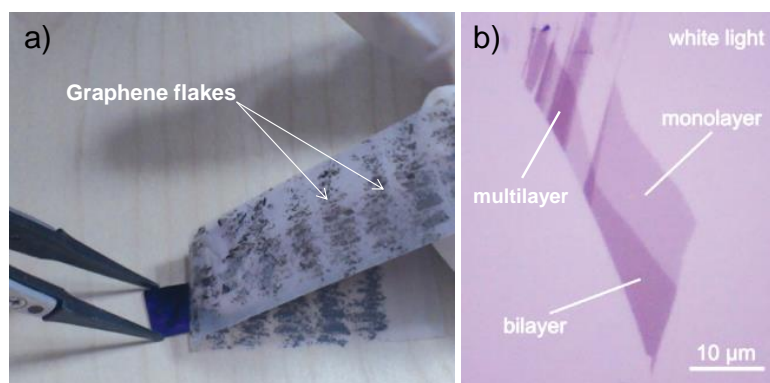


Figure 2.3: (a) Digital image of mechanical exfoliation and transfer process of graphene flakes. (b) Optical microscopic image of a graphene flake showing different contrasts for monolayer, bilayer and multilayer graphene [54].

for large scale industrial applications. Nevertheless, the quality of graphene produced by the mechanical exfoliation technique still outperforms the quality of graphene grown by other methods. Mobilities in excess of $200,000 \text{ cm}^2 \text{ V}^{-1} \text{ s}^{-1}$ were achieved for current annealed suspended single layer graphene devices at room temperature [48, 49], while as-fabricated unsuspended graphene devices typically show mobilities in the range of $10,000$ to $20,000 \text{ cm}^2 \text{ V}^{-1} \text{ s}^{-1}$ [56]. Due to the inexpensive nature of producing flakes, along with the ability to achieve excellent crystal quality, mechanical exfoliation technique is predominantly used for research purposes to demonstrate proof-of-concept devices and to develop an in-depth understanding of chemical, electrical, mechanical and optical properties of graphene.

2.4.2 CVD growth on metals

The CVD grown graphene on metal substrates is one of the most successful growth techniques developed for mass production. Previous studies have shown that graphene can be grown on a wide range of metals, including, Pt, Cu, Au, Rh, Ir, Ni, Co and Ru [53, 57-59]. However, metals like Ti, Hf, Zr and Ta were found to be not compatible for the graphene growth, because of their large lattice mismatch ($>20\%$) and carbide forming nature [53, 57, 58]. The growth on Pt, Au and Ir is rather expensive for commercial production, in comparison to metals such as Ni and Co, hence large proportion of studies were mainly focused on these metals. In addition, the lattice mismatch between Ni and Co with graphene is less than 2% . Nevertheless, the uniformity of graphene films grown on these metal films is highly inhomogeneous with considerable variation in thickness.

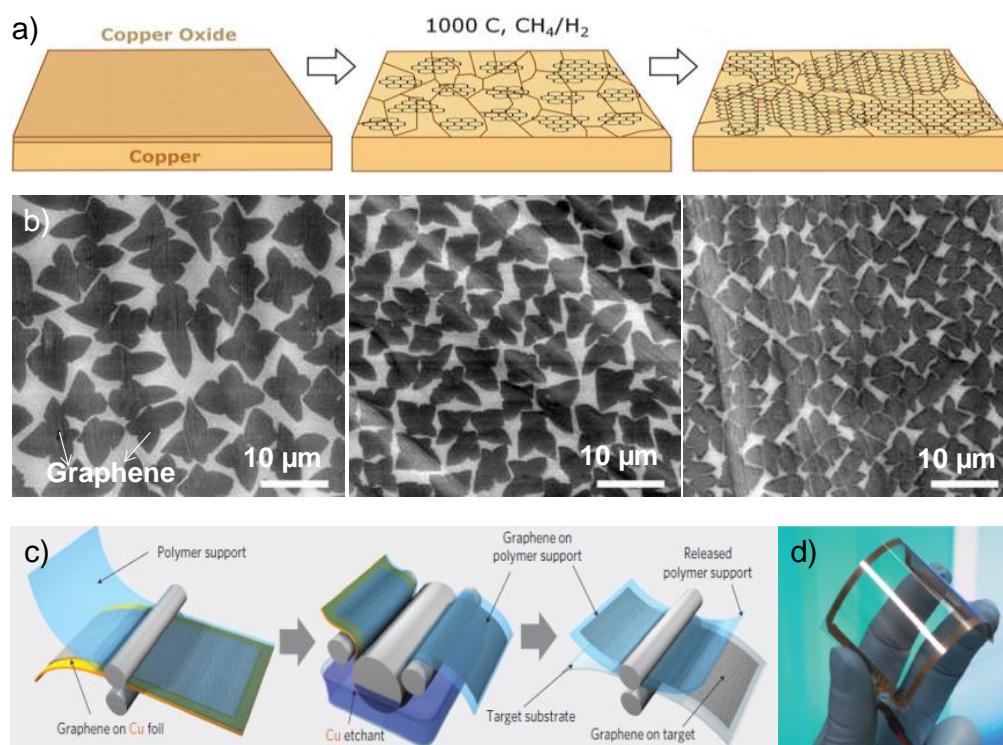


Figure 2.4: (a) Schematic of the CVD growth process on Cu foils. (b) SEM images showing the evolution of individual graphene domains to form a continuous film (c) illustration of roll-to-roll production of CVD graphene (d) a prototype of a graphene based touch screen display [23,58,59].

The first successful attempt to grow large area ($\sim\text{cm}^2$) uniform graphene film on a metal surface was performed by Ruoff *et al.* in 2009 on polycrystalline Cu foils [60]. The major advantage of growing graphene on Cu is that the growth is self-limited, i.e. the growth of graphene stops as soon the Cu surface is fully covered with graphene. Using this technique, single layer graphene can be grown uniformly on the Cu surface and just 5% of the area was found to be of bilayer and trilayer graphene. The growth of such controlled thickness over large areas was possible mainly due to the low carbon solubility in Cu and its mild catalytic activity. Here, the typical growth process includes, annealing of Cu foil in Ar/H₂ atmosphere at around 1000°C to remove impurities and oxides from the Cu surface and to increase the Cu grain size. This is followed by introducing hydrocarbon source such as methane in to the Ar/H₂ gas flow and again annealing at around 1000°C, which leads to the graphene formation. The growth mechanism was found to be nucleation of carbon atoms on Cu after decomposition of hydrocarbons, in which the nuclei grow into large domains as shown in the Figure 2.4(b). Mobilities achieved using this CVD growth technique on metals are usually between 1000 to 7,000 $\text{cm}^2 \text{V}^{-1} \text{s}^{-1}$ at room temperature.

Following the initial work, graphene growth on Cu was scaled up to an incredible 30 inches using roll-to-roll process [23]. The relatively cheap nature of Cu and the high yield production of reasonably good quality graphene films makes the Cu based CVD growth approach attractive for mass production. For instance, graphene grown by CVD approach is currently being considered for non-electrically active applications such as transparent conducting electrodes for touch screen displays, solar panels and for flexible electronic applications as shown in Fig. 2.4(d). However, despite the large area uniform growth of graphene, there are some challenging issues and drawbacks with this technique for electronic applications. First, an order of magnitude difference in thermal expansion coefficient between graphene and Cu leads to wrinkling of graphene film during the cooling stage of the growth process. The wrinkles are defective in nature and degrade the performance of a device significantly through defect scattering, similar to the effect of grain boundaries observed in conventional materials [61]. In addition, as the growth is performed on conductive metal substrates, transfer of graphene film to other insulating substrates such as SiO₂ is required for using in electronic device applications. The PMMA resist, which is commonly used as a support layer during the transfer, significantly contaminates the graphene film with resist residues even after its removal and hence high temperature thermal annealing is required for cleaning these as-transferred graphene films [62]. In addition, breaking of graphene film or mechanical damage to the film is highly likely during the transfer process, leading to a compromised quality of the final transferred layers.

2.4.3 Epitaxial growth on SiC

Epitaxial graphene growth on SiC has been proposed as a promising route to produce high quality wafer scale graphene films for electronic device applications [33]. This method is based on thermal decomposition of SiC at high temperatures in ultra-high vacuum (UHV) or argon atmosphere conditions. The advantage of this method is insulating SiC substrates can be used for the graphene growth so that additional transfer or cleaning step is not required. Key factors that govern the epitaxial graphene synthesis are the quality of the SiC substrate, specifically its orientation, surface preparation and sublimation conditions.

2.5 SiC as a template for the graphene growth

SiC is a wide-bandgap (2.2 to 3.3 eV) compound semiconductor composed of silicon and carbon atoms in equal stoichiometry [63]. SiC is mechanically robust and exhibits high

breakdown voltage, high thermal conductivity and high saturation velocity. Due to these unique properties SiC is commonly used in high temperature, high power and high frequency device applications [64, 65]. In addition, SiC is also used as a substrate material for GaN based light-emitting diodes (LEDs) [66].

2.5.1 SiC crystal structure

The atomic structure of SiC consists of a silicon (carbon) atom covalently bonded to four carbon (silicon) atoms in tetrahedral configuration with a bond length of 1.89 \AA as shown in Figure 2.5(a) [9]. Combining these tetrahedral structures together, a planar hexagonal symmetry is formed as shown in Figure 2.5(b). Such a layer is referred to as a SiC bilayer, which acts as a basic building block for the SiC crystal structure. The bulk structure of SiC can be formed by stacking these hexagonal SiC bilayers on top of each other. SiC exhibits about 200 polytypes with equal number of Si and C atoms [63]. The most stable polytypes are 3C-SiC, 4H-SiC and 6H-SiC as shown in Figure 2.5 with the layer orientation and the stacking sequence for each polytype indicated by a bold dark line. Here, C and H represents ‘cubic’ and hexagonal’ respectively. Figure 2.5(c) shows the cubic structure with three bilayers per unit cell, hence the name 3C-SiC, whereas, Figure 2.5(d) represents the hexagonal structure with four bilayers per unit cell, 4H-SiC and Figure 2.5(e) also shows the hexagonal

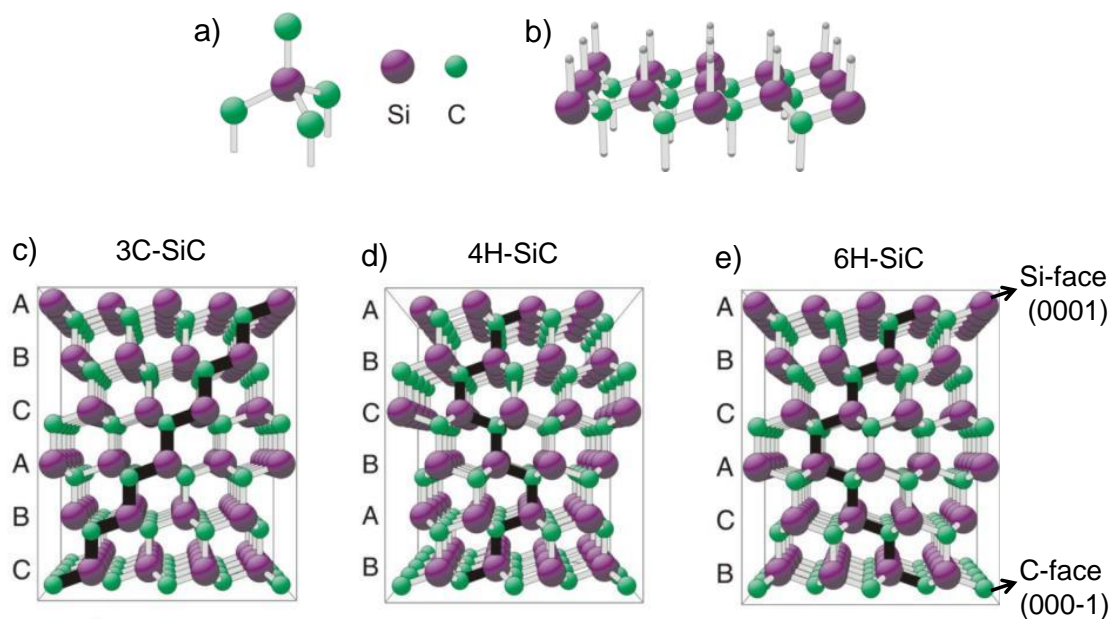


Figure 2.5: (a) Tetrahedral bonding in SiC (b) Hexagonal SiC as a basic building block of the SiC crystal structure. Crystal structures of (c) 3C-SiC (d) 4H-SiC and (e) 6H-SiC [9].

Table 2.1: Comparison of material properties of 3C-SiC, 4H-SiC and 6H-SiC to those of Si and GaAs at room temperature ([67])

Material properties	3C-SiC	4H-SiC	6H-SiC	Si	GaAs
Band gap (eV)	2.2	3.26	3.02	1.11	1.43
Thermal conductivity (W/cmK)	5.0	5.0	5.0	1.5	0.5
Electron mobility ($\text{cm}^2 \text{V}^{-1} \text{s}^{-1}$)	1000	900	450	1400	8500
Maximum operating temperature ($^{\circ}\text{C}$)	1240	1240	1240	300	460
Breakdown field (MV/cm)	-	3.0	3.0	0.3	0.4

structure with six bilayers per unit cell, 6H-SiC. All these polytypes exhibit different physical properties as shown in the Table 2.1, particularly, the stacking sequence effects the bandgap, in which it ranges from 2.2 for 3C-SiC to 3.26 for 4H-SiC. Currently the SiC wafers that are used for commercial electronic applications are predominantly produced in 4H and 6H-SiC polytypes.

2.5.2 SiC surface preparation and graphene growth

As shown in Figure 2.5(a-c), SiC consists of two polar surfaces perpendicular to the c -axis: a Si-terminated SiC (0001) surface often referred to as Si-face and the C-terminated SiC (000-1) referred to as C-face. Regardless of the polarity of the surface (i.e. either C-face or Si-face), surface preparation of SiC prior to graphene synthesis is essential for achieving high quality uniform graphene films. As even the highest grade SiC wafers have surface scratches as a result of chemical mechanical polishing (Figure 2.6(a)), it is important to remove the polishing damage before the samples can be graphenised. The most popular method used for efficient cleaning of SiC surfaces is H_2 etching. Here, SiC samples are usually subjected to a flow of H_2 at temperatures of 1600°C around 100 mbar pressures. At these conditions, H_2 etches away approximately 200 to 500 nm of the original SiC top surface, removing the surface polishing damage and leaves behind highly ordered atomically flat stepped surfaces as shown in Figure 2.6(b). After this initial surface preparation, epitaxial graphene is grown by thermal annealing of the sample at elevated temperatures in different annealing environments. However, it should be noted that the graphene growth mechanism and surface morphology is very different on the Si-face of the SiC substrate, in comparison to the C-face, as described below.

2.5.2.1 Graphene growth on Si-face

Initial studies on the Si-face epitaxial graphene growth were performed in UHV environment at temperatures just above 1150 °C [21, 68]. Here, annealing SiC at such high temperatures leads to the sublimation of Si atoms from the substrate due to the high vapour pressure of Si, leaving behind carbon atoms. These left-over carbon atoms rearranges to form a commensurate superstructure on top of the SiC surface with $(6\sqrt{3} \times 6\sqrt{3})R30$ periodicity and interacts strongly with the SiC substrate as depicted in Figure 2.7 [69]. This layer is also called as an interface layer, buffer layer or a zero layer. It was shown that this interface layer is always oriented 30° with respect to SiC substrate due to the difference in graphene lattice constant (2.46 Å) to that of SiC (3.07 Å). Despite being geometrically similar to graphene, the interface layer does not possess any of the graphenic properties due to its covalent interaction with the dangling Si atoms on the Si-face of the SiC [69, 70]. This interface layer is electrically inactive. Upon annealing for longer time, more Si atoms sublime, resulting in the formation of a first graphene layer as shown in the Figure 2.7. However, as shown in Figure 2.6(c), synthesis of graphene under UHV conditions produces very rough film morphology,

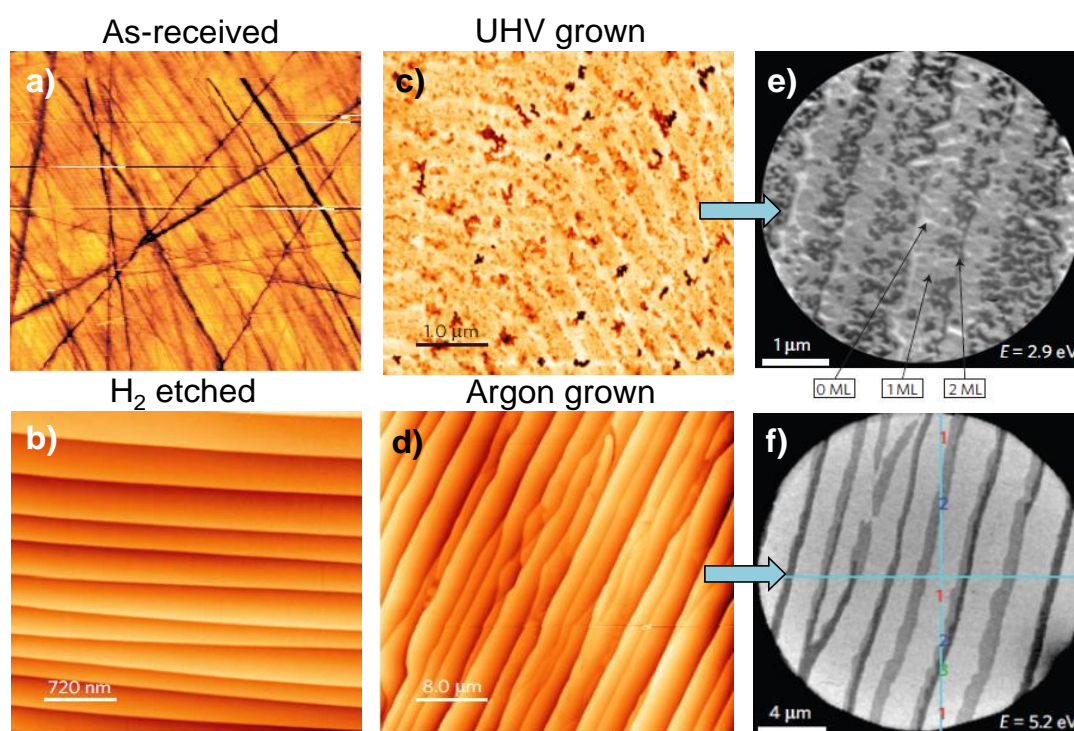


Figure 2.6: (a) as-receive SiC substrate showing polishing damage on the surface (b) Formation of smooth steps after H₂ etching (c) Swiss-cheese like pattern of the graphene surface after UHV growth (d) Increased SiC step terrace width after graphene growth in Ar (e) and (f) LEEM images of corresponding UHV and Ar grown graphene film morphology, respectively [71,72].

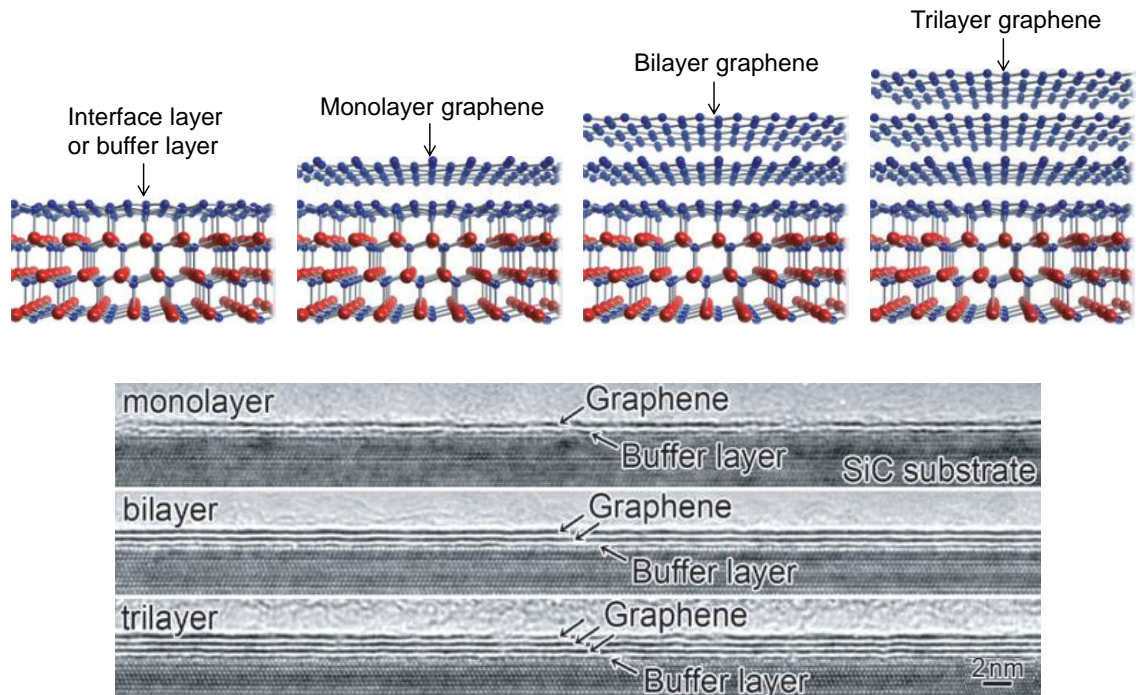


Figure 2.7: (top) Images showing the interface layer, monolayer, bilayer and tri-layer graphene films on 6H-SiC (0001) substrate. (bottom) Corresponding TEM images [69].

consisting of irregular steps and terraces with pit formation of up to 10 nm in depth, leading to non-uniform growth of graphene with varying thickness across the substrate.

In order to produce homogenous large area graphene films, annealing SiC in an Ar environment was proposed [71, 72]. This method involves heating the substrate at high temperatures to sublime Si and form graphene layers as in the first method; however, in the presence of Ar atmosphere instead of vacuum. The presence of Ar leads to reduced sublimation rates of Si due to the backscattering of Si atoms to the SiC surface after collision with Ar atoms. Hence the annealing temperature to form graphene is increased significantly to above 1600°C in comparison to vacuum annealing process. This increased temperature leads to improved growth kinetics of the graphene in terms of its homogeneity and thickness over wafer-scale range [71, 72].

The AFM topography image in Figure 2.6(d) shows the smooth terraces after the graphene growth, compared to a highly disordered “Swiss-cheese” like appearance for the UHV grown sample (Figure. 2.6(c)). The thickness of graphene grown on the Si-face of SiC using Ar approach is typically one to about three layers as shown in the corresponding low-energy electron microscopy (LEEM) image in Figure 2.6(c,f). Similar to the UHV approach, the first layer grown after sublimation of Si is an interface layer followed by single and bilayers

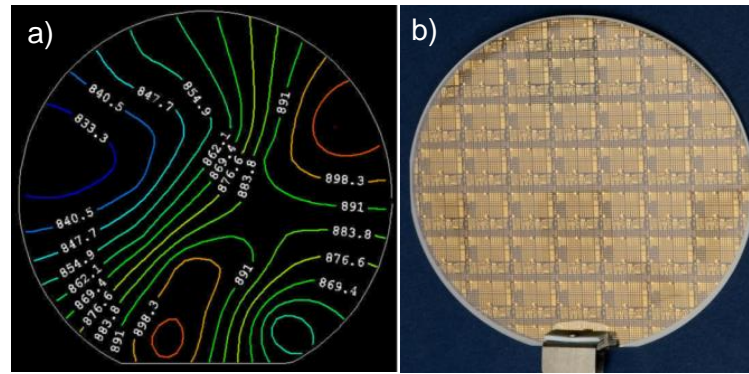


Figure 2.8: (a) Leighton image of epitaxial graphene grown on 72 mm diameter 6H-SiC (0001) wafer and (b) Processed epitaxial graphene wafer into MOSFETs [73].

situated predominantly at the terrace and step-edge regions respectively (Figure 2.6(f)). Graphene layers grown on top of this buffer layer are Bernal stacked, which are oriented with a 60° rotation relative to the bottom graphene layer about z-axis with half of the carbon atoms lying directly over the centre of a hexagon and half directly over the carbon atoms of the lower graphene sheet. The electronic nature of graphene grown using this approach on the Si-face of SiC shows n-type character due to the electron doping from the dangling bonds of Si. Typically, this charge transfer is between $\sim 5 \times 10^{12} \text{ cm}^{-2}$ to $1 \times 10^{13} \text{ cm}^{-2}$ and the room temperature mobility is around $700 \text{ cm}^2 \text{ V}^{-1} \text{ s}^{-1}$ to $2000 \text{ cm}^2 \text{ V}^{-1} \text{ s}^{-1}$.

Recently, Moon and Gaskill *et al.* [73] have shown the graphene sheet resistance variation, as measured by contactless Leighton resistivity mapping technique (Figure 2.8) on a 75 mm Si-face 6H-SiC wafer ranged from $825 \text{ } \Omega/\text{sq}$ to $920 \text{ } \Omega/\text{sq}$ (5.5% variation), demonstrating the superior control of thickness using the Ar mediated growth approach.

2.5.2.2 Graphene growth on C-face

Graphene grown on C-face is very different from Si-face, both in terms of growth mechanism and electron transport properties [74]. For example, the growth rate is significantly higher on C-face, which generally leads to graphene layers of about 5-10 layers thick. As a result of its high reactivity, growing monolayer films is extremely challenging on the C-face of SiC. The growth of graphene does not only start at the step edges but also on terraces in multilayer form and then grows in all directions of the surface. These as-grown multilayer graphene films are less homogenous, in comparison to Si-face graphene [74]. AFM topography image in Figure 2.9 shows the difference in surface morphology of graphene grown on the Si-face and the C-face of 6H-SiC. In C-face, the stacking sequence of graphene

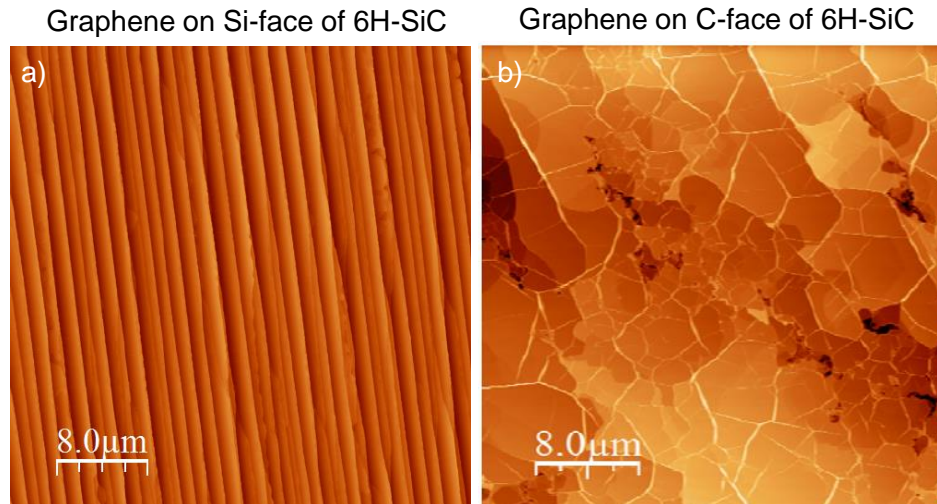


Figure 2.9: AFM topography image of as-grown graphene on the (a) Si-face of the 6H-SiC and (b) C-face of the 6H-SiC

is rotationally disordered with weak interaction between layers.

Unlike graphene on the Si-face, graphene grown on the C-face does not have interface layer, thus no significant charge is induced from the SiC substrate. Incredibly, the charge carrier type and carrier density varies with the layer depth [75]. For instance, it was shown that graphene layers(s) closest to the SiC substrate are slightly n-type in character due to the dangling bonds of the carbon rest atom in the SiC (0001) surface reconstruction, whereas, intermediate layers were found to be nearly charge neutral and the layers exposed to the ambient air were doped p-type due to the charge transfer from the hydroxyl or oxygen molecules. Nevertheless, as an aggregate, these graphene layers act as p-type, with carrier densities between ~ 0.2 to $1 \times 10^{13} \text{ cm}^{-2}$ and typical mobilities in the range of 10,000 to 30,000 $\text{cm}^2 \text{ V}^{-1} \text{ s}^{-1}$ at room temperature. Although graphene on C-face has superior electronic properties, it is currently less desirable for high frequency device applications due to the high charge density, which varies with the depth, making the device gating difficult.

2.5.3 Effect of SiC polytype on the graphene growth

In addition to surface polarity and growth conditions, very recently Yakimova *et al.* [76, 77] have shown that the polytype of SiC substrate also has substantial impact on the graphene growth morphology, which indirectly affects the graphene electrical properties. In particular, a significant variation in the thickness uniformity of monolayer graphene was observed on 4H-SiC (0001), 6H-SiC (0001) and 3C-SiC (111) substrates. Figure 2.10(a,b,c) shows the AFM topography images of all three polytypes exhibiting different step morphology and

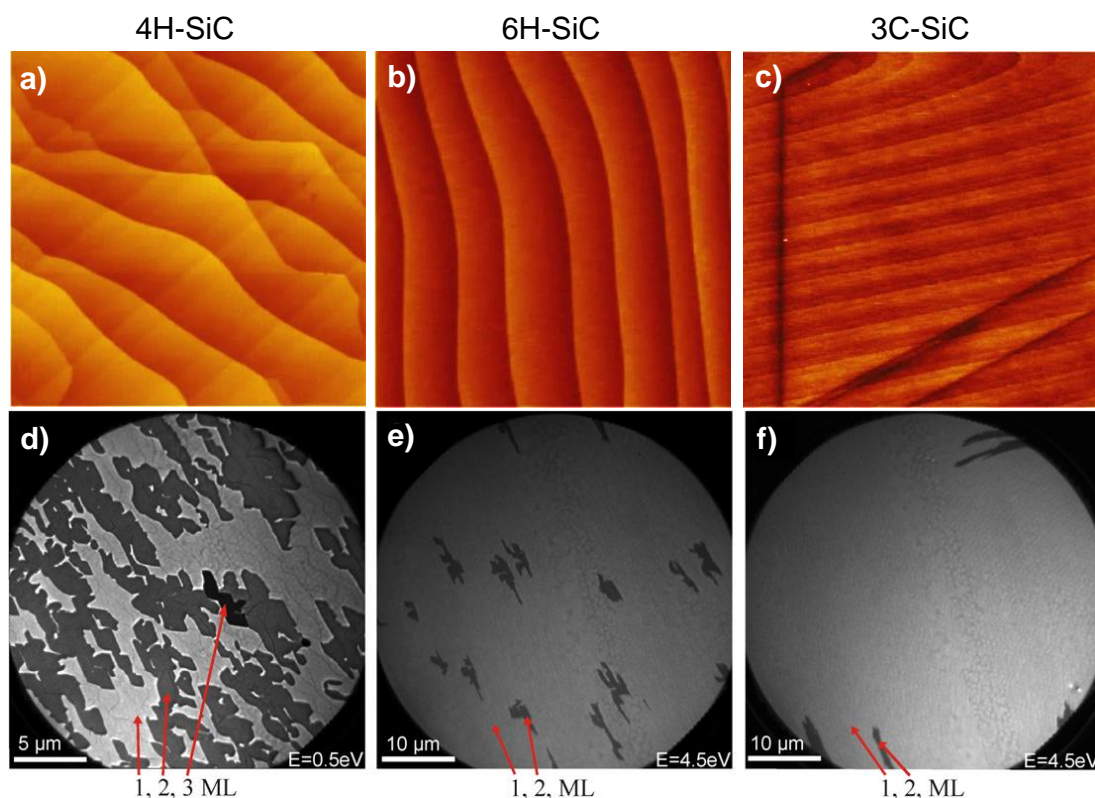


Figure 2.10: (a),(b) and (c) AFM topography images of different SiC polytypes. (d),(e) and (f) are the corresponding LEEM images showing the graphene thickness uniformity [76,77].

Figure 2.10(d,e,f) shows the LEEM images of graphene grown on these substrates. As can be seen from the contrast, graphene growth on 4H-SiC (0001) mainly results in 60% coverage of monolayer, whilst bilayer and trilayer constitute for remaining 40%. In the case of 6H-SiC (0001), 92% of the substrate is covered with monolayer graphene, whereas, an incredible 98% monolayer coverage was achieved using 3C-SiC (111) substrates, demonstrating superior growth kinetics achieved using 3C-SiC polytype. However, the main limitation in using 3C-SiC substrates is, they are not currently commercially available. Nevertheless this work is a significant step forward in realisation of graphene based electronics for practical applications. In this thesis, all epitaxial graphene samples were grown on 6H-SiC substrates.

2.5.4 Other growth methods on SiC

In addition to Si sublimation approach, epitaxial graphene on SiC can also be grown using other approaches such as CVD technique, in which, a combination of propane and argon gas at temperatures between 1500-1700°C graphene results in the formation of high quality epitaxial graphene films. Similarly, growth of graphene using MBE approach has also been

demonstrated in producing uniform graphene films. For more information regarding these techniques see references [78] and [79], respectively.

2.6 Importance of metal contacts on graphene

Since graphene is sensitive to the surrounding environment, any materials such as metal electrodes that come in to direct contact with the graphene surface can have dramatic impact on its electronic properties [35]. Since electronic devices inevitably require metal contacts, understanding the electrical characteristics of metal-graphene interfaces is therefore crucial for the performance of graphene devices.

Figure 2.11 shows the energy band diagrams of a) metal-semiconductor b) metal-metal and c) metal-graphene contact interfaces [80]. In the first case, when a metal and a semiconductor come into contact, charge transfer occurs from higher energy state to the lower energy state until the Fermi energy levels of both metal and semiconductor are balanced in thermal equilibrium state. This builds-up Schottky barrier, $\phi_B = \phi_M - \chi$ at the interface, where ϕ_M and χ are the work function of a metal and the electron affinity of a semiconductor, respectively. Due to the small density of states in a semiconductor, energy band bending occurs as shown in Figure 2.11(a), in the depletion region with a depletion width of W_{dp} . In contrast, the metal/metal contact has no potential barrier and hence charge carriers transfer directly through the interface to cancel the difference in work functions. However, the small redistribution of the electron cloud can screen this potential difference

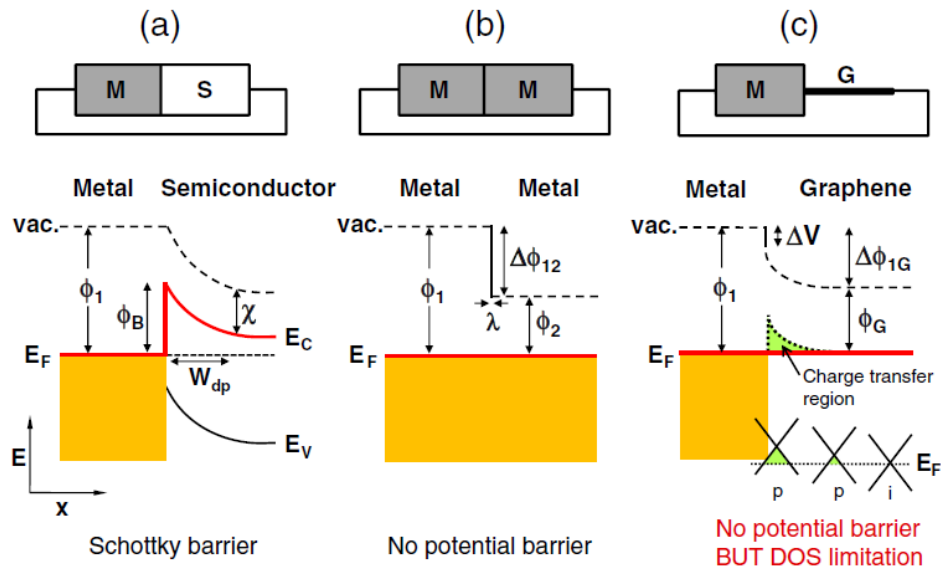


Figure 2.11: Schematic illustration of the interface at (a) metal-semiconductor (b) metal-metal and (c) metal-graphene interfaces [80].

because of the large carrier density. In general the screening length is very short in metals (typically in fraction of a nm), therefore the vacuum level changes sharply at the metal-metal interface [80].

In the case of metal-graphene contact, the interface can be considered similar to that of metal-metal contact due to the semi-metallic behaviour of graphene. Nevertheless, metal electrodes often dope graphene when in contact, in which, the type and the magnitude of doping depends on the metal work function. Such doping behaviour cannot be explained by the conventional Schottky–Mott model and hence Giovannetti *et al.* [81, 82] have developed a model in which Pauli’s repulsive interaction and electron transfer are assigned as two main factors for interfacial doping. Figure 2.11(c) shows the charge transfer process at metal-graphene interface, which gradually decreases from the interface. As a result of the charge transfer, a dipole layer at the interface is formed with an associated potential step ΔV , which depends on the strength of the metal-graphene interaction.

Giovannetti *et al.* showed that the interaction of metal contacts with graphene can be classified in to two categories: physisorption and chemisorption [82]. Here, physisorption refers to weak bonding of metal atoms with the carbon atoms in the graphene film, whilst chemisorption refers to strong covalent bonding with the graphene film. It was found that the transmission probability of charge carriers across the metal-graphene interface significantly increases for chemisorbed metals, in comparison to the metals that physisorbs to graphene due to the short metal-graphene distances. The direction and the magnitude of the charge transfer, however depend on the nature of metal contacts. For example, as shown in the Figure 2.12(top), deposition of weakly interacting metals such as Ag and Cu shifts the Dirac point of graphene towards negative gate voltages, whereas, positive voltage shift was observed for Au contact, which also has weak interaction with the graphene [83].

It can also be seen in Figure 2.12(middle) that that the electronic band structure of graphene obtained by DFT calculations showed no significant alteration after the deposition of these metals [82]; however, E_F shifted away from E_D , resulting in an effective increase in carrier density (electrons or holes) in graphene underneath the metal. For instance, an upward shift in E_F was observed for Ag and Cu contacts, making graphene n-type, whilst a downward shift in E_F was seen for Au, suggesting p-type doping of the graphene film. With the increasing metal coverage, the alignment of E_F with the graphene reduces the charge transfer rate and thus the shift becomes smaller as shown in Figure 2.12 (top).

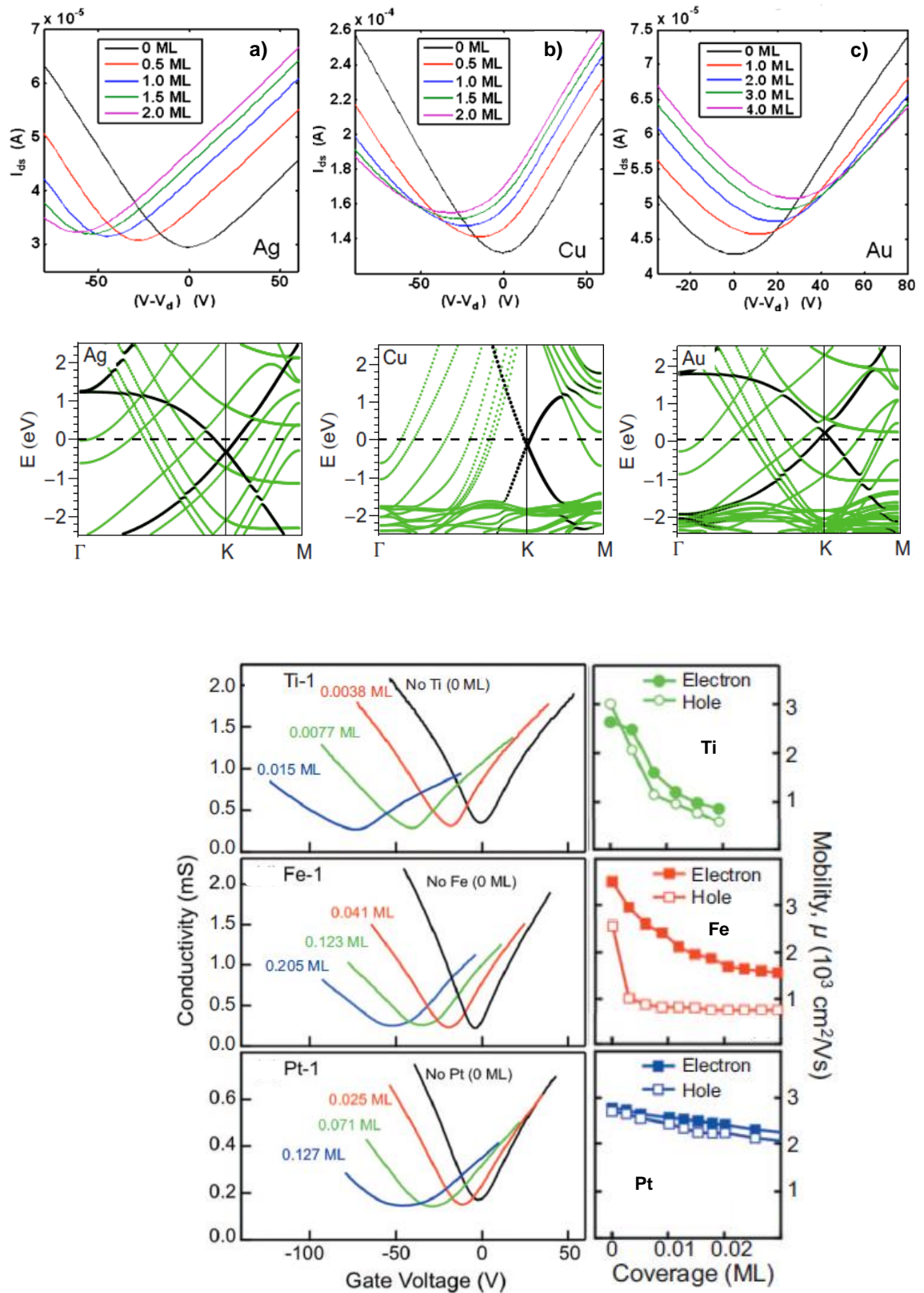


Figure 2.12: (top) Effect of metals (a) Ag (b) Cu and (c) Au on the Dirac point of graphene (middle) Corresponding band structure of graphene when in contact with these metal films [82,83]. (bottom) Effect of metal films on the electrical conductivity and the carrier mobility

In addition to the metal induced change in electronic nature of graphene, the intrinsic properties of graphene such as the mobility and the conductivity also change considerably, depending on the metal [84]. For example, as shown in Figure 2.12(bottom), the conductivity of graphene drastically reduces for the sub-monolayer coverages of strongly interacting metals such as Ti and Fe, in comparison to the weakly interacting metal Pt. In particular, Ti showed a strong negative shift in gate voltage along with the drastic reduction in carrier mobility [84]. Such degradation in electronic properties of graphene after Ti deposition is due to the highly reactive nature of Ti, which consumes the graphene underneath to form titanium carbide (TiC) at the interface and acts as a barrier in the efficient carrier transmission, thereby resulting in very high contact resistance and poor performance of the device [35, 85, 86]. The formation of TiC at the room temperature was experimentally demonstrated by Leong *et al.* using XPS analysis [85]. The C1s spectra in Figure 2.13 show the evolution of TiC with the increasing thickness of Ti on an as-grown graphene film on Cu. Similarly, Pd was also found to strongly interact with the graphene (Figure 2.14), resulting in the formation of palladium carbide (PdC) at the metal-graphene interface [85]. This carbide formation process becomes even more prominent, when graphene devices are subjected to high temperature annealing and further restricts the transmission of charge carriers across the interface. In addition to doping, metal contacts also induce compressive or tensile strain in graphene due to the lattice mismatch, which also significantly affect the graphene electronic properties [87, 88]. Therefore, appropriate selection of metal contacts is of critical importance for the better performance of graphene electronic devices.

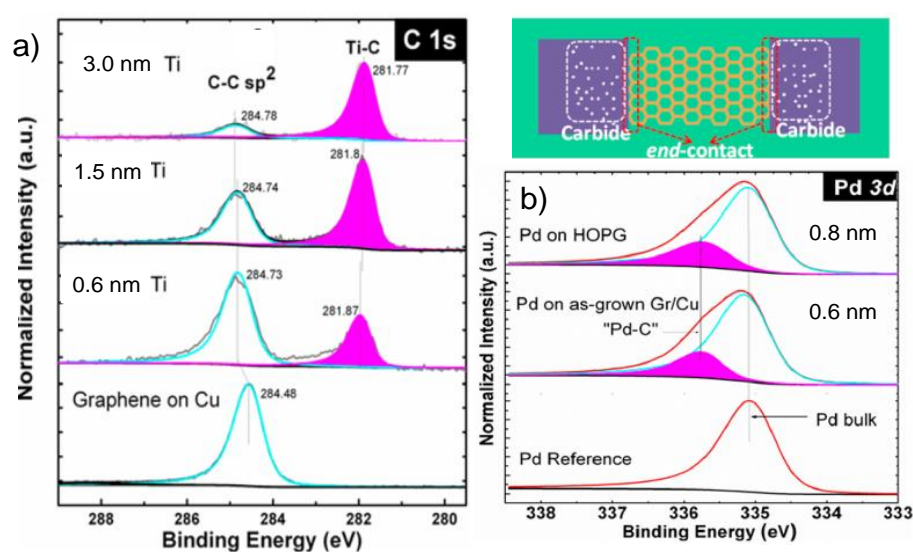


Figure 2.13: (a) Evolution of the high resolution XPS C1s spectra of graphene with the increasing (a) Ti and (b) Pd metal films [85]

2.7 Significance of graphene functionalisation

Although pristine graphene has many outstanding electronic properties, several issues need to be addressed before the full potential of graphene can be realised. For example, unlike conventional semiconductors, graphene does not possess a bandgap and hence graphene based field-effect-transistor (GFET) cannot be turned-off completely [89-91], limiting its use in digital electronic applications, where high ON/OFF ratios are critical. In addition, the highly hydrophobic nature of graphene surface results in weak adhesion of metal electrodes, leading to metal delamination [92]. Furthermore, since graphene is chemically inert, chemical sensors made of pristine graphene typically suffer from weak sensing responses, poor selectivity issues and extremely long recovery times due to the lack of polar functional groups on the surface [28, 93]. The absence of these polar groups also makes interfacing graphene with other chemical moieties extremely challenging, thereby limiting its use in biological applications. Hence, surface functionalisation of graphene is essential to enhance its capabilities and promote chemical reactivity on its surfaces.

Nevertheless, surface functionalisation of graphene basal planes is challenging, because, each carbon atom in graphene has a p_z orbital in the direction perpendicular to the basal plane, forming a self-passivating π -conjugated system with highly delocalised network [94]. Attaching functional species to such a thermodynamically stable and chemically inert structure requires controlled modification techniques with high energy reactants that can break the carbon-carbon π bonds and distort the surrounding lattice without damaging the carbon-carbon σ bonds of graphene. In principle graphene can be functionalised using two approaches: a) non-covalent functionalisation and b) covalent functionalisation [95-98]. Non-covalent functionalisation offers possibility of attaching functional groups without disrupting the structural properties of graphene [99, 100]. Here the adsorbed molecules interact with the π -electrons of graphene, resulting in the change in electronic and chemical properties of the graphene due to the charge transfer process [100]. The nature of charge transfer or magnitude of doping depends on the electronic nature of the graphene surface and the chemical nature of the analyte being tested. For instance, negative surface charges on the epitaxial graphene are expected to attract the positive-charged poles of molecules, which strongly adsorb to graphene. This strong interaction leads to charge transfer between the adsorbed analyte and graphene, which greatly affects its charge carrier concentration depending on the analyte type [98, 101]. Although this non-covalent functionalisation

approach preserves the structural properties of graphene, the long-term stability of adsorbed functional groups is an important issue [102], where, due to their weak binding nature with the graphene surface, these physisorbed functional groups desorb when the graphene device is operated under high bias or operated continuously for several cycles.

In contrast, covalent functionalisation is relatively more stable due to the strong bonding of functional groups with the graphene surface [99, 102]. Highly reactive species such as hydrogen, fluorine, chlorine and oxygen are commonly used for covalent functionalisation [97, 103, 104], which have sufficient energy to overcome the kinetic and thermodynamic barriers associated with the covalent chemical reactions on the graphene basal plane. In order to make the covalent bonding possible, the carbon atoms in graphene change their hybridization from sp^2 to sp^3 as shown in Figure 2.14 [105], which leads to the opening of a band gap [106, 107]. This transformation not only affects the sp^3 carbon atom that is undergoes reaction, but also creates geometric distortion that extends over multiple lattice positions [105]. Although, hydrogenation, fluorination and chlorination of graphene exhibit interesting chemical and electrical properties, oxidation of graphene is particularly attractive for a wide range of applications. For example, oxygen functionalisation can induce strong photoluminescence behaviour in single layer graphene [108], which could be utilised for realising graphene based optoelectronic devices. In addition, oxygen functionalisation induces p-type doping in graphene due to the highly electronegative nature of oxygen (3.5), in comparison to carbon (2.3), leading to charge transfer from graphene to the adsorbed oxygen species. This is significant because, the as-grown epitaxial graphene on the Si-face of SiC is highly n-doped and in order to reduce this intrinsic n-type character, oxygen

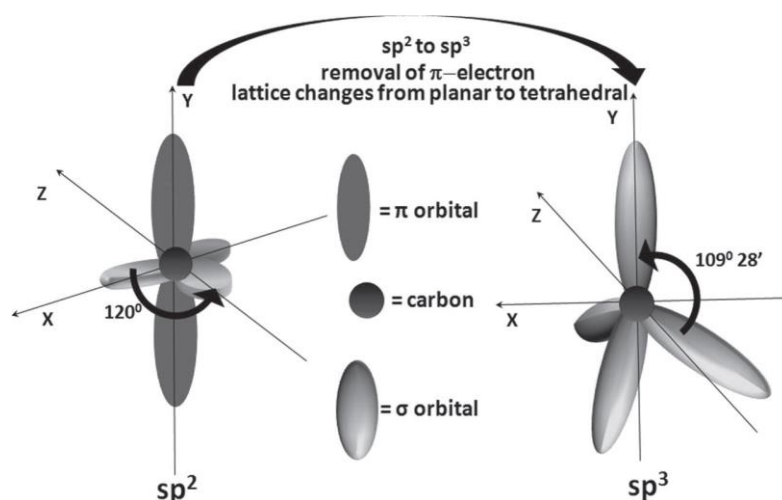


Figure 2.14: Transformation of sp^2 hybridisation to sp^3 hybridisation upon functionalising graphene with reactive chemical species [105].

functionalisation is necessary. Apart from changing the polarity, oxygen functional groups were also found to induce a band gap in single layer graphene [109, 110]. The DFT simulations in Figure 2.15 show the change in DOS for SLG and BLG with epoxy and hydroxyl configurations [109]. It is known that SLG is a zero-bandgap semiconductor with vanishing DOS at E_F . However, chemisorption of oxygen atoms strongly affects the electronic structure of SLG, in which, the increase in epoxy functional group density creates a bandgap of ~ 1.5 eV [109, 110]. This bandgap increases with the increasing concentration of epoxy functional groups and reaches 3.2 eV at 50% oxygen coverage. In contrast, as shown in Figure 2.15, O-functionalisation did not induce bandgap in BLG and hence retains its characteristic semi-metallic behaviour.

The presence of polar oxygen functional groups converts the highly hydrophobic nature of graphene to more hydrophilic in character [92]. Figure 2.16 summarises the contact angle measurements of graphene under different conditions.

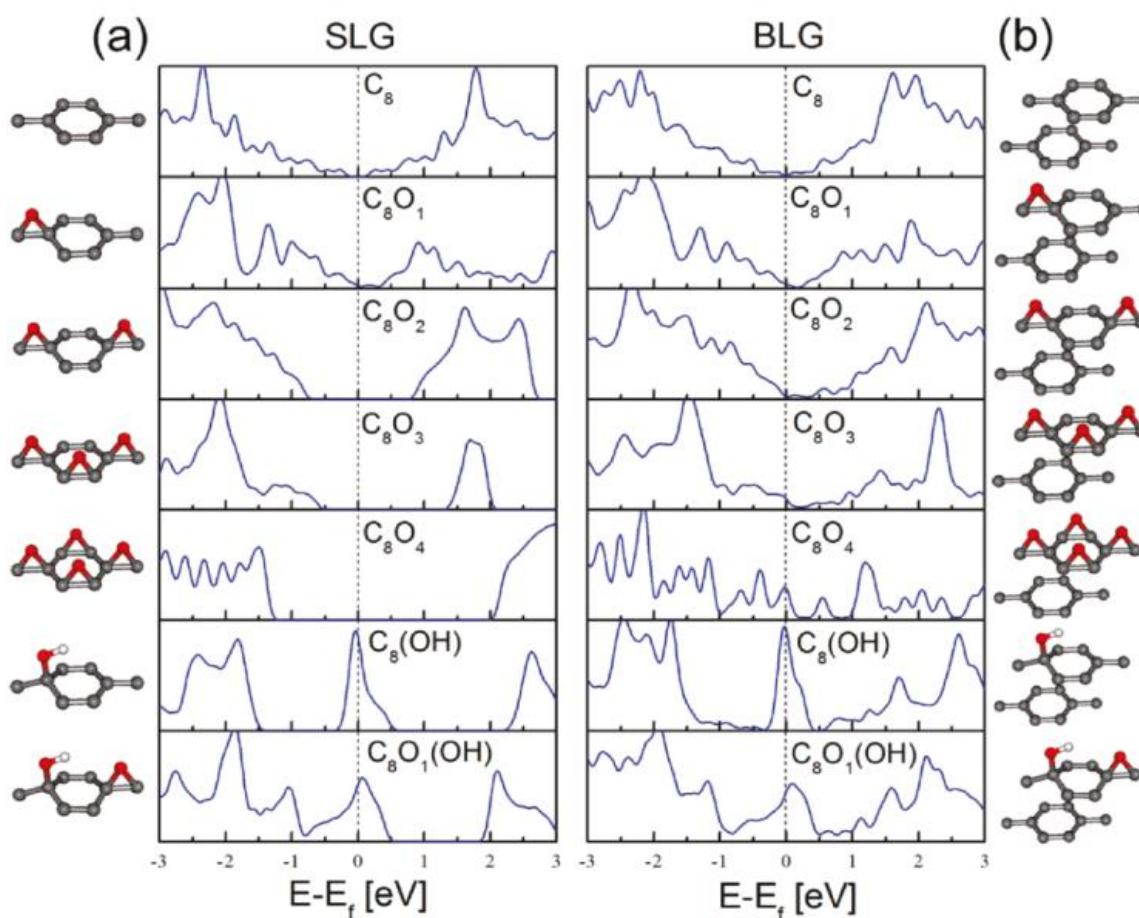


Figure 2.15: Evolution of the band structures of (a) SLG and (b) BLG with O-functional groups [109]

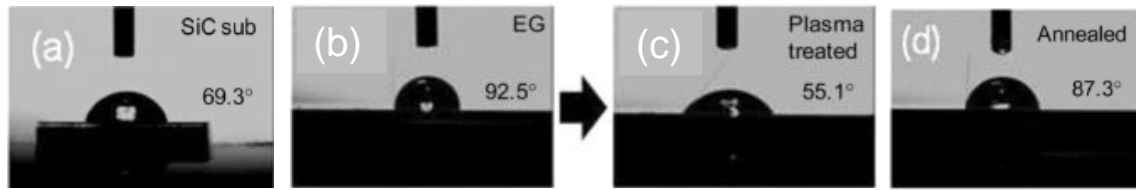


Figure 2.16: Contact angle measurements of (a) SiC substrate (b) epitaxial graphene on SiC (c) oxygen plasma treated epitaxial graphene and (d) after annealing plasma treated graphene [92].

Firstly, the contact angle of water on SiC before graphene growth was measured as 69.3° . After the growth of epitaxial graphene, the contact angle increased to as high as 92.5° , indicating the hydrophobic nature of as-grown graphene. However, immediately after oxygen functionalisation the contact angle decreased to 55.1° , demonstrating the change in the hydrophobic nature of graphene to more hydrophilic in character. Such hydrophilic behaviour is crucial for the wetting of metal films on graphene, where the oxygen functional groups significantly improves the adhesion strength of deposited metal contacts, thereby eliminating metal delamination issues [92]. It was also shown that by annealing this O-functionalised sample at 300°C in ultra-high vacuum (UHV) for 30 min, the intrinsic hydrophobic nature of graphene can be recovered with a contact angle of 87.3° , indicating no significant damage to the graphene has occurred as a result of this O-functionalisation process [93]. It was further reported that the presence of oxygen at the metal-graphene interface significantly enhances the thermal transport across the metal-graphene interfaces, enabling efficient heat transport to the surrounding device architecture [111].

2.7.1 Oxidation of graphene

Three main experimental routes have been developed to oxidise graphene. The first method involves direct oxidation of graphene using strong oxidants such as concentrated sulphuric acid, nitric acid and potassium permanganate [112]. The second method is the most popular and commonly employed approach using aggressive acidic solutions based on modified Hummer's method [113], where the graphite layers are oxidised first, followed by exfoliation into two-dimensional graphene oxide (GO). The third approach is oxygen plasma technique [114], which involves exposing graphene to energetic oxygen radicals at either room or high temperatures for covalent attachment of O-functional groups on to the graphene surface.

Although synthesising GO using wet-chemical methods is relatively easy and inexpensive, the resultant GO material is chemically inhomogeneous, electrically insulating

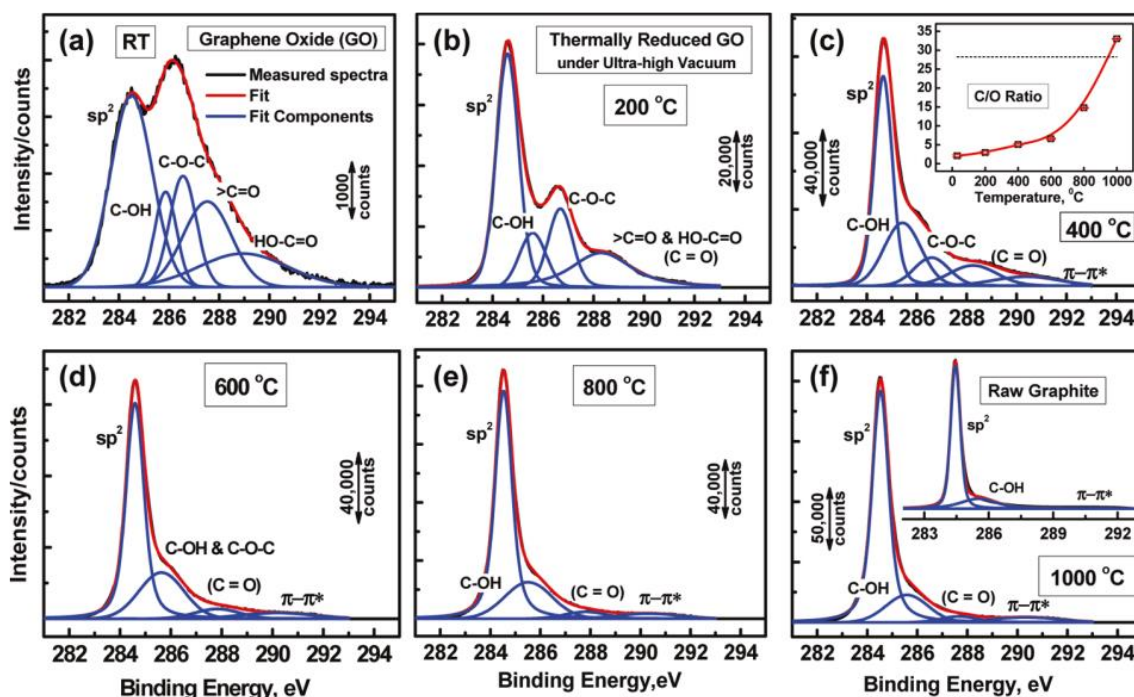


Figure 2.17: XPS C1s spectra of (a) as-synthesised GO (b) thermally reduced GO in UHV at 200 °C (c), (d), (e) and (f) reduction of oxygen functional groups with the increasing annealing temperature to up to 1000 °C [115].

and structurally defective due to the extensive use of harsh acidic treatments [115, 116]. In order to reduce the insulating nature of GO, strong acids and/or several hours of high temperature thermal annealing is commonly employed to reduce the concentration of O-functional groups on the graphene surface [115]. Nevertheless, these reduced GO (rGO) films still suffer from inferior electrical properties due to the destruction of graphene lattice as a result of harsh treatment conditions. Figure 2.17 shows the high resolution XPS spectra of the evolution of surface chemical composition of GO when subjected to high temperature annealing in ultra-high vacuum (UHV) [115]. It is very challenging to control the type and concentration of functional group(s) present on the graphene surface, using wet chemical functionalisation techniques.

Although plasma functionalisation is a promising approach for selective modification of graphene surfaces, the aggressive nature of plasmas usually results in the etching of the graphene film [117, 118]. For instance, as shown in the Figure 2.18, even for an extremely low plasma power (5 W) and very short exposure time (5 s) time, a significant increase in the defect peak (D-peak) was observed along with the a new D' peak as a shoulder to G-peak. After 80 s of exposure, the 2D-peak, which represents the sp^2 bonding in graphene, has completely vanished, indicating the etching of the graphene film. This irreversible damage to

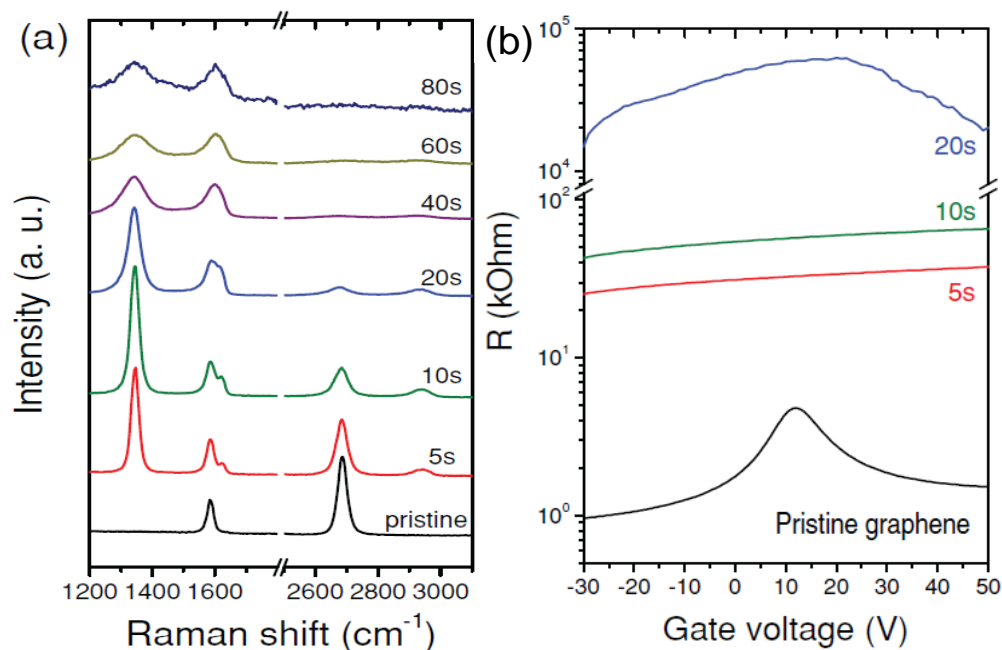


Figure 2.18: (a) Evolution of the Raman spectra of single layer graphene upon oxygen functionalisation with varying functionalisation times. (b) The corresponding electrical characteristics of the functionalised graphene [117]

the graphene lattice is enhanced by the presence of higher energy ions such as O_2^+ that can sputter carbonaceous material. The destruction in the graphene lattice was further confirmed by the electrical characteristics of the graphene film, in which, the sheet resistance increased by more than three orders of magnitude for just 20 s of plasma exposure, making it highly insulating in character. For electronic applications, specifically electronic sensor applications which rely on the changes in resistivity of the graphene film, low sheet resistances along with no appreciable damage to the graphene lattice are required.

Hosseini *et al.* [119] recently demonstrated that the etching of graphene film can be significantly suppressed by performing functionalisation in UHV atmosphere with thermally cracked atomic oxygen instead of plasmas. In this study epitaxial graphene grown on SiC (0001) was exposed to atomic oxygen species, which resulted in homogeneous coverage of only one type of functional group (epoxide), bonded to the graphene surface. This was observed by scanning tunnelling microscopy (STM) imaging, which showed random distribution of chemisorbed oxygen species that appears as bright protrusions in Figure 2.19(b) and 2.19(c) and was further conformed by Auger and XPS. Such protrusions are characteristic of epoxy oxygen atoms lying out of the graphene plane as depicted in Figure 2.19(d). These chemisorbed epoxy functional groups are completely reversible by thermal

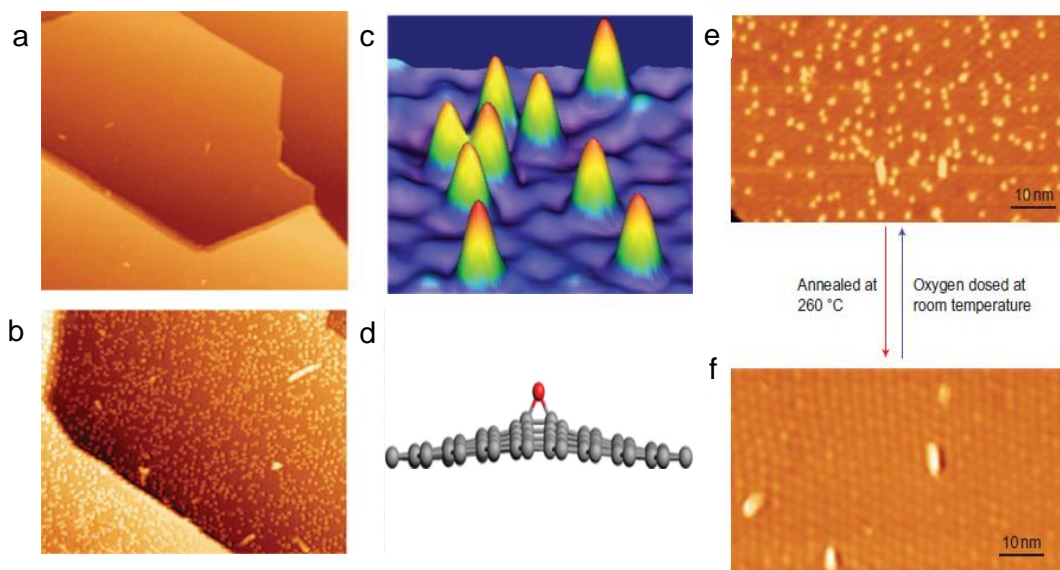


Figure 2.19: STM topography image of epitaxial graphene (a) before and (b) after oxygen functionalisation (c) STM protrusions showing the epoxy functional groups (d) Schematic illustration of the epoxy functional group bonded to the graphene surface (e) and (f) functionalisation and the annealing induced recovery of the graphene [119].

annealing the sample at 260°C as shown in Figure 2.19(e,f), without significantly disturbing the intrinsic graphene lattice structure [119].

2.8 Graphene as a chemical sensor

Chemical sensors play a crucial role in monitoring harmful gases/chemicals in the environment without the human intervention [120, 121]. Chemical sensors work on the principle of adsorption and desorption of analyte molecules on the sensor surface [121]. Here, the adsorbed analyte molecules usually disrupt the intrinsic character of the sensor material by either forming a physical bond or a chemical bond, which leads to the change in conductance, resistance or capacitance of a material. In order to detect such changes, specifically changes of low analyte concentrations, highly sensitive and selective sensor materials are required, which should ideally be inexpensive to operate, easy to integrate and importantly compatible with the existing fabrication techniques.

Several materials such as semiconducting metal oxides [122], conductive polymers [123] and polymer composites [124, 125] have been utilised as chemical sensors, showing their surface sensitivity to different chemical species. However, the use of metal oxide based sensors in many applications is limited by their high power consumption, high operating

temperatures ($>200^{\circ}\text{C}$) and poor selectivity issues, while the poor environmental stability associated with conjugated polymers limits their use in practical applications. As an alternative, nanoscale sensors such as CNTs and metal nanowires have been proposed for the reliable chemical detection [126-128]. Although, these materials are highly sensitive to different chemical species, complex growth procedures [129] and non-uniform growth on wafer-scale synthesis associated with the nanowires and CNT films [130, 131], along with the high intrinsic $1/f$ noise limits their use in practical applications [132].

In contrast, graphene possesses a large surface area to volume ratio ($2630\text{ m}^2/\text{g}$), in which every atom in the graphene sheet is exposed to the surface adsorbates [44]. Combining this large surface area with its exceptional electronic properties, graphene can be an excellent candidate for detecting any molecular disruption on its surface. Moreover, due to the quality of the crystal lattice, graphene has low electrical noise [133], which can be reduced further by optimising its band structure by stacking more graphene layers. Also, fabricating graphene sensors is practically viable as they can be processed using conventional lithographic techniques [71].

Schedin *et al.* [93] first demonstrated the chemical sensing behaviour using mechanically exfoliated graphene as shown in Figure 2.20(a). Upon exposing graphene to different gaseous species such as NO_2 , NH_3 , I_2 , H_2O , and CO , change in resistivity of graphene was observed, in which, the polarity and the magnitude of the change was found to be strongly dependent on the properties of gas species. For example, NH_3 produced immediate increase in the resistivity of graphene, followed by the saturation region (region II), where the resistivity changed relatively slowly due to the redistribution of adsorbed gas molecules on the graphene surface. After the chamber was evacuated, a very slow and small change (region III) in resistivity was observed indicating the adsorbed gas molecules are still attached to the graphene surface. However, by annealing at 150°C under vacuum these devices restored to their original state (region IV). In contrast, exposure to NO_2 resulted in a sharp decrease in graphene sheet resistance, which also exhibited regions of adsorbate saturation (region II), slow recovery (region III) and annealing induced recovery (region IV). Here, the increase or decrease in resistivity is related to the electron donating or withdrawing behaviour of NO_2 and NH_3 , respectively. In addition to these species, H_2O and I_2 were found to act as acceptors, whilst CO and ethanol showed electron donating behaviour. This change in carrier type and carrier density is the basic mechanism that governs the operation of all conductivity or resistivity based graphene chemical sensors.

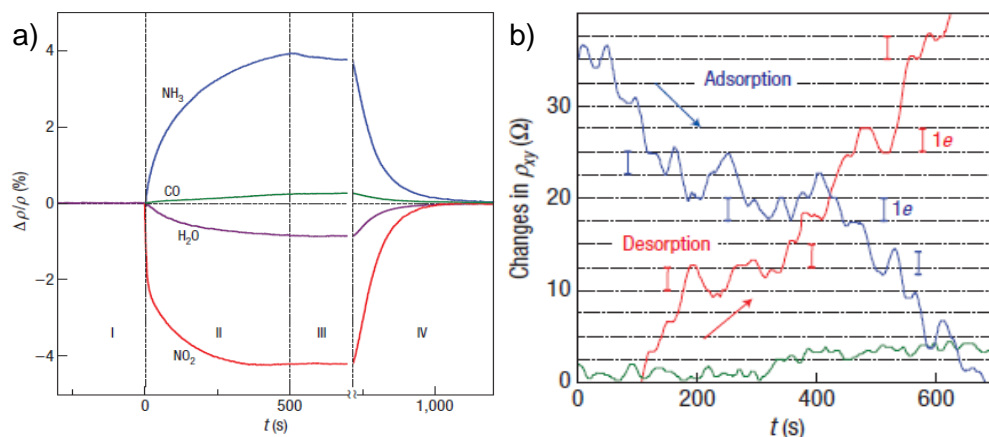


Figure 2.20: (a) Response of exfoliated graphene sensor to electron donating and electron withdrawing gas species and (b) Monitoring the single molecule detection of NO_2 during adsorption and desorption from the graphene surface [93].

Simultaneous Hall measurements performed under same exposure conditions revealed that the change in carrier density (Δn) varies linearly with the analyte concentration. However, surprisingly, despite the presence of extra charge carriers, no degradation in Hall mobility was observed even for carrier densities exceeding 10^{12} cm^{-2} . This is in striking contrast to conventional two-dimensional systems, in which such high densities of charge impurities were found to be detrimental for the ballistic transport. Long term experiments with extremely diluted NO_2 gas showed a distinct and discrete step like changes in resistivity (Figure 2.20(b)), corresponding to single molecules of the gas adsorbing and desorbing from the graphene surface. Such ultra-low detection of gas molecules has sparked immense interest in developing graphene sensors for a wide range of applications.

Pearce *et al.* [28] performed one of the first investigations on the sensing behaviour of epitaxial graphene grown on SiC. Specifically, the effect of thickness of graphene on the sensor response to NO_2 gas was investigated at different operating temperatures. When a MLG based sensor was exposed to NO_2 gas, resistance decreased at all measured temperatures (25°C to 100°C). Nevertheless, the recovery time was significantly longer in the range of few hours even at the highest test temperature (100°C), indicating strong chemical bond formation between the adsorbed molecules and the graphene surface. In addition, the sensor base line also changed considerably during the operation of the sensor, as seen in Figure 2.21(a). However, the response of MLG device towards NO_2 was several orders of magnitude smaller than the response of the SLG, which was thought to be due to a screening effect, whereby current flows through non-exposed carbon layers in the MLG sensor. When

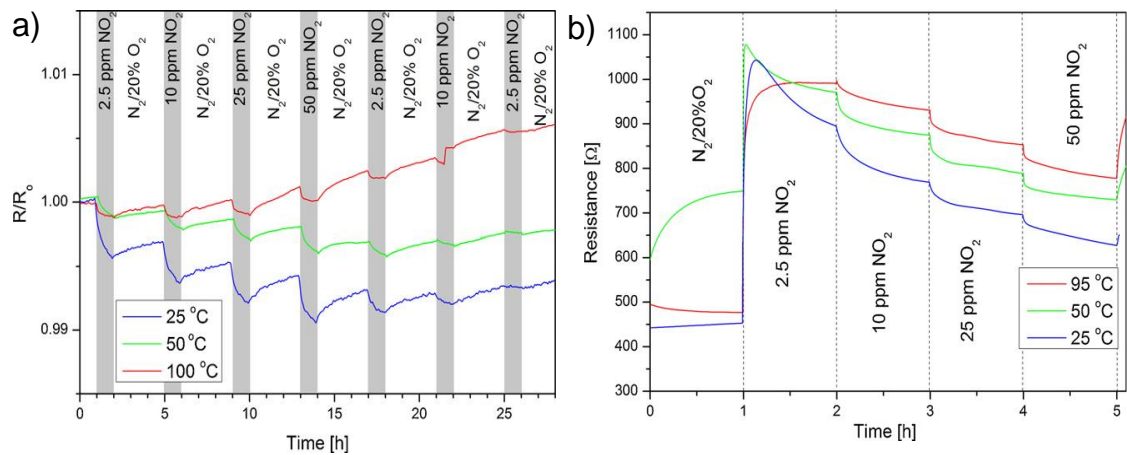


Figure 2.21: (a) Electrical response of multi-layer epitaxial graphene sensor to NO_2 gas at different temperatures and (b) Response of single layer graphene to the same gas species [28].

SLG was exposed to NO_2 gas, an n-p shift was observed upon at all attempted temperatures as shown in Figure 2.21(b).

The majority of chemical sensor studies on graphene were primarily based on monitoring changes in the resistance of a device upon exposure to different gas species. Rymnesteve *et al.* [134] however, used a different technique to understand the sensing mechanism of graphene. They employed low-frequency noise measurements, in combination with resistance measurements to evaluate the sensing response of pristine graphene to a wide range of organic chemicals. As can be seen in the figure 2.22(a), different chemicals produced different noise characteristics (i.e. Lorentzian noise bulges), particularly at low-frequencies (<100 Hz) that are specific to a chemical type. These bulges can be better seen in Figure

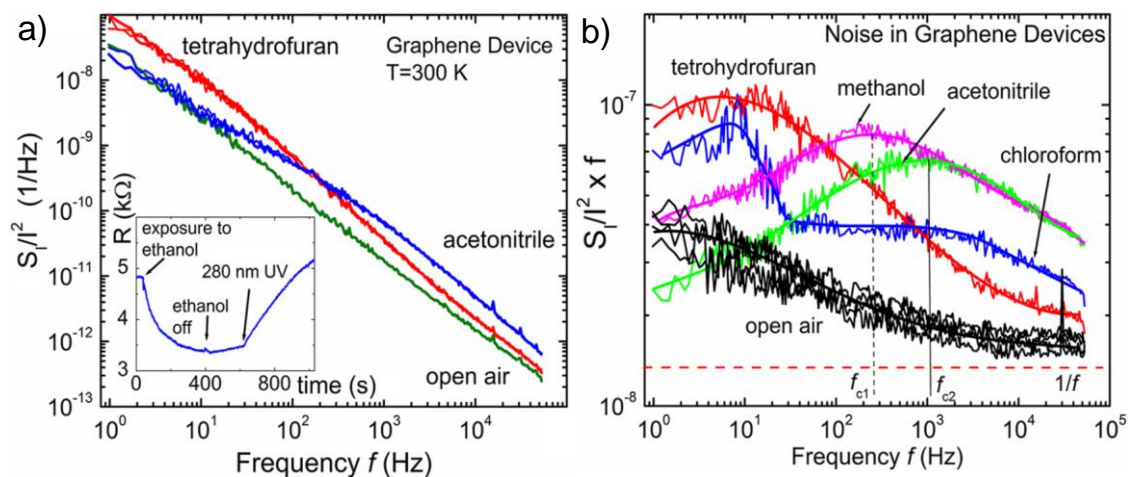


Figure 2.22: (a) $1/f$ noise deviation and appearance of bulges after exposure of different chemical vapours and (b) More pronounced effects of $1/f$ noise bulges showing different characteristics frequencies for different chemical species [134].

2.22(b), the characteristic noise frequency for ethanol vapour was between 400-500 Hz, in comparison to tetrahydrofuran which has distinctive characteristic frequency at around 10-20 Hz. This shows that, noise measurements, in combination with resistance measurements can be used to understand the underlying sensing mechanism of the graphene based chemical sensors.

2.8.1 Influence of resist contamination on the graphene sensor response

In a very important study by Dan *et al.* [36], it was found that the sensing responses produced by graphene after exposing the device to different analytes is actually not from the graphene itself but from the lithographic contamination that was present on the graphene surfaces. For example as shown in the Figure 2.23, exposing as-fabricated graphene sensor to water, octanoic acid, Trimethylamine, and nonanol vapour showed very high responses to these chemicals. However, interestingly, when the graphene was annealed in Ar/H₂ atmosphere to remove resist residues from the graphene channel and then re-exposed to these same chemicals at similar experimental conditions, there was hardly any response seen. This is not

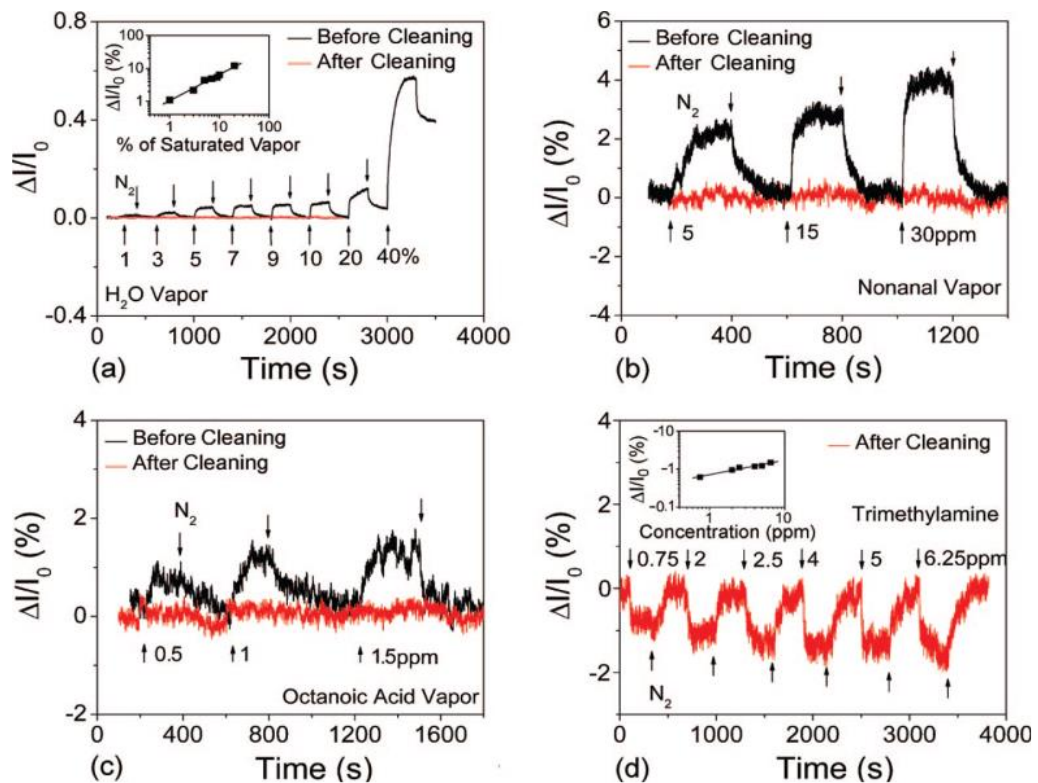


Figure 2.23: Effect of photoresist contamination on the chemical sensing responses of exfoliated graphene sensor for (a) water vapour exposure (b) nonanal (c) octanoic acid and (d) trimethylamine vapours, respectively [36].

entirely unexpected because, it is known that pristine graphene is chemically inert and hence exposure to mild concentrations of different vapour or gas molecules should not induce drastic changes in the graphene electrical behaviour. This indicates that some the early reports that demonstrated chemical sensing in graphene may not necessarily be due to the changes in graphene layer itself but may be from the influence of resist contamination. The resist contamination in as-fabricated devices unintentionally functionalises graphene resulting in uncontrolled sensor responses. Hence, immediately after fabrication and prior to any characterisation, as-fabricated graphene devices, in particular graphene based sensors must be thoroughly cleaned to avoid any spurious sensing results. Nevertheless, this study has illuminated the pathway for careful intentional functionalisation of graphene to enhance the sensor response.

2.8.2 Impact of oxygen functional groups on the sensor response

Chung *et al.* [135] have shown that by functionalising graphene with ozone, an eight fold increase in sensor response (i.e. magnitude of resistance change) can be achieved along with significantly faster response time and lower detection limits (Figure 2.24(a)). Such an enhancement in sensor response was attributed to the presence of oxygen functional groups on the graphene surface enabling favourable adsorption sites for gas molecules to strongly adsorb and thereby resulting in strong responses. Similarly, using reduced graphene oxide sensors, Robinson *et al.* [136] demonstrated successful detection of an explosive 2,4 dinitrotoloune and three chemical warfare agents such as hydrogen-cyanide, chloroethylethyl sulphide and dimethylphosphonate (Figure 2.24(b)). Here, reduced graphene oxide can be thought of a graphene device functionalised with oxygen functional groups. The high sensing

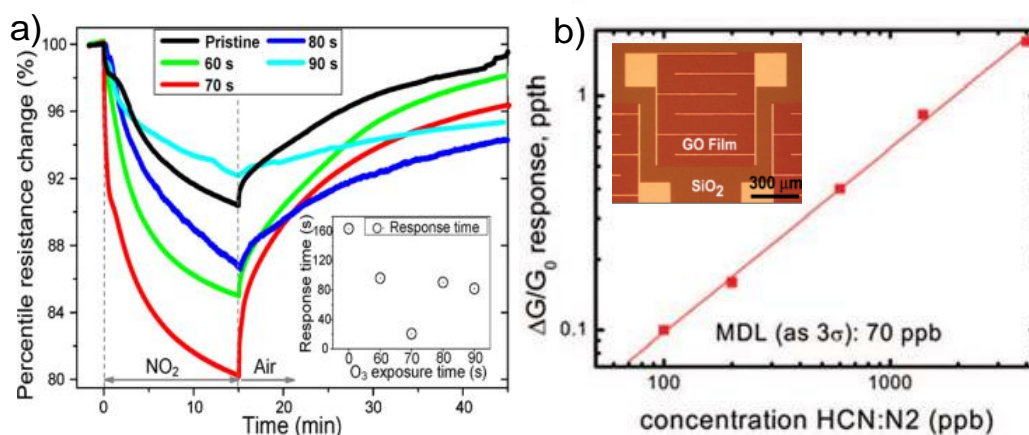


Figure 2.24: (a) Effect of oxygen functional groups on the enhancement of the sensor response and (b) rGO sensor response to different molecular gases at different concentrations [135,136].

performance of these rGO sensors is due to the strong adsorption of target analyte molecules on the rGO surface, resulting in significant charge transfer between the analyte and rGO.

2.9 Summary

In summary, this chapter has provided a brief background on different topics of graphene that will be used throughout this thesis. First, a general introduction to graphene, its electronic properties and different growth procedures have been presented. In particular, an extensive analysis on the growth mechanisms of epitaxial graphene on SiC substrates, the effect of SiC polarity and the influence of SiC polytypes on the surface morphology of epitaxial graphene films has been detailed.

Since graphene is an all-surface material, any adsorbate or any other material that it comes in contact with will have significant effect its unique material properties. Hence, a brief section has been devoted to emphasise the importance of metal contacts and the significance of surface functionalisation on the electrical, chemical and physical properties of graphene. The background information described in these sections play a key role in understanding the performance of graphene devices reported in this thesis.

In addition, this chapter has also covered the important background information from the literature on the chemical sensing behaviour of graphene films to a wide range of analyte species. In particular, the sensing mechanisms of graphene to electron withdrawing and electron donating chemical species were discussed in detail. Moreover, the effect of photoresist contamination and the effect of functionalisation on the graphene sensing responses have also been highlighted.

Chapter 3

Experimental methods

3.1 Epitaxial graphene growth process

The epitaxial graphene films were synthesised on SiC substrates via Si sublimation approach in both vacuum and argon environments, using an Axitron/Epigress VP508 Hot-Wall chemical vapour deposition (CVD) reactor, as shown in Figure 3.1(a). This reactor consists of a processing tube with graphite foam insulation and a rotating susceptor plate, as shown in Figure 3.1(b) and (e). Here, the rotatory shaft is crucial in distributing the temperature uniformity across the samples during the growth process. The variation in temperature was found to be $\sim 2\text{-}4^\circ\text{C}$ across 100 mm area making it useful for growing wafer scale graphene films. As shown in Figure 3.1(d), the CVD reactor is equipped with different gases such as argon (Ar), hydrogen (H_2), silane (in hydrogen, SiH_4/H_2) and propane (C_3H_8). However, for the graphene growth process used this thesis, only Ar and H_2 gases were used. For growth purposes, 0.5° off-axis, 76.2 mm diameter, semi-insulating 6H-SiC (0001) wafers with chemical-mechanical polished (CMP) surfaces were obtained from II-VI, Inc. These wafers were subsequently diced into $8\times 8\text{ mm}^2$ samples before being loaded into the growth chamber, as shown in Figure 3.1(c).

3.1.1 Substrate preparation

Prior to dicing of the wafer, a $1.8\text{ }\mu\text{m}$ layer of Shipley's S-1818 photo resist was spin-coated on to these wafers at 4500 rpm and hard baked in an oven at 90°C for 30 minutes to minimise

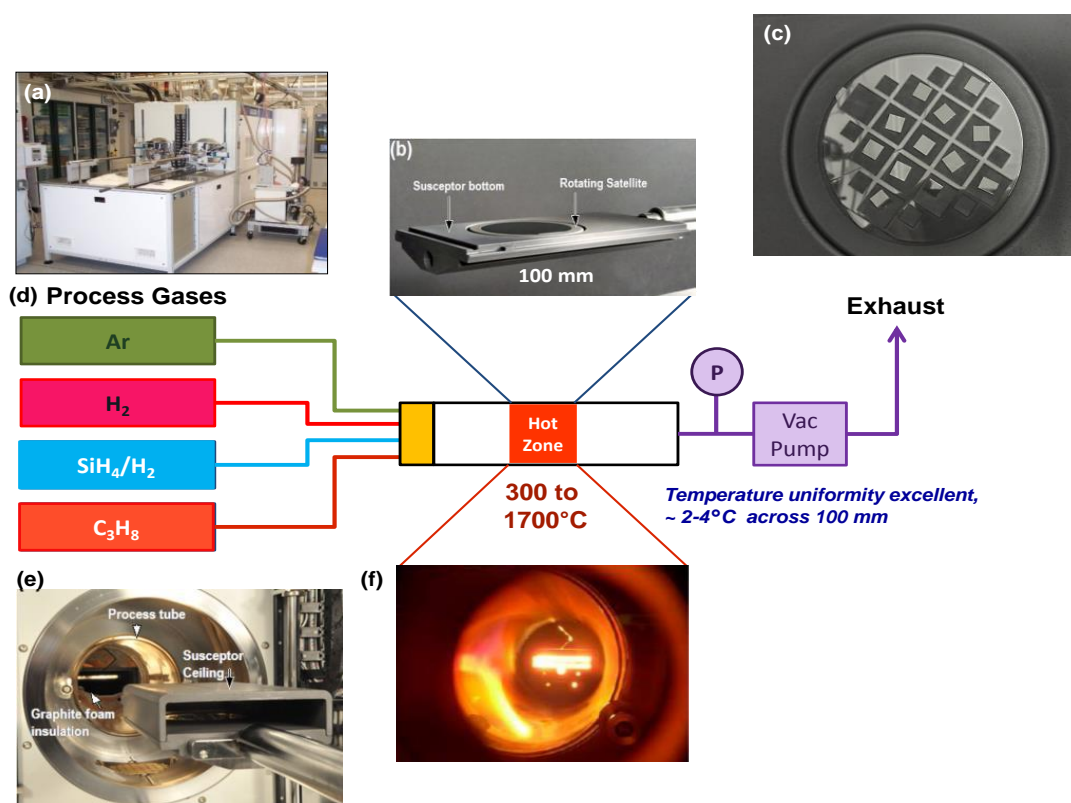


Figure 3.1: Overview of the experimental set-up used for growing epitaxial graphene films on SiC substrates. (a) AXITRON CVD reactor system (b) Rotatory shaft used for placing the samples and also for spinning during the growth (c) Sample used in this thesis before graphene growth (d) Feed through of gases available for the graphene growth. (e) Growth chamber showing loading of samples and (f) SiC samples during the graphene growth.

the contamination from dicing debris. After the dicing of these wafers in to $8 \times 8 \text{ mm}^2$ samples, they were subjected to chemical cleaning as follows: five minutes of acetone and isopropanol (IPA) rinse each at 45°C to remove oil and grease from the surface followed by a ten minute piranha clean to remove surface organic contamination. Further chemical clean of Standard Clean 1 (SC-1) was performed for fifteen minutes, followed by a ten minute rinse in a solution containing deionized water, ammonium hydroxide and hydrogen peroxide mixed in the ratio of 5:1:1.

After performing the initial chemical based cleaning, samples were loaded in to the CVD reactor to remove mechanical polishing damage from the SiC surface. This was performed by *in situ* H₂ etching in the chamber at 1520°C for 30 min. This process usually etches around 200 nm of SiC surface, leading to the formation of smooth steps as shown in Figure 3.3.

3.1.2 Graphene growth

The growth of graphene was initially synthesised in vacuum conditions of about 10^{-5} mbar and the annealing temperature of 1500°C for 90 min. However, due to the poor growth uniformity and inferior structural and electrical properties, this approach was not further studied. Almost all the work reported in this thesis was performed on samples grown in Ar

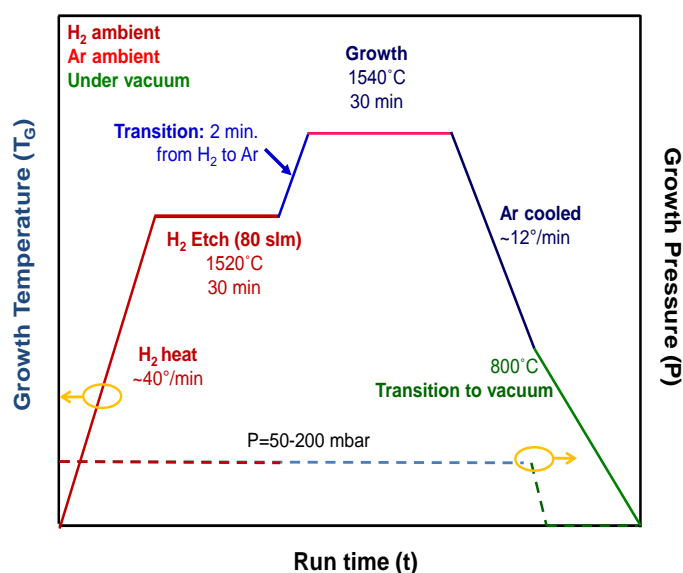


Figure 3.2: Graph showing different temperature cycles and ambient environments used during the graphene growth process.

atmosphere, due to its superior control on the graphene growth and its subsequent physical and electrical properties. The graphene synthesis process in Ar atmosphere is shown in Figure 3.2. After H₂ etching, the ambient is switched from H₂ to Ar with a stabilisation period of 2 min and the temperature was increased to a constant rate of 1540°C . The graphene growth was performed at this temperature for 30 min under a flowing Ar ambient of 10 slm

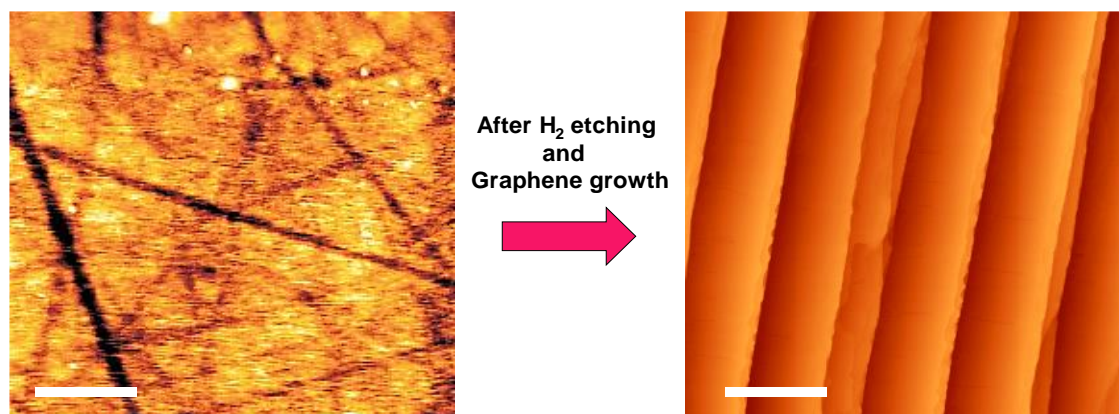


Figure 3.3: AFM topography images showing the surface of SiC after H₂ and graphene growth. Scale bar represents $2\ \mu\text{m}$.

at 100 mbar. Following graphene growth, the samples were cooled in Ar to 800°C at 12°C per minute in order to suppress Si sublimation and limit contaminants that may adhere to the surface. The samples were then left under vacuum until they attained room temperature. This recipe is known to yield uniform graphene with $\sim 2.3\%$ sheet resistance variations across a vicinal 76.2 mm diameter wafer. For more information on the graphene growth morphology and the operation of CVD reactor, see references [137, 138].

3.2 Oxygen plasma functionalisation process

Plasma functionalisation is an efficient method to modify the physical, chemical and electrical properties of large area graphene films. Different types of plasma functionalisation approaches have been reported to-date, including, capacitively [139] or inductively coupled plasma [140], radio frequency (RF) plasma [141], microwave plasma [142] and reactive-ion-etch (RIE) plasma techniques [143]. In these techniques, plasmas are usually produced by supplying energy to electrons through an external electric field generated by a power supply and applied to the low pressure gas. This external electric field heats plasma electrons to a temperature of several eV, which results in ionization, excitation and other collision processes. The resultant plasmas therefore contain chemically active species such as neutral radicals and atoms/molecules in excited state, ions, electrons, and photons. The highly reactive nature of these plasmas strongly interact with the graphene and break the carbon-carbon sigma bonds of the lattice, creating active sites for binding different functional groups, thereby modifying chemical and physical properties of the graphene film. Hence, the high ion-energies produced using these plasma approaches often cause irreversible damage to the graphene due to the ion-induced etching of the film [117].

In contrast, electron beam (e-beam) generated plasmas were demonstrated to be inherently well suited for functionalising ultra-thin materials such as graphene [144, 145], because they offer high plasma densities in range of 10^{10} to 10^{11} cm^{-3} , along with the low electron temperatures (<1 eV) [144, 146]. Such low electron temperatures are due to the use of high energy electron beams to drive the plasma production rather than external electric fields. In noble gas atmosphere such as Ar, the elastic scattering and the ambipolar electrostatic cooling are the main energy loss mechanisms, which limit electron temperatures at around 1 eV [146]. In the presence of molecular gases, the inelastic collision between electrons and gas molecules leads to further reduction in electron temperatures to less than 0.3 eV. As a consequence, large fluxes of low energy (3-5 eV) ions are delivered to the

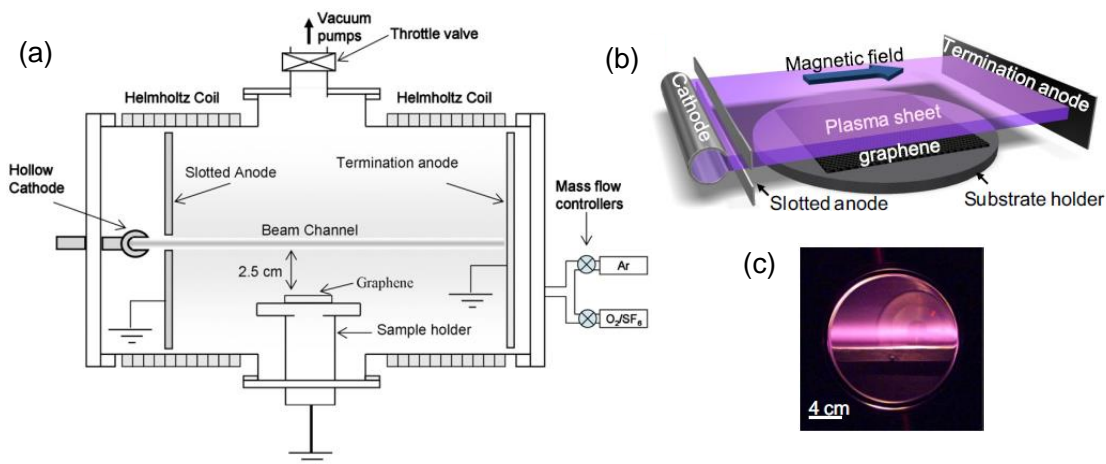


Figure 3.4: (a) Schematic view of the e-beam plasma reactor used for oxygen functionalisation process. (b) Schematic illustration of the plasma during the exposure and (c) Real time digital image of the sheet like plasma produced during the functionalisation process [145,147].

material surfaces. Such ion-energies are crucial in preserving carbon basal planes from ion-induced etching, due to the low energy thresholds for vacancy creation (7.44 eV) and displacement (35 eV) in graphite [147]. For more information on the e-beam generated plasmas and the operation of plasma processing reactor, see references [146, 148].

In this thesis, e-beam generated oxygen plasmas were used for functionalising epitaxial graphene films. Here, the experiments were performed at room temperature in a custom made plasma reactor system, enclosed by magnetic field coils to produce uniform magnetic field within the chamber, as shown in Figure 3.4. The vacuum chamber consists of a hollow cathode e-beam source, a slotted anode, an e-beam termination anode and a sample holder. E-beam generated plasmas were produced by injecting a 2 keV e-beam in to the mixture of Ar and O₂. This beam passes through the anode slot in a grounded anode and terminates at a grounded termination anode. The resulting e-beam plasma is magnetically confined by applying a magnetic field of 150 G to minimise the spreading, thereby producing a large area (60×25 cm²) sheet-like plasma as shown in Figures 3.4(b) and (c). For this work, the operating pressure was varied between 25 and 90 mTorr, by controlling by the total gas flow rate (75-180 sccm). For all conditions, the reactive gas (O₂) was introduced at 5% of the total flow rate with argon as the remainder gas to dilute the impact of the oxygen plasma functional species on the graphene surface. Note that unlike other plasma exposure techniques, the e-beam generated plasmas do not directly interact with the sample surface. For instance, as shown in the Figure 3.4, the epitaxial graphene samples on the sample holder is placed at 2.5 cm from the electron-beam axis, avoiding direct contact with the energetic plasmas.

3.3 Fabrication of graphene devices

Photolithography is the main technique used for fabricating graphene devices described in this thesis. Usually ultraviolet (UV) light is used as an exposure source in this technique to transfer the geometric patterns of the photomask to the photosensitive chemical (photoresist). An image reversal photoresist was used here to fabricate different device patterns, including, transmission line model (TLM) test structures, Van der Pauw structures and Hall bar patterns. In order to realise these devices, two different lithography processes were utilised. Each lithography process has several sub-process steps as explained below. First lithography process is known as direct photolithography, in which, the regions where the photoresist was exposed to the UV light are removed when immersed in a photoresist developer. This lithography process was used to create graphene mesa patterns/isolate graphene devices and to remove unwanted graphene regions from the sample. Second lithography process is known as reverse photolithography, where the polarity of the photoresist is reversed, resulting in the removal of regions of photoresist that were unexposed to the UV light. This type of lithography was employed for patterning the photoresist to deposit ohmic metal contacts.

3.3.1 Direct photolithography

Typical process steps followed for direct photolithography are sketched in Figure 3.5. Surface preparation is an important step prior to the application of photoresist as it improves the adhesion of photoresist and provides a contaminant free resists film in order to get maximum process control and reliability. Standard solvent cleaning procedure was used here, which includes rinsing the sample in acetone and IPA for 5 min each at 45°C, followed by cleaning in de-ionised (D.I) water and blow dry N₂. Immediately after surface cleaning, samples were subjected to dehydration bake at 150°C in the ambient air using an oven for 30 min to remove adsorbed water content from the graphene surface.

Following dehydration bake, AZ5214-E image reversal photoresist was spin coated on to the sample with an initial spin of 500 rpm in 75 ramps for 5 s, followed by a final spin at 5000 rpm in 75 ramps for 40 s. This process usually results in the photoresist film thickness of around 1.25 µm. After the spinning, samples were pre-baked in the oven at 90°C for 15 min to drive off excess solvent from the resist. Reproducing desired patterns on the photomask onto the photoresist was performed by exposing the sample to UV light for 13s

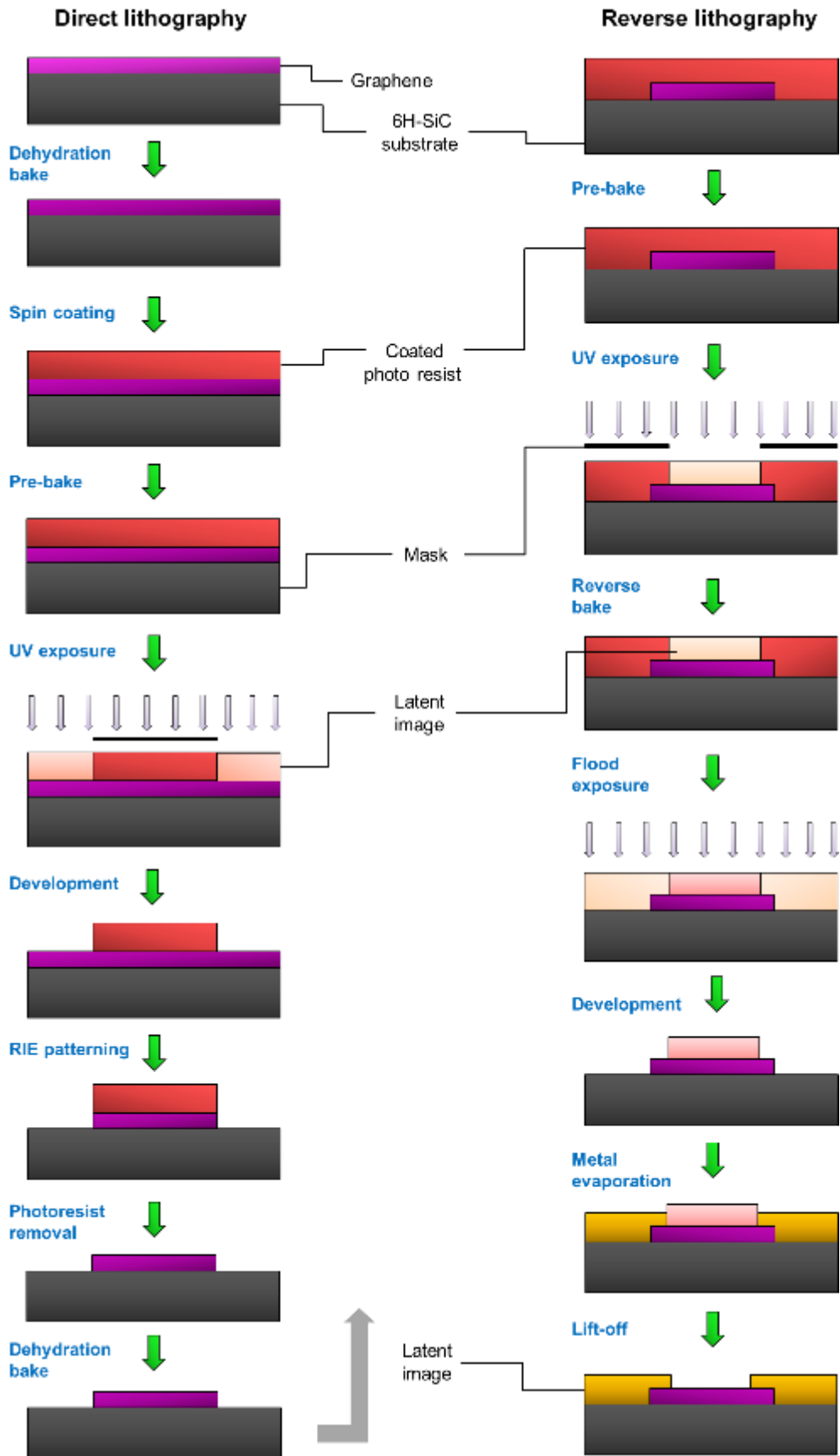


Figure 3.5: Schematic illustration of process steps followed for the fabrication of graphene devices.

using Karl Suss MJB3 mask aligner, which is capable of achieving feature sizes of 1.0 μm with an UV exposure intensity of 6.4 mW/cm^2 at 405 nm (h-line). Following exposure, samples were immersed into AZ326-MIF photoresist developer to remove UV exposed regions of the photoresist. In order to isolate graphene devices, a Plasma-Therm 790 series reactive-ion-etching (RIE) system was used to etch away unwanted graphene areas in Ar/SF₆ plasmas. Here, the etching was performed at 50 mTorr pressure with an RF power of 50 W for 2 min with an Ar and SF₆ flow rates of 18 sccm and 72 sccm, respectively. After patterning the graphene film, photoresist was removed by rinsing in either acetone/n-methyl-2-pyrrolidone (NMP), IPA and DI water stream for 10 min each at 45°C followed by drying in N₂ gas.

3.3.2 Reverse photolithography

A second photolithography process was used to pattern the photoresist for depositing metal films. Surface preparation, dehydration bake, spin-coating, pre-bake and UV exposure steps were identical to those employed in direct lithography process. However, after UV exposure, samples were reverse baked in oven at 100°C for 10 min to reverse the polarity of the photoresist. Following the reverse baking step, samples were flood exposed to the UV light (i.e. without the mask) for 60 s. This leads to the reversal of polarity of those previously exposed resist regions, resulting in the removal of unexposed regions, when immersed in the resist developer and subsequent opening of contact windows for metal deposition.

3.3.3 Metal deposition

After photoresist patterning, metal films were deposited using BOC-Edwards Auto e-beam evaporator fitted with four hearth crucibles. Different metal films such as Al, Ti, Cr, Au, Ni, Pd and Pt were utilised as contact electrodes for the graphene device fabricated in this thesis. Here, the target metal film was deposited under the system base pressure of 7×10^{-7} mbar by applying e-beam current ranging from 10 mA to 200 mA depending on the metal, which leads to the vaporisation of metal. The evaporation rates of all metals were maintained between 0.1 nm/s to 0.2 nm/s to ensure uniform coverage of deposited metal films. After metal deposition, lift-off process was performed in warm acetone (45°C) to remove unwanted regions of metals as well as photoresist from the sample surface.

3.3.4 Rapid thermal annealing

Rapid thermal annealing is an important processing step that is commonly employed in the semiconductor industry after fabrication of electronic devices to make the deposited metal

contacts ohmic. Although the interface between metal and graphene is already ohmic in nature due to the semi-metallic behaviour of graphene, rapid thermal annealing is still needed for removing lithography induced chemical contamination from the graphene surfaces. Since all the atoms in graphene is exposed to the surrounding environment, even trace amount of resist residue present on the surface can have significant impact on the device electrical characteristics, specifically on the graphene sensing responses, as described in previous chapter. Hence, achieving clean graphene surfaces is crucial for the development of graphene electronic device applications (more details in chapter 4).

In this work, all fabricated samples were annealed in the JetFirst 200 bench top RTP system, by heating up the chamber to the desired temperature (typically between 200°C to 400°C) in 10 s and maintaining at that temperature for a desired annealing time (typically 5 min to 60 min) and then rapidly cooling down to room temperature in 120 s. The environment used for annealing the samples is either in high vacuum (10^{-7} mbar) or N₂/H₂ (95%/5%) atmosphere. After the thermal treatment, samples were left in the annealing chamber for 20 min to reach absolute room temperature conditions before they were taken out, in order to minimise the impact of aggressive doping from the ambient atmosphere, which is commonly seen in post-annealed graphene samples.

3.4 Microscopic and spectroscopic characterisation

3.4.1 Atomic force microscopy

Atomic force microscopy (AFM) is commonly used for analysing the surface topography of metals, insulators, semiconductors and other biological specimens. AFM uses a sharp tip of radius 10-20 nm attached to the cantilever, which is positioned close to the surface of the sample in such a way that it can interact with the atomic/molecular forces associated with the sample surface. Figure 3.6(a) shows a plot of change in inter atomic forces as the distance between the sample and the tip is varied [149]. At shorter distances, tip experiences repulsive Van der Waals forces, whilst attractive forces become dominant when the tip moves further away from the surface. Based on these interaction forces between the tip and the sample, there are three operational modes in AFM: contact, non-contact and tapping mode.

In the contact mode, the force between the tip and the sample is kept constant. Here, when the tip is brought in contact with the sample, it experiences repulsive forces, which leads to the deflection of the cantilever. These deflections are measured by focusing a

collimated laser beam onto the cantilever and collecting the reflected laser signal using a position sensitive photodiode diode (i.e. photodetector) as shown in the Figure 3.7(a). Usually, the tip is scanned in a raster-like pattern as shown in the Figure 3.7(b) [149].

In non-contact mode, the cantilever is vibrated near the surface of the sample at its resonant frequency. The resonant frequency and the vibration amplitude of the cantilever vary as the tip is brought closer to the sample and this variation in frequency or amplitude could be used in the feedback circuit to generate the surface topography. A mode whose operation lies in between the modes of contact-AFM and non-contact AFM is known as tapping mode or intermittent-contact mode. Here, the vibrating cantilever taps the sample surface at the lowest point in its vibration cycle. By maintaining constant oscillation amplitude, a constant tip-sample interaction is ensured to obtain the image of the surface.

The surface morphology and the surface roughness of all epitaxial graphene samples used in this study were measured in non-contact mode using an ultra-sharp Si tip of 15 nm

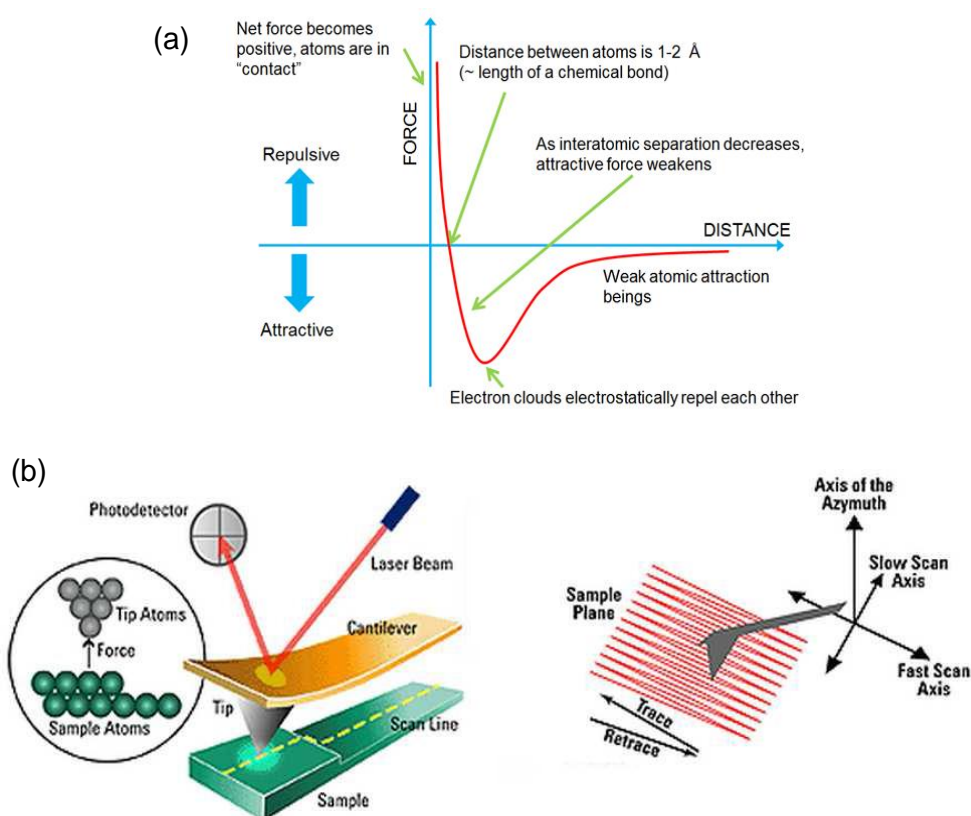


Figure 3.6: (a) Typical Van der Waals force curve used for repulsive and attractive forces of contact and non-contact mode AFM (b) AFM illustration showing the laser beam deflected signal from the cantilever collected by a photodetector and typical raster like scanning performed during the topography measurement [149].

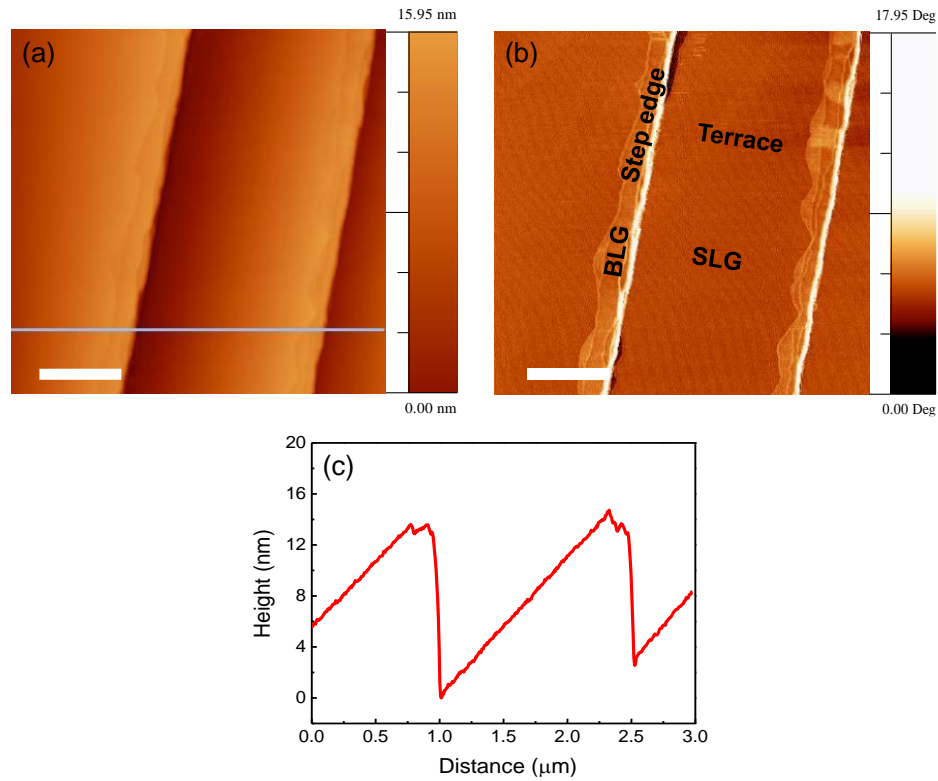


Figure 3.7: (a) AFM surface topography of epitaxial graphene grown on 6H-SiC substrate taken in non-contact mode. Scale bars represent 600 nm. (b) Corresponding phase image of the sample revealing different contrast brightness at step terraces and step edges, indicating variation in thickness at these regions. (c) The Height profile of the topography image shown in (a).

radius and a scan rate of 0.5Hz. The measurements were performed using XE-150 Park systems and all acquired images were analysed using WSxM 5.0 software. In order to reduce external noise sources, measurements were performed in an acoustic isolation chamber

Using AFM, both topography and phase images of graphene can be recorded simultaneously. In the topography image, the physical height appears as the contrast, whilst the phase image includes information mainly on rigidity, viscosity and viscoelasticity. In the case of graphene on SiC, the graphene exhibits larger phase difference because it is less rigid and more viscous than SiC. In addition, the phase image also reveals the relative thickness variation of graphene across the substrate, where the thick graphene layers exhibit a large phase difference with bright contrast.

Figure 3.7 shows an example of AFM topography and height profile, along with the phase image of epitaxial graphene grown on SiC (0001) substrate. As can be seen, the topography image shows smooth graphene surfaces with an average ($3 \times 3 \mu\text{m}^2$ area) root-mean square (RMS) roughness of 1.93 nm (this includes SiC step edges). In the

corresponding phase image, a strong variation in contrast can be seen at the step edges and step terrace regions, indicating differences in graphene thickness. The bright contrast observed at step edges correspond to thick graphene films (predominantly bilayer), in comparison to faint contrast seen at terrace regions, mainly consisting of monolayer films. Almost all samples used this thesis have similar surface topographies with monolayer and bilayer graphene film coverage at step terrace and step edge regions.

3.4.2 X-ray photoelectron spectroscopy

X-ray photoelectron spectroscopy (XPS) is also known as electron spectroscopy for chemical analysis (ESCA) or core-level photo electron spectroscopy (CLPES). It is a surface sensitive technique commonly used for analysing the chemical composition of different materials by irradiating the sample with low energy X-rays in the UHV environment. This process leads to the emission of photoelectrons from the core energy levels determined by the electronic structure of the material, as displayed in Figure 3.8. Here, when an X-ray beam is directed on to the sample surface, the energy of the X-ray photon is completely absorbed by the core electron of an atom. If the incident photon energy, $h\nu$ is high enough, the core electron escapes from the atom and emits out of the surface [9]. This emitted electron is referred to as the photoelectron, which can subsequently be detected by a spectrometer shown in Figure 3.8(b). In general the kinetic energy, E_K and the escape angle can be measured using this spectrometer. The kinetic energy contains the information about the energy of the initial state, and the escape angle contains the information about the momentum of the initial state in the solid. The kinetic energy of this photoemitted electron depends upon the photon energy of the primary X-ray source. Usually, the X-ray sources based on Mg- K_α and Al- K_α radiation are commonly used with excitation energies of 1253.6 eV and 1486.6 eV,

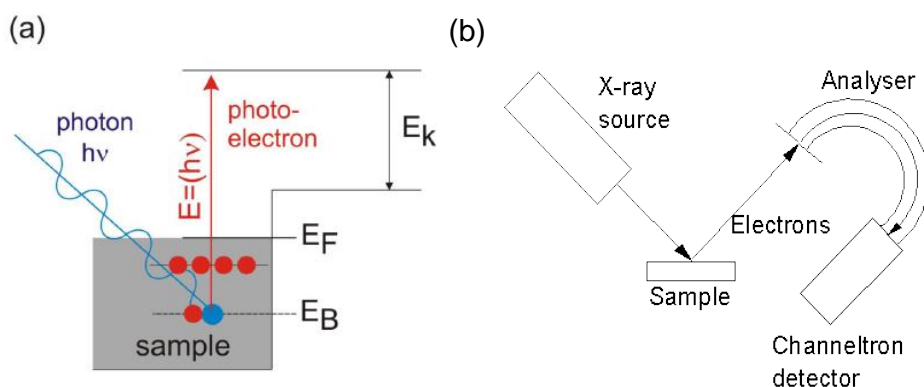


Figure 3.8: (a) Illustration of photoelectron emission process in XPS and (b) Schematic of an XPS experimental set-up for analysing samples [9].

respectively. The measured kinetic energy, E_K can be related to the binding energy of the electron in the solid by:

$$E_B = h\nu - E_K - \Phi_s$$

where $h\nu$ is the X-ray photon energy, E_K is the kinetic energy of the emitted photoelectron, Φ_s is the spectrometer work function and E_B is the binding energy referenced to the E_F of the material. It should be noted that only the elastically scattered electrons are of interest, because they contain information related to the initial state in the valance band or the core level region. Since the mean free path of electron in solids is very small, the emitted photoelectrons can only travel in the range of few nanometres. Hence, a vast majority of the emitted electrons originate from the uppermost atomic layers (around 10-12 atomic layers), thus the technique is considered as surface sensitive.

In order to identify the elements that are present in the material, a survey scan or wide energy scan is usually recorded. Each element has a characteristic XPS spectrum with chemical shifts ranging from a fraction of an eV up to several hundreds of eV. Figure 3.9 shows an example of the survey spectrum of epitaxial graphene grown on 6H-SiC (0001) substrate. As can be seen, sharp peaks related to Si and C atoms dominate the spectrum, along with a relatively small peak, corresponding to oxygen. Here, the presence of oxygen is mainly attributed to the oxygen being trapped at the SiC and graphene interface, resulting in the formation of silicon oxide and silicon oxycarbide (explained in detail in chapter 5).

After identifying the elements present on the surface, a quantitative description of these elements on the chemical composition can be acquired by performing high resolution core level spectral scan. However, prior to analysing the spectra, a background subtraction has to

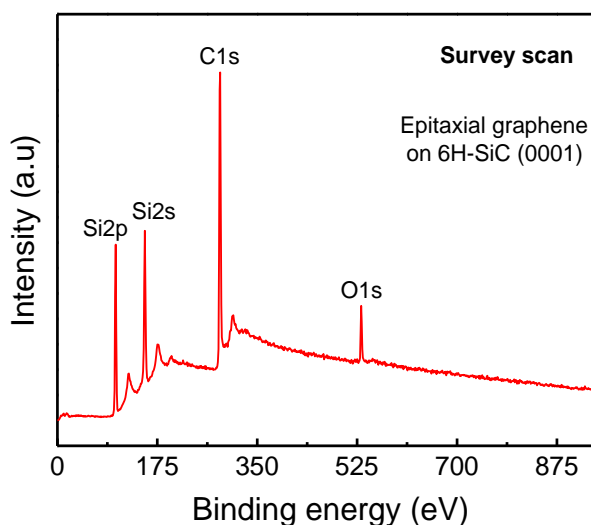


Figure 3.9: A typical XPS wide energy scan of an as-grown epitaxial graphene sample showing Si, C and O as main elements present on the surface.

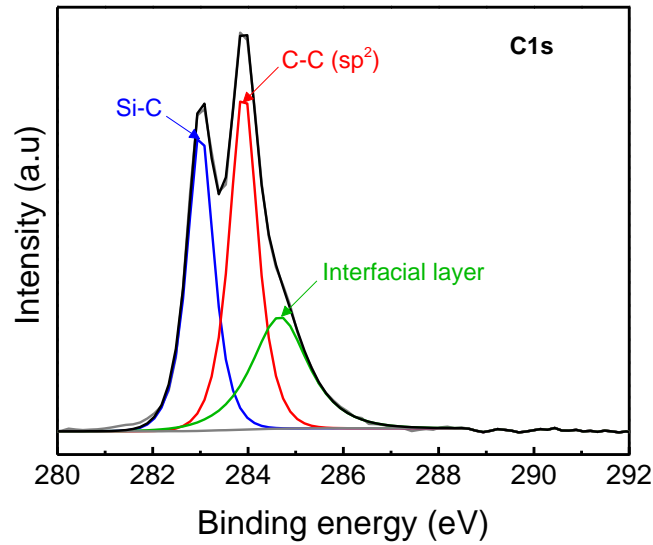


Figure 3.10: High-resolution XPS C1s spectra of as-grown epitaxial graphene showing Si-C, C-C and the interface layer, respectively.

be performed using either a linear or a Shirley base line to remove the background noise caused by inelastic electron scattering. The peak fitting of SiC and graphene core level peaks can then be performed using a Voigt line shape, which is a convolution of Lorentzian and Gaussian functions that account for two types of broadening effects [7, 9]. The Lorentzian function describes intrinsic broadening due to the finite lifetime of the core hole. The width of the Lorentzian peak is determined by Heisenberg's uncertainty principle as $\omega L \sim \hbar/\tau$, where τ is the lifetime of the core hole produced in the photoemission process [9]. The Gaussian broadening arises from several contributions, including an instrumental resolution determined by that of the analyser and the light source, broadening caused by inhomogeneity of the sample when, for example, chemical state of surface atoms, i.e. their binding energy, is affected by slight variations of bond length or bond angles and finally, contributions due to phonon broadening. Using this peak fitting procedure, the chemical composition as well as the concentration of functional groups present on the graphene surface can be calculated. Furthermore, since the binding energies of atoms are sensitive to the surrounding environment and the bonding configuration, the core level XPS peak shifts can also be used to determine the chemical nature of the material. For instance, upon adsorption of oxygen on the epitaxial graphene surface, the high electronegativity of oxygen reduces the electron concentration in graphene, resulting in the shift of graphene Fermi level closer to the Dirac point. As a consequence, the binding energy of graphene C1s peak also shifts, which could be used to estimate the resultant doping of the graphene.

In this thesis, the surface chemistry of all epitaxial graphene samples was analysed using Thermo Scientific K-Alpha XPS spectrometer with a monochromatic source Al-K α (1486.6 eV) at room temperature with an emission angle of 70°. All samples were measured under high vacuum conditions of 3×10^{-8} mbar and at room temperature. The survey and high resolution spectra were collected using pass energies of 200 eV and 20 eV respectively with a spot size of ≈ 400 μm . Each high resolution scan collected is an average of twenty scans taken using an energy step of 0.15 eV and a dwell time of 100 ms. In order to identify the chemical composition of species present on these samples, high resolution C1s, O1s, Si2p and Ti2p spectra were fitted with mixed Gaussian-Lorentzian functions after performing Shirley background subtraction using CasaXPS software. During peak fitting, the full-width at half maximum (FWHM) values were fixed at a maximum limit of 1 eV for all analysed peaks. A quantification scaling was performed, where all spectra presented in this thesis have been normalised with respect to the intensity of C1s peak and also to the corresponding sets of O1s and Si2p data. Further, all C1s peaks displayed here were calibrated for minor sample charging by shifting the SiC C1s peak to 283.1 eV [150] with respect to O1s and Si2p spectra.

Figure 3.10 shows the typical high resolution C1s spectra of an as-grown epitaxial graphene film on SiC (0001) fitted with three Gaussian-Lorentzian peaks at 283.1 eV, 284.0 eV and 285.1 eV, corresponding to Si-C bond, C-C bond (graphene) and interfacial layer, respectively. No additional peaks related to carbon-oxygen functional groups were observed within the resolution limit of the XPS system, indicating pristine nature of the graphene surfaces. Nevertheless, lithography processing, thermal annealing and oxygen functionalisation process will have significant effect on the surface chemical composition of graphene, resulting in considerable changes to the C1s spectrum. Hence, knowledge of chemical state of graphene is critical for understanding the electrical and sensing responses.

3.4.3 Raman spectroscopy

Raman spectroscopy is a powerful, fast and non-destructive technique based on inelastic scattering of monochromatic light (usually from a laser source), whereby phononic properties of the crystal or the vibrational properties of the molecule is obtained. Raman scattering is not only a surface sensitive technique, but can also probe the bulk properties of the material. For example, in epitaxial graphene samples, the surface related graphene signals as well as bulk related SiC signals could be recorded (details below). A typical Raman experimental setup is shown in Figure 3.11(a), consisting of a laser wavelength in the visible

range (514.5 nm used in this work) with a diameter of the laser spot of around 700 nm. Upon irradiating the laser beam onto the sample, the incident photons at molecules or solids result in both elastic and inelastic scattering. As shown in Figure 3.11 (b), for the energy levels in a molecule, the incident photon creates a virtual energy state. After de-excitation the system may either be in its initial state or in a vibrational state. If initial and final state coincides, the scattering is called elastic Rayleigh scattering. If the final vibrational state of the molecule (or solid) possesses more energy than the initial state, the photon wavelength is shifted towards lower values giving rise to Stokes signal. If the final vibrational state has less energy, photon wavelength is shifted towards higher values, resulting in anti-Stokes signal.

3.4.3.1 Raman spectroscopy of graphene

Raman spectroscopy has been commonly used in the structural characterisation of carbon based materials such as diamond, graphite and carbon nanotubes. In recent years, it has been extensively used for characterising graphene and graphene related materials. Raman spectroscopy can be used to determine the thickness of graphene, to monitor defects, disorder, doping, chemical modifications, and strain. As the unit cell of graphene contains two carbon atoms, there exists six phonon dispersion bands, three of which three are acoustic (A) branches and the other three are optical (O) phonon branches. For one acoustic (A) and one optical (O) phonon branch, atomic vibrations are perpendicular to the graphene basal plane, which correspond to out-of-plane (o) phonon modes [151]. In the case of two acoustic and two phonon branches the vibrations are in-plane (i). In general, the directions of phonon modes are considered relative to the nearest C-C atoms, which can be classified as longitudinal (L) or transverse (T). Hence, along the high symmetry directions, $\Gamma M \Gamma K$, the six phonon modes can be assigned to LO, iTO, oTO, LA, ITA and oTA (Figure 3.11(c)).

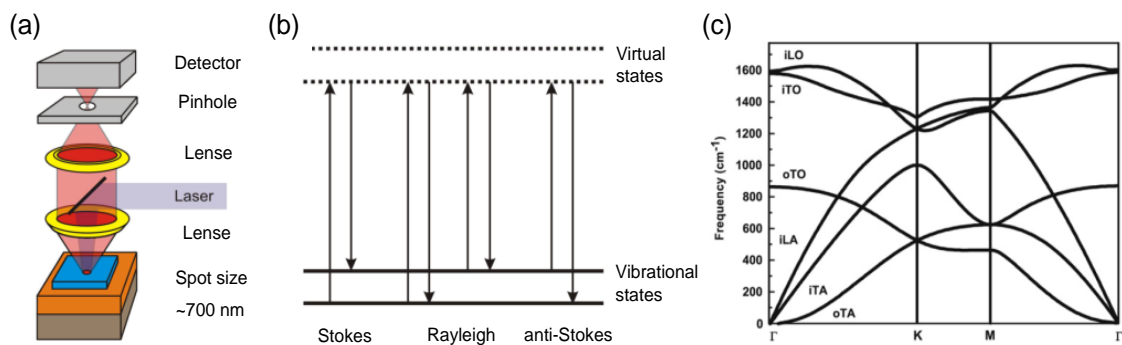


Figure 3.11: Schematic view of a typical Raman spectroscopy set-up. (b) Energy level diagram showing stokes, anti-stokes and Rayleigh scattering and (c) Phonon spectrum of graphene [9].

Nevertheless, only a few phonon modes are Raman active, which are responsible for generating the most prominent features in the Raman spectrum of a pristine graphene, which include, the G-peak at around 1580 cm^{-1} and the 2D-peak at around 2670 cm^{-1} , using a laser excitation of 514.5 nm , as shown in Figure 3.12(a). In the case of disordered graphene, a new defect related peak (the D-peak) arises at about half of the frequency of the 2D band (around 1350 cm^{-1}), as shown in Figure 3.12(b). In addition, another defect activated peak called the D'-peak also can also be seen in the Figure 3.12(b) as a shoulder to the G-peak at around about 1620 cm^{-1} . The physical origin of these peaks and the scattering process in the electronic band structure of graphene is shown in Figure 3.13. First, in the case of G-peak, when the laser beam with a photon of energy, E_{laser} is irradiated onto graphene, it excites electrons into the conduction band. This excited electron is inelastically scattered by a phonon of energy, E_{Phonon} , before recombining by emitting a photon of energy, $E_{\text{photon}} = E_{\text{laser}} - E_{\text{Phonon}}$. Here, the G-peak is associated with the doubly degenerate (iTO and LO) phonon modes at the Brillouin zone centre and represents in-plane vibrations of the graphene lattice as depicted in Figure 3.13(a). The G-peak in graphene is the only peak arising from a normal first order Raman scattering process, whilst the 2D-peak comes from either a doubly resonant Raman process with an iTO phonon or a triply resonant process. D and D' do not exist in pristine graphene and generally requires a defect to activate it. Here, the D-peak originates from a second-order process, involving one graphene phonon and one defect.

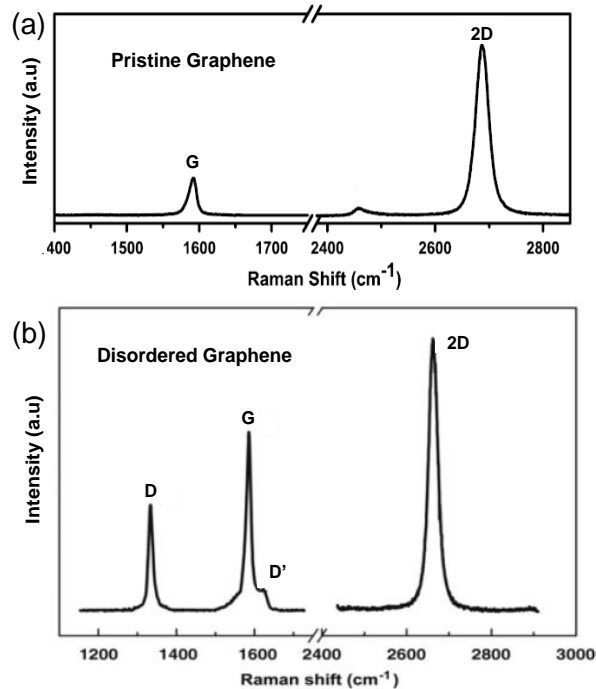


Figure 3.12: (a) Raman spectrum of a pristine graphene showing characteristic G and 2D peaks and (b) Raman spectrum of a disordered graphene with an intense D and D' peaks [151].

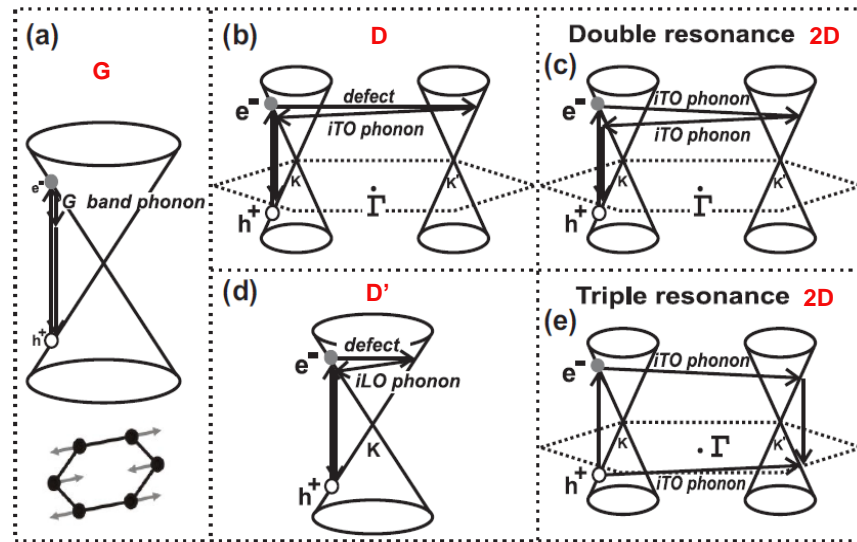


Figure 3.13: (a) First order G-band process (b) and (d) Intervally and intra-valley one-phonon second order double resonance process for D-band and D' bands respectively (C) two-phonon second order double resonance and (e) triple resonance process for 2D-peak [151].

Note that both the D and the 2D peak frequencies are dependent on the laser energy, in which, they shift upwards with increasing laser energy.

3.4.3.2 Graphene thickness determination

Ferrari *et al.* [152] and later many other researchers have demonstrated that the Lorentzian peak fitting of the graphene 2D-peak can serve as the fingerprint to distinguish single layer, bilayer, trilayer and few-layer graphene [153]. For example, as shown in Figure 3.14, the 2D-peak of a single layer graphene can be fitted with a single Lorentzian function, whilst four Lorentzians are used for fitting the bilayer graphene, because, the two π -bands allow for four different double resonance scattering processes to occur. In addition to peak fitting process, Figure 3.14 also shows that the position and the full-width at half maximum (FWHM) of the

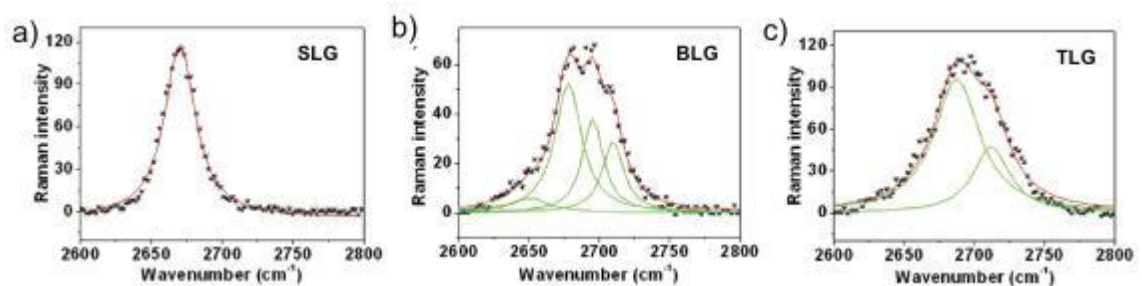


Figure 3.14: Raman peak fitting procedure using Lorentzian functions for identifying (a) single layer, (b) bi-layer and (c) tri-layer graphene films [153].

2D peak change dramatically with the increase in number of graphene layers and hence can be used in determining the thickness of graphene. However, unlike 2D-peak, the position and the FWHM of the G-peak do not considerably vary with the graphene thickness.

3.4.3.3. Calculating defect density

Raman spectroscopy can be used to identify the level of disorder in the graphene, which is particularly important when measuring the quality of as-grown epitaxial graphene and when characterising functionalised graphene films. It is known that, a certain level of disorder or short range defects will be introduced in the graphene film upon functionalisation, in the form of sp^3 bonded carbon, which behaves similarly to defects such as missing carbon atoms caused by ion bombardment. These defects give rise to the D-peak as discussed above. The ratio of the integrated intensity of the D peak to that of the G peak (i.e. I_D/I_G) gives information on the concentration of defect sites present in the film. Figure 3.15(a) shows the development of the Raman spectrum for SLG irradiated to five different levels of ion-bombardment which correspond to five different inter defect distances, L_D (2-24 nm) [154]. The I_D/I_G ratios of defective graphene films is plotted in Figure 3.15(b), which were acquired using three different laser wavelengths and fitted (solid lines) to the following equation [155]:

$$\frac{I_D}{I_G} = C_A \frac{(r_A^2 - r_S^2)}{(r_A^2 - 2r_S^2)} \left[e^{-\pi r_S^2/L_D^2} - e^{-\pi(r_A^2 - r_S^2)/L_D^2} \right]$$

where r_A and r_S are length scales that determine the region where the D-peak scattering takes place. More precisely r_S determine the radius of the structurally disordered region caused by

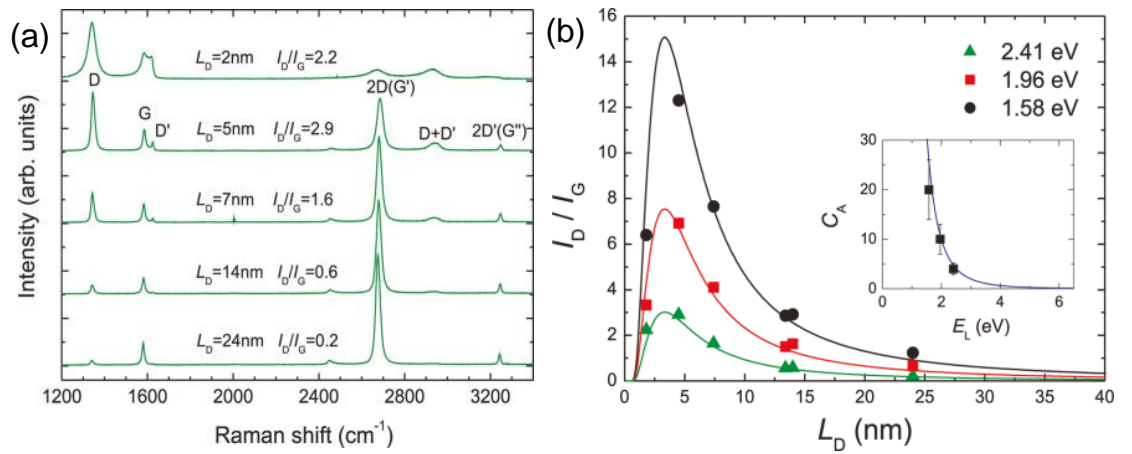


Figure 3.15: (a) Evolution of defect density from $L_D=24$ nm to $L_D=2$ nm in an ion-bombarded graphene flake and (b) Intensity of I_D/I_G ratio of the defective graphene as a function of increasing defect density in the graphene [154].

the ion bombardment and r_A is defined as the radius of the area surrounding the point defect in which the D-peak scattering takes place. It can be seen in the Figure 3.15(b) that the I_D/I_G ratio has a non-monotonic dependence on L_D , increasing with increasing L_D up to ~ 4 nm and decreasing for $L_D > 4$ nm. It is known that the D-peak arises due to the breathing modes of six atom rings in graphene and requires defect for its activation. Nevertheless, the increase in defect density also results in the destruction of hexagonal ring structure of graphene. Such destruction leads to the reduction in decrease in the intensity of D-peak, which indirectly reduces I_D/I_G ratio as seen in Figure 3.15(b). Hence, in order to prevent the etching of the graphene film during plasma functionalisation process, L_D should be restricted to below 4 nm (more details in chapters 5 and 6).

3.4.3.4. Monitoring doping effects

In addition to thickness determination and monitoring disorder, Raman can also be used to estimate the doping effect in the graphene film. This can be done by monitoring the position of both G-peak and 2D peaks. In its pristine state, the G-peak lies at around 1580 cm^{-1} , whilst 2D peak is situated at 2680 cm^{-1} as represented by the solid red line in the Figure 3.16(a) and

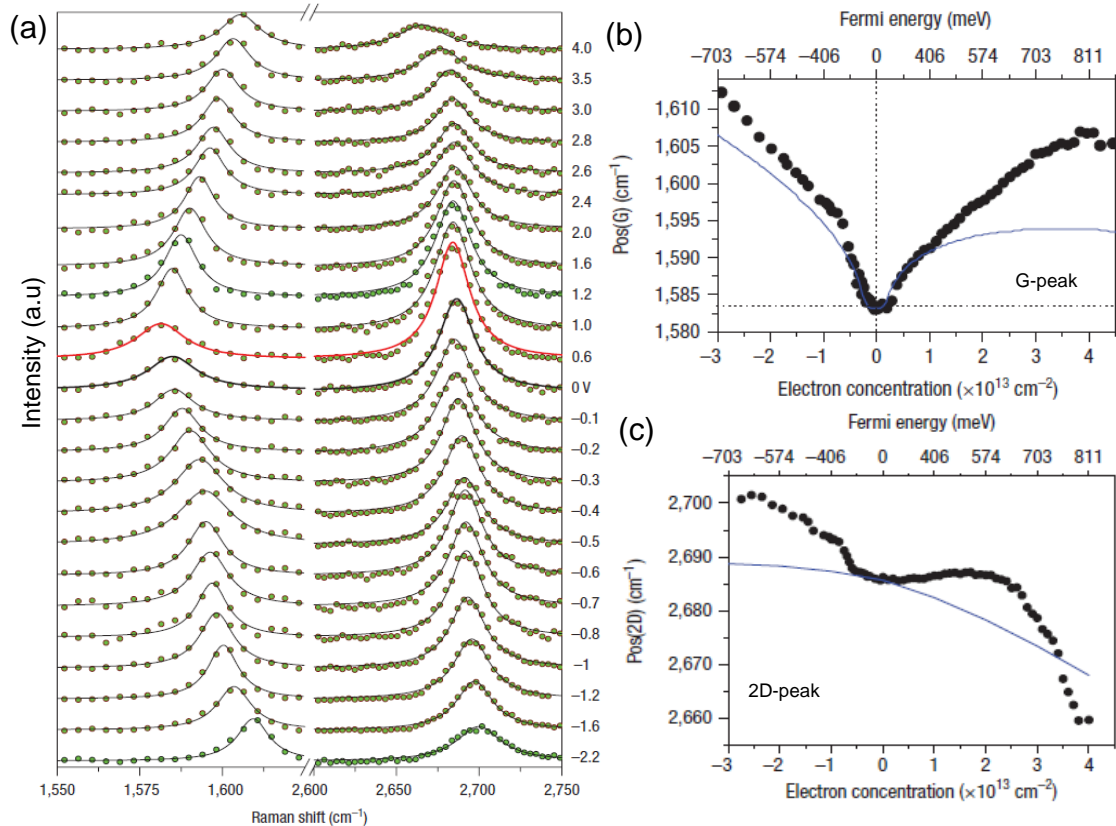


Figure 3.16: (a) Evolution of G and 2D peaks of the graphene with n and p-doping. (b) and (c) shows the shift in the position of G and 2D peaks as a function of carrier concentration [156].

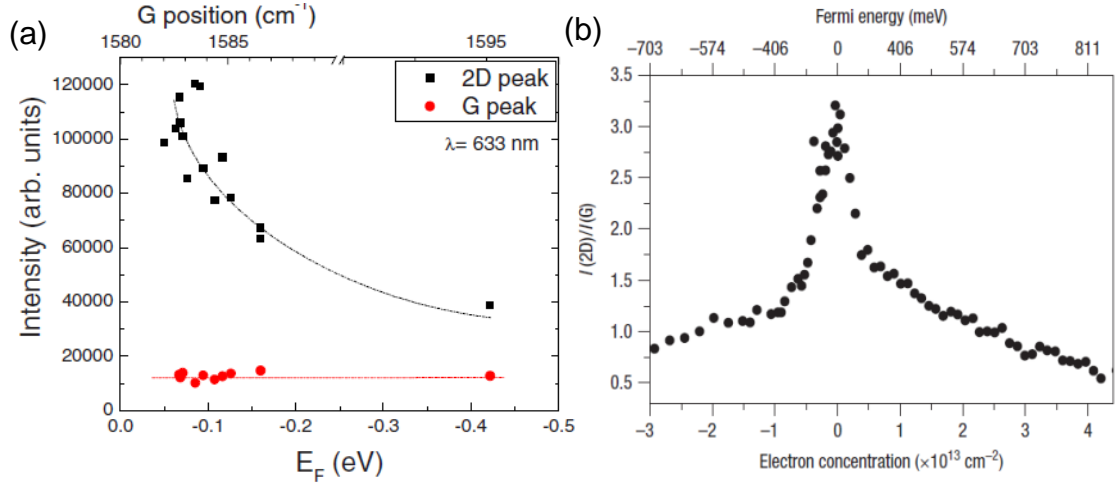


Figure 3.17: (a) Effect of doping on the intensities of G and 2D peaks and (b) Influence of doping on the I_{2D}/I_G ratio of Raman spectrum [156,157].

upon doping, the position of both G and 2D peaks shift considerably. Here, the electron and hole doping was induced by means of a top gate in the graphene FET device geometry [156]. As can be seen in the Figure 3.16(a), irrespective of the dopant type, the frequency of the G-peak upshifted with the increasing doping concentration. This effect can be clearly seen in the Figure 3.16(b), where the position of G-peak showed V-type behaviour with the increasing doping concentration and to the corresponding E_F . In contrast, no significant change in position was observed for the 2D-peak for low electron doping concentrations, whilst its position decreases for the high electron doping density. In the case of hole doping, the position of the 2D-peak increases with the increasing doping and eventually saturates for doping concentrations $>10^{14}$ cm⁻².

In addition to shift in peak frequencies, doping also had a significant effect on the intensity of the 2D-peak (I_{2D}) in particular. For instance, as shown in Figure 3.17(a), I_{2D} decreased substantially with the increasing doping concentration, whilst no noticeable change in intensity was observed for the G-peak (I_G) [157]. Hence the I_{2D}/I_G ratio can be directly used to monitor the doping effect in the graphene sheet. Figure 3.17(b) further shows that irrespective of the doping type, the I_{2D}/I_G ratio decreases with the increasing doping concentration. With the increase in doping, the charge carriers in the graphene will increase and therefore the probability of scattering events also increase, resulting in a decrease in the intensity of 2D-peak. Hence, the shift in G-peak position and the I_{2D}/I_G ratio can serve as fingerprint to monitor doping, whilst, position of 2D-peak can be used to identify the polarity of the doping type.

3.4.3.5. *Monitoring strain induced variations*

Finally, Raman spectroscopy can also be utilised to estimate the strain in graphene. As depicted in Figure 3.18, for an unstrained graphene, the G-peak is situated at 1580 cm^{-1} , whilst the 2D-peak is usually positioned at 2670 cm^{-1} . By inducing compressive or tensile strain, G and 2D-Peaks either red shift (i.e. down shift) or blue shift (i.e. upshift), respectively. It should be noted that, both doping and strain could result in the graphene peak shifts. However, if the shift is due to doping, then the magnitude of 2D peak shift is always less than the magnitude of the G-peak shift. Conversely, if the strain is the major contributor to the observed peak shifts, then magnitude of 2D peak shift will always be greater than the magnitude of the G-peak shift (more details in chapters 5 and 6). In other words doping is more prominent on the G-peak, whilst 2D-peak is more sensitive to strain induced variations.

Figure 3.19(a) and (b) shows the evolution of the G and 2D-peaks under tensile strain, which red-shifted significantly with the increasing strain pressure [158]. In particular the G-peak showed a unique behaviour of peak splitting (G^* and G^+) after applying $\sim 0.6\%$ of strain. Such splitting behaviour was attributed that the graphene was under uniaxial strain, which is explained in detail in references. This red shift can further be clearly seen in Figures 3.19(c) and (d), where the slopes of these shifts were calculated as $-31.7\text{ cm}^{-1}/\%$ and $-10.8\text{ cm}^{-1}/\%$ for G^* and G^+ , respectively, whilst it was estimated as $-64\text{ cm}^{-1}/\%$ for the 2D-peak. Here, the red shift of G and 2D-peaks is due to the elongation of carbon-carbon bonds, which weakens the bond strength, thereby lowering their vibrational frequency.

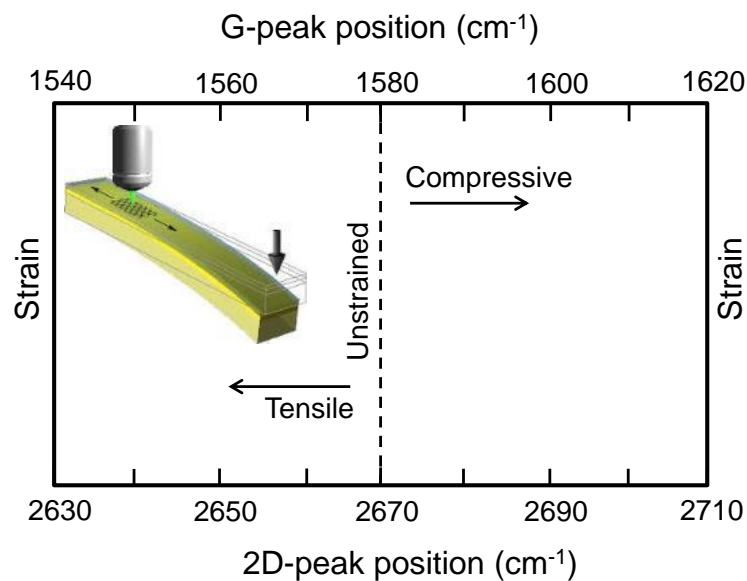


Figure 3.18: Sketch of Raman peak positions of graphene for tensile and compressive strains.

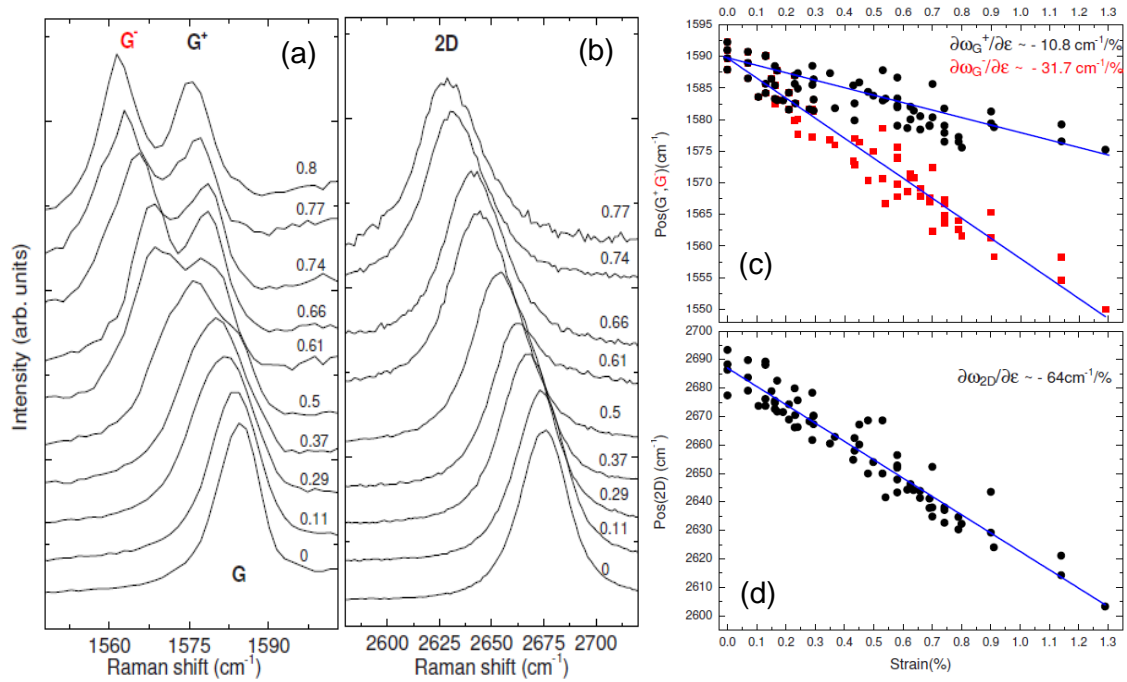


Figure 3.19: (a) Evolution of G and 2D peaks under uni-axial strain. Peak splitting of the G-peak can be seen here. (c) and (d) decrease in peak positions on graphene with the increasing strain [156].

In addition to estimating the intentionally induced mechanical strain, the intrinsic strain in graphene can also be calculated. For example, as shown in Figure 3.20, the Raman spectra of as-grown epitaxial graphene on SiC showed GG and 2D-peak positions at 1587 cm⁻¹ and 2719 cm⁻¹, respectively [159]. Note these values are significantly higher than the values expected for an undoped and unstrained graphene. Such an upshift in peak frequencies was

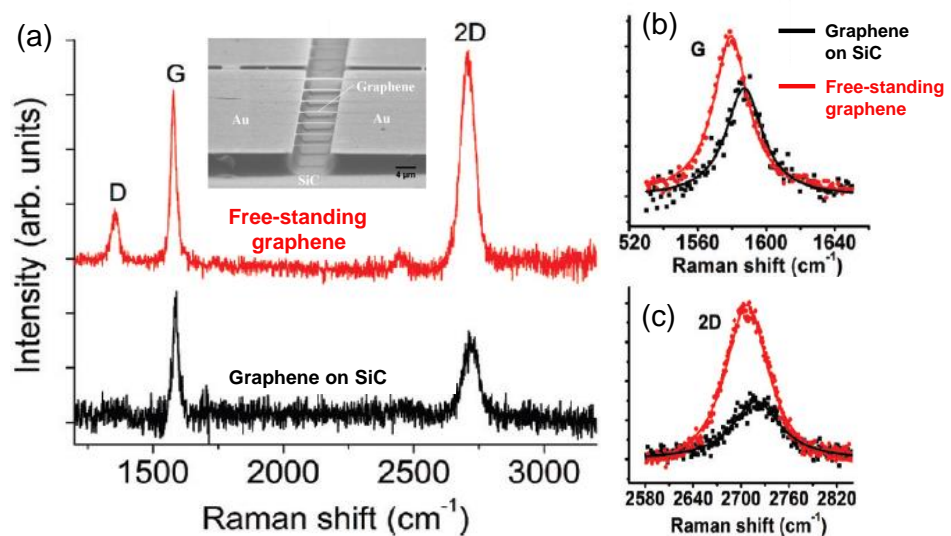


Figure 3.20: (a) Raman spectra of graphene on SiC and free-standing graphene. (b) and (c) Change in intensity and the peak positions of G and 2D peaks respectively [159].

attributed to the unintentional compressive strain in epitaxial graphene films grown on SiC substrates. This intrinsic compressive strain in graphene develops during the cooling stage of the growth process, because of the large variation in coefficients of thermal expansion between SiC and graphene, where SiC contracts and the graphene expands during cooling [160]. The intensity of G and 2D peaks of graphene in contact with the SiC substrate are significantly lower than the intensities that were measured for the same graphene film in a free-standing state. Here, the free-standing was possible by partially etching the SiC substrate underneath graphene using photoelectrochemical etching technique (see the inset of Figure 3.20(a)). In addition to peak intensities, the shift in the G-peak (Figure 3.20(b)) and the 2D-peak positions (Figure 3.20(c)) were also observed before and after etching the SiC substrate. For instance, after making the graphene free-standing, the 2D-peak shifted from 2720 cm^{-1} to 2707 cm^{-1} , whereas, the G-peak decreased from 1587 cm^{-1} to 1580 cm^{-1} , respectively. This down shift in peak positions was attributed to the intrinsic strain relaxation in graphene upon making it free-standing. A small D-peak was also observed in the Raman spectrum of this free-standing graphene, which was attributed to the disorder introduced in graphene after the SiC etching process. Nevertheless, this shows that by monitoring the G and 2D peak positions, the strain and strain relaxation effects in graphene can be estimated.

In this thesis, the structural quality of graphene films were monitored by Horiba Jobin-Yvon LabRam confocal Raman microscope fitted with an argon ion laser. The spectra were taken using a $100\times$ objective lens, an excitation wavelength (λ) of 514.5 nm , spot size of $0.70\text{ }\mu\text{m}$ and an incident laser power of $\approx 10\text{ mW}$ at room temperature. The laser exposure time was 30 s and the collected spectra were averaged three times with a dwell time of 1 s . For peak analysis, SiC background contribution was subtracted to extract the graphene peaks followed by Salvatzky-Golay smoothing to improve the signal-to-noise ratio of the acquired spectra. The characteristic D, G and 2D peaks of graphene were fitted with Lorentzian spectral line shapes for quantitative analysis of these samples. All spectral analysis was performed using LabSPEC 5.0 software provided by the manufacturer.

Figure 3.21 shows the typical Raman spectra of a SiC (0001) substrate and as-grown epitaxial graphene on SiC (0001) before subtraction. As can be seen, SiC background peaks dominate the graphene spectrum, especially between 1200 cm^{-1} to 2000 cm^{-1} . Only the 2D-peak is well isolated with peak position at around 2600 cm^{-1} to 2800 cm^{-1} away from the SiC peaks. Hence in order to extract the complete epitaxial graphene spectrum, the Raman contribution from the SiC substrate is subtracted using the LabRam software and the

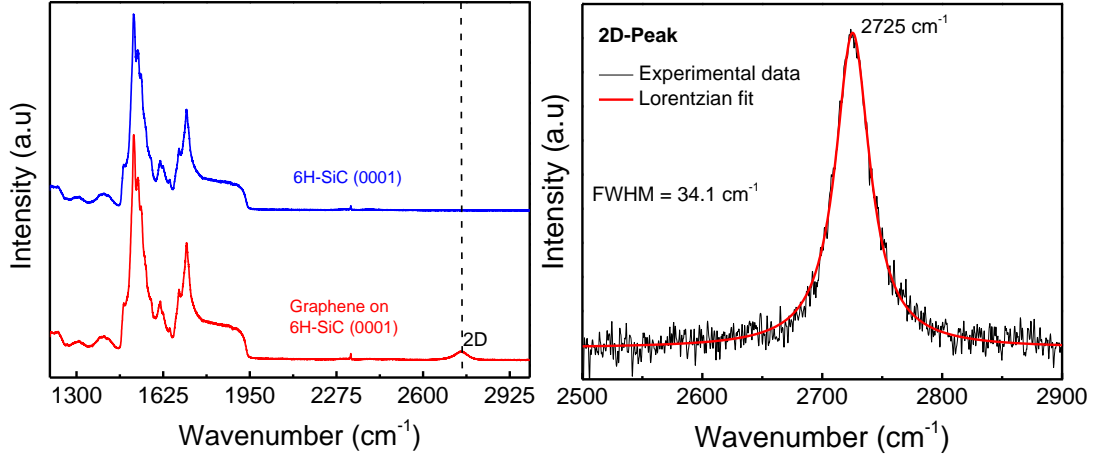


Figure 3.21: (left) As-taken Raman spectra of before and after graphene growth on 6H-SiC substrate. (right) 2D-peak fitting with single Lorentzian function.

resultant spectrum is shown in Figure 3.21(b). The G and 2D-peaks clearly dominate the spectrum with no observable D-peak, indicating the high crystalline quality of the as-grown graphene film. Fitting the 2D-peak with a single Lorentzian function (see Figure 3.21(b) inset) the thickness of graphene was confirmed to be monolayer. All samples (Ar grown) used in this thesis have similar quality and uniform thickness coverage (SLG at terraces and BLG at edges) across the substrate.

3.5 Electrical characterisation

3.5.1 Transmission line model measurements

The transmission line model (TLM) measurement is a two-probe technique, commonly used to determine the contact resistance, the sheet resistance, and the transfer length characteristics of interfaces. TLM test structure usually consists of a series of metal electrodes patterned in a resistor network separated by a varying channel length, L_{ch} , as shown in the Figure 3.22(a). Both the width (W) and the Length (L) of each TLM contact electrode are fixed and only L_{ch} is varied. The total resistance, R_T is then measured between the adjacent metal electrodes using the equation [161]:

$$R_T = R_{sh} \left(\frac{L_{ch}}{W} \right) + 2R_C$$

where R_C is the contact resistance and R_{sh} is the sheet resistance. As mentioned in chapter 2, R_C includes the resistance at the metal-graphene interface, the resistance of the graphene

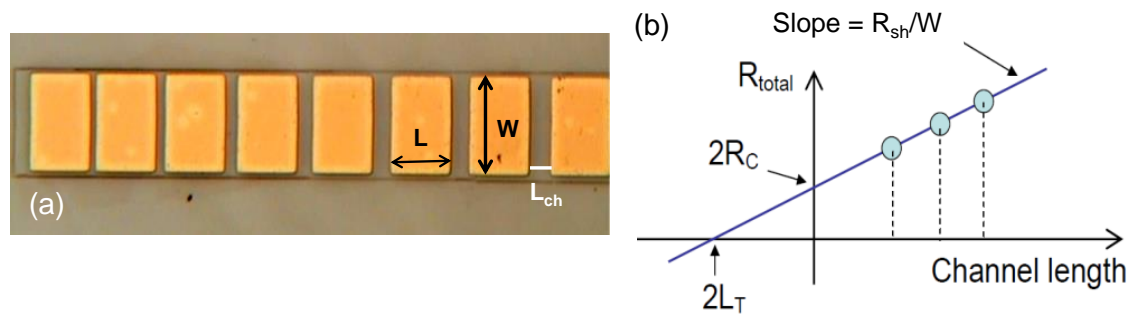


Figure 3.22: (a) Optical microscopic image of a typical TLM test structure fabricated in this work. (b) TLM plot of total resistance as a function of channel length.

under the metal contact, and the spreading resistance from the graphene underneath the contact to the channel area. The R_{sh} is the resistance of the graphene sheet at the channel regions. By plotting the measured total resistance, R_T as a function of channel length, L_{ch} , both R_C and R_{sh} can be calculated from the linear fit to the experimental data shown in the Figure 3.22(b). For example, R_{sh} can be deduced from the slope of the linear fit by using, $\text{slope} = R_{sh}/W$, whilst, R_C can be extracted from the Y-intercept of the linear fit. Here, the extracted R_C value is multiplied by the width of the contact to calculate the contact width normalised contact resistance value. In addition to these parameters, the transfer length L_T , in which the applied voltage drops to $1/e$ of its value [161], can also be obtained from the X-intercept of the TLM plot. Here, the comparison of L_T with the actual contact length L_{ch} is useful in estimating whether the induced charge carriers are restricted to the edge of the contact or flows into the complete contact. Note that the calculation of L_T is based on the assumption that sheet resistance of graphene under the contact is equal of the sheet resistance between the contacts. Nevertheless, in reality, the graphene underneath the metal contact is usually doped or perturbed, depending on the metal used, leading to different density of states in graphene underneath the metal, in comparison to the channel areas, thereby resulting in very different sheet resistances. Hence, the conventional method of extracting L_T does not apply for graphene films. Since the channel lengths used in this work are significantly larger than ($> 5 \mu\text{m}$) the carrier mean free-path in the graphene, the approach used to extract R_C and R_{sh} is still valid. TLM measurements were mainly used in chapters 4 and 6 to evaluate electrical properties of metal-graphene and metal-oxygen functionalised graphene interfaces.

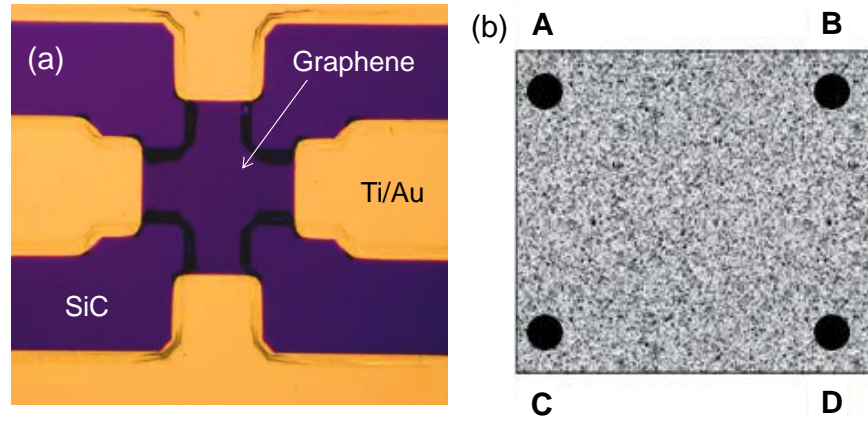


Figure 3.23: (a) Optical microscopic image of a fabricated Van der Pauw device (Hall cross) used in this thesis and (b) the sketch of an as-grown graphene sample measured in another Van der Pauw configuration.

3.5.2 Van der Pauw and Hall measurements

In order to minimise the contribution of metal contacts to the measured resistance values, four-probe measurements were used in Van der Pauw configuration, as shown in Figure 3.23(a) and (b). This technique can be used to measure the electrical properties of materials of any arbitrary shape. It however requires ohmic metal contacts placed at the perimeter of the sample as shown in Figure 3.23(b). Here, when a current (I) is passed between contact A and B (I_{AB}), the resultant voltage drop is measured between contact C and D (V_{CD}) with no externally applied magnetic field. From this the resistance can be calculated by

$$R_{AB,CD} = \frac{V_{CD}}{I_{AB}}$$

By measuring another edge $R_{AC,BD}$, and also their reciprocals $R_{CD,AB}$ and $R_{BD,AC}$, and further averaging, precise measurements of sheet resistance can be calculated.

Hall measurement is an important electrical characterisation technique commonly used to determine the sheet carrier density (n), carrier polarity and the mobility (μ) of conducting and semi-conducting materials by measuring the Hall voltage (V_H) and the sheet resistance simultaneously. Two main geometries, Van der Pauw structure or Hall bar structure can be used to extract these electrical parameters (see Figure 3.24). Here, a constant current (I) is forced through the sample between two non-neighbouring contacts, while the voltage is measured between the other two contacts. When a magnetic field (B) is applied perpendicular

to such a current carrying conductor, the charge carriers experience a transverse magnetic force and are deflected towards the side or edge of the conductor. These accumulated charge carriers at the edge generates a potential difference perpendicular to both the current flow direction and the magnetic field applied. The magnitude of Hall voltage (V_H) is calculated by,

$$V_H = \frac{R_H I B}{d}$$

where R_H is the Hall coefficient, I is the applied electric current, B is the magnetic field and d is the sample thickness. Here, R_H is defined by,

$$R_H = \frac{1}{nq}$$

where q is the electronic charge and n is the carrier density. The carrier type (i.e. p-type or n-type) and the density can therefore be determined from the Hall coefficient. Hall mobility is subsequently determined by the equation,

$$\mu_H = \frac{R_H}{R_s},$$

where μ_H is the Hall mobility, R_H the Hall coefficient, and R_s is the sheet resistance. The sheet resistance is obtained using either Van der Pauw or Hall bar geometry.

In this thesis, Hall measurements were performed at room temperature to measure the variation in parameters such as sheet conductivity, mobility, carrier type and density using Hall measurement system from MMR technologies. The measurements were performed in Van der Pauw configuration using indium probe tips, with a magnetic field between 0.025 Tesla and 0.3 Tesla and sample currents of 30 μA to 150 μA .

Figure 3.25 shows the extracted Hall mobility and sheet carrier density values of twelve $8 \times 8 \text{ mm}^2$ area as-grown graphene films on the Si-face of the 6H-SiC substrates used in this

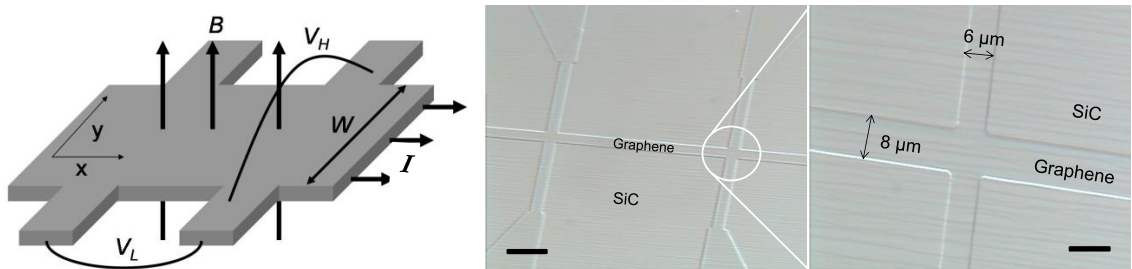


Figure 3.24: (left) Typical Hall bar structure (right) Hall bar pattern fabricated in this work.

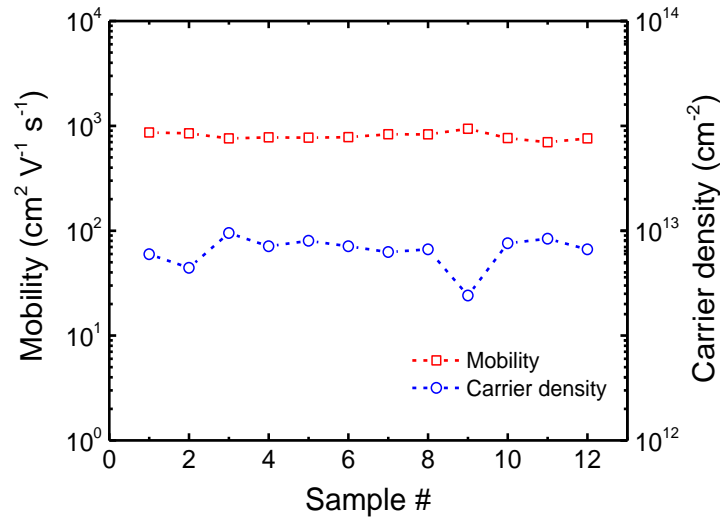


Figure 3.25: Extracted mobility and carrier densities of as-grown blanket epitaxial graphene samples used this thesis.

thesis. All samples showed n-type conduction in graphene, as expected for epitaxial graphene on SiC (0001) with average carrier mobilities and densities of $850 \text{ cm}^2 \text{ V}^{-1} \text{ s}^{-1}$ and $8.0 \times 10^{12} \text{ cm}^{-2}$, respectively.

3.5.3 Low-frequency noise measurements

Electrical noise is present in all circuits and devices and can substantially vary from material to material or even device to device, because it can be generated from different sources such as thermal induced effects, mechanical vibrations and electromagnetic fields [162]. Noise is an unwanted oscillation of the electric signal and is considered as an undesirable parameter in electronic devices. However, the electronic noise spectrum of the device itself can be

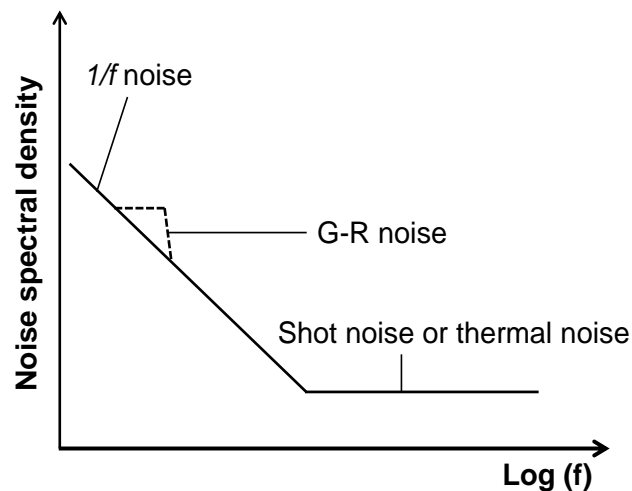


Figure 3.26: Different noise types present in a low-frequency noise spectrum

utilised for studying important characteristics such as quality, performance and the reliability of a material. There are different types of noise components in a typical noise spectrum as shown in Figure 3.26 such as, thermal or Johnson noise, flicker noise or $1/f$ noise, shot noise and generation-recombination (G-R) noise [162]. Thermal and shot noise arises due to the random motion of charge carriers. They are also known as white noise, because their spectral density does not depend on the frequency. The G-R noise and the $1/f$ noise are particularly important in analysing the noise behaviour of the device, as they are usually found at low-frequencies (less than 100 Hz) of the noise spectrum. G-R noise occurs as a result of individual trapping and de-trapping of charge carriers to and from the traps available in the material with a spectral density described by Lorentzian spectrum:

$$S(\omega) \propto \frac{\tau}{1 + (\omega\tau)^2}$$

where τ is the time constant of the G-R process and $\omega = 2\pi f$ is the circular frequency [133, 162]. On contrary, the flicker noise or $1/f$ noise is due to the characteristic spectral dependence on the frequency with $S_V(f) \propto 1/f^\lambda$, where $\lambda=1$. This noise component involves a number of fluctuation processes with a time constant distribution composing $1/f$ dependence in the noise spectra [131,149]. Unlike other types of noise, $1/f$ noise can originate from fluctuations due to number of charge carriers (N) or mobility (μ) or both. There are different theories proposed for the origin of $1/f$ noise in different materials such as CNTs and graphene. These are detailed in chapters 6 and 7.

It has been previously shown that graphene based devices exhibit significant fluctuations in the low-frequency regime which is usually dominated by the $1/f$ noise [133]. For applications such as high frequency communications, analogue circuits and chemical and gas sensors, the noise amplitude is an important figure of merit that contributes to the phase-

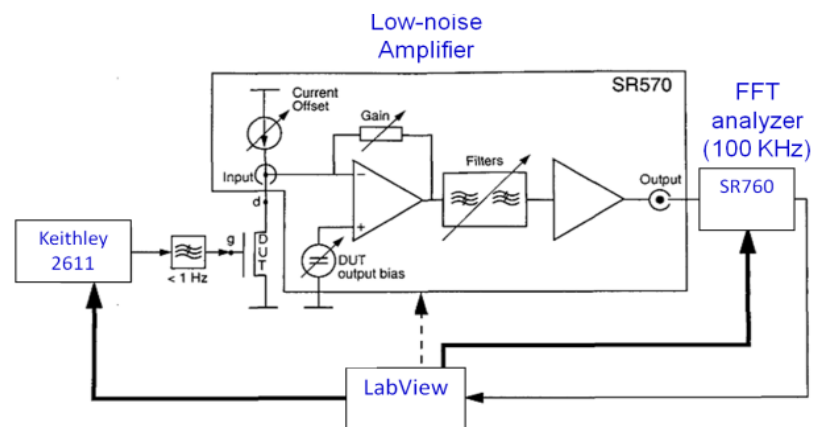


Figure 3.27: Block diagram of a typical low-frequency noise measurement set-up.

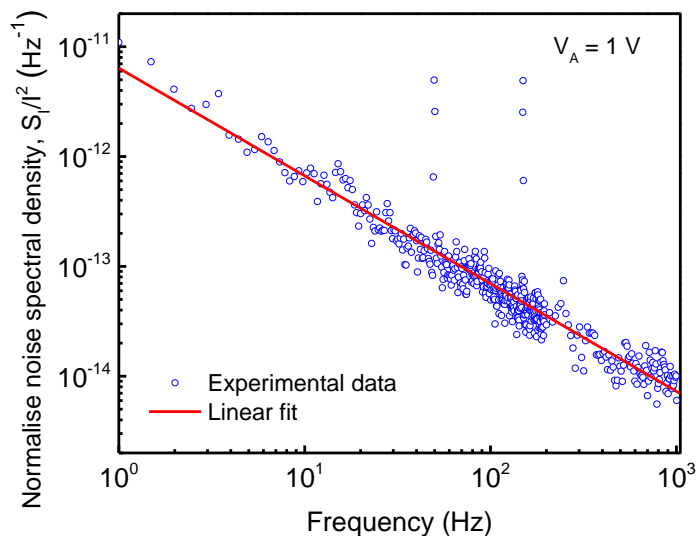


Figure 3.28: Typical $1/f$ noise spectrum observed in graphene.

noise of communication systems such a microwave oscillators or mixes and also affects the detection limits of a sensor. Hence determining the magnitude of $1/f$ noise in graphene and its origin is crucial not only for understanding the underlying noise mechanism but also for assessing the potential of graphene devices for electronic and sensor applications.

In this work, the noise measurements were performed in a two probe configuration by first amplifying the electrical signal of the device under investigation using a Stanford research SR560 low noise current amplifier (LNA) with a 5.0 V built in voltage source. This is to ensure that noise magnitude is elevated above the system level to prevent it from mixed/multiplied into the background noise. Stanford research SR760 fast Four Transform analyzer (FFT) was then used to examine the frequency components of the noise. The measurements were performed between 1 Hz and 100 kHz and averaged over 15 times to minimise the noise magnitude span. The low-frequency noise characterization block diagram is provided in Figure 3.27. All noise measurements were done in a shielded Cascade probing station supported on an anti-vibration table at room temperature and ambient air atmosphere. A typical low frequency noise spectrum of graphene is shown in Figure 3.28.

3.6 Summary

In summary, this chapter has covered the important processing steps and instruments used in the fabrication, functionalisation and characterisation of graphene devices. Synthesis of epitaxial graphene films on SiC (0001) substrates and the e-beam generated oxygen plasma functionalisation procedures were discussed briefly. The details regarding the processing

steps followed for the fabrication of different device structures such as TLM, Van der Pauw and Hall bar patterns using direct and reverse photolithography techniques, along with the post-lithography steps such as metal deposition and rapid thermal annealing have been presented in detail.

The important microscopic and spectroscopic characterisation techniques such as AFM, XPS and Raman spectroscopy were described in detail. In particular, a great emphasis was placed on graphene specific data acquisition procedures and the interpretation of unique spectral signatures of the XPS and Raman spectra of graphene were illustrated. The analysis based on these two techniques forms an integral part of this thesis in explaining the observed chemical and structural changes to the graphene film.

In addition, the operating procedure and analysis of different electrical characterisation techniques such as TLM, Hall and low frequency noise measurements have also been presented. These, techniques are crucial in evaluating the performance and the quality of graphene based electronic devices discussed throughout this thesis.

Chapter 4

Effect of metal contacts and thermal annealing on the electrical properties of graphene

4.1 Introduction

The extraordinary material properties of graphene have attracted considerable interest in developing advanced device concepts, including high-speed field-effect-transistors [163], ultra-wideband optical saturable absorbers [164], ultra-sensitive chemical sensors [93], high-frequency low-noise amplifiers [165], ambipolar radio-frequency mixers [166] and terahertz modulators [167, 168]. The performance of these electronic devices greatly depends on the nature and the quality of the metal-graphene interface, where a unique challenge arises as charge carriers are injected from a three-dimensional metal film into a two-dimensional graphene sheet, which have very different density of states (DOS) and work functions [35]. Carrier transport at the metal-graphene interface can be envisioned as a two-step process, where the initial carrier injection occurs from the metal into the underlying graphene (T_{M-G}) followed by transport of charge carriers from the graphene underneath the metal into the graphene channel (T_{G-GC}), as shown in Figure 4.1 (left). Intimate contact between graphene and metal is essential for achieving high quality electrical contact to maximise carrier injection across the interface. However, it is known that conventional lithography processing techniques (both photolithography and e-beam lithography) used for graphene device

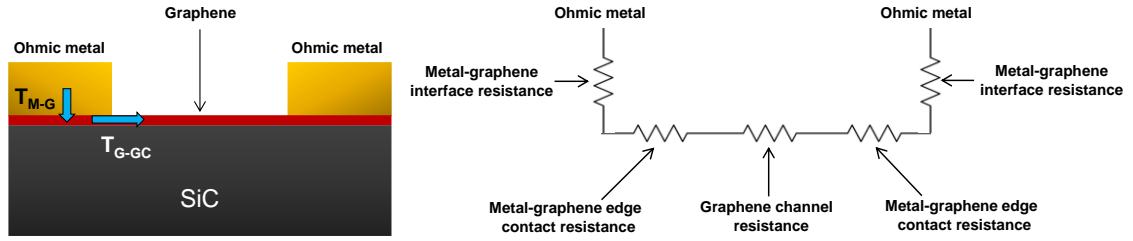


Figure 4.1: (left) schematic cross section of a two-terminal graphene device showing the transfer of injected carrier from the metal into the graphene channel. (right) An equivalent circuit for the contact resistance as a series resistor network.

fabrication significantly contaminate the graphene surface with resist residues [36, 37, 169, 170], which cannot be removed by standard organic solvents such as acetone or *n*-methyl-2-pyrrolidone (NMP). These resist residues can act as external scattering sites and degrade the intrinsic properties of graphene [171, 172]. The presence of such chemical contamination increases the graphene sheet resistance, reduces the carrier mobility and also prevents metal electrodes in making effective contact with the graphene film [173]. As a result, the carrier transmission probability at metal-graphene interface decreases dramatically [171], leading to a high interfacial contact resistance, (R_C). Figure 4.1(right) shows the equivalent circuit representation of Figure 4.1(left) with different types of resistances typically exists in a graphene-metal contact system.

In order to improve the performance of graphene based electronic devices and to access the unique transport properties offered by the graphene channel, R_C associated with the metal-graphene interface should be very low [171, 172]. State-of-the-art silicon metal-oxide semiconductor field-effect-transistors (MOSFETs) demands for a resistance of $80 \Omega\text{-}\mu\text{m}$ per contact [174]. However, contact resistance values of graphene regularly demonstrate higher than this minimum requirement [175-177], greatly impeding the potential of graphene based electronics. Moreover, the reported R_C values are highly inconsistent and vary considerably from a few hundred to a few thousand $\Omega\text{-}\mu\text{m}$, even for the same metal type. For example, a channel width normalised R_C of $10^3\text{-}10^6 \Omega\text{-}\mu\text{m}$ has been reported for Ti/Au-graphene interface [177], contradictory to other studies, which reported $184 \Omega\text{-}\mu\text{m}$ for the same Ti/Au metal configuration [178]. Similarly, in one study, an R_C of $80,000 \Omega\text{-}\mu\text{m}$ was extracted for Cr/Au contacts [179] and in another work it was reported as $\sim 550 \Omega\text{-}\mu\text{m}$ [180]. In the case of Pd-graphene interface, R_C values varied between $450 \Omega\text{-}\mu\text{m}$ [181] and $3000 \Omega\text{-}\mu\text{m}$ [179], whilst for Cu based contacts, R_C was found to be as low as $125 \Omega\text{-}\mu\text{m}$ [181] to as high as $2900 \Omega\text{-}\mu\text{m}$ [182].

The ambiguity in R_C values in these studies is due to a combination of a number of factors including, the methods used for metal deposition, lithographic surface contamination, pre or post-fabrication treatments, measurement conditions and the quality of graphene layers. Since graphene is sensitive to its surrounding environment, all these process dependent factors result in large variation in both R_C and R_{sh} . First, metal films deposited by sputtering technique were shown to introduce structural defects in the graphene film [183, 184], resulting in extremely large R_C ($>10^6 \Omega \cdot \mu\text{m}$), in comparison to metals deposited by e-beam evaporation [184]. Second, employing post-fabrication treatments such as thermal annealing yields different R_C values depending on process conditions used [32, 182, 185], such as annealing temperature and annealing environment (e.g., vacuum, Ar/H₂, O₂, N₂ etc.). Third, the quality of graphene layers also determines R_C , where, a strong interaction of metals is expected to take place with a defective or a polycrystalline graphene film (grown by chemical vapour deposition approach) due to the presence of reactive sites, in comparison to high quality homogeneous films (e.g., exfoliated graphene flakes and epitaxial graphene on SiC). Fourth, and importantly, both R_C and R_{sh} strongly rely on the lithographic process used for the graphene device fabrication. For example, photoresists were found to significantly contaminate graphene surface, in comparison to PMMA resists due to the strong interaction of aromatic molecules present in the photoresist with the graphene film [186]. Moreover, the magnitude of contamination depends on the type of resist used during fabrication, in which, resists such as positive, negative or image reversal photoresists and PMMA, all result in different degree of contamination, thereby resulting in different R_C values. Thorough cleaning of graphene surfaces is therefore necessary to minimise the influence of lithographic resists on R_C .

Surface cleanliness of graphene is also critical for applications such as chemical sensors to measure true responses of adsorbate-graphene interactions and to avoid spurious sensing results. Maintaining clean surfaces are also essential to carry out controlled functionalisation of graphene to target its chemical reactions with designated analyte species. Therefore, to fully exploit the superior properties of graphene, the development of a reliable and reproducible metal contact process technique, which can achieve low contact and low sheet resistances without contaminating the graphene surface, is needed for the advancement of graphene based electronics.

In this chapter, detailed experimental studies on the effect of metal contacts, influence of photolithography processing and the impact of thermal annealing on the electrical characteristics of epitaxial graphene devices were studied. Transfer length method (TLM)

structures were fabricated on different graphene samples to extract the R_C from a wide variety of metallisation schemes including, Ti/Au, Cr/Au, Ni/Au, Au, Pd/Au and Pt/Au contacts. Here, the chapter is organized into three main subsections (4.3.1, 4.3.2 and 4.3.3), in which, the first section (i.e. 4.3.1) discusses the high-temperature electrical characteristics of metal contacts on vacuum grown epitaxial graphene from 20°C to 400°C. In section two (i.e. 4.3.2), the effect of rapid thermal annealing on the electrical, chemical and surface morphological characteristics of argon grown epitaxial graphene-metal contact interfaces is reported. Finally in section three (i.e. 4.3.3), the effectiveness of using a sacrificial layer in maintaining clean graphene surfaces during lithography and the effect of different contact metals on R_C is discussed.

4.2 Experimental details

Epitaxial graphene films were grown on the Si-face of semi-insulating 6H-SiC substrates via the Si sublimation approach. Two types of epitaxial graphene films were used here: a) graphene grown in vacuum and b) graphene grown in argon atmosphere. For the vacuum growth method, graphene films were grown on two 5×5 mm² substrates at 1500°C in a vacuum of $\sim 10^{-5}$ mbar for 90 min and for argon growth, graphene films were grown on seven 8×8 mm² substrates at 1540°C for 30 min.

For electrical measurements, TLM, van-der-Pauw and two-terminal devices were fabricated using AZ5214-E image-reversal photoresist and AZ326-MIF photoresist developer. For convenience, details regarding the fabricating procedure and the device dimensions are provided in the sections 4.3.1, 4.3.2 and 4.3.3 as they appear.

Raman spectroscopy was used to identify the thickness and the quality of graphene layers using an excitation wavelength of 514.5 nm, spot size of 0.70 μm and an incident laser power of ≈ 10 mW. For peak analysis, the SiC background contribution was subtracted from the epitaxial graphene Raman peaks, followed by Salvatzky-Golay smoothing to improve the signal-to-noise ratio of the acquired spectra. The surface morphology and the roughness of graphene films were measured using atomic force microscopy (AFM) in non-contact mode. The surface chemistry of epitaxial graphene was monitored by X-ray photoelectron spectroscopy (XPS) by collecting the high-resolution C1s spectra using pass energy of 20 eV and a spot size of ≈ 400 μm . The C1s spectra were fitted with mixed Gaussian-Lorentzian functions after performing Shirley background subtraction. More detailed information on the XPS spectral acquisition conditions is presented in chapter 3. Hall measurements were

performed to extract carrier mobility, carrier density and carrier type of graphene using a magnetic field of 0.3 Tesla and a current of 100 μA . Here, Raman, XPS, AFM and Hall measurements were all performed after each major processing step in ambient air conditions and at room temperature.

4.3 Results and Discussion

4.3.1 High temperature measurements of metal-graphene interfaces

Figure 4.2(a) shows the AFM topographic image ($40 \times 40 \mu\text{m}^2$) of the graphene film formed on irregular SiC steps, with an average surface root-mean-square (RMS) roughness of 3.9 nm (includes step edges). Hall measurements of this as-grown graphene ($5 \times 5 \text{mm}^2$ area) showed intrinsic n-type character with average sheet carrier density and mobility of $7 \pm 1 \times 10^{12} \text{cm}^{-2}$ and $230 \pm 43 \text{cm}^2 \text{V}^{-1} \text{s}^{-1}$ respectively. Figure 4.2(b) shows the Raman spectra of an as-grown sample, where a small D-peak was observed at $1350 \pm 1 \text{cm}^{-1}$ and a G-peak at $1585 \pm 1 \text{cm}^{-1}$. The I_D/I_G ratio was calculated as 0.21, which indicates the presence of defect sites in the as-grown film.

In order to understand the effect of metal contacts on the electrical characteristics of epitaxial graphene, TLM test structures were fabricated by standard photolithographic techniques as shown in the Figure 4.3. Metal film stacks of Cr/Au and Ti/Au (5 nm/150 nm) contacts were deposited using e-beam evaporation followed by lift-off in warm acetone (45°C). To make a qualitative comparison and also to eliminate any sample to sample related variations, both Cr/Au and Ti/Au contacts were deposited on the same sample using

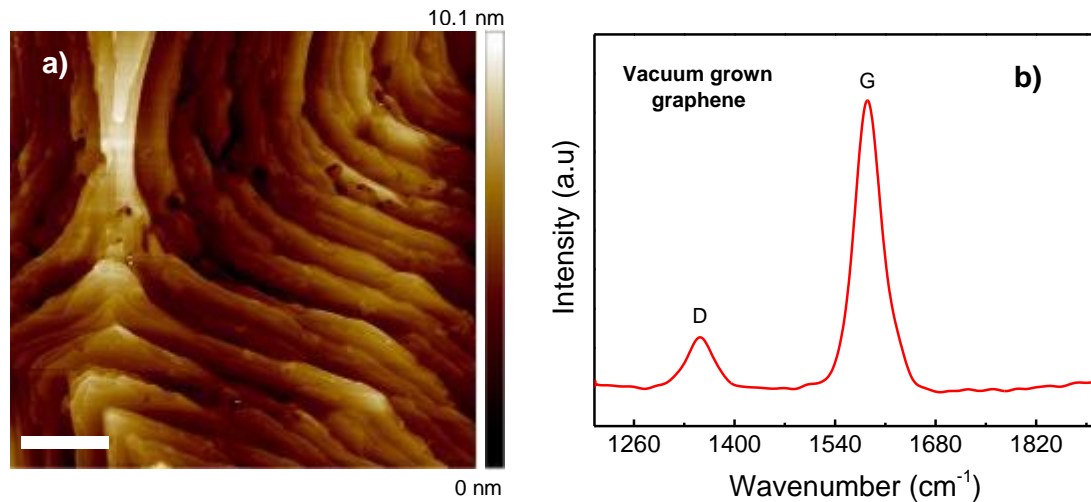


Figure 4.2: a) AFM topography image of an as-grown epitaxial graphene in vacuum. Scale bar is 10 μm and b) Raman spectrum of the as-grown graphene film.

identical TLM test patterns. Here, Cr and Ti were chosen because, apart from their good wettability nature, they are commonly used as adhesion layers in the fabrication of graphene devices, whereas, Au was used to protect Cr and Ti from oxidation and also to serve as a contact metal for wire-boding purposes. The dimensions of TLM structures consists of 200 μm wide (W) and 100 μm long (L) contacts with channel lengths (L_{ch}) varying from 10 μm to 50 μm , in steps of 10 μm . No special cleaning or annealing steps were performed prior to electrical measurements and all measurements were performed at temperatures between 20°C and 400°C.

The ohmic nature of both Cr/Au and Ti/Au contacts was verified from the linear I-V characteristics, as shown in Figure 4.4(a), which also revealed significant difference in electrical resistance. Figure 4.4(b) shows the TLM plot of total resistance against the varying channel length, L_{ch} for both Cr/Au and Ti/Au contacts, showing the differences that exists between these two contact types. Here, R_{C} can be calculated from the y-intercept of a linear fit to the experimental data shown in the Figure 4.4(b). The slope of this linear fit gives channel width normalised value of sheet resistance, R_{sh} , which was calculated as 1219 Ω/sq for Cr/Au contacts and 2668 Ω/sq for Ti/Au contacts, at 20°C. Such a large variation in R_{sh} is surprising, considering that both contact types were fabricated on the sample and have

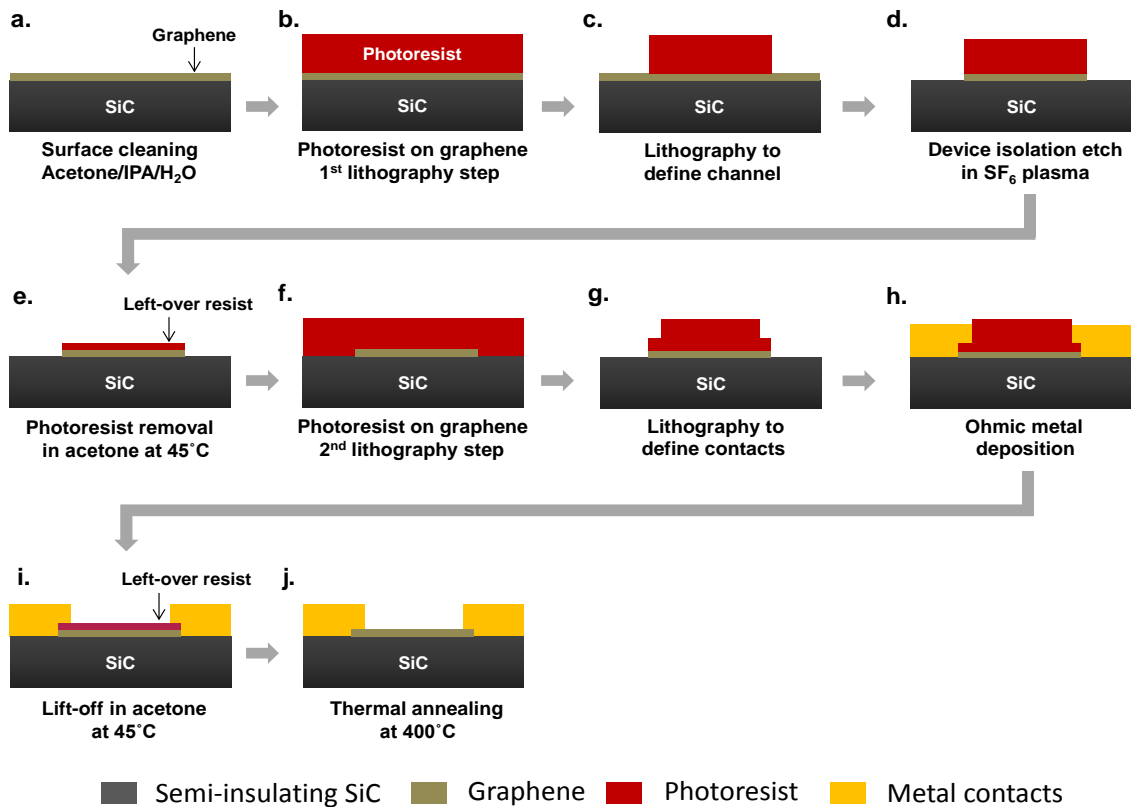


Figure 4.3: Conventional lithography process steps followed for the graphene device fabrication.

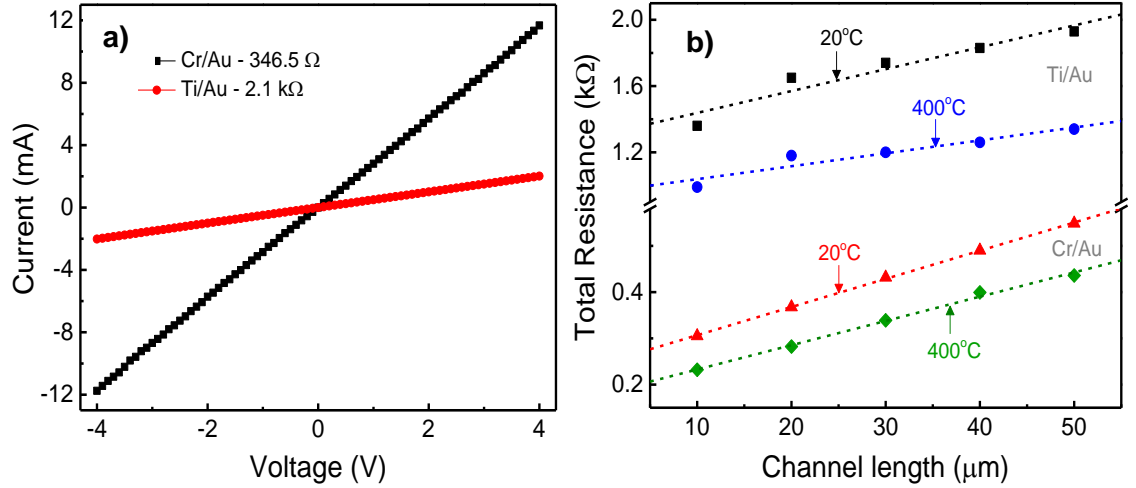


Figure 4.4: (a) I-V characteristics of Cr/Au and Ti/Au metal contacts (b) TLM plot of total resistance against varying channel lengths for Cr/Au and Ti/Au contacts at 20°C and 400°C.

identical TLM dimensions. Raman spectra revealed that the variation in R_{sh} is related to the difference in epitaxial graphene thickness at these two contact areas. Fitting the Raman 2D-peak taken from the two contact locations to a sum of Lorentzian functions, the thickness of the graphene was determined to be two monolayers at Ti/Au contact region (Figure 4.5(a)) and three monolayers near Cr/Au contact area (Figure 4.5b). As the number of layers increases, the charge carrier density also increases due to the increased Density of States (DOS) at the Fermi level (E_F), resulting in lower values of R_{sh} .

In addition to variations in R_{sh} , significant differences in R_C was also observed for both contact types, with 24.6 $k\Omega\cdot\mu m$ for Cr/Au and 131 $k\Omega\cdot\mu m$ for Ti/Au contacts at 20°C.

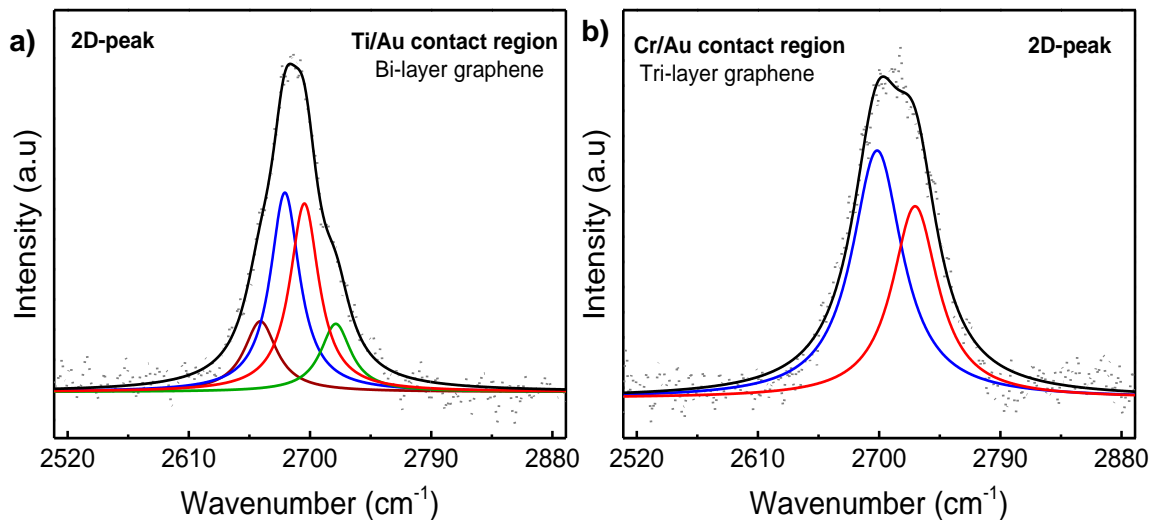


Figure 4.5: (a) Raman 2D-peak taken from the (a) Ti/Au contact location, which showed bi-layer graphene and (b) Cr/Au contact regions, showing tri-layer graphene.

Although one might expect this variation is also due to the difference in graphene thickness, previous studies have indicated that R_C is independent of layer thickness [175]. This behaviour was ascribed to the fact that only the top layer (or two) was involved in effective contact formation, shielding the remaining graphene layers underneath from the influence of metal contacts. Such a large variation in R_C between Cr/Au and Ti/Au is attributed to the nature of interaction of these metals with the graphene. For example, Ti was shown to chemisorb to the graphene surface, leading to the destruction of the graphene band structure, whilst Cr results in physisorption, which does not induce any significant distortion to the graphene lattice [187, 188].

In order to improve the electrical characteristics of graphene, high temperature annealing was performed *in-situ*, in which probe station hot chuck was heated up to 400°C in 50°C steps and the corresponding device electrical characteristics were recorded simultaneously at each annealing temperature. As shown in Figure 4.6(a), when the temperature was increased from 20°C to 400°C, R_{sh} decreased significantly from 1219 Ω /sq to 1050 Ω /sq (14% reduction) for Cr/Au contacts and from 2668 Ω /sq to 1550 Ω /sq (40% reduction) for Ti/Au contacts, respectively. While the decrease in R_{sh} with temperature may seem to follow the behaviour of typical semiconductors, the actual cause for this decrease is due to the reduction in residual contamination on the graphene channel surface with the rise in temperature (more details in section 4.3.2).

In addition to R_{sh} , a substantial decrease in R_C was also observed with temperature (Figure 4.6(b)), resulting in 18 $k\Omega\cdot\mu m$ for Cr/Au contacts and 88 $k\Omega\cdot\mu m$ for Ti/Au contacts respectively at 400°C. This decrease can be attributed to the improved contact interfaces,

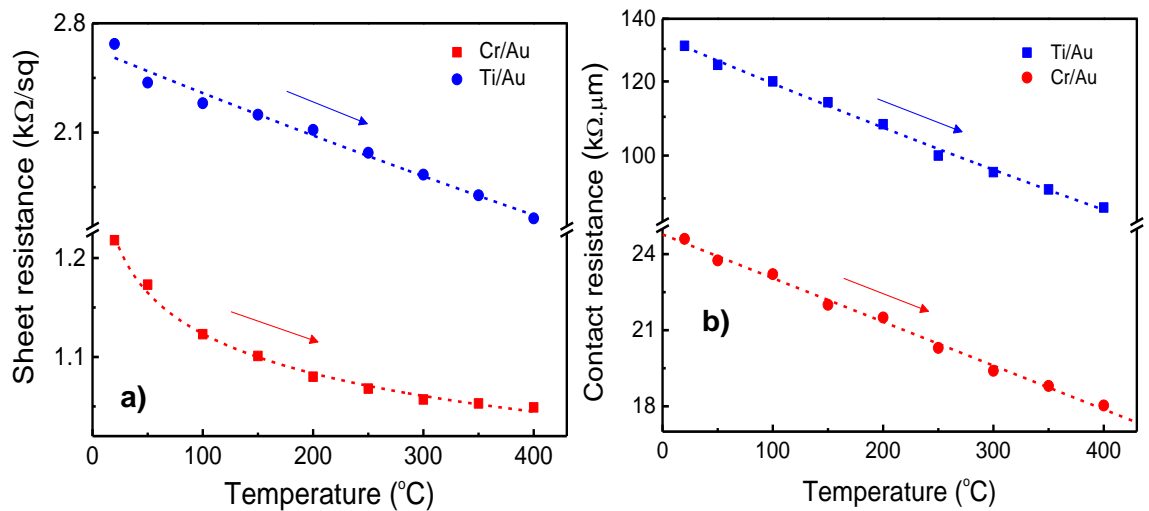


Figure 4.6: (a) Temperature dependence of sheet resistance extracted from TLM method and (b) comparison of contact resistance between Cr/Au and Ti/Au contacts as a function of temperature.

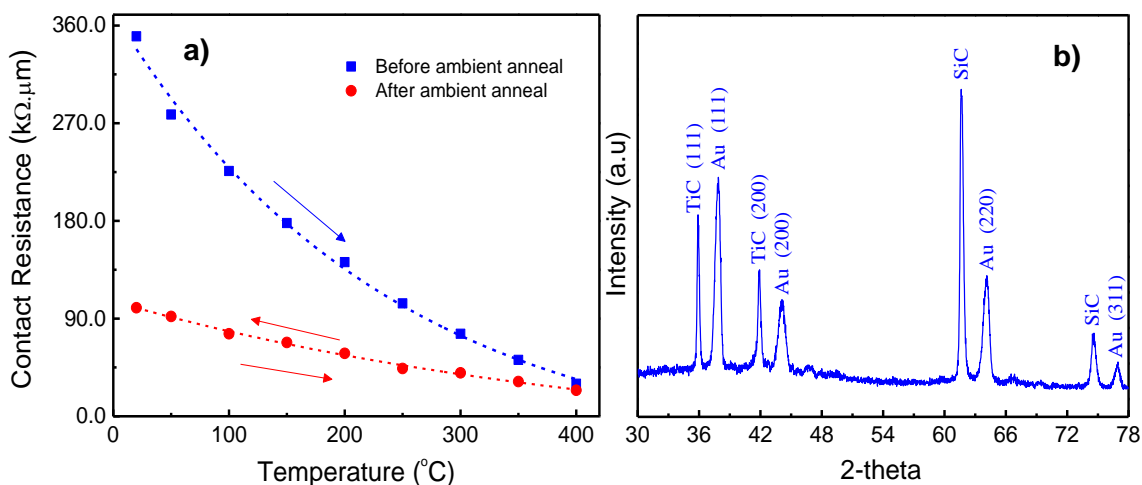


Figure 4.7: (a) Effect of ambient annealing on R_C of Ti/Au contacts, which resulted in considerable improvement in the room temperature performance of the contacts. (b) GAXRD spectrum of the samples after annealing.

which results in the enhancement of thermally generated electron-hole pairs and an increased carrier transmittance across the interface [35]. In order to further verify the effect of ambient annealing on R_C , another set of Ti/Au TLM structures were fabricated on the second sample with identical contact dimensions as those described previously but with different channel lengths ranging from of 80 μm to 180 μm . As shown in Figure 4.7(a), quasi-linear drop in R_C was observed with increasing temperature and when the same measurements were repeated, a 70% decrease in R_C was observed compared to the as-deposited contacts at 20°C. However, no noticeable change was observed for subsequent thermal annealing cycles, indicating that the contacts had stabilised as a result of the annealing process.

Glancing angle x-ray diffraction (GAXRD) was used to analyse the effect of annealing on the metal-graphene interfaces, which showed the existence of (111) and (200) TiC planes (Figure 4.7(b)) for the Ti/Au-graphene contacts [189]. Although GAXRD was performed post high temperature measurements, Roth et.al had observed the TiC formation even at the room temperature [190]. However, TiC is likely to have more prominent effect at higher temperatures due to the thermodynamic stable phase of carbides. Here the formation of TiC occurs either by Ti reacting with the carbon atoms in the left-over resist residue present on the graphene surface or by consuming graphene underneath the contacts. Despite TiC being metallic in nature, its presence can still act as an additional barrier for the charge carriers to efficiently tunnel through the interface. In addition, the reaction of Ti atoms with oxygen cannot be ruled out due to the higher affinity of Ti towards oxygen species, which can further

increase the inhomogeneity of the contact by creating areas with insulating characteristics. These two effects result in carrier injection occurring predominantly along the edges of the metal-graphene contact, leading to current crowding, which can play a dominant role in the observed high R_C . GXRD data did not show any evidence of carbide formation for Cr or Au, as the equilibrium phases for CrC and AuC are not thermodynamically stable for the temperatures studied here [191]. The absence of a carbide layer for Cr/Au contacts and the low R_C values suggests that carbide formation has a significant impact on the device electrical characteristics.

Nevertheless, despite of its highly reactive nature, Ti is usually preferred as an adhesion layer over Cr, because, the high binding energy and the formation of TiC layer at the interface ensures strong adhesion to the graphene film, which is critical for successful wire-bonding of graphene devices onto the chip carrier. In contrast, although Cr/Au metal stack results in low R_C , the weak binding energy of both Cr and Au on graphene results in delamination of these metal films after lift-off process. Moreover, the weak adhesion of Cr also cannot withstand the mechanical pressures applied during the wire-bonding process and often results in metal peel-off from the graphene surface, a serious drawback when considered for use in practical device applications.

4.3.2 Cleaning graphene surfaces using rapid thermal annealing

The above results show that annealing has strong impact on the electrical characteristics of graphene, in which, the contact resistance and sheet resistance can be significantly reduced by subjecting graphene to high temperature annealing. In order to further understand the effect of thermal treatment on the graphene device performance, a comprehensive analysis on the chemical, electrical and surface morphological properties of epitaxial graphene/metal contact interfaces has been performed at different annealing environments such as in vacuum, N_2/H_2 and in the ambient air using rapid thermal annealing process.

Three epitaxial graphene samples were used for this study, which were all grown in Ar atmosphere and in the same run to minimise growth induced variations to the graphene film quality. Hall measurements on these three as-grown samples ($8 \times 8 \mu m^2$ area) showed the typical n-type character of graphene with a carrier density and mobility of $8.5 \pm 0.5 \times 10^{12} \text{ cm}^{-2}$ and $810 \pm 50 \text{ cm}^2 \text{ V}^{-1} \text{ s}^{-1}$, respectively. Figure 4.8(a) shows the Raman spectrum of an as-grown graphene sample with characteristic G and 2D peaks at $1597 \pm 1 \text{ cm}^{-1}$ and $2740 \pm 1 \text{ cm}^{-1}$ respectively taken from the terrace region of SiC steps. No D-peak was observed across

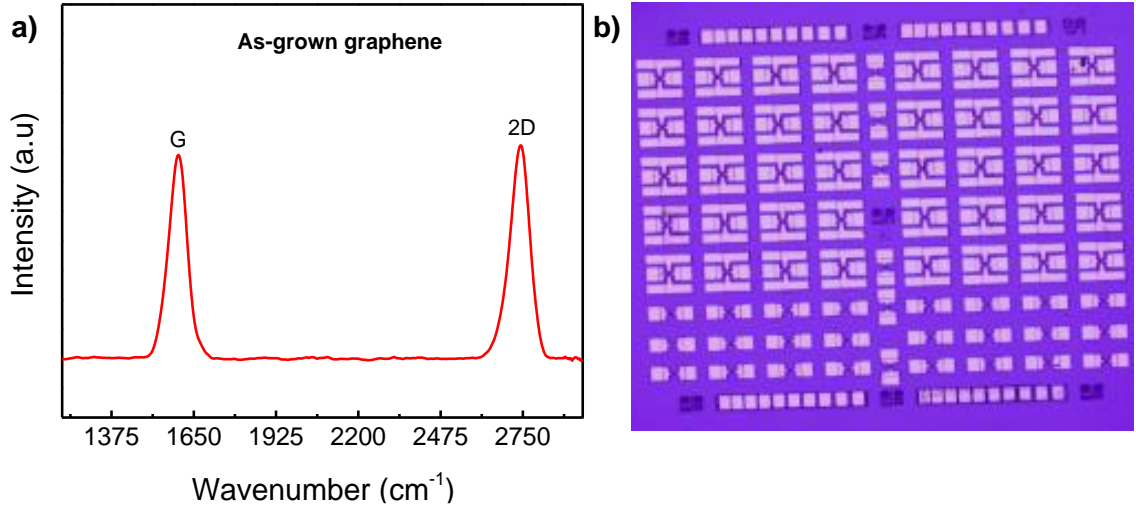


Figure 4.8: (a) Raman spectrum of as-grown graphene film in Ar atmosphere, showing characteristics G and 2D peaks. (b) Optical microscopic image of different types of fabricated devices on the epitaxial graphene.

several probed areas on all three samples, demonstrating high crystalline quality of as-grown graphene films. The 2D-peak was fitted with a single Lorentzian, indicating the thickness of graphene to be one monolayer.

For electrical measurements, an array of forty identical Van-der Pauw structures, thirty two-terminal devices and four sets of identical TLM test structures were fabricated on all three samples as shown in Figure 4.8(b). Ti/Au (10 nm/175 nm) metal films were used as contact electrodes, which were deposited using e-beam evaporation followed by lift-off in warm acetone (45°C). The lithography processing steps followed here were similar to that used for the devices described in section 4.3.1. The active channel area of Van-der-Pauw and two-terminal structures consists of $40 \times 40 \mu\text{m}^2$ channel cross and $40 \times 20 \mu\text{m}^2$, respectively, while each set of TLM test structures have contact dimensions of $150 \mu\text{m}$ wide and $100 \mu\text{m}$ long with L_{ch} varying from $5 \mu\text{m}$ to $60 \mu\text{m}$, in steps of $5 \mu\text{m}$. Note, all three samples were processed in the same batch under similar conditions and all electrical measurements on these samples were performed in the ambient air at room temperature ($\sim 20^\circ\text{C}$). The only difference that exists among these samples is the environment in which they were annealed (i.e. in air, vacuum or $\text{N}_2(95\%)/\text{H}_2(5\%)$). Rapid thermal annealing of the fabricated devices were performed in the RTP furnace system, in which the samples were heated up to the desired temperature in 10 s and maintained at that temperature for 60 min and then rapidly cooled down to room temperature in 120 s. Measurements on different set of samples (not shown here) indicated 60 min as the optimum time for annealing graphene

devices and any prolonged annealing (i.e. > 60 min) at the same temperature showed no noticeable improvements in either electrical or surface chemical properties of graphene.

4.3.2.1 Electrical measurements

The two-probe measurements of as-fabricated devices ($40 \times 20 \mu\text{m}^2$) on all three samples showed ohmic behaviour with linear I-V characteristics and an average resistance of 90 k Ω . However, as mentioned above, the conventional lithographic process significantly contaminates graphene surfaces, which will have strong influence on the graphene electrical properties. Therefore, high temperature thermal annealing is required to recover the intrinsic properties of graphene. In order to identify optimum annealing temperature and ideal annealing environment for post process cleaning of devices, as-fabricated samples were thermally treated in ambient air, vacuum and N_2/H_2 atmospheres for 60 min each at 200°C, 300°C, 350°C, 400°C, 450°C and 500°C sequentially and the corresponding I-V characteristics were measured after each annealing treatment. It is worth noting that, unlike *in-situ* temperature measurements performed in previous section, where both annealing and I-V measurements were done simultaneously, here, samples were annealed first in the RTA system in the designated annealing environment and then taken out of the system and measured at room temperature in the ambient air. As can be seen in Figure 4.9(a), this process resulted in a decrease in total resistance, R_T for all annealing environments, similar to the behaviour seen above. Nevertheless, the magnitude of decrease was found to be larger, when N_2/H_2 annealing was employed, where the resistance decreased from $\sim 92 \text{ k}\Omega$ to $\sim 20 \text{ k}\Omega$ at 400°C. However, note that the resistance of devices annealed in all three environments

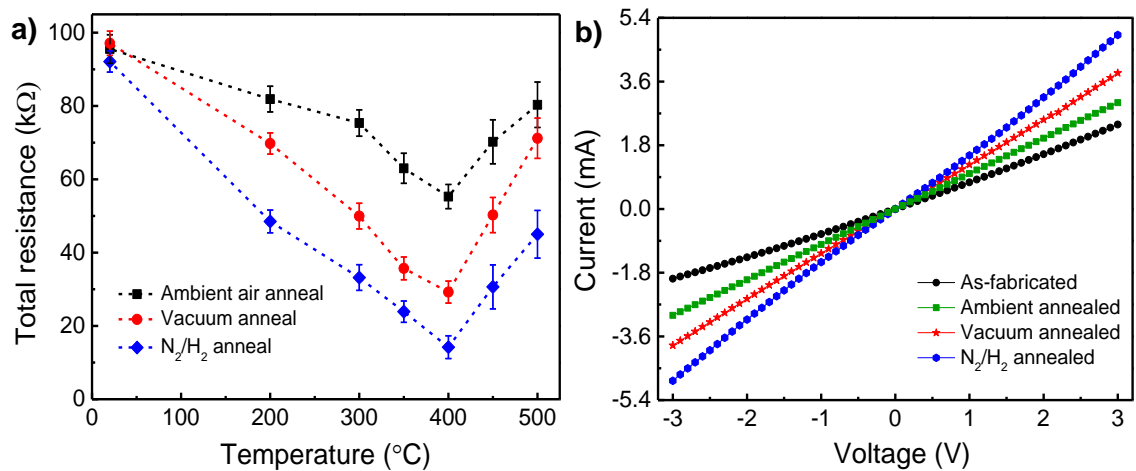


Figure 4.9: (a) Effect of annealing environment on the device electrical resistance (b) I-V characteristics of devices annealed in different annealing environments, showing ohmic behaviour.

remarkably increased when the annealing temperature reached 450°C and 500°C. This was due to the degradation of metal contacts, in particular, Au metal films, which started to delaminate at 450°C, irrespective of the annealing environment, thereby resulting in an overall increase in resistance. These results indicate that annealing at very high temperatures has a detrimental effect on the device performance due to metal contact failure issues and therefore finding an optimum temperature to anneal fabricated graphene devices is critical in improving the device electrical characteristics. For the annealing conditions studied here, 400°C in N₂/H₂ atmosphere was found to provide best results in terms of electrical resistance of the device.

To understand the effect of annealing environment on the device electrical characteristics, contact and sheet resistances were extracted from the fabricated TLM test structures. Figure 4.10 shows TLM plots of three samples with the change in R_T as a function of L_{ch} before and after annealing. As can be seen, all three thermal treatment methods resulted in a decrease in R_T after annealing for 60 min at 400°C, irrespective of the annealing environment. The sheet resistances extracted from the slope of TLM linear fits for all three as-fabricated samples were calculated as 6.88, 7.29 and 6.74 kΩ/sq. After annealing in the ambient air, R_{sh} decreased by 12.79% from 6.88 kΩ/sq to 6.0 kΩ/sq, whilst annealing in vacuum resulted in a 26.55% reduction from 6.74 kΩ/sq to 4.95 kΩ/sq (Figure 4.11(a)). Nevertheless, annealing in N₂/H₂ atmosphere was found to be most effective method with the largest decrease in R_{sh} by 66.11% from 7.29 kΩ/sq to 2.47 kΩ/sq. Here the decrease in R_{sh} after thermal annealing is attributed to desorption of closely bound molecular species of photoresist adsorbed on to the graphene channel, which break away and decompose at high temperatures (more details below).

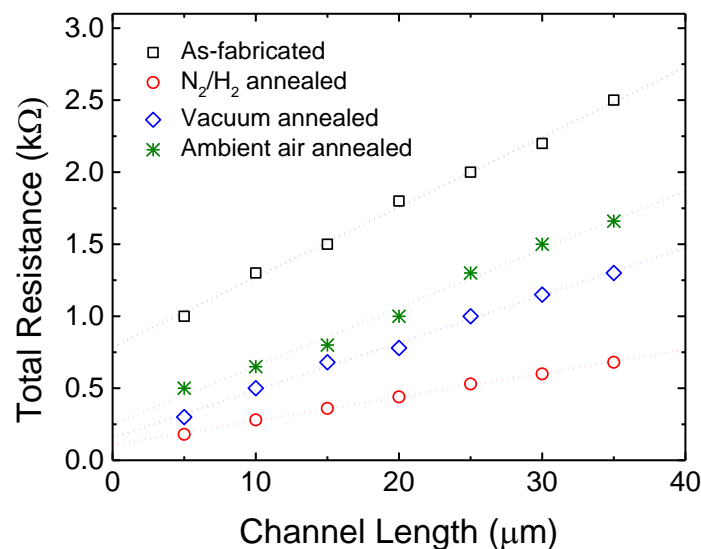


Figure 4.10: TLM plots of samples annealed in a) ambient air, b) vacuum and c) N₂/H₂ atmosphere.

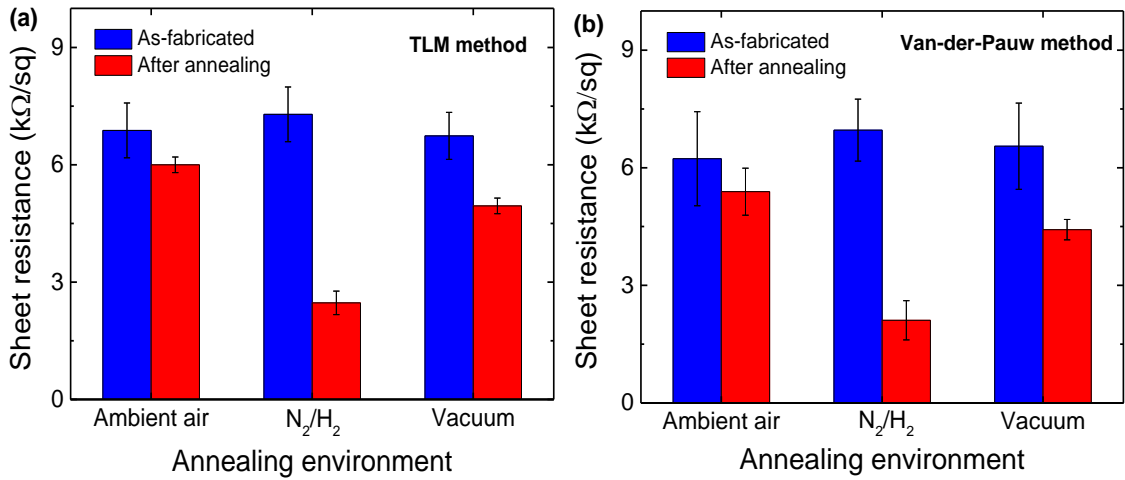


Figure 4.11: (a) Extracted sheet resistance values from (a) TLM and (b) Van-der-Pauw test structures before and after annealing in different annealing environmental conditions.

In addition to TLM measurements, graphene sheet resistances were also independently measured by $40 \times 40 \mu\text{m}^2$ Van-der-Pauw test structures, which yielded R_{sh} values of 5.39 kΩ/sq, 2.11 kΩ/sq and 4.42 kΩ/sq after annealing in air, N₂/H₂ and vacuum, respectively (Figure 4.11(b)). These are very close to the extracted R_{sh} values (post annealing) from TLM measurements, further validating TLM analysis.

Similar to the observation for R_{sh} , the rapid thermal annealing process also had a significant impact on R_{C} . For example, as shown in Figure 4.12, the channel width normalised R_{C} for all three samples before annealing was calculated as 57.21, 58.92 and 54.98 kΩ.μm, respectively. However, after annealing in the ambient air, R_{C} decreased from 58.88 kΩ.μm to 18.53 kΩ.μm (68.52% reduction), in comparison to 86.67% reduction shown by N₂/H₂ annealing, which reduced from 61.07 kΩ.μm to 8.14 kΩ.μm, and a 78.77% decrease in the case of vacuum annealing from 54.98 kΩ.μm to 11.67 kΩ.μm. The decrease in R_{C} indicates increased carrier transmission across the metal-graphene interface as a result of thermal annealing. Here, the carrier injection efficiency at the interface can be classified into two regimes: ballistic transport limit and diffusive transport limit [35]. In the ballistic transport limit, where the scattering mean free path (λ) is greater than the metal-graphene coupling length (λ_{m}), maximum carrier transmission occurs and the contact behaves ideally. In the diffusive transport limit, where $\lambda \ll \lambda_{\text{m}}$, a much reduced transmission probability is expected. For as-fabricated devices studied here, the presence of resist residues on the graphene surface π -orbitals in graphene, leading to a larger λ_{m} . Both these effects are expected to reduce the carrier transmission probability and increase the contact resistance. However, after thermal

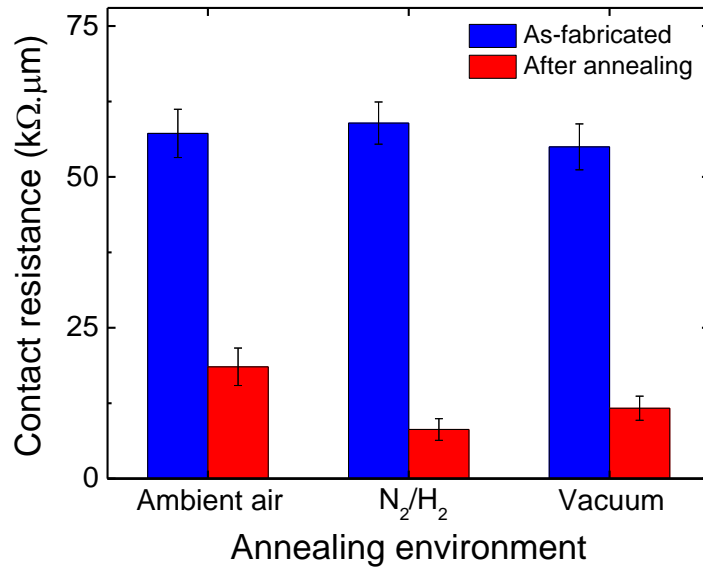


Figure 4.12: Influence of different annealing environments on the contact resistance.

annealing, the reduction in residual contamination improves the scattering mean free path, λ in graphene and also increases the metal-graphene interaction, resulting in shorter metal-graphene coupling length λ_m [35]. As a consequence, carrier injection efficiency increases at the interface, leading to a reduced contact resistance. These results demonstrate that the performance of graphene devices can be significantly improved by high temperature annealing at 400°C, where both R_{sh} and R_C significantly decreases, particularly in the presence of N₂/H₂ environment.

4.3.2.2 AFM analysis

In addition to electrical measurements, the effect of N₂/H₂ thermal treatment on the morphological characteristics of graphene surfaces was examined by AFM in non-contact mode. Figure 4.13 shows the AFM topographic images and the corresponding height profiles of the graphene surface at different stages of the treatment process. As can be seen, the as-grown graphene film showed clean surfaces with smooth SiC steps and flat terraces. The average RMS roughness of the as-grown graphene film taken from 10×10 μm² area of the samples was measured as 2.0±0.7 nm. Note this value includes the roughness of step edges. However, after fabrication, the RMS roughness significantly increased to 11.1±2 nm due to the contamination of the graphene surface with resist residues. As a result, SiC steps are no longer easily identified in the height profile image.

Here the thickness of the resist contamination layer on the graphene surface was found to be around 10 nm in height (see 4.3.3). The formation of this undesirable photoresist scum can be related to the highly viscous nature of photoresists, where the interaction among the polymer chains is significant due their high overlapping, resulting in the polymer chains becoming entangled. When such a polymer solution is coated on graphene, these entangled

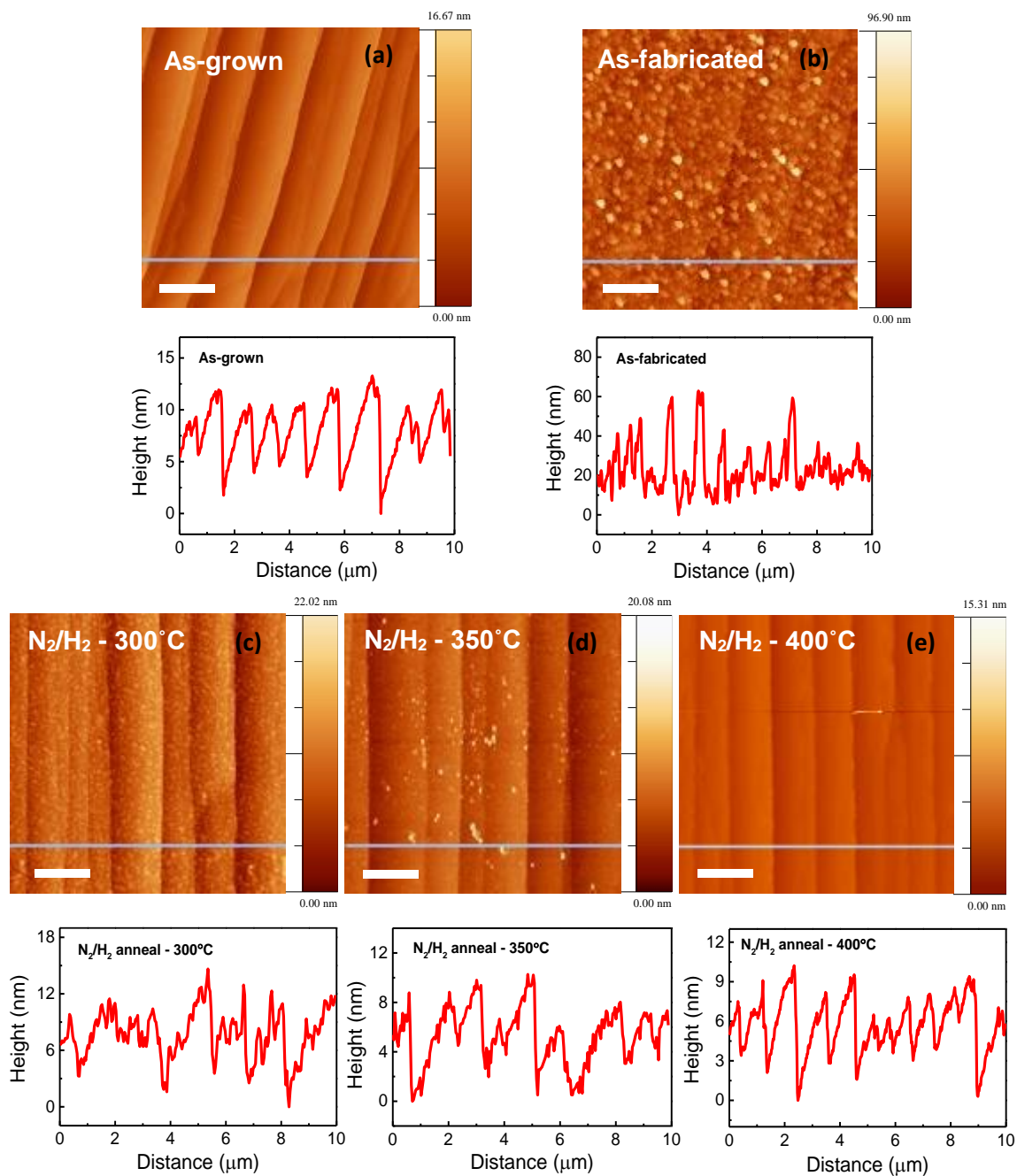


Figure 4.13: AFM topography images of the graphene surface at different annealing temperatures and the corresponding height profile images. All scale bars in the figures are 2 μm.

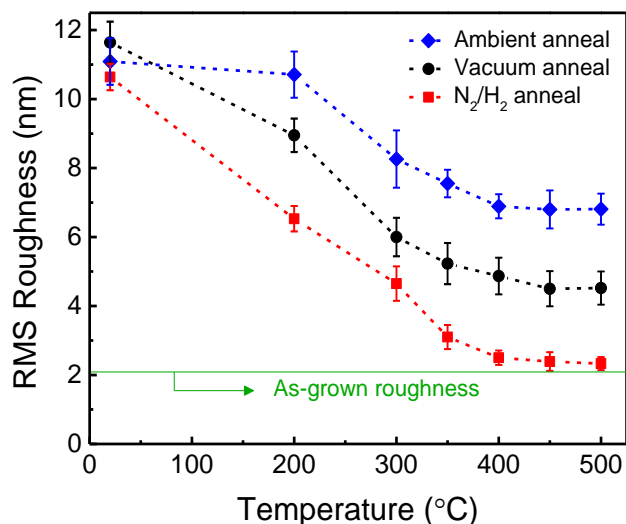


Figure 4.14: RMS surface roughness of epitaxial graphene as a function of temperature at different annealing environments.

polymer chains cannot be readily dissolved in conventional solvents, thereby leaving high concentration of polymer residues on graphene surfaces, including the large polymer humps seen in Figure 4.13(b). In an attempt to remove this resist contamination and to fully restore the intrinsic graphene surface, the sample was subjected to N₂/H₂ annealing at different temperatures for 60 min. As shown in Figure 4.13(c), photoresist contamination cannot be effectively removed at 200°C although the RMS roughness of the graphene decreased to 6.5 ± 0.4 nm due to the partial desorption of resist residues. Using transmission electron microscopy (TEM), Lin *et al.* [169] showed that the decomposition of PMMA resist residues on graphene occurs in a two-step scheme, in where the resist layer facing the air has a lower decomposition temperature, whilst the scission reaction occurs at a higher temperature. Assuming that photoresist also follows similar decomposition mechanisms, the decrease in surface roughness seen after annealing at 200°C could be attributed to the removal of photoresist residues that were exposed to air, which was substantiated by the re-appearance of SiC steps post-annealing treatment.

Annealing at 300°C showed a partial recovery in surface roughness, which reduced to 4.65 ± 0.5 nm, but the graphene surface remained covered with the resist residues as seen in Figure 4.13(d). However, after thermal treatment at 350°C, the majority of these resist residues from the graphene surface were removed as shown in Figure 4.13(e), resulting in a much smoother surface with a RMS roughness of 3.1 ± 0.3 nm. By further annealing at 400°C, the surface appears to be even cleaner and the corresponding height profile showed the recovery of SiC step morphology with the average roughness of 2.5 ± 0.2 nm. This indicates

that the resist residue on graphene surface, which comes from the photolithography process, was effectively removed. Further increase in temperature to 450°C and 500°C did not result in any noticeable change in topography apart from a minor reduction in surface roughness. Figure 4.14 shows the comparison between N₂/H₂, vacuum and ambient annealing on the RMS roughness. As can be seen, annealing as-fabricated devices in N₂/H₂ was found to be far more effective in reducing the residual contamination present on the graphene channel, in comparison to other two annealing methods consistent with the electrical measurements.

4.3.2.3 XPS analysis

In order to evaluate the effect of N₂/H₂ annealing on the surface chemistry of graphene, XPS was performed after each thermal treatment step. Figure 4.15 shows the evolution of high-resolution C1s core-level spectra with annealing time. For the as-grown graphene film (Figure 4.15(a)), the C1s peak was fitted with three Gaussian-Lorentzian components corresponding to Si-C bond at 282.97 eV, C-C (*sp*²) bond at 284.28 eV and the interfacial layer (IFL) at 285.10 eV. No evidence of carbon-oxygen bonding was found within the resolution of the spectrometer for the areas investigated. However, immediately after device fabrication, a clear change in the chemical composition of the graphene film was observed (Figure 4.15(b)) with a broadened C1s spectrum along with shoulder peaks appearing at higher binding energies, representing different functional species originating from photoresist residues on the graphene surface. Here, the peaks at 286.13 eV, 287.37 eV and 288.65 eV correspond to hydroxyl functional group (C-OH), carbonyl functional group (C=O) and carboxylic functional group (O-C=OH) respectively. This shows that photoresist residues were not completely removed from the graphene surface after standard acetone cleaning process, consistent with the data from AFM measurements shown above. Image-reversal (IR) photoresists consists of four basic elements: cresol novolak resin (a phenol-formaldehyde copolymer), diazonaphthoquinone (a photoactive compound), 1-methoxy-2-propyl acetate (an organic solvent) and an additive such as monazoline, imidazole or triethylamine. The π -conjugated aromatic components in novolak resin bind strongly to the graphene surface due to the attractive π - π interaction between aromatic molecules and the graphene surface. As a result, resist residues bonded to graphene cannot be dissolved in conventional organic solvents.

In order to reduce the surface contamination, high temperature annealing was performed in N₂/H₂ atmosphere for 60 min at different temperatures. Figure 4.15(c)-(f) shows the

corresponding core-level spectra of the sample, representing the chemical state of the graphene surface. For example, after annealing the as-processed sample at 200°C, the intensity of the observed polymer peaks reduced considerably due to the breakage of bonds

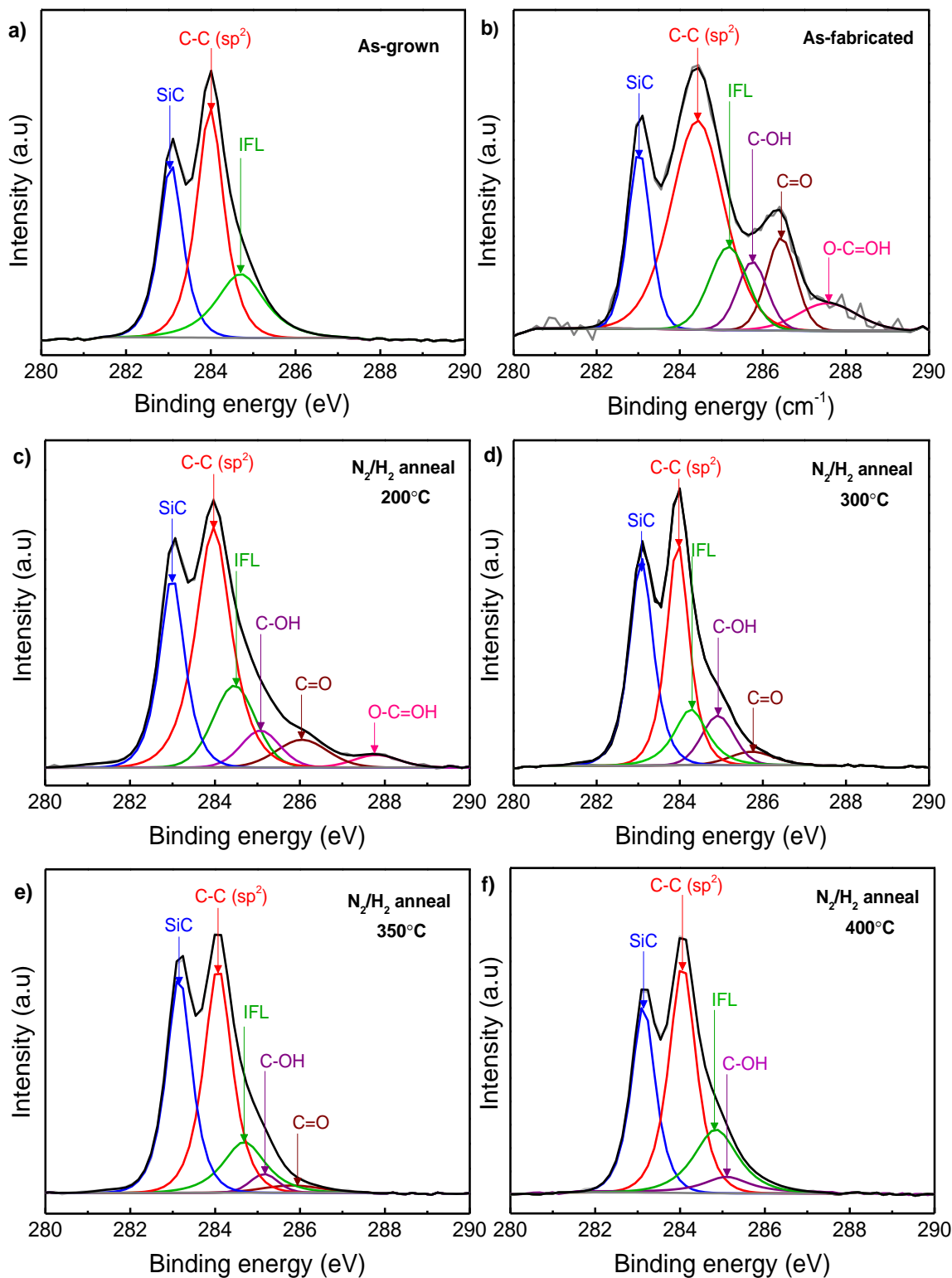


Figure 4.15: Surface chemistry of graphene surface for a) as-grown, b) as-fabricated, c) N_2/H_2 annealed at 200°C, d) 300°C, e) 350°C and f) 400°C.

within the photoresist layer that is exposed to air. The breakage of bonds is due to the vapourisation temperature of compounds present in the photoresist. Specifically, 1-methoxy-2-propyl acetate, a solvent used in the production of IR-photoresists vapourises at 145°C, whereas, the boiling points of different species of cresol (C₇H₈O), a conjugated aromatic compound used in the production of novolac resin resists are in the range of 191°C to 202°C. Despite this initial decrease, annealing at 200°C was found to be insufficient to completely remove the resist residues, as the temperature is very low, making it difficult to break the bonds between photoresist and the graphene.

Upon increasing the annealing temperature to 300°C, a sharp decrease in the intensity of all polymer peaks (i.e. C-OH, C=O and O-C=OH) was observed, indicating the decrease in concentration of resist residues on the graphene. Further annealing the sample at 350°C showed a significant decline in both C-OH and C=O functional group intensities along with the disappearance of O-C=OH peak. Here, the absence of carboxylic peak (O-C=OH) indicates that the actual decomposition reactions of the polymer starts at 350°C by breaking the bonds between the graphene and the polymer residues. More drastic changes were found to occur at 400°C annealing temperature, where the carbonyl peak also disappears and the intensity of hydroxyl peak reduces drastically. Both carbonyls and carboxylic groups form the central structure of the photoresist and their absence indicates depolymerisation and decomposition of residues from the graphene surface.

The thermal decomposition of novolac resins present in the photoresist is characterised by a complex mechanism, involving reactions of chain scission and polymer-cross linking. It was shown that the thermal degradation of novolacs in the non-oxidising atmosphere proceeds in two steps [ref], beginning with the breakdown of –OH groups attached to the benzene ring followed by a depolymerisation process, where the breaking of bonds occur between aromatic rings and methylene bridges as depicted in Figure 4.16(c).

Using gas-chromatography, Skyes *et al.* [192] have shown that the primary species that release during the initial stages (from 150°C) of resist decomposition process is predominantly H₂O as a direct result of the thermal breakdown of –OH groups. When the annealing temperature reaches 350°C and above, major volatile products were found to release, including, CO₂, CO, C₆H₆, C₆H₅OH, H₂O, CH₄, and (CH₃)₂C₆H₃OH, indicative of thermal breakdown of the polymer. Therefore, the absence of both carboxylic and carbonyl peaks at 350°C and 400°C, respectively could be attributed to the decomposition of resist residues in the form of different volatile organic by-products, thereby eliminating the resist

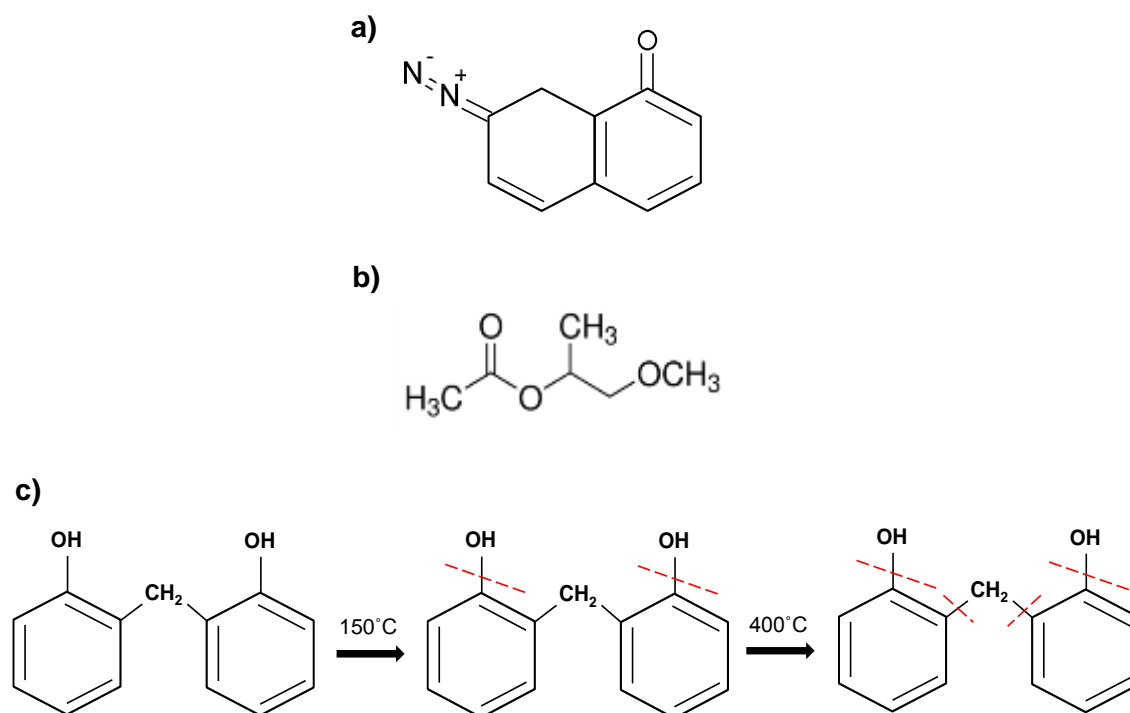


Figure 4.16: Structures of chemical compounds present in a typical novolac photoresist: a) DNQ or Diazonaphthoquinone b) 1-methoxy-2-propyl acetate and c) novolac resin.

contamination. Note, the small concentration of C-OH peak was still present even after annealing the sample to up to $500^\circ C$. This is mainly because of the re-adsorption of H_2O or oxygen molecules on to the graphene surface when exposed to ambient air after the thermal annealing treatment, consistent with observations in other studies. Note, as the XPS survey spectra showed no evidence of nitrogen in the elemental analysis, the possibility of nitrogen adsorption and therefore its effect on graphene is excluded here.

4.3.2.4 Hall measurements

Hall measurements were performed on $40 \times 40 \mu m^2$ Van der Pauw test structures to ensure no degradation in transport properties of graphene has occurred as a result of the thermal annealing process. Figure 4.17(a) and (b) show the plots of change in carrier mobility and sheet carrier density of two samples annealed in vacuum and N_2/H_2 , respectively, as a function of annealing temperature. Before annealing, the average carrier mobility and carrier density for twenty four Van der Pauw devices on both samples were measured as $915 \pm 50 \text{ cm}^2 \text{ V}^{-1} \text{ s}^{-1}$ and $5 \pm 1.2 \times 10^{12} \text{ cm}^{-2}$, respectively. This small improvement in mobility and small reduction in carrier density, in comparison to as-grown graphene films indicates that the left-over photoresist residues act as electron withdrawing molecules, extracting charge carriers

from the graphene sheet. Nevertheless, as-fabricated devices showed n-type character, indicating that AZ5214E photoresist residues on graphene do not significantly dope the film, when compared to other resist types such as PMMA or SU-8.

Upon annealing these as-fabricated devices in vacuum and N_2/H_2 atmosphere, substantial improvements to the device electrical characteristics were observed, in which the carrier mobility increased with the increasing annealing temperature to up to 400°C . Such an increase in mobility with temperature is attributed to combination of reduction in surface contamination on the graphene channel, resulting in a decrease in charge impurity scattering from the removal of photoresist contamination layer on top of the graphene, as well as increase in charge carrier doping from the ambient atmosphere. It is known that oxygen acts as a p-type dopant to graphene due to its high electronegativity, in comparison to carbon, leading to a reduction in electron carrier density in the exposed graphene regions. Many studies have shown that graphene becomes even more active to molecular adsorption after annealing, whereby it attracts oxygen more strongly from the ambient air post-high temperature annealing. However, the influence of oxygen on as-fabricated graphene devices will be significantly reduced due to the presence of photoresist contamination layer on the graphene surface. Nevertheless, with the increase in annealing temperature, resist residues and trapped adsorbents by the photoresist start to decompose, providing adsorption sites for O_2 and H_2O molecules present in the ambient air, thereby increasing the interaction between graphene and adsorbed molecular species. As a consequence, the electron withdrawing nature of oxygen decreases the carrier density in electron rich epitaxial graphene film, resulting in a significant increase in the mobility, consistent with previous studies on epitaxial graphene. Here, the magnitude of increase was found to be dependent on the environment in which the devices were annealed. For example, annealing in vacuum showed

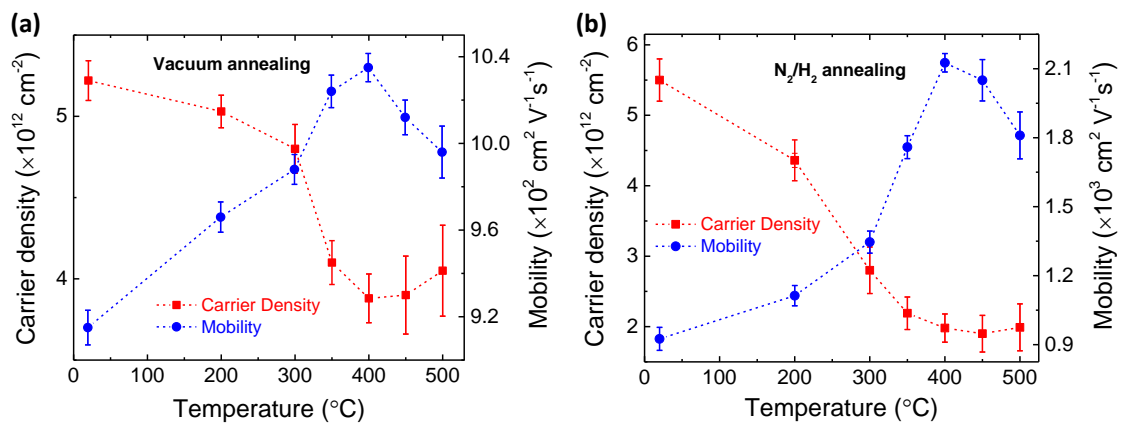


Figure 4.17: The impact of a) vacuum annealing and b) N_2/H_2 annealing the graphene mobility.

an increase in mobility from $915 \pm 8 \text{ cm}^2 \text{ V}^{-1} \text{ s}^{-1}$ (before annealing) to $1035 \pm 8 \text{ cm}^2 \text{ V}^{-1} \text{ s}^{-1}$ (after annealing at 400°C). In contrast, annealing in N_2/H_2 atmosphere resulted in an increase from $925 \pm 50 \text{ cm}^2 \text{ V}^{-1} \text{ s}^{-1}$ to as high as $2126 \pm 72 \text{ cm}^2 \text{ V}^{-1} \text{ s}^{-1}$ after thermal treatment at 400°C , indicating, the presence of reducing gas atmosphere leads to a stronger reduction in surface contaminants and hence a large number of available adsorption sites for oxygen molecules to adsorb and decrease the intrinsic carrier density. Note, this unintentional doping process from the ambient atmosphere post-annealing treatment does not change the polarity of epitaxial graphene, but only reduces the electron concentration in graphene by moving the Fermi energy closer to the Dirac point, thereby retaining the n-type character. However, similar to that observed in two-terminal resistance measurements, annealing above 400°C either in vacuum or N_2/H_2 atmosphere resulted in a decrease in graphene device mobility, primarily due to the Au contact delamination issues. Thus for the optimal electrical performance of graphene devices and for recovering resist-free graphene surfaces, post-processing annealing temperature of 400°C in N_2/H_2 environment for 60 min is recommended.

4.3.3 Electrical characteristics of graphene fabricated using aluminium sacrificial layer approach

Although rapid thermal annealing of as-fabricated devices in N_2/H_2 provides an easy means to remove polymer residues on the graphene channel, it is not very effective in cleaning graphene surfaces that are already covered with metal contacts. This is because, metal films act as a barrier layer and restricts the resist residues from decomposing during the annealing process, thereby reducing the impact of thermal treatment in efficient cleaning of graphene at contact interface regions. As a result, the final annealed device will consist of regions with clean graphene surfaces (i.e. at channel areas) and the regions that are still contaminated with photoresist residues (i.e. at metal-graphene interface areas). Such a varying nature of surface chemical composition introduces uncertainty into studies of intrinsic properties of graphene devices, leading to low device reliability with poor performance. For example, despite the improvement in device electrical characteristics after N_2/H_2 thermal treatment, the final contact resistance value is still very high ($\sim 3.75 \text{ k}\Omega \cdot \mu\text{m}$), most likely due to the persistent presence of resist residues at the interface. Unfortunately, thermal annealing cannot be employed just after patterning of contact windows and prior to metal deposition because of the issues with the resist flow, loss of features, resist cross linking etc. To overcome this

issue, a number of alternatives have been suggested to control the contamination at contact regions prior to metallisation, which includes, AFM tip based mechanical cleaning [193], mild UV ozone treatment [178, 194], low-power oxygen plasma treatment [185, 195], contact area patterning of graphene into nanoribbons [181] and metal catalysed etching at the contact regions [196]. Although these approaches are helpful in reducing organic residues and/or improving the metal-graphene interfacial characteristics, they are either time consuming or damaging to the graphene lattice structure. For instance, the use of AFM based cleaning is limited to laboratory-scale, because of the extremely low-throughput, whereas, UV ozone and oxygen plasma treatments results in generation of defect sites in random fashion and if the process conditions are not tuned appropriately these techniques will result in significant loss of graphene and/or enhanced scattering in the contact region, leading to a degraded contact resistance [181]. In the case of contact area patterning approach, it require additional lithography steps to pattern graphene into nanoribbons followed by more than ten hours of high temperature annealing. Similarly, metal catalysed contact patterning technique needs additional lithography steps in depositing the metal film followed by high temperature annealing in hydrogen, resulting random etch pits in the graphene film. These additional process steps are damaging to the graphene film and also complicate the fabrication process. Therefore the development of an alternative method to minimise the surface contamination as well as improve the electrical properties at metal-graphene interfaces without significantly degrading the intrinsic structural properties of graphene is highly desirable.

In this study, an alternative approach has been developed to eliminate resist residues using sacrificial layer technique [197]. Instead of cleaning the contaminated surface, a sacrificial layer was deposited onto the graphene film to prevent graphene from coming into direct contact with the photoresist during lithography. After processing, photoresist and sacrificial layers were removed without damaging or contaminating the graphene film underneath [172, 197].

Five samples were used in this study, which were all grown in the same run as the samples used in section 4.3.2 and have very similar electrical, structural and morphological properties as them. For electrical measurements, thirty identical two-terminal devices ($40 \times 20 \mu\text{m}^2$), an array of forty identical Van der Pauw structures ($40 \times 40 \mu\text{m}^2$) and four sets of TLM test structures ($W=150 \mu\text{m}$, $L=100 \mu\text{m}$ and $L_{\text{ch}}=5 \mu\text{m}$ to $45 \mu\text{m}$) were fabricated on four samples using a slightly modified lithography process as shown in Figure 4.18. Unlike the conventional acetone/IPA/ H_2O used for cleaning graphene surfaces, all samples for this study were cleaned in dimethylformamide (DMF) solvent at 20°C for 5 min followed by 5

min clean in H_2O and dried in dry N_2 . Although acetone removes residual organic contaminants from the graphene surface (before lithography), its high vapour pressure leads to extremely fast vaporisation of the solvent, resulting in re-deposition of these contaminants back onto the graphene surface. Therefore, an additional follow-up clean with either methanol or IPA is usually performed to achieve clean surfaces. Nevertheless, the advantage of using DMF as a primary cleaning solvent is, in addition to the effective removal of organic residues, the usual follow-up clean with IPA or methanol is not required due to the high vapour pressure and the high boiling point of DMF, which ensures the contaminants that were removed from the graphene surface remain in the solvent itself, thereby reducing an additional process step.

After this initial cleaning procedure, the device fabrication started with the deposition of a 10 nm thick blanket Al sacrificial layer on the as-grown graphene film of all four samples using e-beam evaporation and oxidised overnight under ambient conditions. The material of choice as a sacrificial layer determines the effectiveness of this approach. Here, Al was chosen for three reasons. First, Al physically adsorbs to the graphene surface and was demonstrated

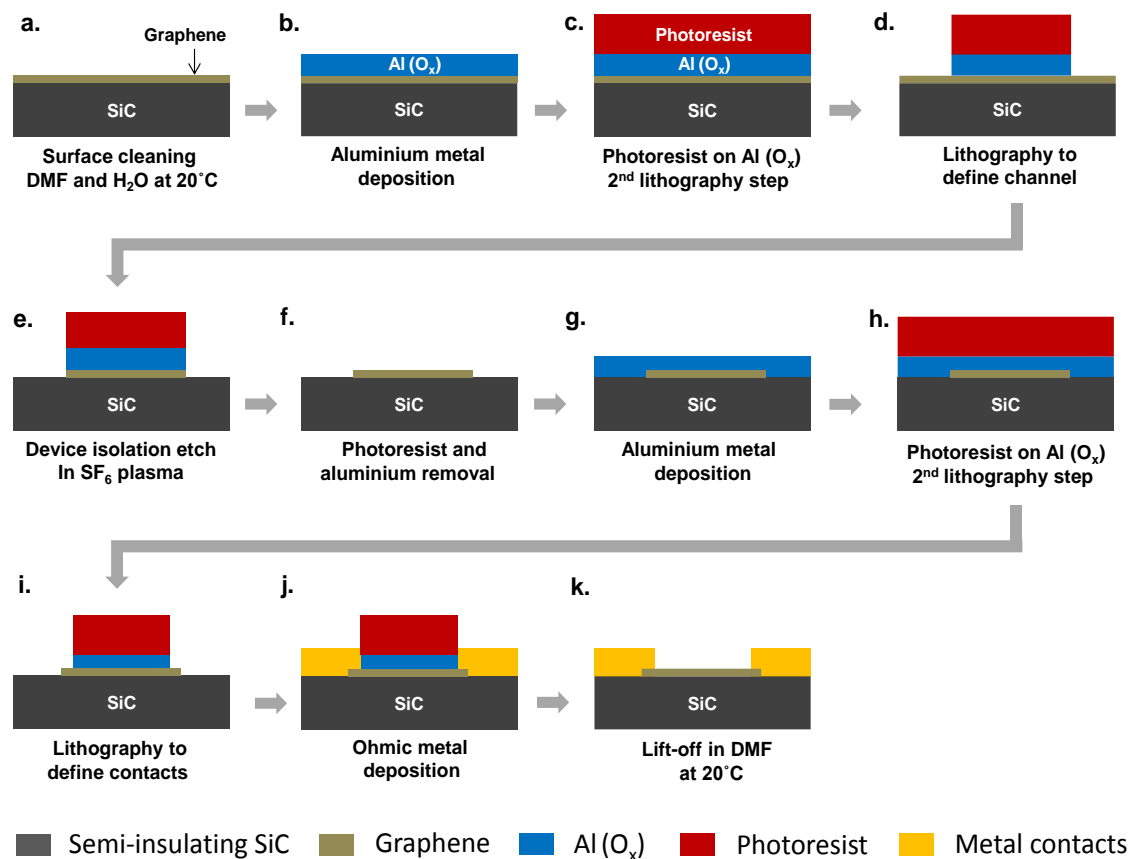


Figure 4.18: Lithography process steps followed for the graphene device fabrication using $\text{Al}(\text{O}_x)$ based sacrificial layer approach.

not to create any defects in the film or modify the band structure [81, 82]. Second, Al is already used in graphene device fabrication as a seed layer for gate dielectric deposition. Third, TMAH, which is the main ingredient used in selective etching of Al can be commonly found in many photoresist developers. After Al deposition and oxidation, subsequently, photolithography was then performed on top of this oxidised Al layer by patterning the AZ5214-E photoresist to create graphene channel and to define metal contact windows. This patterned photoresist was developed in AZ326-MIF developer, which contains 2.38% tetramethylammonium hydroxide (TMAH). Here, the Al(O_x) layer at these contact window regions were removed at the same time during the development of photoresist just by increasing the developing time by a few seconds, thereby eliminating additional steps required in etching Al(O_x) layer separately.

For electrodes, different metal film stacks such as Ti/Au, Cr/Au, Ni/Au, Pd/Au, Pt/Au (10 nm/175 nm) and Au (175 nm) were deposited with a base pressure of 7×10^{-4} mTorr. Following metal deposition, lift-off was done overnight in DMF at 20°C and the finally the Al(O_x) layer was removed in AZ326-MIF developer. No acidic treatments were utilised at any stage of the fabrication process, thereby eliminating the risk of unintentional modification or destruction of the graphene film. Moreover, no thermal annealing and no special cleaning steps were performed prior to chemical, electrical and surface characterisations.

4.3.3.1 AFM analysis

The topography images in Figure 4.19(a) ($10 \times 10 \mu\text{m}^2$) and (b) ($3 \times 3 \mu\text{m}^2$) of an as-grown graphene film shows clean surfaces with smooth terraces as indicated by the respective height profile images. The average RMS roughness of these as-grown films measured from all four samples was 2.2 ± 0.5 nm (this includes step edges). Figure 4.19(c) and (d) shows the topography profiles of sample after removal of Al(O_x) and just before metal deposition. As can be seen from these topography profiles, no visible contamination on the graphene surface was observed within the resolution of the system, indicating the effectiveness of Al(O_x) sacrificial layer in maintaining clean surfaces during the lithography. The RMS roughness of graphene was measured as 2.3 ± 0.8 nm, demonstrating that the use of Al(O_x) layer does not induce any unwanted surface modifications to the graphene surface morphology. Similar clean graphene surfaces were observed on all four samples fabricated using the sacrificial layer approach. Nevertheless, note that, in order to achieve clean

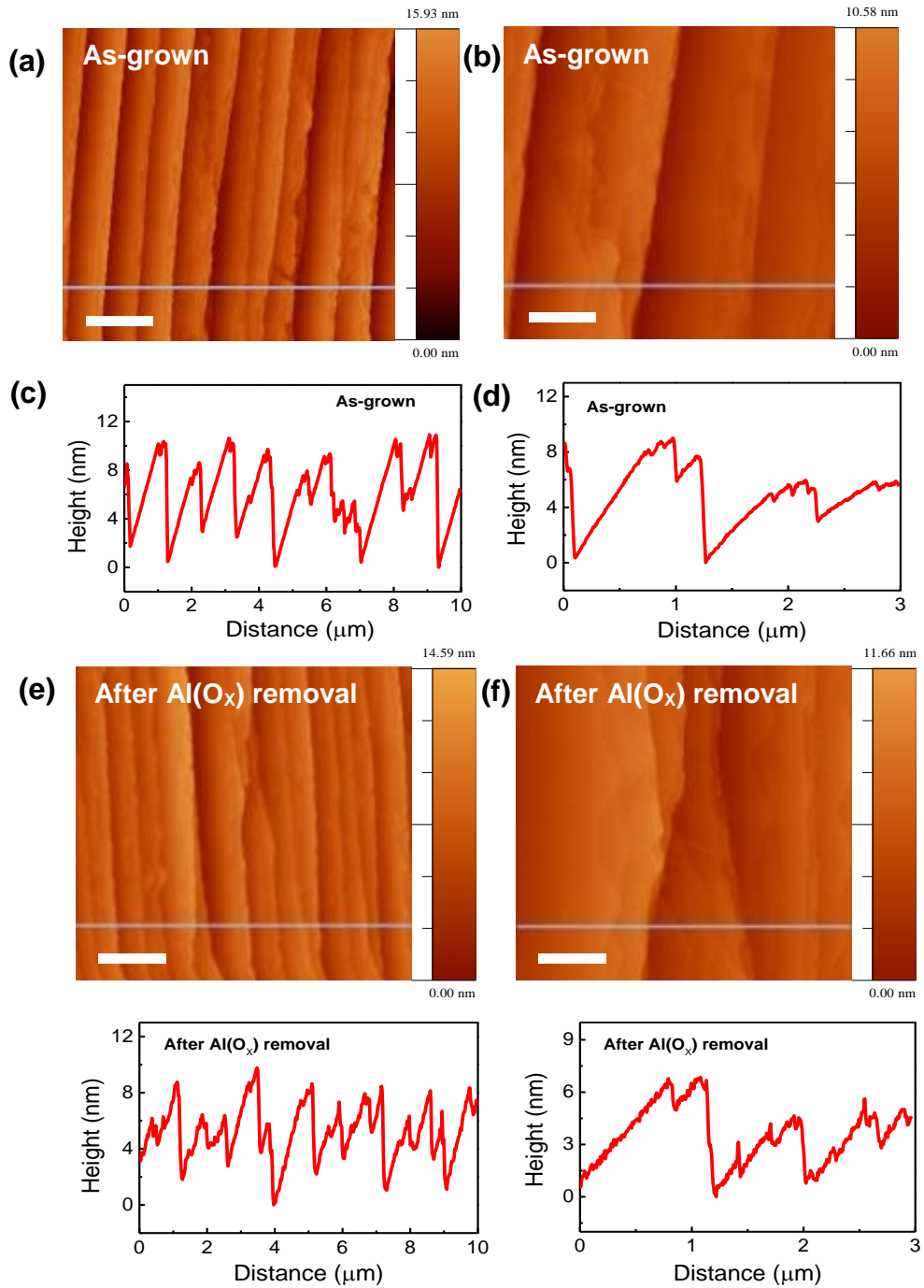


Figure 4.19: AFM topography and line profile images (a) as-grown graphene surface $10 \times 10 \mu\text{m}$ (left) and $3 \times 3 \mu\text{m}$ area (right). (b) Just after lithography and before the metal deposition. Scale bars in the images (a) and (e) are $2 \mu\text{m}$, whilst its 600 nm for the images (b) and (f)

graphene surfaces using this sacrificial layer technique, Al layer thickness of at least 10 nm is required for efficient protection of the graphene from the photoresist residues (thickness of 5 nm was found contaminate the graphene film).

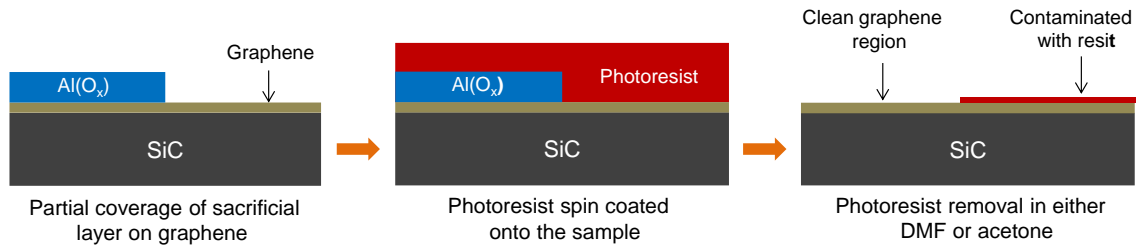


Figure 4.20: Process flow used for examining the surface cleanliness of graphene using conventional direct lithography and sacrificial layer approach.

In order to understand the level of cleanliness achieved using the sacrificial layer approach, in comparison to the conventional fabrication process, a separate sample was used to fabricate the graphene channel that has two different regions, in which, one region was covered with Al(O_x) layer and the other region was intentionally left exposed as shown in Figure 4.20. The image-reversal AZ5214-E photoresist was then spin coated uniformly on

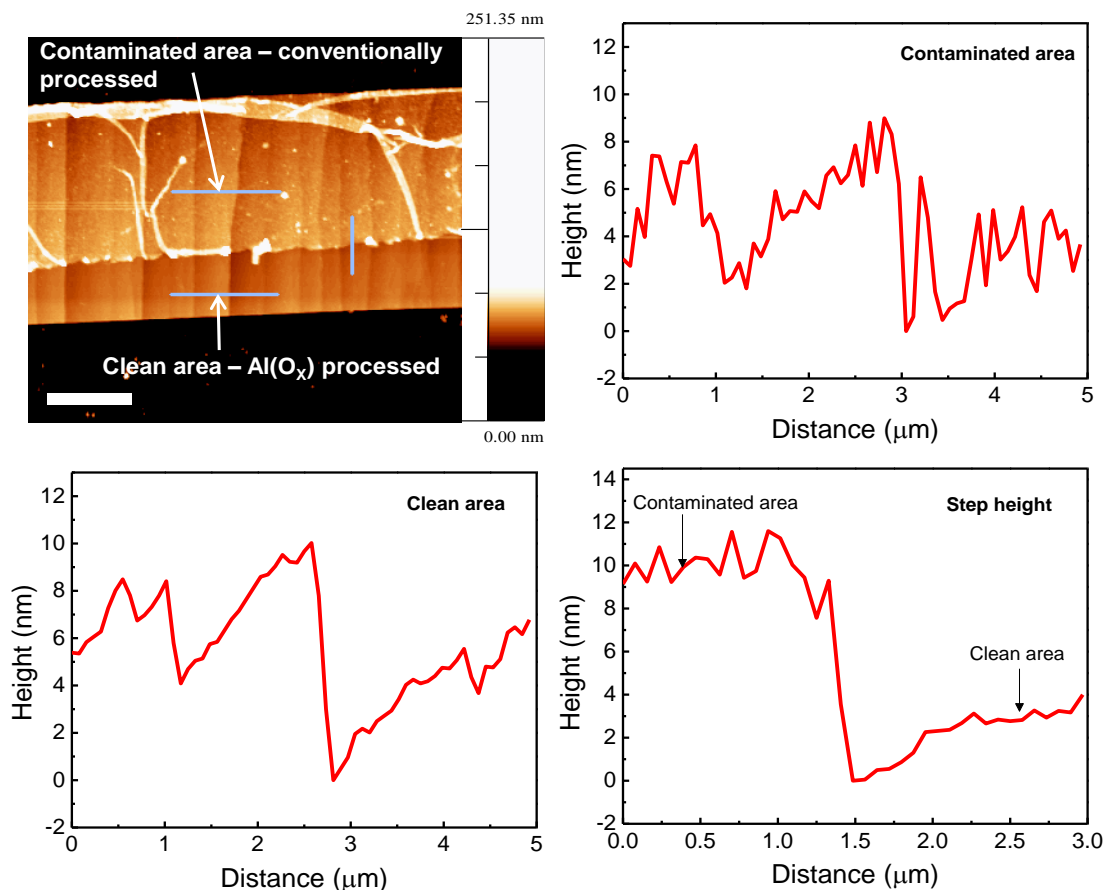


Figure 4.21: AFM topography image of the graphene channel region, showing clean and contaminated areas after photoresist removal. Clean region was initially covered with Al(O_x) layer prior to photoresist spinning, whilst other half the sample was left as-is. The corresponding height profiles show that thickness of resist residues were found to be as high as 10 nm. Scale bar is 4 μm.

this sample, followed by soft bake at 115 °C for 15 min. After this step, the sample was dipped in either acetone/IPA or DMF for 30 min to remove the photoresist. The Al(O_x) layer was further etched away in AZ326-MIF developer for 10 min. AFM was utilised to directly compare the surface conditions of graphene between these two differently processed regions. Figure 4.21 shows the AFM topography image and the corresponding height profile of the graphene channel. The area of the sample that was covered with Al(O_x) layer prior to resist coating, appears smoother with an RMS roughness of 1.9±0.3 nm and with no visible resist residues after stripping the photoresist and the Al(O_x) layer.

In contrast, the region that was unprotected showed a roughness of 8.3±1.7 nm with significantly contaminated regions consisting of photoresist residues. The step height between these two regions (Figure 4.21(d)) shows that the thickness of the leftover resist residual layer after standard solvent cleaning process was around 10 nm.

4.3.3.2 XPS analysis

The surface chemistry of as-fabricated graphene devices using sacrificial approach were examined by performing high-resolution C1s XPS scans. Figure 4.22(a) shows the typical C1s-core level spectra of as-grown epitaxial graphene fitted with three Gaussian-Lorentzian peaks at 283.10, 284.06, and 284.9 eV representing SiC, C-C (sp²) and IFL respectively. After the device fabrication and Al(O_x) removal, no significant changes were observed to the C1s spectra (Figure 4.22(b)), apart from the new peak appeared at 285.3 eV, which corresponds to hydroxyl functional group. The presence of hydroxyl groups is expected for the graphene sample that was exposed longer to the ambient air and/or for the sample that has undergone typical solvent and H₂O cleaning cycles during device fabrication. However, importantly, no additional peaks (i.e. C=O or O-C=OH) related to photoresist residues were observed

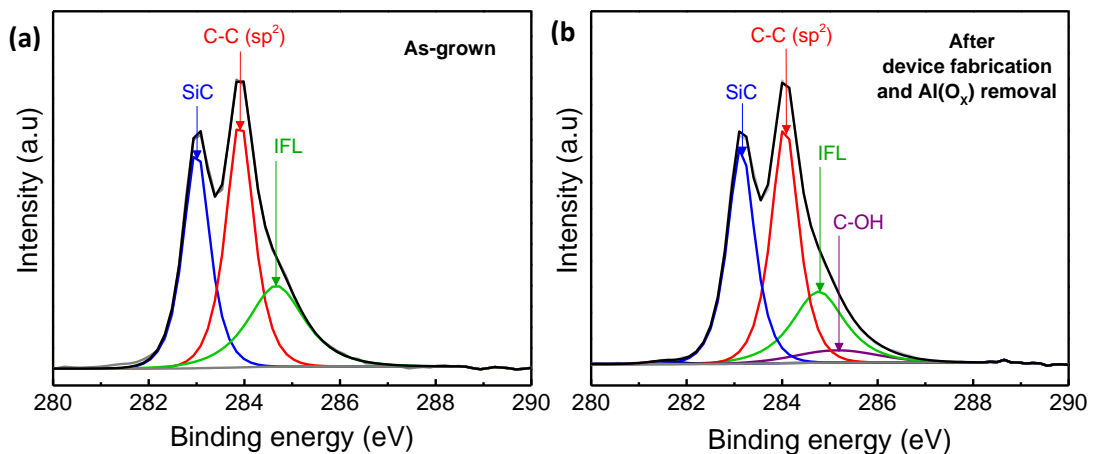


Figure 4.22: C1s spectra of (left) as-grown and (right) Sacrificial layer treated epitaxial graphene.

(within the resolution of the system), indicating resist free graphene surfaces for the areas examined. This shows that using $\text{Al}(\text{O}_x)$ as a protective layer can indeed result in much better graphene surfaces with negligible or no resist contamination.

4.3.3.3 Electrical measurements

Figure 4.23(a) shows the comparison of total resistance, R_T of twenty measured two-terminal devices with Ti/Au contacts fabricated using conventional lithography approach, $\text{Al}(\text{O}_x)$ sacrificial layer approach and conventionally fabricated devices annealed in ambient air, vacuum and N_2/H_2 atmosphere. As can be seen from the data, the type of fabrication method and the environment of thermal annealing can have significant impact on the device electrical characteristics. For example, the average R_T of as-fabricated devices using conventional approach was recorded as $93 \text{ k}\Omega$, whilst the devices fabricated by $\text{Al}(\text{O}_x)$ sacrificial layer approach showed R_T as low as $3.2 \text{ k}\Omega$. Although annealing conventionally fabricated devices in N_2/H_2 atmosphere at 400°C results in a decrease in R_T to $14.2 \text{ k}\Omega$, this is still higher than the resistance achieved by the sacrificial layer method.

Figure 4.23(b) shows the TLM plot of Ti/Au contacts fabricated using $\text{Al}(\text{O}_x)$ sacrificial layer approach along with the plot of TLM structures annealed in N_2/H_2 environment for comparison. From the slope of these plots, R_{sh} for sacrificial layer approach was calculated as $0.94 \pm 0.9 \text{ }\Omega/\text{sq}$, which is 62% lower than the R_{sh} recorded for N_2/H_2 annealed sample, which was extracted as $2.47 \pm 0.4 \text{ k}\Omega/\text{sq}$. Similarly, a 25% reduction in R_C was observed for the sample fabricated using sacrificial layer method ($6.08 \pm 0.1 \text{ k}\Omega \cdot \mu\text{m}$), in comparison to N_2/H_2 annealed sample ($8.14 \pm 0.8 \text{ k}\Omega \cdot \mu\text{m}$). The superior performance in both R_{sh} and R_C

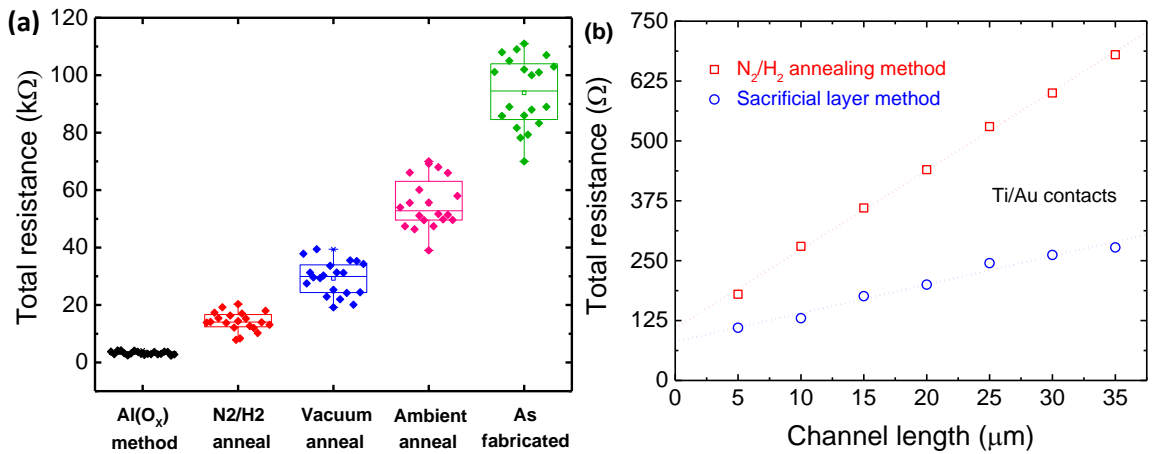


Figure 4.23: (a) Effect of different processing conditions on the device electrical resistance. (b) TLM plot of N_2/H_2 annealed and $\text{Al}(\text{O}_x)$ sacrificial layer fabricated structures.

demonstrates the effectiveness of using the sacrificial layer as a protective coating on graphene during the device fabrication process. Unlike the case of N₂/H₂ sample, where the contact interfaces regions remain contaminated with resist residues even after thermal annealing, the contact interfaces for sacrificial layer processed sample were found to be free from lithographic contamination as shown in AFM topography images above. When the metal films are deposited onto such clean graphene surfaces, a strong interaction between the metal d-states and π -orbitals in graphene takes place, leading to a smaller metal-graphene coupling length, λ_m . As a result, enhanced carrier transmission is expected at this interface, increasing the density of states in graphene underneath the metal, thereby reducing R_C .

In an effort to further reduce R_C , different metal film stacks were investigated using TLM test structures with same contact dimensions as above. It is known that metal contacts have substantial impact on R_C due to their strong influence on the graphene electronic properties. The adsorption of metals on graphene can be divided into two groups based on the binding energy: a physisorption group (e.g., Al, Au, Cr, Cu and Pt) and a chemisorption group (e.g., Co, Ni, Ti and Pd). Physisorbed metals do not form chemical bonding and preserve the band structure of graphene [81, 82]. Charge transfer occurs at these metal-graphene interfaces, leading to p-type or n-type doping of the graphene. In contrast, chemisorbed metals form chemical bonding and significantly distort the intrinsic band structure of graphene through a strong hybridisation between d -orbital of a metal and the π -orbital of graphene [81, 82]. In order to evaluate the effect of these two adsorption groups on the electrical characteristics of metal-graphene interfaces, six different metallisation schemes were selected here, which include three physisorption metals such as Cr, Au and Pt and three chemisorption metals of Ti, Ni and Pd. These metals are 10 nm thick and are assumed to be of primary interaction with the graphene film. A 175 nm Au metal film was deposited on top these metals as a capping layer to protect them from oxidation. Here, all six contacts showed ohmic behaviour with linear I-V characteristics.

The TLM plot of Ti/Au and Ni/Au contacts in in Figure 4.24(a) shows significant variation in R_T , indicating that despite Ti and Ni belonging to the same chemisorption group, they have very different effect on the graphene electrical characteristics. Figure 4.24(b) shows the sheet resistance of all metal contacts calculated using both TLM and Van der Pauw structures. As can be seen, the sheet resistances extracted from Van der Pauw method are in agreement with the values recorded using TLM method, validating the TLM analysis. On an

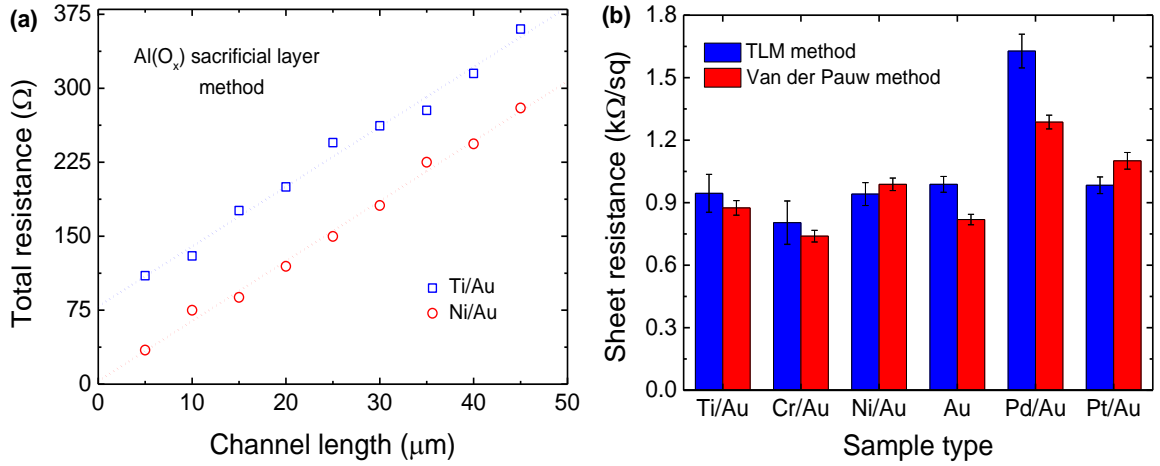


Figure 4.24: (a) TLM plot of Ti/Au and Ni/Au contacts showing the variation in total resistance (b) Sheet resistance of Al(OX) layer processed sample extracted using TLM and Hall measurements.

average, R_{sh} was found to be between $0.91 \text{ k}\Omega/\text{sq}$ to $1.62 \text{ k}\Omega/\text{sq}$ for all metal contact types. Note, these values are significantly lower than R_{sh} values achieved using rapid thermal anneal method, which were around $2.47 \text{ k}\Omega/\text{sq}$.

Figure 4.25 shows the extracted R_{c} values for all metal contact types along with their work functions. As can be seen, Ti/Au showed highest R_{c} of $6.08 \pm 0.3 \text{ k}\Omega \cdot \mu\text{m}$, whereas Ni/Au showed lowest R_{c} of $0.24 \pm 0.1 \text{ k}\Omega \cdot \mu\text{m}$. The extracted contact resistances for Cr/Au, Au, Pd/Au and Pt/Au are $3.81 \pm 0.52 \text{ k}\Omega \cdot \mu\text{m}$, $0.6 \pm 0.2 \text{ k}\Omega \cdot \mu\text{m}$, $1.49 \pm 0.3 \text{ k}\Omega \cdot \mu\text{m}$ and $2.25 \pm 0.2 \text{ k}\Omega \cdot \mu\text{m}$, respectively. Such a large variation in R_{c} is due to the differences in interaction of

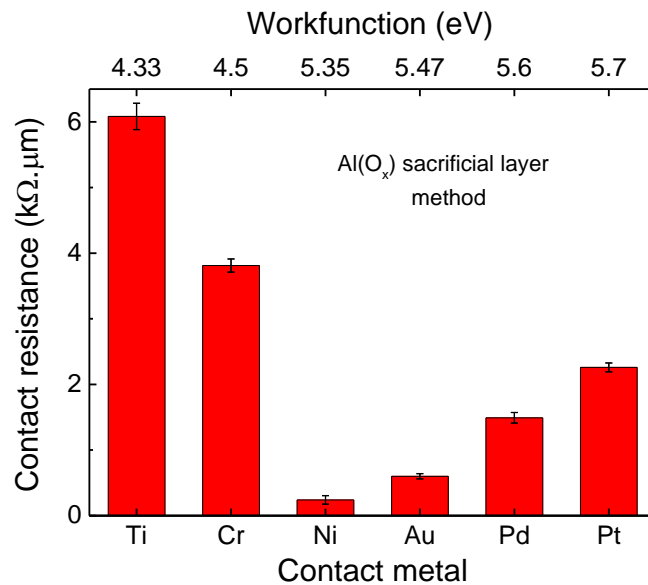


Figure 4.25: Evaluation of contact resistance of metal-graphene interfaces for a wide range of metallisation schemes. Note, all these metals were capped with 175 nm Au layer.

these metal contacts with the graphene film. For instance, work function, binding energy (B.E), and diffusion energy barrier (E_{Diff}) of metals would all affect the graphene electrical properties at the interface. Due to the work-function difference between the metal and graphene, interface charge transfer occurs, even for weakly interacting metals and dopes the graphene underneath the metal contact. Here, the work-function of a metal determines the nature and the magnitude of the doping, whilst, B.E and E_{Diff} provides the information about the adhesion strength and homogeneity of deposited metal films.

Table 4.1: Work function (WF), binding energy (B.E), Diffusion energy barrier (E_{Diff}), effective metal-graphene distance ($d_{\text{M-G}}$) and lattice mismatch of all metals used in this study.

Contact metal	WF (eV)	B.E (eV)	E_{Diff} (eV)	$d_{\text{M-G}}$ (Å)	Lattice mismatch (%)	R_C ($\text{k}\Omega \cdot \mu\text{m}$)
Al	4.28	0.97	0.11	3.65	N/A	N/A
Ti	4.33	1.70	0.59	2.18	3.7	6.08 ± 0.2
Cr	4.50	0.18	0.006	2.36	3.3	3.81 ± 0.1
Ni	5.35	1.51	0.22	2.11	1.2	0.24 ± 0.06
Au	5.47	0.09	0.006	3.62	1.6	0.6 ± 0.04
Pd	5.60	1.06	0.03	2.79	3.1	1.49 ± 0.08
Pt	5.70	1.56	0.17	3.59	2.5	2.25 ± 0.06

Ti strongly chemisorbs to the graphene surface with a high binding energy of 1.70 eV and results in a continuous film formation due to the significant diffusion energy barrier (0.59 eV) of Ti atoms [188]. Previous experimental studies have shown that Ti acts as an n-type dopant when adsorbed on to the graphene surface, shifting the Fermi level further away from the Dirac point [198]. Nevertheless, the magnitude of charge transfer is smaller due to the small work-function difference between Ti and graphene (-0.17 eV), resulting in a limited number of participating conduction modes in graphene underneath the Ti. Moreover, the strong chemical interaction between Ti $3d$ and graphene p_z -orbitals lead to the destruction of the graphene lattice underneath the contacts and this result in degradation of the hopping conduction. In addition, the chemically reactive nature of Ti was shown to introduce additional carrier scattering at the interface due to the interaction with the residual oxygen atoms during deposition, which further reduces the effective contact area. All these factors will contribute to the high R_C observed for Ti/Au contacts.

For Cr/Au contacts, the weak binding energy of Cr (0.18 eV) results in physical adsorption to the graphene film, without significant modification of the band structure [188].

This is due to the negligible diffusion energy barrier of Cr atoms (0.006 eV) on graphene, where the interaction between adjacent Cr atoms will be much greater than between Cr and C. As a result, when Cr is deposited on graphene, the Cr atoms undergo high inter-diffusion and form clusters [188]. Nevertheless, these Cr clusters have an insignificant effect on the graphene, because of the negligible work function difference between Cr and the graphene. However, the small equilibrium distance (2.36 Å) between adsorbed Cr atoms and graphene, together with the perseverance of band structure of graphene leads to lower R_C for Cr/Au contacts, in comparison to Ti/Au electrodes.

In the case of Ni/Au contacts, Ni atoms chemisorb on to the graphene surface with a high B.E of 1.51 eV and also results in continuous film formation due to high E_{Diff} of 0.22 eV. Despite its strong chemical interaction with graphene, it was found that a strong charge transfer occurs at the Ni/graphene contact interface without significant alteration to the graphene's electronic band structure. However, Ni with higher work-function causes the E_F to shift below E_D and leads to p-type doping of graphene underneath the contacts. As the work-function of Ni is 0.85 eV greater than that of graphene, the shift in Fermi level after metallisation results in a considerable increase in DOS in the graphene. This increased DOS, together with the very small $d_{\text{M-C}}$ results in an increased carrier transmission probability through the metal-graphene interface and hence results in low R_C .

The R_C values for Ti, Cr and Ni shown here appears to follow the work-function of a metal and suggest that low work function metals must be avoided for good R_C ; however, a high work function does not necessarily guarantee low R_C , as seen for the cases of Pd and Pt. This is contradictory to the trend proposed by theoretical studies, where it was argued that the largest work-function difference between the metal and graphene would result in highest doping, increasing the DOS underneath the metal contact and therefore reduces the R_C . Nevertheless, these studies did not take into account the issue of resist contamination at metal-graphene interfaces, which severely undermines the true nature of interaction with the graphene. Therefore, the reported R_C values could be as a result of interaction of both the deposited metal films as well as the interference of resist residues with the graphene surface.

In order understand the observed R_C values here, the effect of lattice mismatch of metal films with the graphene was also investigated. As shown in Table 1, Ti with 3.7% has the largest lattice mismatch with graphene, which also resulted in the highest R_C of 12.0 ± 0.1 $\text{k}\Omega \cdot \mu\text{m}$, whilst Ni was found to have lowest lattice mismatch with 1.2%, leading to a lowest R_C of 0.22 ± 0.1 $\text{k}\Omega \cdot \mu\text{m}$. In fact, Ni is the closest lattice matched interface with respect to

graphene of all transition metals, indicating its suitability as an ideal electrode material for graphene based electronics.

Although, Loeng *et al.* [196] showed the lowest R_C of $100 \text{ k}\Omega\cdot\mu\text{m}$ for Ni, a pre-fabrication process treatment is needed for their approach, which includes deposition of a thin Ni film (2 nm) at the contact regions to form clusters, followed by a thermal annealing step in the Ar/H₂ atmosphere for around 10 min at 580°C. This process results in random etching of the graphene film around these Ni clusters at the contact regions. After this etching, graphene devices were isolated using RIE and then a 100 nm thick Ni film was deposited to form source-drain contact electrode. In contrast, the R_C value achieved here is close to the value reported by Leong *et al.* [196] but importantly does not require any thermal processing apart from two additional steps, i.e. deposition of sacrificial layer before performing lithography and its removal after the fabrication of the final device. Moreover, the R_C achieved here is on par with the lowest contact resistances reported to-date utilising different metal contacts and different treatment conditions. Table 4.2 shows the list of some of the best R_C values reported in the literature using different pre or post-fabrication treatments techniques. Due to the ease of processing, sacrificial layer technique can be easily integrated into other photolithography and e-beam lithography processes and also can be further extended to other two-dimensional materials to achieve better device performances. In addition, this process is also compatible with standard Si fabrication techniques that can be performed on wafer-scale dimensions. Moreover, the sacrificial layer technique would also greatly benefit practical applications that rely on graphene transfer, such as for flexible electronics. For example, the transfer of CVD grown graphene to flexible polymer substrates usually requires etching of Cu or Ni films with PMMA coating, which inevitably contaminates the graphene surface with resist residues. However, high-temperature annealing or acid treatments cannot be employed to remove these residues, because of their aggressive nature of cleaning that would degrade the overall quality of polymer substrates. Alternatively, Al(O_x) sacrificial layer can be used instead of PMMA during the transfer process, thereby eliminating the residual contamination and any need for additional cleaning procedures.

Table 4.2: Comparison of the best reported contact resistance values in the literature using different pre or post fabrication treatment with the current study.

Refs.	Contact metal	Graphene type	Pre or post-fabrication treatment	Measurement method and conditions	R_c ($k\Omega \cdot \mu m$)	ρ_c ($\Omega \cdot cm^2$)
[177]	Ni	Exfoliated graphene	Ar/H ₂ anneal at 300°C for 60 min	Cross-bridge Kelvin structure in vacuum at 20°C	-	$\sim 5 \times 10^{-6}$
[196]	Ni	Exfoliated graphene	Ni-catalysed etching + Ar/H ₂ anneal at 580°C for 10 min	Four-probe in ambient air at 20°C	100	-
[185]	Ti/Au	Epitaxial graphene on SiC	O ₂ plasma treatment + N ₂ /H ₂ anneal at 460°C for 15 min	TLM in ambient air at 20°C	-	7.5×10^{-8}
[181]	Cu	Epitaxial graphene on SiC	Contact area patterning + UHV anneal at 350°C for 15 h	TLM in ambient air at 20°C	125	-
[199]	Cu	Exfoliated graphene	260°C+306°C vacuum anneal for 15 h	TLM in ambient air at 20°C	241	-
[178]	Ti/Au	CVD graphene	UV ozone treatment before metallisation	TLM in ambient air at 20°C	184	-
[182]	Pd	CVD graphene	N ₂ /H ₂ annealing at 300°C for 1 min	TLM in ambient air at 20°C	570	-
[171]	Ti/Pd/Au	CVD graphene	5 nm Al(O _x) sacrificial layer	Two-probe in vacuum at 20°C	320	-
[200]	Ti/Pd/Au	CVD graphene	Vacuum anneal at 150°C for 10 h	Four-probe in vacuum at 20°C	250	-
[201]	Ni/Au	Exfoliated graphene	Ar/H ₂ anneal at 300°C for 5 min	TLM in ambient air at 20°C	~ 300	-
This work	Ni/Au	Epitaxial graphene on SiC	10 nm Al(O _x) sacrificial layer	TLM in ambient air at 20°C	~ 240	-

4.4 Summary

In summary, the influence of metal contacts, the effect of lithography processing and high-temperature thermal annealing on the electrical characteristics of metal-graphene interfaces was studied. Ti/Au and Cr/Au contacts on vacuum grown graphene showed significant variation in resistance parameters at 20°C, which decreased substantially as the temperature increased to 400°C. It was found that highly reactive metals such as Ti can destroy the graphene lattice, degrading the hopping conduction and leads to high R_C . GAXRD revealed the existence of a TiC layer at the Ti/Au-graphene interface, which is believed to play a significant role in the high R_C associated with the Ti/Au-graphene contacts.

In order reduce photolithography induced surface contamination form the graphene surfaces, rapid thermal annealing of as-fabricated samples was performed in different annealing environments such as in ambient air, vacuum and in N_2/H_2 atmosphere. However, annealing in N_2/H_2 at 400C for 60 min was found to be the optimum condition for removing lithography residues from the graphene surface, which was verified by AFM and XPS measurements. In addition, this thermal treatment approach at 400C showed an order of magnitude improvement in R_C after the annealing process along with the reduction in carrier concentration and a corresponding increase in the Hall mobility of graphene.

In an effort to further reduce R_C , Al layer was used as a sacrificial layer on top of graphene to separate graphene from coming into direct contact with the photoresist during lithography. This sacrificial layer approach was demonstrated to be very effective in maintaining clean graphene surfaces during photolithography and importantly showed almost three orders of magnitude in improvement in R_C , in comparison to conventionally fabricated and thermally annealed devices, thereby eliminating the need for post fabrication annealing treatments. Due to the simplicity of this approach, it can be easily integrated into other photolithography and e-beam lithography processes. This approach is also compatible with the traditional Si based electronics and also with polymer based flexible electronics, making it highly attractive treatment method in maintaining clean surfaces of graphene and other low-dimensional materials.

Chapter 5

Oxygen functionalisation of epitaxial graphene films using e-beam generated plasmas

5.1 Introduction

Owing to its exceptional material properties, graphene has been extensively studied for applications such as interconnects [202, 203], thermal management in nanoelectronic circuits [45, 203, 204], flexible electronic displays [26], photodetectors [205, 206] and as electrodes for solar cells [24], light emitting diodes [207] and memory devices [25]. However, the same intrinsic structure of graphene that provides many of the desired properties also results in poor wettability and low chemical reactivity due to its structural homogeneity and highly delocalised electronic structure. This limits the suitability of graphene for other important applications. For example, chemical sensors made of pristine graphene typically suffer from weak sensing responses, poor selectivity issues and extremely long recovery times due to the lack of polar functional groups on the surface [28, 208]. The absence of these polar groups also makes interfacing graphene with other chemical moieties extremely challenging, thereby limiting its use in biological/biomedical applications. Moreover, the highly hydrophobic nature of pristine graphene surface inhibits uniform deposition of ultra-thin (2–10 nm) high- k dielectric layers [209-211], further impeding the development of graphene-based electronics for high frequency applications. Here, the hydrophobicity of graphene is due to the lack of polar functional groups on its surface, which leads to the chemically inert nature

of graphene. In order to overcome these issues, functionalisation of graphene is essential to enhance its capabilities and promote chemical reactivity on its surfaces.

There have been many studies in the past demonstrating the chemical modification of graphene using highly reactive species such as hydrogen, fluorine, chlorine, oxygen and other organic functional groups [109, 140, 211-218]. These reactants were shown to not only change the surface chemistry of graphene, but also greatly alter the hybridisation state of carbon atoms, charge carrier type and density, resulting in transformation of graphene from a semi-metal to a semiconductor or a strong insulator [219, 220]. Among these functional species, oxygen is of particular interest, because of the advantages it offers for diverse range of applications. For example, unpaired electrons of oxygen make it highly reactive to surface adsorbates and allow the derivative oxygen functional groups to act as anchoring sites for the attachment of designated molecules or enzymes, making it attractive for chemical [221-223] and bio-sensor applications [136, 224, 225]. Oxygen functional species also reduce the hydrophobicity of graphene and make the surface more hydrophilic [92, 226]. This change in surface wettability significantly increases the adhesion strength of metal contacts on graphene, which otherwise suffer from metal delamination issues [185, 226, 227]. In addition, it has also been demonstrated that O-plasma treatment increases the thermal transport across the metal/graphene interfaces, enabling efficient heat transport to the surrounding device architecture [111]. Furthermore, it was shown that O-functionalisation creates a band-gap of over 1 eV [110] and induces a strong photoluminescence behaviour in graphene [108], which could pave the way towards developing graphene based electronic and optoelectronic devices.

To date, a wide variety of techniques have been proposed for functionalising graphene with oxygen species, including exposure to ozone [228, 229], wet solution of strong acids [113, 230-233], oxygen plasma [109, 110, 117, 140, 234], and photochemical oxidation [235, 236]. Among these techniques the most popular and commonly employed approach is using aggressive acidic solutions based on modified Hummer's method, where the graphite layers are oxidised first, followed by exfoliation into two-dimensional graphene oxide (GO). However, the resultant GO material is chemically inhomogeneous, electrically insulating and structurally defective due to the extensive use of harsh acidic treatments. Although, reduction of GO (i.e reduced graphene oxide, rGO) by strong acids and several hours of thermal annealing was shown to partially recover the structural characteristics of graphene [237-240], these rGO films still suffer from inferior electrical properties and also leads to inevitable

contamination by unwanted functional groups during reduction process. Moreover, accommodation of such oxidation/reduction steps involving toxic chemicals and/or multiple annealing cycles into a CMOS process flow is highly undesirable.

Alternatively, plasma treatment is attractive because, plasmas are extensively used in semiconductor fabrication process and are also capable of modifying material surfaces with nanoscale precision [241]. Moreover, plasma processing has advantages of shorter reaction times, solvent free, non-polluting process and provides a wider range of functional groups depending on parameters such as power, treatment time, gases used and operating pressure.

Previous studies on O-plasma functionalisation were primarily based on either exfoliated graphene flakes or chemical vapour deposition (CVD) grown graphene, while epitaxial graphene on SiC has received much less attention. More often in these studies, the functionalisation state reached at the end of the oxidation treatment was examined, whereas the nature of oxygen containing functional groups formed at different oxidation stages and their impact on the chemical, structural and electrical properties of graphene were rarely investigated. Since oxidation of graphene is known to produce more than one covalent functional group, in comparison to hydrogen, fluorine or chlorine [140, 214, 216], it is important to understand the evolution of oxygen species and their impact on the epitaxial graphene properties. However, the covalent modification of graphene with precise control on the concentration and the type of O-functional groups attached to the surface is challenging, because of the aggressive nature of oxygen plasmas, which usually leads to etching of the graphene film even for short exposure times [117, 118, 216]. Thus, despite its high potential, achieving controlled plasma functionalisation of graphene surfaces with oxygen remains elusive.

In this chapter, the selective modification of epitaxial graphene films using electron-beam generated Ar/O₂ plasmas at room temperature is demonstrated. This technique not only provides a better control over the concentration of functional groups present on the graphene surface but also is compatible with the state-of-the art silicon fabrication process. Importantly, the functionalisation process does not result in appreciable etching of graphene films due to the unique nature of e-beam plasmas. A detailed study on the effect of e-beam plasma treatment on the chemical, electrical, morphological and structural characteristics of epitaxial graphene films has been performed from initial to advanced oxidation stages using X-ray photoelectron spectroscopy (XPS), Raman spectroscopy, atomic force microscopy (AFM) and Hall measurements respectively.

5.2 Experimental details

5.2.1 Graphene growth and functionalisation

The epitaxial graphene films were synthesised on five 8×8 mm² semi-insulating, 0.5° off-axis 6H-SiC (0001) substrates via sublimation of Si at 1540°C in an argon atmosphere. All substrates used here were diced from the same SiC wafer, underwent similar pre-cleaning procedures and synthesised all in the same batch to minimise any substrate related or growth induced variations between samples.

For functionalisation, blanket graphene films of four substrates were exposed to e-beam generated oxygen plasmas at operating pressures of 25, 50, 75 and 90 mTorr, whilst the fifth substrate was used as a control sample. As mentioned in chapter 3, e-beam generated plasmas have the unique property that limits the kinetic energy of ions at the sample surface to less than ≈ 3 eV, thereby eliminating ion-induced etching or sputtering of carbon atoms in the graphene basal plane [73]. Here, plasmas were produced at room temperature by applying a 2 keV e-beam into mixtures of Ar and O₂ respectively with O₂ at 5% of the total flow rate. The total treatment time was 60 s and the plasma exposure time was 6 s. Note that apart from varying the operating pressure, all samples were functionalised under identical experimental conditions with variables such as functionalisation time, plasma power, concentration of Ar/O₂ gases and the temperature kept constant.

5.2.2 Surface characterisation

The surface chemistry of graphene before and after O-functionalisation was analysed using XPS with a spot size of ~ 400 μm . All samples were immediately transferred to the XPS system after growth and O-functionalisation and were quickly pumped down to a high vacuum of 3×10^{-8} mbar in an attempt to minimise atmospheric effects on the surfaces examined. The survey and high-resolution spectra were collected using pass energies of 200 eV and 20 eV respectively. Each high resolution scan collected is an average of twenty scans taken using an energy step of 0.15 eV and a dwell time of 100 ms. In order to identify the chemical composition of species present on these samples, high resolution C1s, O1s and Si2p spectra were fitted with mixed Gaussian-Lorentzian functions after performing Shirley background subtraction. A quantification scaling was performed, where all spectra presented here have been normalised with respect to the intensity of C1s peak and also to the

corresponding sets of O1s and Si2p data. Further, all C1s peaks displayed here were also calibrated for minor sample charging by shifting the SiC C1s peak to 283.1 eV [150] with respect to the O1s and Si2p spectra.

The surface morphology and the roughness of as-grown and as-functionalised graphene films were measured using AFM in non-contact mode. The structural quality of graphene films were monitored by Raman spectroscopy using an excitation wavelength (λ) of 514.5 nm, spot size of 0.70 μm and an incident laser power of ≈ 10 mW. For peak analysis, SiC background contribution was subtracted to extract the graphene peaks followed by Salvatzky-Golay smoothing to improve the signal-to-noise ratio of the acquired spectra. The characteristic D, G and 2D peaks of graphene were fitted with Lorentzian spectral line shape for quantitative analysis of these samples.

Hall measurements were performed on all as-grown and as-functionalised samples at room temperature to measure the variation in parameters such as sheet conductivity, mobility, carrier type and density using the Hall measurement system from MMR technologies. The measurements were performed in van-der Pauw configuration using indium probe tips and a magnetic field of 0.3 Tesla with a sample current of 100 μA .

5.3 Results and Discussion

5.3.1 XPS Analysis – identifying chemical moieties on the graphene surface

Following graphene growth and prior to functionalisation, all samples were investigated using XPS to analyse the surface chemistry of as-grown graphene films. The survey spectra in Figure 5.1(a) show that carbon, silicon and oxygen are the dominant components with no other foreign element found within the XPS detection limits. The presence of oxygen (~ 2.5 at %) in the as-grown sample can be attributed to the residual contamination from the ambient atmosphere. Similar concentration of residual oxygen was observed on all other as-grown samples used in this study. To remove this residual oxygen and any associated surface contaminants, all as-grown samples were treated in HF (48 %) solution for 2 min followed by a quick rinse in DI water and dried using dry nitrogen. This cleaning process resulted in the reduction of oxygen peak intensity as shown in the Figure 5.1(a). However, as can be seen, a small concentration (< 1.5 at %) of oxygen was still found to persist even after multiple cleaning cycles on all samples. In order to understand the continued presence of oxygen even after aggressive acidic treatments, the high resolution Si2p scan was performed

to analyse the role of oxygen with the SiC substrate. Figure 5.1(b) shows the Si2p spectrum of a sample after HF treatment, revealing three components at 100.2, 101.2 and 102.4 eV. The peak at 100.2 eV is assigned to SiC component, while the peaks at 101.3 eV and 102.4 eV have been identified as silicon oxycarbide (O-Si-C) and silicon oxide (SiO_x) respectively [242, 243]. This indicates that the oxygen observed in these samples is located in SiC underneath the graphene and not on the graphene itself. This observation is consistent with previous studies on epitaxial graphene [244, 245], in which, oxygen was found to persist in as-grown samples even after annealing at 1000°C and was shown to be incorporated in SiC substrate in the form of O-Si-C and not in the graphene as GO or any other related species. Here, the presence of oxygen in the samples investigated in this thesis is due to the oxygen gas leak in the growth chamber. Since SiC is highly reactive to oxygen species, it immediately forms strong covalent silicon oxide and oxycarbide bonds even before the growth of graphene starts. However, these bonds does not form a continuous layer, instead forms patches. Shemella *et al.* [246] reported that the presence of oxygen underneath graphene leads to a sharing of charge carrier density and thus results in the modification of electronic structure of graphene by means of band-gap opening. This mechanism could explain the occasional reports on the substrate induced band gap opening in epitaxial graphene on SiC [247, 248].

Figure 5.2 shows the survey spectra of an HF treated sample along with the samples functionalised at different operating pressures. For convenience, HF treated sample(s) will be referred to as ‘as-grown’ in the rest of the manuscript unless otherwise specified. The intensity of oxygen peak was found to increase with the increasing pressure, indicating the

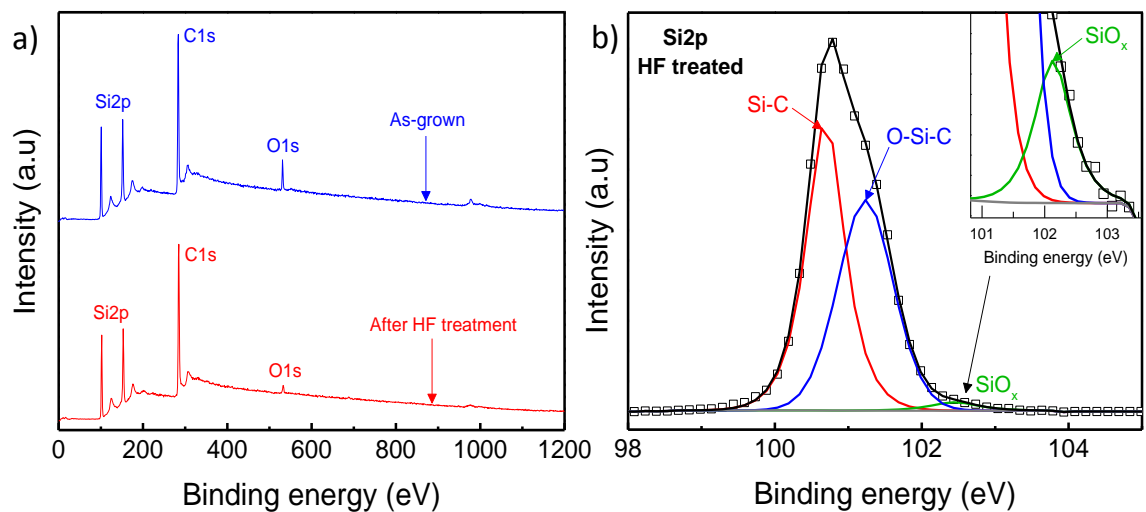


Figure 5.1: a) XPS survey spectra of graphene before and after HF treatment and b) deconvoluted high resolution XPS Si2p spectra after HF treatment showing Si-C, O-Si-C and SiO_x peaks.

rise in oxygen functional groups on the graphene surface. The surface atomic concentrations of oxygen and carbon are shown in the Figure 5.3(a), in which oxygen concentration increased with the plasma pressure, whilst the concentration of carbon decreased rapidly, indicating plasma oxidation effect. Increasing the plasma pressure increases the production of charged particles and reactive neutrals and thus the delivery of these species on to the graphene surface. At high pressures, large amount of reactive oxygen species available in the plasma enhances the relative oxygen content on the surfaces of graphene. The surface atomic concentration of oxygen on the graphene was calculated as 5.1 at % for 90 mTorr functionalised sample. Here, the elemental quantification from the survey spectra was performed by dividing the integrated area of signal intensity with element specific relative sensitivity factor values and normalising over all elements detected. The corresponding atomic ratio of carbon to oxygen (C/O) for the sample functionalised at 25 mTorr was

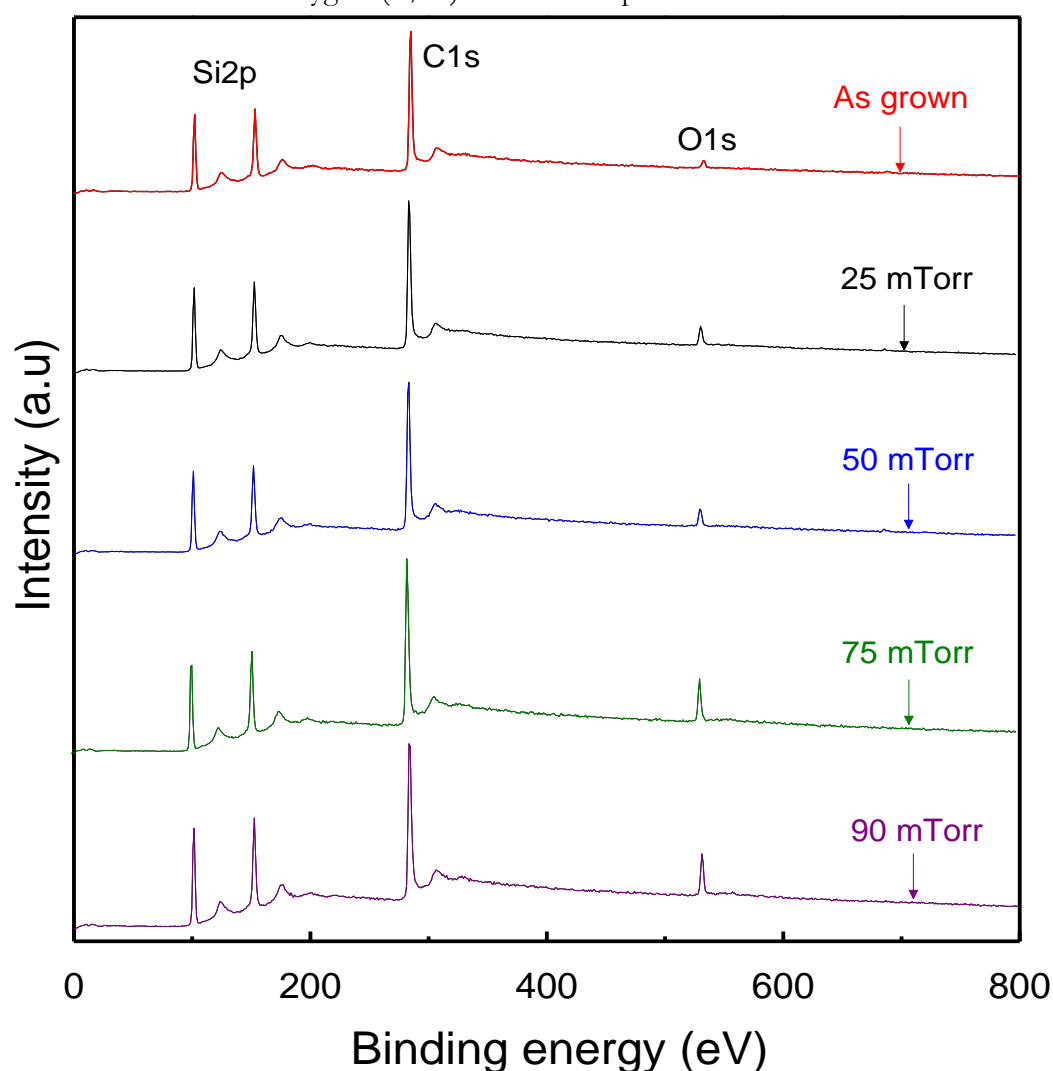


Figure 5.2: XPS Survey spectra of as-grown and as-functionalised epitaxial graphene samples at different operating pressures.

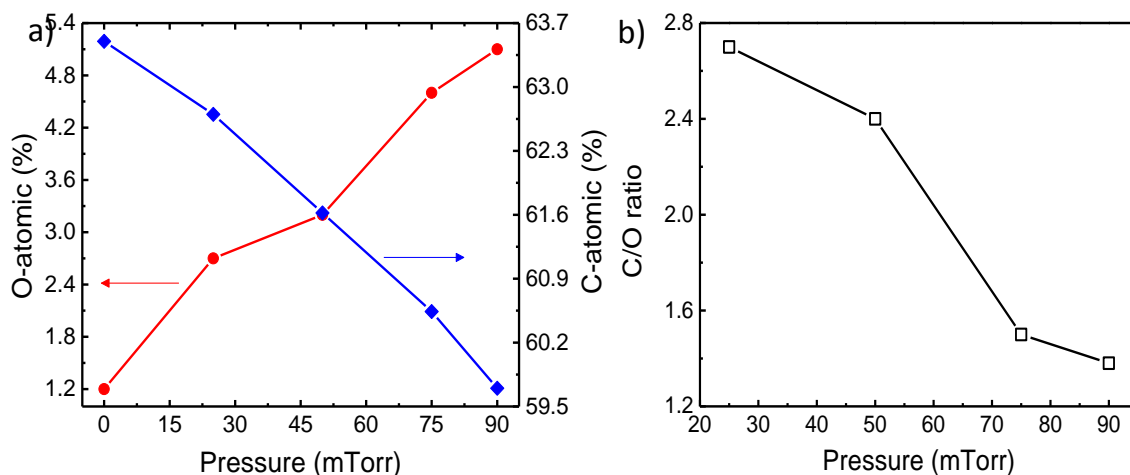


Figure 5.3: a) surface at% of oxygen and carbon derived from the XPS survey spectra with the increasing plasma pressure. b) Effect of plasma pressure on C/O ratios in functionalised graphene.

calculated as 2.7 and decreased to 1.38 at 90 mTorr as shown in the Figure 5.3(b). In order to identify the nature of carbon-oxygen bonding, the high resolution C1s and O1s spectra were analysed.

5.3.1.1 C1s core level spectroscopy

Figure 5.4 shows the typical C1s spectrum of a pristine epitaxial graphene fitted with three major peaks at around 283 eV, 284 eV and 284.5 eV, corresponding to SiC substrate, C-C (graphene) and the interfacial layer respectively.

Following oxygen plasma treatment, a clear change in the chemical composition of graphene was observed (Figure 5.5) for all samples with a broadened C1s spectrum, reduction in the sp^2 peak intensity along with shoulder peaks appearing at higher binding energies, representing different functional species. Note that many studies in the literature have assigned different binding energy values to these functional species, however the relative shift of various carbon-oxygen functionalities is nearly constant in almost all of these studies [249-252]. Based on these reports, following chemical shifts relative to C-C (sp^2) peak were adopted here: 1.0-1.6 eV for C-OH (hydroxyl) bond, 2.0-2.6 eV for C-O-C (epoxy), 3.0-3.6 eV for C=O (carbonyl) and 4.0-4.6 eV for O-C=O (carboxylic) bond.

The C1s spectrum in Figure 5.5(a) shows that at 25 mTorr pressure, hydroxyl groups (a peak at 285.5 eV with a relative shift of +1.5 eV) are the sole functional species present on the graphene surface within the resolution limit of the XPS system. Previous reports on oxygen functionalised graphene and rGO have indeed identified hydroxyls as the favourable

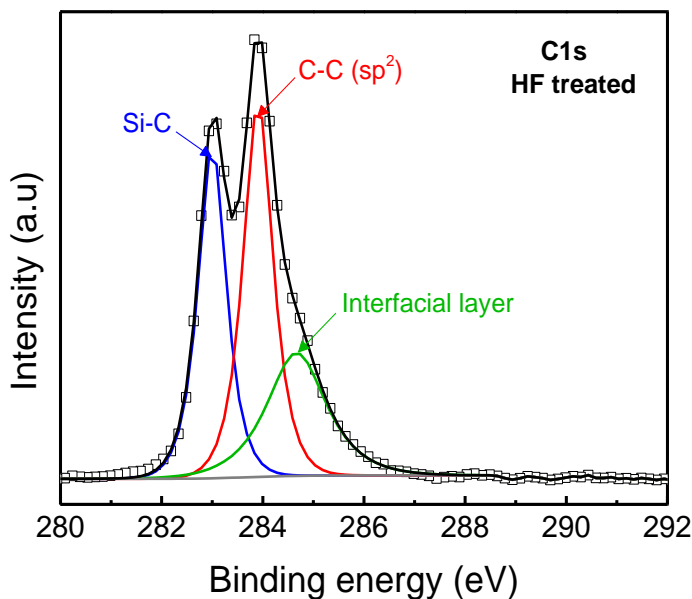


Figure 5.4: High resolution C1s spectrum of an as-grown, HF treated sample showing deconvoluted peaks of SiC, graphene and interfacial layer respectively.

functional groups present at low surface coverages due to their low chemisorption energy, in comparison to other oxygen species. DFT simulations showed that hydroxyl groups chemisorb to the graphene surface with oxygen preferentially situated on top of the carbon atom perpendicular to the graphene basal plane and hydrogen pointing in the direction of the centre of the hexagon [253, 254]. Hydroxyl groups were shown to induce significant distortion to the graphene lattice, where the carbon atom involved in bonding with the oxygen atom was shown to move upwards by 0.34 Å, relative to the graphene plane, resulting in an increase in C-C bond length of neighbouring carbon atoms from 1.42 Å to 1.48 Å [253]. The adsorption of –OH species also disturb the charge distribution of C-C bonds at the proximity of the adsorbate, resulting in the change in adsorption energy for subsequent oxygen adsorbate species near the defect site.

With the increase in plasma pressure (50 mTorr), a new component develops at 286.1 eV (relative shift of +2.1 eV) followed by a weak component at 287.5 eV (relative shift of +3.5 eV), representing epoxy and carbonyl groups respectively (Figure 5.5(b)). The epoxy functional groups were found to coexist with hydroxyl groups on the graphene basal plane [254, 255]. Using STM, XPS and DFT calculations, Hosseni *et al.* [119] and Vinogradov *et al.* [256] have determined that the most favourable adsorption site for epoxy oxygen atoms on epitaxial graphene is the bridge site (i.e. just above the bond connecting between two carbon atoms), where the hybridisation of O2p states with the 2p_z orbitals of two carbon

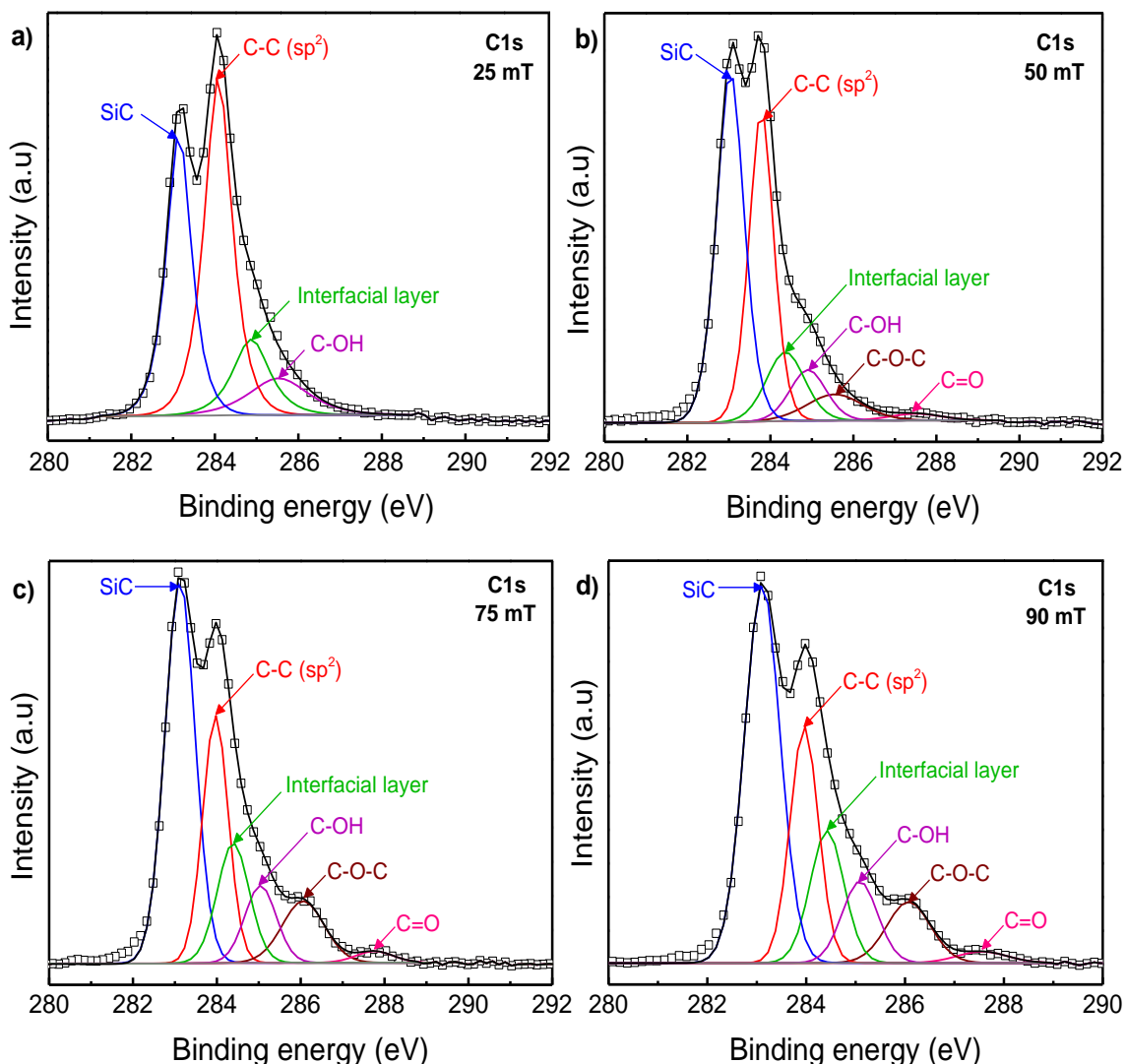


Figure 5.5: High resolution XPS C1s deconvoluted spectra of as-functionalised graphene samples at a) 25 mTorr, b) 50 mTorr, c) 75 mTorr and d) 90 mTorr. Increasing the pressure leads to an increase in the concentration of oxygen functional groups.

atoms takes place. It was also reported that, despite the presence of both single layer (at terraces) and bi-layer (at step edges) regions of graphene on SiC (0001), no noticeable difference in the concentration of oxygen was observed as a function of graphene thickness [119]. Similar to the case of hydroxyl groups, the chemisorption of epoxy oxygen also leads to distortion in the graphene lattice by pulling two carbon atoms bonded to the oxygen atom upward by 0.37 \AA . As a consequence, the distance between two carbon atoms involved in the bonding increases from 1.42 \AA to 1.51 \AA , resulting in significant structural deformations to the graphene backbone [253-255]. This value is closer to the standard value for diamond (1.54 \AA), suggesting the transition of graphene structure from the planar sp^2 symmetry to distorted sp^3 hybridization.

In the case of C=O species, there have been many conflicting reports on their very existence in the oxidised graphene. The basic structural model proposed by Lerf-Klinowski *et al.* [257] and later by many others [257-259] have not accounted for any C=O moieties, claiming that doubly bonded oxygen species exist only as part of carboxylate or ester groups at the edge sites of GO sheets and assumes that epoxides and hydroxyls to be main functional species on the graphene basal plane. In contrast, the Dekany model [232] and later many other studies [116, 239, 260-262] identified the presence of C=O species and argued its importance to the structural frame work of GO. However, for the samples investigated in this study (Figure 5.5(b)-5.5(d)), XPS has showed a clear, albeit small peak related to C=O groups at around 287 eV, which can be confidently assigned to C=O bonding, because the carboxylate groups (O-C=O) has an essentially different binding energy (~ 288.5 eV) and thus a different relative shift (+4.0-4.5 eV). Using molecular dynamic simulations, Bagri *et al.* [116] have recently reported that the formation of carbonyls is linked to the interplay between hydroxyl and epoxy groups, where, in the presence of excess oxygen, hydroxyl and epoxy groups rearrange to form carbonyl species. Unlike other oxygen species, the presence of carbonyl groups (C=O) was found to maintain the planar sp^2 structure of graphene [116] and therefore does not have the same structural influence as -OH or C-O-C groups.

Further increasing the plasma pressure to 75 and 90 mTorr did not reveal any new functional species in the C1s spectrum, but caused significant changes to existing functional groups as shown in Figure 5.5(c) and 5.5(d). In order to characterise the degree of oxidation in these functionalised samples, the area under C-C peak and carbon-oxygen peaks was

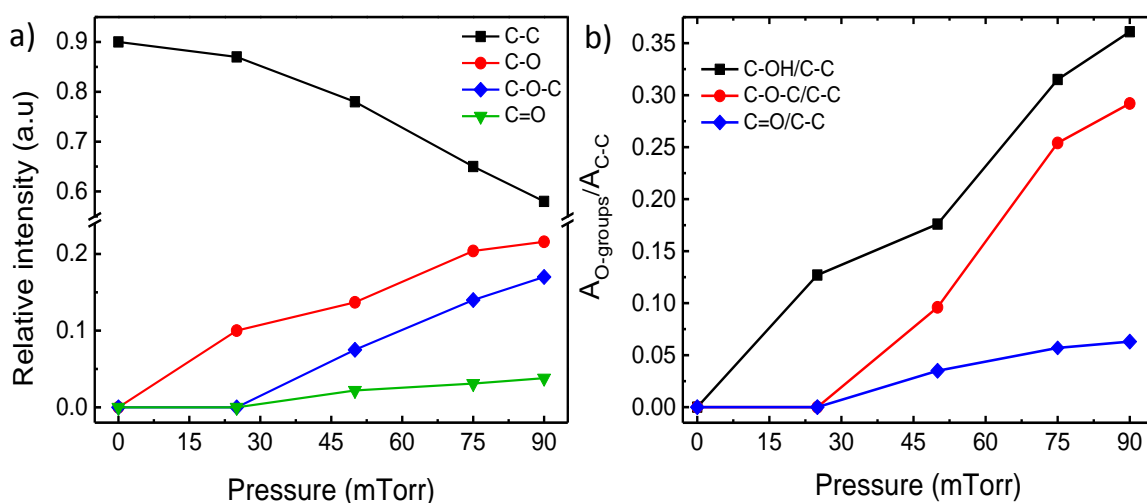


Figure 5.6: a) the relative contribution of C1s peak components estimated by dividing the area under each component by whole C1s peak area. b) Estimation of the distribution of O-functional groups on the graphene surface by dividing the area of area O-functional groups to the area of C-C peak.

divided with the total C1s peak area (Figure 5.6(a)). This showed an increase in the intensity of carbon-oxygen functional groups and an associated decrease in the sp^2 carbon to SiC peak ratio with the pressure, indicating the rise in number of carbon atoms involved in the oxidation process. Here, the contribution of different functional groups to the total oxygen concentration can be calculated by analysing the peak area ratios of C-O/C-C, C=O/C-C, and C=O/C-C from the deconvoluted C1s spectra. As shown in Figure 5.6(b), hydroxyl and epoxide groups were dominant functional species observed at all operating pressures with carbonyl groups accounting for minor contribution. This is in agreement with previous studies, where, using nuclear magneto resonance (NMR) spectroscopy, Lerf *et al.* [257], He *et al.* [258] and Cai *et al.* [263] confirmed that hydroxyls and epoxides as major functional groups present on the graphene surface. The limited number of carbonyls and the absence of carboxyl groups represent negligible edge sites present in the graphene film and that functionalisation process has a minimal effect on the graphene lattice.

5.3.1.2 O1s core level spectroscopy

Additional investigation on carbon-oxygen bonding was performed by recording O1s spectra which can complement the information provided by the C1s spectra. Since O1s photoelectron kinetic energies are lower than those of C1s, the sampling depth of O1s spectra is smaller and therefore is slightly more surface specific. Figure 5.7 shows the deconvoluted O1s spectra of all functionalised samples at different operating pressures. In addition to the peaks representing O-Si-C and SiO_x bonds, a variety of carbon-oxygen functional species were observed in the spectrum with different chemical nature and concentration depending on the plasma pressure. Contrary to the C1s spectra, where the assignment of carbon-oxygen bonds is straightforward, in the case of the O1s spectra the assignment is more varied, especially because of the presence of O-Si-C and SiO_x bonds, which complicates the assignment process. Nevertheless, the generally accepted deconvolution of O1s spectra consists of a component at the lowest binding energy corresponding to double (C=O) or triple bonded (O-C=O) oxygen peaks and the component at the highest binding energy corresponding to singly bonded oxygen (C-OH). Using this assignment scheme and by reference to the C1s peak, the following relative shifts of oxygen functional groups with respect to the SiO_x peak were used here; 1.0 eV for ether groups, 1.1-1.5 eV for hydroxyl groups, 1.8-2.5 eV for epoxide groups and 2.8-3.0 eV for carbonyl groups.

Figure 5.7(a) shows the O1s spectrum of the sample functionalised at 25 mTorr, revealing three peaks at 531, 531.5, 532.5 eV. The peak centred at 531 eV is attributed to carbon bonded to oxygen in hydroxyl configuration similar to that observed in C1s spectrum and peaks at higher binding energies are related to O-Si-C (531.5 eV) and SiO_x (532.5 eV) respectively.

Upon increasing the pressure to 50 mTorr, two new peaks appear at lower binding energies (529.5 eV and 530.6 eV), corresponding to epoxide and carbonyl groups respectively (Figure 5.7b). The quantitative analysis (Figure 5.8) of these functional species revealed that the relative atomic concentration of epoxide groups is 31 at%, whilst hydroxyls and carbonyls account for 27 at% and 3 at% of the coverage respectively.

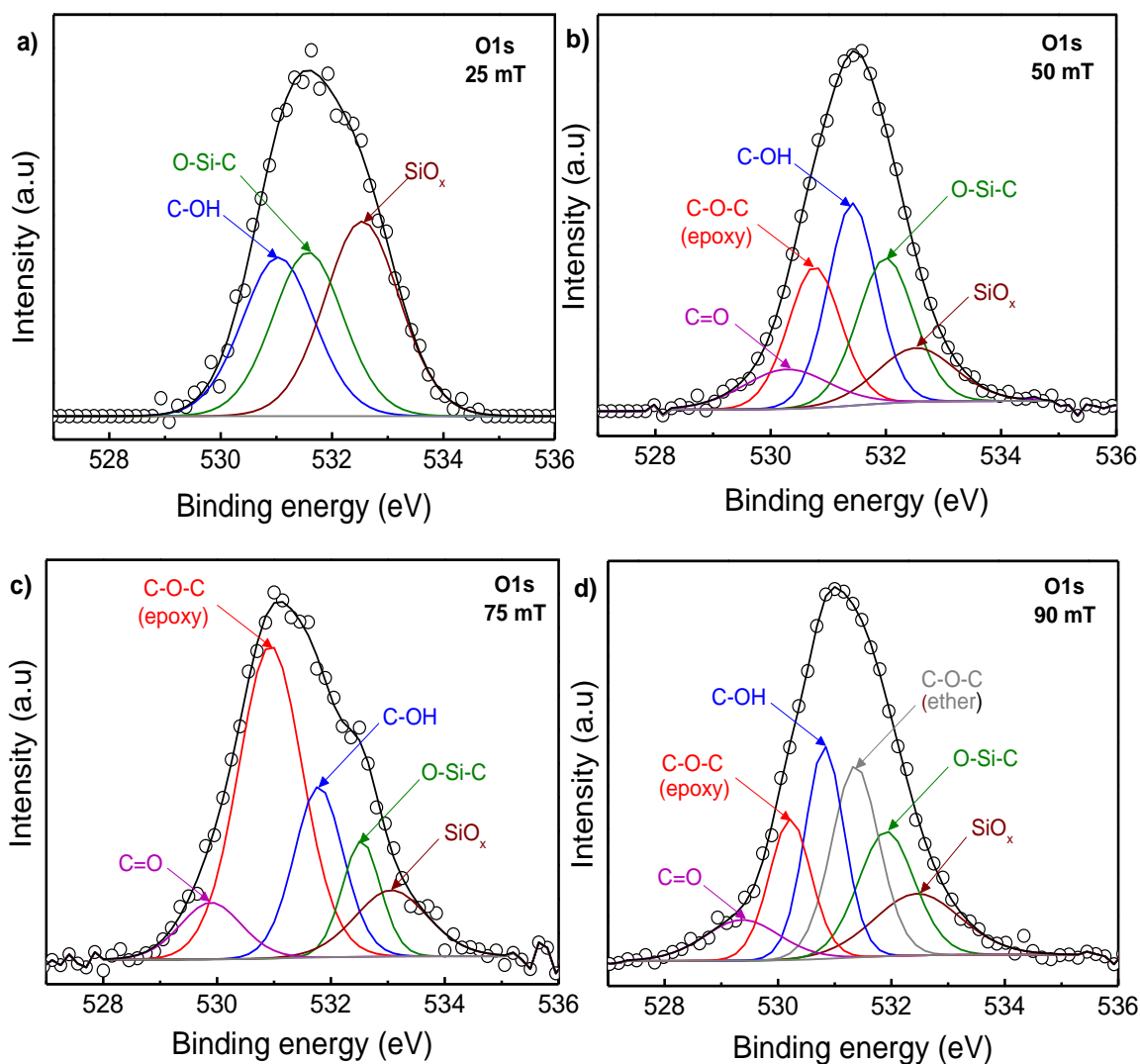


Figure 5.7: Deconvoluted XPS O1s spectra of as-functionalised samples at a) 25 mTorr b) 50 mTorr, c) 75 mTorr and d) 90 mTorr pressure.

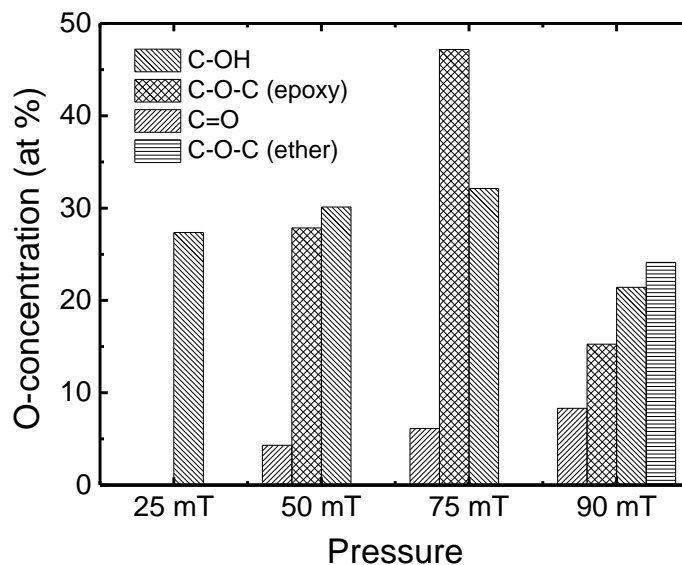


Figure 5.8: Concentration of oxygen functional groups on the graphene surface functionalised at different operation pressure.

With the increase in plasma pressure to 75 mTorr, no additional peaks were observed (Figure 5.7(c)), but the relative concentration of hydroxyls and carbonyls further increased to 32 at% and 6 at% respectively. Despite this increase, epoxy groups clearly dominate the spectrum with 47 at% of the total coverage, indicating the favourable chemisorption energy for their formation at 75 mTorr. By increasing pressure to 90 mTorr, a further increase in carbonyls was observed, nevertheless, both epoxides and hydroxyls showed reduction in concentration (Figure 5.7(d)). However, surprisingly a new peak at 532.2 eV was observed between C-OH and O-Si-C peak, which is assigned to ether functional groups, C-O-C (with no bond between C atoms). Note that the peak related to this functional group was not observed in the C1s spectrum shown above, because the binding energy for ethers is ~ 285.3 eV, which is exactly where the interfacial layer is situated and hence it is challenging to identify ether groups in the epitaxial graphene C1s spectrum. This shows that in order to extract complete bonding characteristics of carbon-oxygen functional groups, it is important to analyse the O1s spectrum of functionalised graphene, especially for epitaxial graphene on SiC (0001) samples in addition to the C1s spectrum. Incidentally, ethers were the majority functional groups present (25 at %) at 90 mTorr with hydroxyl, epoxides and carbonyls accounting for 22 at %, 15 at% and 8 at % each. Unlike other functional species, oxygen in ethers is incorporated into the graphene lattice by substituting for carbon atom in the honeycomb network. The formation of ether groups is possible because of the change in surface energy of graphene due to the presence of other functional species, which weakens

the C-C bond strengths [261]. In this situation, the additional reactive oxygen species available in the plasma, especially at higher pressure (90 mTorr) can easily displace the weakly bonded carbon atoms and form as substitutional dopants in the graphene lattice. Although the presence of ethers has been identified in GO and rGO [234], its impact on the graphene structural and electronic properties is not currently very well understood.

Nevertheless, this shows that a wide variety of carbon-oxygen functional groups can be introduced onto epitaxial graphene by e-beam plasma treatment, in which just by controlling the plasma pressure can control the concentration of the functional groups. For example, by functionalising graphene at 25 mTorr, a hydroxyl only surface can be created, whereas, almost an equal concentration of both hydroxyl and epoxide species can be achieved at 50 mTorr. Furthermore, by increasing the plasma pressure to 75 mTorr, an epoxy rich surface can be realised, whilst as many as four different O-functional groups can be generated at 90 mTorr pressure with oxygen situated both on the basal plane of graphene and in the lattice. Controlling the nature and density of functional groups adsorbed on to the surface of graphene is crucial for applications such as sensors, because the interaction of different chemicals or gases will vary depending on the functional species present on the surface. For example, rGO with $-OH$ and $C=O$ as major functional groups was shown to be highly sensitive to volatile organic chemicals [136], whereas graphene with high concentrations of carbonyl and carboxyl groups on the surface was found to be reactive to highly polar chemical species [224]. In addition, Mattson *et al* identified that epoxy groups on rGO play a key role in the sensing mechanism of NH_3 [264, 265]. Thus, e-beam plasma functionalisation can be used as a versatile technique for the modification of graphene surface chemistry to enhance the sensitivity and selectivity of graphene sensors by controlling the concentration of O-functional groups on the graphene surface.

5.3.1.3 *Si2p core level spectroscopy*

In order to evaluate the possibility of plasma induced etching of the graphene film, Si2p spectra of all functionalised samples were analysed. Any etching of graphene or even incomplete coverage of the graphene film would directly expose the SiC substrate to oxygen plasma and in turn should increase the concentration of O-Si-C and SiO_x bonds significantly after functionalisation. However, as shown in the Figure 5.9, no noticeable change in the chemical nature of the spectra was observed at all operating pressures, demonstrating that the plasma functionalisation used here does not create holes in the graphene film. Further,

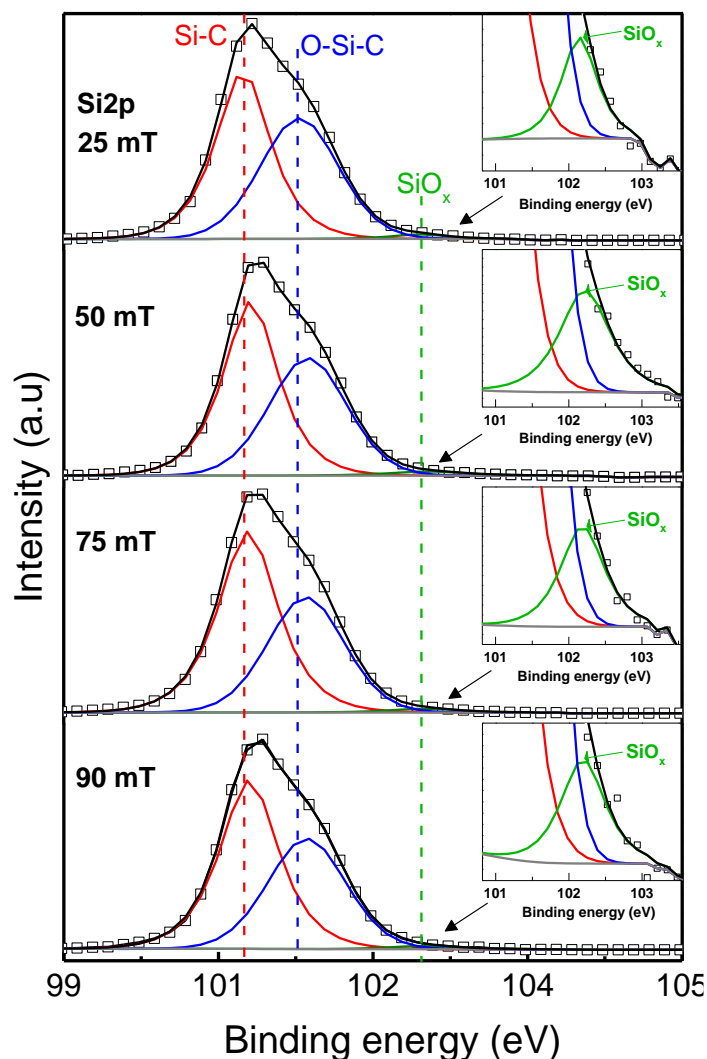


Figure 5.9: Deconvoluted Si2p spectra of functionalised samples at different operating pressures, showing negligible change to the O-Si-C or SiO_x peaks.

this also supports that epitaxial graphene film is continuous over the SiC substrate for the areas investigated on all functionalised samples.

5.3.2 AFM Analysis – examining surface morphological changes

AFM was used to examine the surface morphological changes to epitaxial graphene films as a result of plasma functionalisation process. The data in Figure 5.10 (top) show the topographic images of as-grown and as-functionalised graphene sample at 90 mTorr. As can be seen, no obvious changes to the graphene surface morphology was observed even at the highest oxidation pressure within the instrument resolution. Nevertheless, the AFM surface roughness of the epitaxial graphene before and after functionalisation shown in the Figure

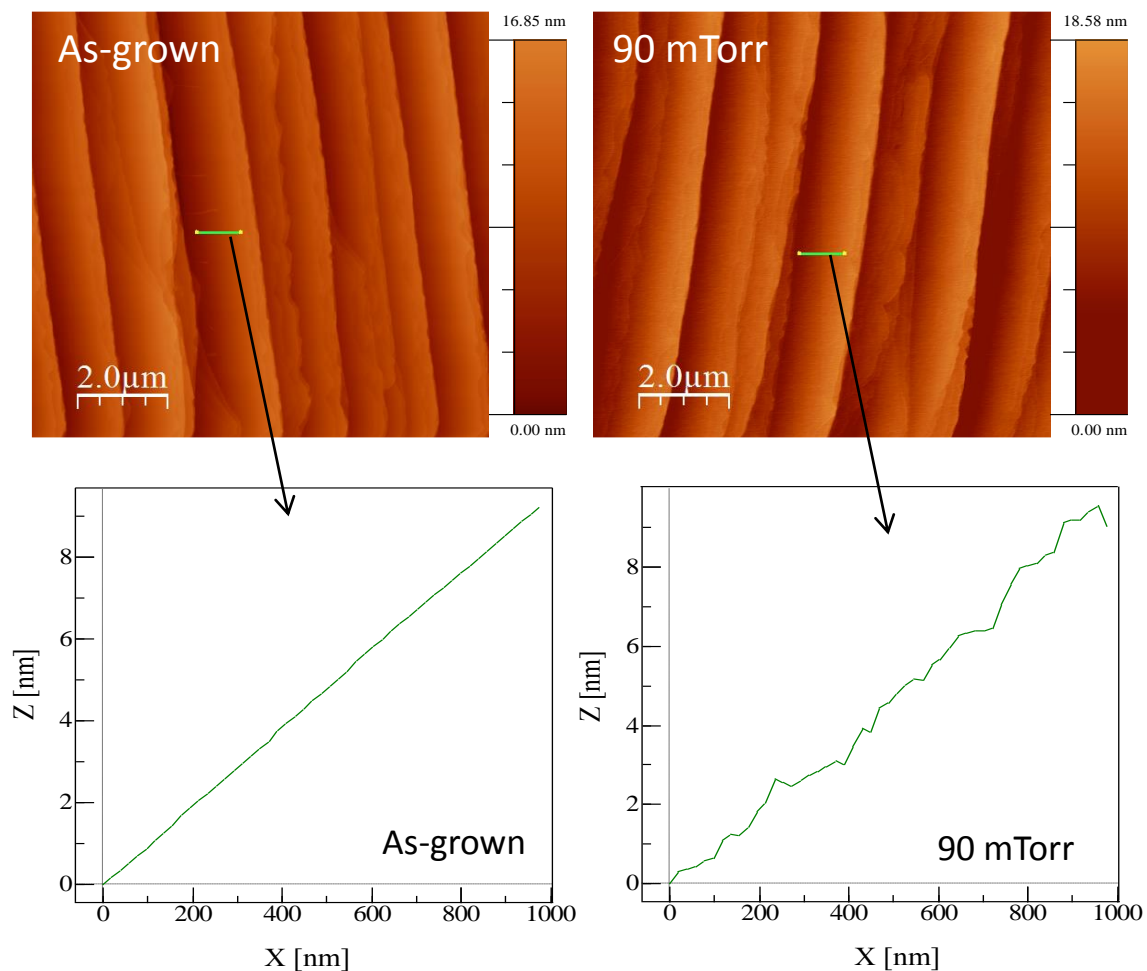


Figure 5.11: (top) AFM topographic images of the graphene surface before and after oxygen functionalisation. (bottom) corresponding surface roughness measured on the sample step terraces

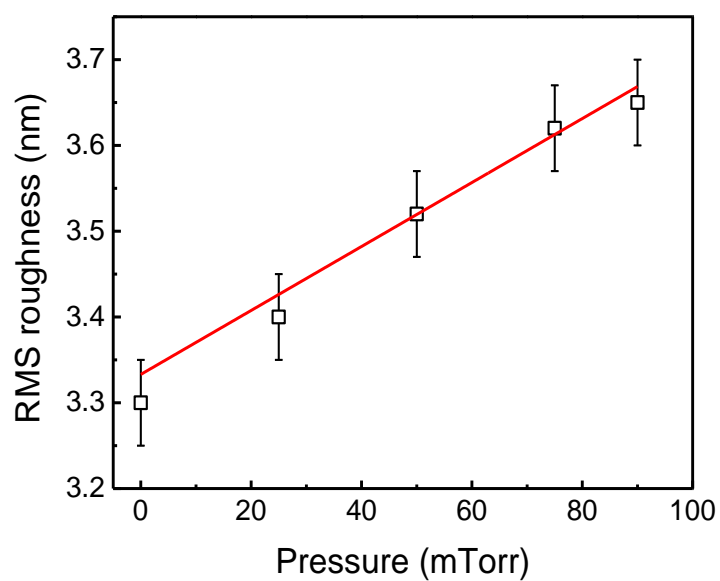


Figure 5.11: RMS roughness of functionalised graphene with the increasing pressure. Solid line is guide to the eye only.

5.10 (bottom), reveals an increase in surface roughness, which is attributed to the out-of-plane chemical bonding of oxygen functional groups, particularly epoxy and hydroxyl species. In addition, the root mean square (RMS) roughness of all functionalised graphene samples plotted as a function of the plasma pressure showed a small increase in the surface roughness with the increasing pressure as shown by the data in Figure 5.11. This implies that the functionalisation does not have a detrimental effect on the epitaxial graphene film quality.

5.3.3 Raman Analysis – monitoring structural characteristics

Raman spectroscopy was used to verify the effect of O-plasma treatment on the structural characteristics of graphene. Figure 5.12 shows the typical Raman spectrum of an as-grown graphene with characteristic G and 2D peaks at $1597 \pm 1 \text{ cm}^{-1}$ and $2740 \pm 1 \text{ cm}^{-1}$ respectively. The FWHM of the 2D peak was measured as 48 cm^{-1} , while it was recorded as 18 cm^{-1} for the G peak. Note that the FWHM of the 2D peak and the position of G (ω_G) and 2D (ω_{2D}) peaks are larger than the expected values of $\sim 35 \text{ cm}^{-1}$, $\sim 1582 \text{ cm}^{-1}$ and $\sim 2677 \text{ cm}^{-1}$ observed on free standing graphene flakes respectively [266], when taken at $\lambda = 514.5 \text{ nm}$. Despite the broadening, the 2D peak can still be fitted with a single Lorentzian as shown in the Figure 5.12, indicating the thickness of graphene in the probed area to be one monolayer [267]. The higher shift in position of G and 2D peak is attributed to compressive strain (more details below). All samples investigated in this study have approximately similar $\omega_{G,2D}$ ($\pm 2 \text{ cm}^{-1}$) and FWHM (G,2D) ($\pm 4 \text{ cm}^{-1}$) before functionalisation. No D-peak was observed across several probed areas on all as-grown samples, demonstrating high crystalline quality of graphene

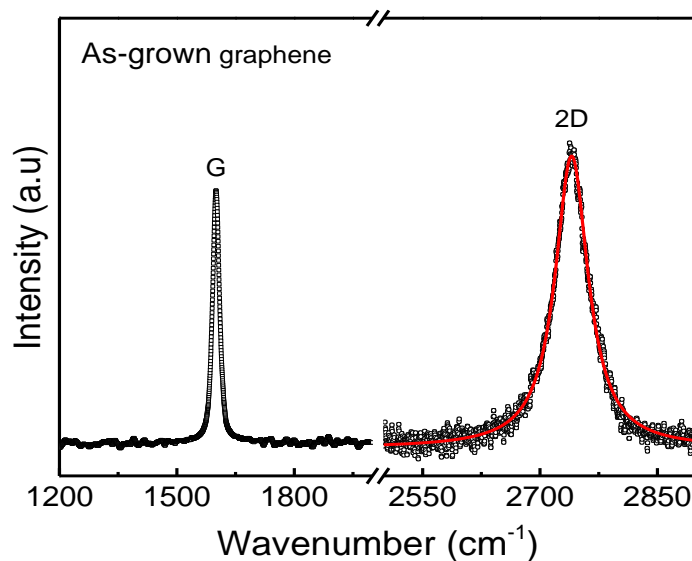


Figure 5.12: Raman spectra of graphene with characteristic G and 2D peaks. Inset shows the 2D-peak fitted with a single Lorentzian.

films. For fair comparison between samples, all Raman data presented here were collected from graphene/SiC step terraces avoiding regions of step edges in an attempt to minimise the differences in thickness and strain variations.

Figure 5.13 shows the evolution of Raman spectra of functionalised graphene at different plasma pressures. As can be seen, the exposure of graphene to O-plasma caused substantial changes to the G and 2D peaks along with a significant increase in the D peak intensity (I_D), indicating structural modifications to the graphene film. Under the functionalisation conditions used here, physical damage to the graphene lattice (i.e etching) is not expected to occur due to the low kinetic energy of ions of the plasma as discussed previously [72,73]. Therefore, the activation of the D peak is directly attributed to the chemisorption of oxygen functionalised species on to the graphene surface, which structurally disrupt the planar sp^2 symmetry of graphene by forming out-of-plane chemical bonds and resulting in sp^3 hybridisation. Note, an additional peak located at 1625 cm^{-1} has been observed at 75 mTorr pressure as a shoulder to the G-peak, representing another defect activated peak (D'), which was later integrated into the G peak at 90 mTorr pressure. Although both D and D' peaks arise due to the disorder induced features, they originate from different mechanisms. The D peak is due to single phonon intervalley and the D' peak is due to intravalley resonant Raman scattering events, where the defect provides the missing momentum in order to satisfy momentum conservation during the Raman scattering process [268].

The I_D/I_G ratio, which is used as a footprint for measuring the concentration of covalent defect sites on graphene, increased with the increasing pressure from 0.6 (25 mTorr) to 1.4 (90 mTorr). The increase in I_D/I_G indicates the transformation of crystalline graphene into nanocrystalline structures due to the adsorption of oxygen functional species, which acts as defect sites, reducing the sp^2 content significantly. From I_D/I_G ratio, the average size of nanocrystalline regions, L_a can be calculated by using the relation [269],

$$L_a(\text{nm}) = (2.4 \times 10^{-10}) \lambda_{\text{laser}}^4 \times \left(\frac{I_D}{I_G}\right)^{-1}$$

At 25 mTorr, L_a was calculated as 28 nm, which decreased to 12 nm at 90 mTorr as shown in the data (Figure 5.14(a)). The linear relationship observed for I_D/I_G and $1/L_a$ in Figure 5.14(b) is in agreement with behaviour demonstrated for Tuinstra-Koenig relation [270].

However, Lucchese *et al.* [155] recently reported that the amount of disorder in graphene is better quantified by measuring the average distance between point like defects, L_D and proposed a model explaining the dependence of I_D/I_G on L_D on two length scales, r_A and r_S

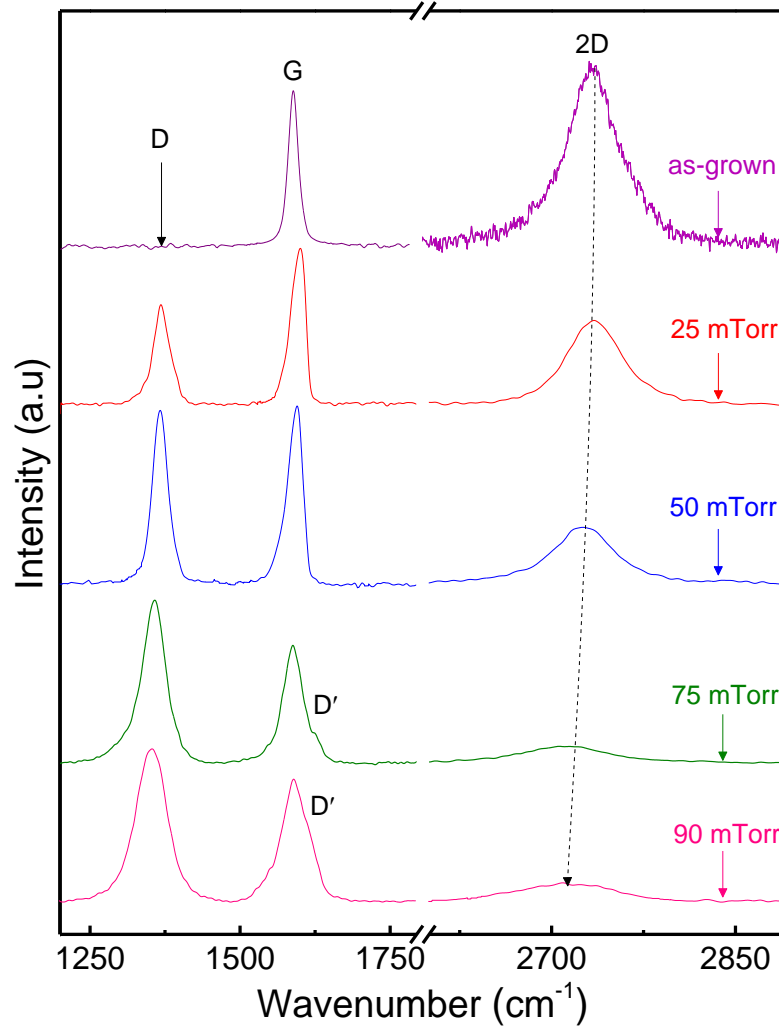


Figure 5.13: Evolution of Raman spectra of epitaxial graphene with the increasing plasma pressure.

(see Figure 5.15(a)). Here, r_A and r_S corresponds to regions where D band scattering occurs, in which, r_S determines the radius of structurally disordered region caused by the impact of a defect, whilst, r_A defines the defect activated region surrounding this point defect site, in which the planar sp^2 structure is preserved and allows for D band scattering process to take place. As a result, the r_A regions will contribute most strongly to the D peak enhancement, whilst the r_S regions make minimum contribution due to the distortion of the lattice structure itself. Applying this model to O-functionalised graphene films, r_S can be assigned to the regions where hydroxyl or epoxide species covalently bonded to graphene, changing the planar sp^2 symmetry to distorted sp^3 configuration and r_A can be assigned to the regions where the charge and bond lengths of carbon atoms surrounding the defect site are altered due to the oxygen adsorption. As the defect density grows with the increasing concentration of O-

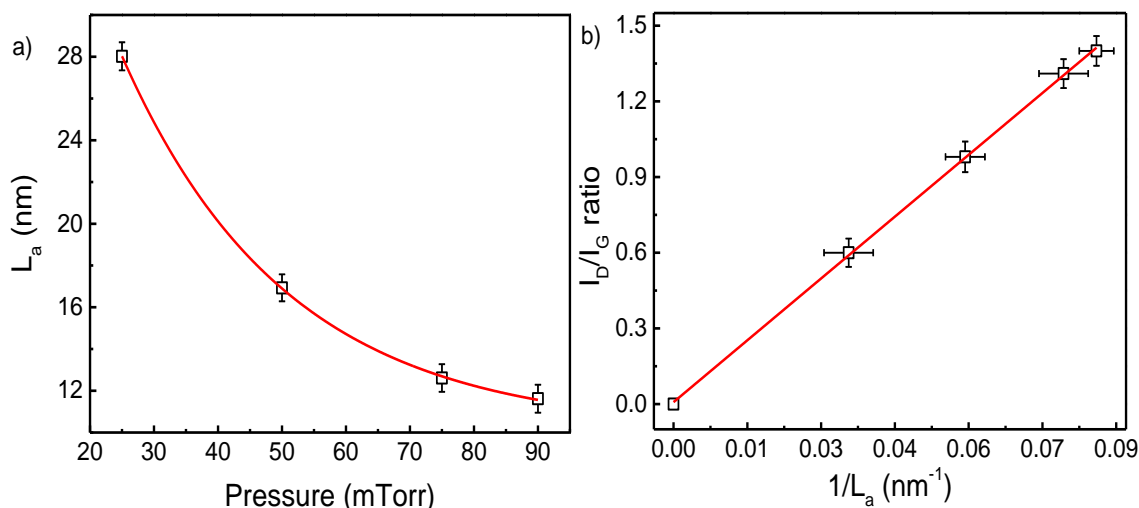


Figure 5.14: a) The plot of an average size of nanocrystallites as a function of plasma pressure b) Correlation between the ratio of the integrated intensities of D and G peaks (I_D/I_G) vs $1/L_a$. Solid lines are guide to the eye only.

functional groups, the D band intensity increases and reaches a maximum value. In the highly disordered regime, these activated regions start to overlap (see Figure 5.15(b)) and eventually saturate. Further increase in defect density results in the decrease of D band intensity because structurally disordered areas start to dominate the activated regions in the graphene sheet. In other words, since the D peak requires the presence of six-fold ring, any damage to this network reflects on the decrease in I_D with the decreasing L_D . However, this latter part of the argument is ignored here, as there was no saturation or decrease observed in the I_D/I_G for the functionalisation pressures studied, indicating that these functionalised graphene films are not in high defect density regime.

In order to quantify the development of defects in these samples, the I_D/I_G ratio was plotted as a function of the average distance between defects, L_D , using [154]:

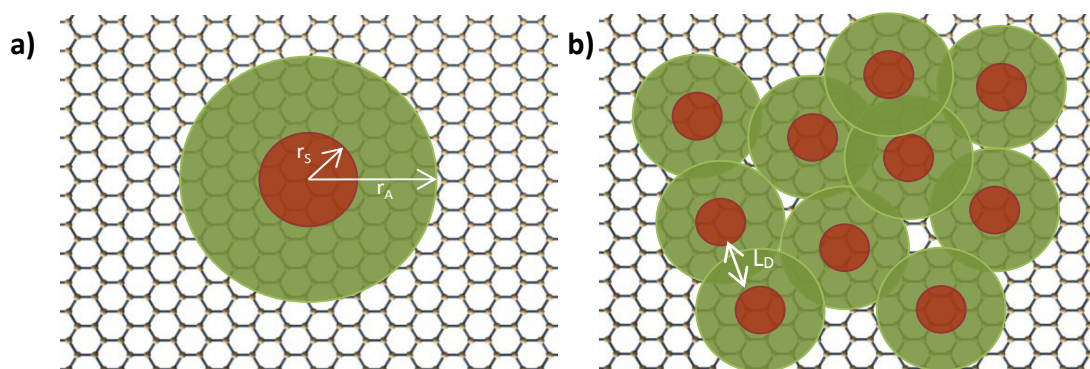


Figure 5.15: Illustration of a) structurally distorted region (red colour) and defect activated region (green colour) b) Evolution of disorder and defect regions with the increasing defect density.

$$L_D^2(\text{nm}^2) = (1.8 \pm 0.5) \times 10^{-9} \lambda_{\text{laser}}^4 \left(\frac{I_D}{I_G}\right)^{-1}$$

Although this equation was proposed for vacancies, Eckmann *et al* [271] have recently shown that this can be extended to sp^3 defects. Figure 5.16(a) shows a monotonic increase in I_D/I_G with decreasing L_D (i.e increasing O-concentration), consistent with the studies in the low defect regime. The average defect density n_D was calculated by using the expression [154]:

$$n_D (\text{cm}^{-2}) = \frac{(1.8 \pm 0.5) \times 10^{12}}{\lambda_{\text{laser}}^4} \left(\frac{I_D}{I_G}\right)$$

The calculated n_D at 25 mTorr was $1.5 \times 10^{11} \text{ cm}^{-2}$, which increased to $3.5 \times 10^{11} \text{ cm}^{-2}$ at 90 mTorr pressure as shown in Figure 5.16(b). The increase in defect density was followed by a strong reduction in the intensity of 2D peak (I_{2D}) as shown by the data in the Figure 5.17(a). It is known that I_{2D} is proportional to the electron/hole scattering rate. O-functional groups adsorbed on to the graphene surface acts as defect sites as well as introduce doping [52,116-119]. Both these effects will increase the probability of scattering events and therefore the intensity of the 2D peak decreases with the increase in dopant concentration. In single layer graphene, I_{2D}/I_G ratio was shown to have a strong dependence on doping. Figure 5.17(a) shows the intensity ratio of the I_{2D}/I_G as a function of plasma pressure and doping. The average I_{2D}/I_G was calculated as 1.15 for the as-grown graphene, which reduced significantly with the pressure and reached 0.27 at 90 mTorr. Since the intensity ratio of I_{2D}/I_G is known

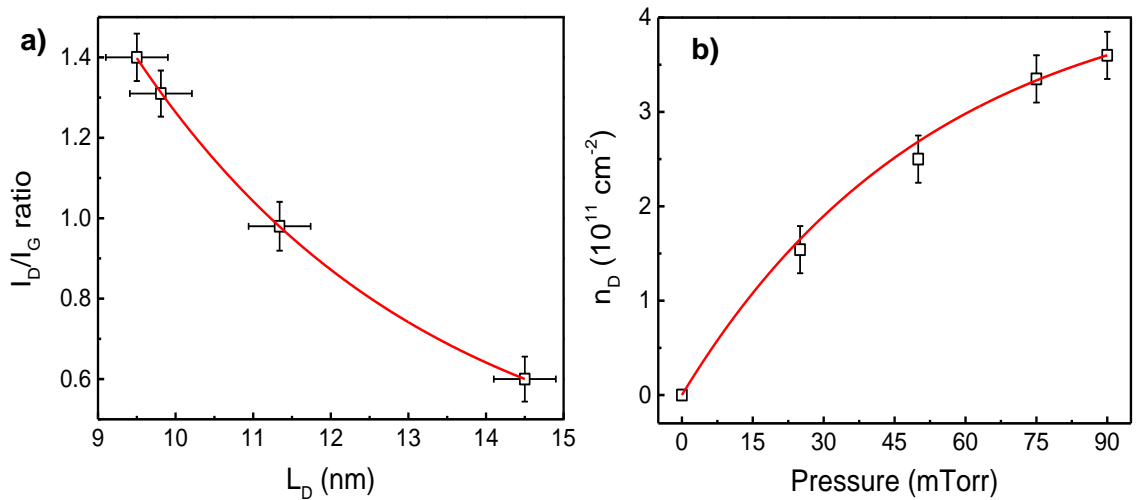


Figure 5.16: a) I_D/I_G ratio of all functionalised samples as a function of average defect distance. b) Estimated defect density at each functionalisation pressure. Solid lines are guide to the eye only.

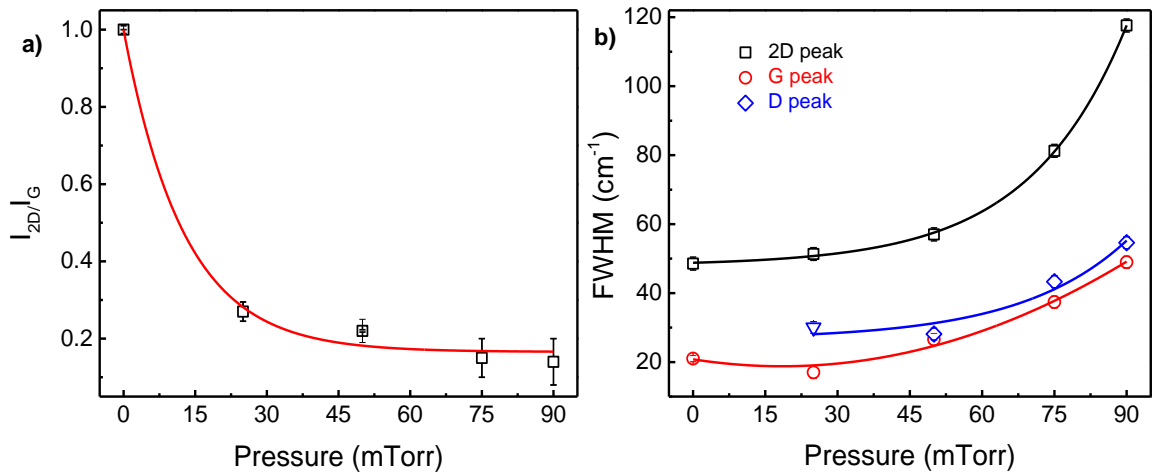


Figure 5.17: Dependence of a) integrated intensity ratio and b) FWHM of 2D and G peaks on the plasma pressure. Solid lines are guide to the eye only.

to be sensitive to doping concentration, an increase in both n or p-type dopants will result in a decrease in the I_{2D}/I_G [156, 272, 273].

In addition to the change in intensity ratios, the FWHM of all peaks increased with the increasing defect density (Figure 5.17(b)). For example, the FWHM of D-peak increased from 30 cm^{-1} to 54 cm^{-1} , whilst the G-peak increased from 18 cm^{-1} to 40 cm^{-1} . The 2D peak FWHM showed an exponential increase with the plasma pressure, reaching the value as high as 115 cm^{-1} at 90 mTorr. The change in FWHM of D, G and 2D peaks observed is consistent with previous O-functionalisation studies on exfoliated single layer graphene flakes. Here, the broadening of 2D-peak was attributed to doping, where the oxygen dopants progressively increase the density of sp^3 clusters in the graphene [156, 272, 273]. Despite the increase in the FWHM, the 2D-peak of all functionalised samples can still be fitted with a single Lorentzian function as shown by the data in Figure 5.18, indicating the thickness of graphene is not altered during functionalisation process and also shows that sp^2 regions are still present even at the highest oxidation pressures investigated here..

The data in Figure 5.19 shows another important observation, where the shift in peak positions was observed. The origin of the observed peak shifts in graphene Raman spectrum after functionalisation was attributed to doping, in which the direction of the shift was used to identify the nature of doping. For example, it was shown that ω_G and ω_{2D} blue shifts for p-doping and red shifts for n-doping [274]. Nevertheless, the relative shift of the 2D peak ($\delta\omega_{2D}$) was always found to be smaller or negligible than that of the relative shift of the G peak ($\delta\omega_G$), i.e. $\delta\omega_{2D} < \delta\omega_G$ irrespective of the doping type. Here, $\delta\omega_G$ and $\delta\omega_{2D}$ are relative shifts in peak positions with respect to ω_G and ω_{2D} of as-grown epitaxial graphene.

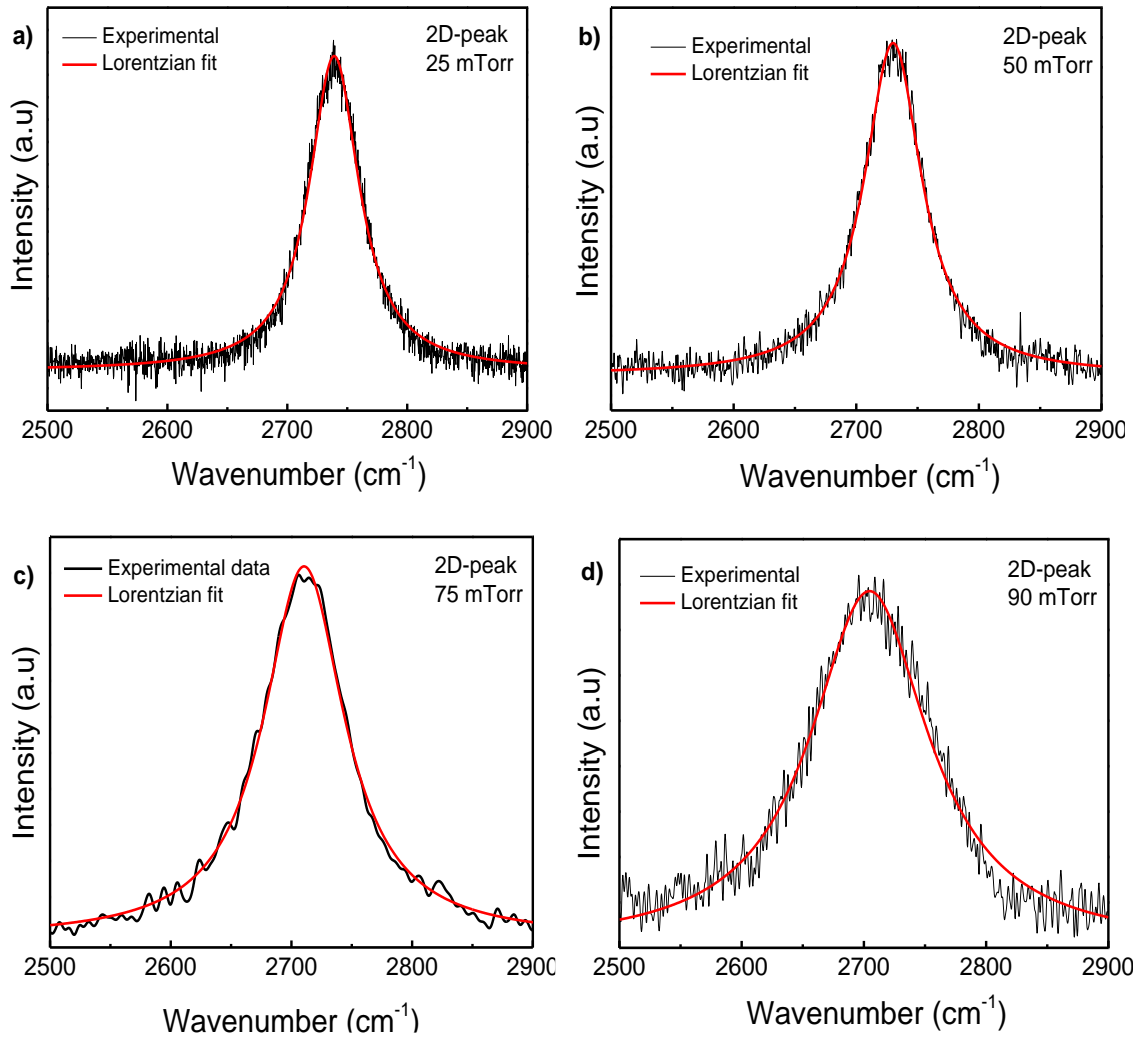


Figure 5.18: Change in the shape and intensity of 2D peak at different plasma pressures and the corresponding peak fitting using single Lorentzian function shown in solid lines.

From Figure 5.19(a), it can be seen that, at 25 mTorr, ω_G is blue shifted from $1597 \pm 1 \text{ cm}^{-1}$ to $1601 \pm 1 \text{ cm}^{-1}$ ($\delta\omega_G = 4 \pm 1 \text{ cm}^{-1}$), while 2D peak is red shifted from $2740 \pm 1 \text{ cm}^{-1}$ to $2739 \pm 1 \text{ cm}^{-1}$ ($\delta\omega_{2D} = 1 \pm 1 \text{ cm}^{-1}$). This red shift is within the resolution of the Raman spectrometer used here and hence will be considered as negligible. Nevertheless, the blue shift of G-peak indicates that graphene is p-doped upon O-functionalisation, which is expected, because of the higher electronegativity of oxygen (3.55) than that of carbon (2.44), consistent with previous observations [275]. However, interestingly, with the increasing plasma pressure, both G and 2D peaks significantly red shifted to 1588 cm^{-1} ($\delta\omega_G = 9 \pm 1 \text{ cm}^{-1}$) and 2710 cm^{-1} ($\delta\omega_{2D} = 30 \pm 1 \text{ cm}^{-1}$) respectively at 90 mTorr pressure. As can be seen, $\delta\omega_{2D}$ is significantly higher than $\delta\omega_G$, i.e. $\delta\omega_{2D} \gg \delta\omega_G$ for samples functionalised between 50 to 90 mTorr (see Figure 5.19(b)), which contradicts the expected doping trend

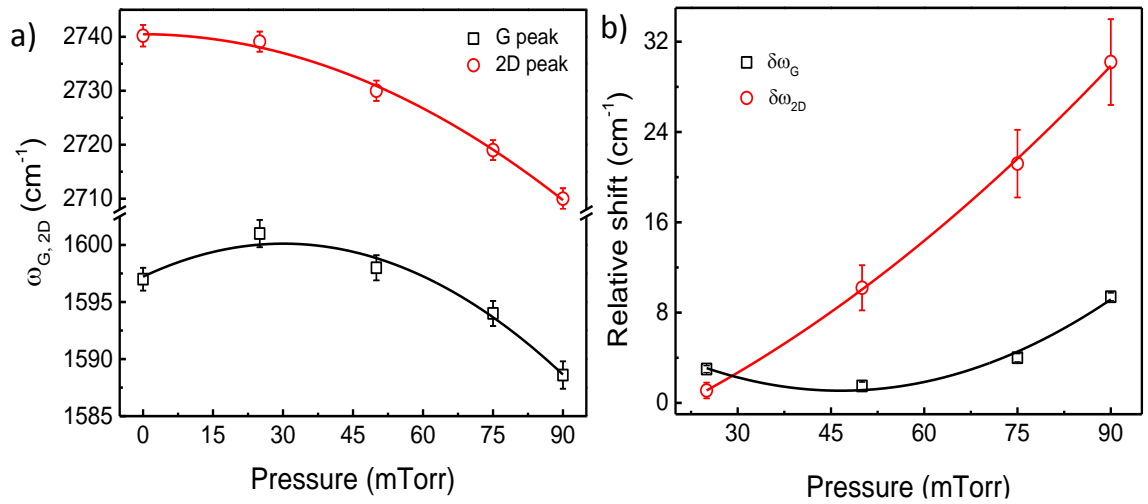


Figure 5.19: a) G and 2D peak positions of graphene with the increasing plasma pressure. b) Relative shift of G and 2D peaks with respect to the as-grown graphene peak positions. Solid lines are guide to the eye only.

for functionalised samples. Here, $\delta\omega_{2D}$ of 30 cm^{-1} is too large to be achieved by doping alone and there should be other competing mechanisms responsible to this peak shifting.

It is well known that G and 2D peaks are not only sensitive to doping, but are also strongly influenced by strain variations in the graphene film. For example, it was shown that compressive strain induces a blue shift of both G and 2D peaks, whilst tensile strain results in their red shift [158, 276]. Since covalent functionalisation alters the planar symmetry of carbon atoms in graphene to a tetrahedral orientation, a shift in inter-atomic spacing between surrounding carbon atoms occurs, leading to a significant localised strain in the neighbouring C-C bonds. For example, the introduction of hydroxyl and epoxy functional groups of graphene increases the bond length of C-C from 1.42 Å (free standing graphene) to 1.47 Å ($\sim 3\%$ increase) and 1.51 Å ($\sim 6.3\%$ increase) respectively. This localised strain would also have an impact on the Raman peak positions. Here, the stretching of C-C bonds upon O-functionalisation would suggest that the graphene is under tensile strain and therefore should result in red shifts of G and 2D peak (as seen here). However, this is only true for unstrained graphene and cannot be applied to epitaxial graphene case. Unlike exfoliated graphene flakes or CVD grown graphene, epitaxial graphene on SiC has a large native compressive strain [160, 277-279], which reduces the C-C bond length from 0.142 Å to 0.135 Å, resulting in significant shifts of the G peak ($\Delta\omega_G = 15 \text{ cm}^{-1}$) and the 2D peak ($\Delta\omega_{2D} = 63 \text{ cm}^{-1}$). Here, $\Delta\omega_{2D}$ and $\Delta\omega_G$ are the relative shifts in peak positions with respect to G (ω_G^0) and 2D (ω_{2D}^0)

peak positions of an unstrained and undoped graphene. This native compressive strain is not completely released, due to a critical strain release barrier arising from the pi-orbital interactions within the graphene lattice [119].

Compressive strain in epitaxial graphene film develops during the cooling stage of the growth process because of the large variation in coefficients of thermal expansion between SiC and graphene (SiC contracts and the graphene expands during cooling). This strain in graphene can be calculated using the expression given by Mohiuddin *et al.* [158]:

$$\Delta\omega_{G,2D} = -2\omega_{G,2D}^0\gamma_{G,2D}\epsilon_{G,2D}$$

where $\omega_{G,D}^0$ is the G or 2D peak positions of pristine graphene (i.e. unstrained and undoped), $\Delta\omega_{G,2D}$ is the shift in G or 2D peak positions due to strain with respect to $\omega_{G,2D}^0$. $\gamma_{G,2D}$ is the Grüneisen parameter of the G or 2D peak and $\epsilon_{G,2D}$ is the strain calculated for the G or 2D peak. The following parameters of pristine graphene were used to calculate the strain: $\omega_G^0 = 1682 \text{ cm}^{-1}$, $\omega_{2D}^0 = 2677 \text{ cm}^{-1}$, $\gamma_G = 1.8$, $\gamma_{2D} = 2.7$ [158, 266]. This leads to a maximum calculated strain of -0.42 % for the 2D peak (ϵ_{2D}) in as-grown epitaxial graphene, which is in agreement with previous studies [278, 279]. Here the negative value represents compressive strain, whereas positive value indicates tensile strain. When such a compressively strained graphene is subjected to oxygen functionalisation, strain relaxation occurs in the carbon hexagonal structure due to the oxygen induced stretching of C-C bonds and thereby compensating for the native strain present in the epitaxial graphene. The variation in C-C bond lengths also changes the phonon frequency, which can be easily detected by Raman spectroscopy. As shown in Figure 5.20, the intrinsic compressive strain in epitaxial graphene was found to decrease with the increasing plasma pressure.

For example, when functionalised at 90 mTorr, the native strain in as-grown graphene decreased from -0.42 % to -0.21 % for ϵ_{2D} and from -0.34% to -0.12 % for ϵ_G . Such strain relaxation behaviour has not been experimentally reported previously on functionalised epitaxial graphene, however, DFT calculations on epitaxial graphene/SiC (0001) have indeed shown that strain relaxation occurs in graphene upon O-functionalisation and identified epoxy oxygen atoms in particular to play a crucial role in perturbing the planar $\pi - \pi$ interactions of the graphene lattice through sp^3 bonding, and act as strain release centres allowing buckling to occur [119]. In other words, while epoxy groups exert significant tensile strain on an unstrained graphene, their presence actually helps to restore an already compressively strained epitaxial graphene film to get closer to the unstrained state.

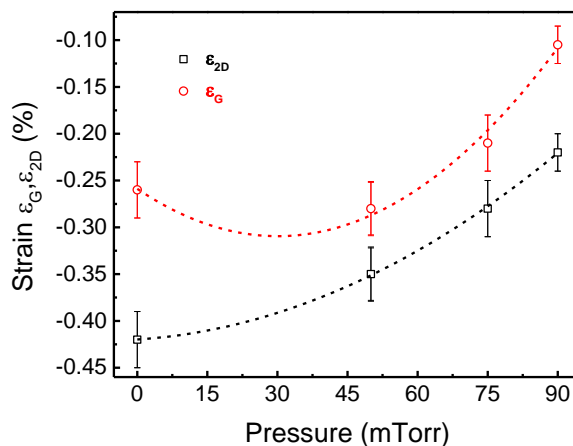


Figure 5.20: Change in intrinsic strain in graphene as a function of plasma pressure. Solid lines are guide to the eye only.

Here, the O-functionalised films are assumed to be under biaxial strain state, because of the absence of peak splitting of G (2D) peak in to two sub-modes, G^- ($2D^-$) and G^+ ($2D^+$) with different vibrational frequencies that is usually seen when the graphene is subjected to uniaxial strain [158, 276]. To quantify the strain coefficient in these functionalised samples, the relative shifts of G and 2D peaks were plotted as a function of strain in Figure 5.21. A linear dependence of G and 2D band frequencies on the strain can be clearly seen with a slope of $\sim 57.7 \text{ cm}^{-1}/\%$ for ϵ_G and $\sim 151.5 \text{ cm}^{-1}/\%$ for ϵ_{2D} respectively. Both these values are in excellent agreement with previously reported biaxial strain values on exfoliated graphene flakes ($\partial\omega_G/\partial\epsilon = -57/\%$ and $\partial\omega_{2D}/\partial\epsilon = -140\text{-}160/\%$) [158, 280]. The calculated strain

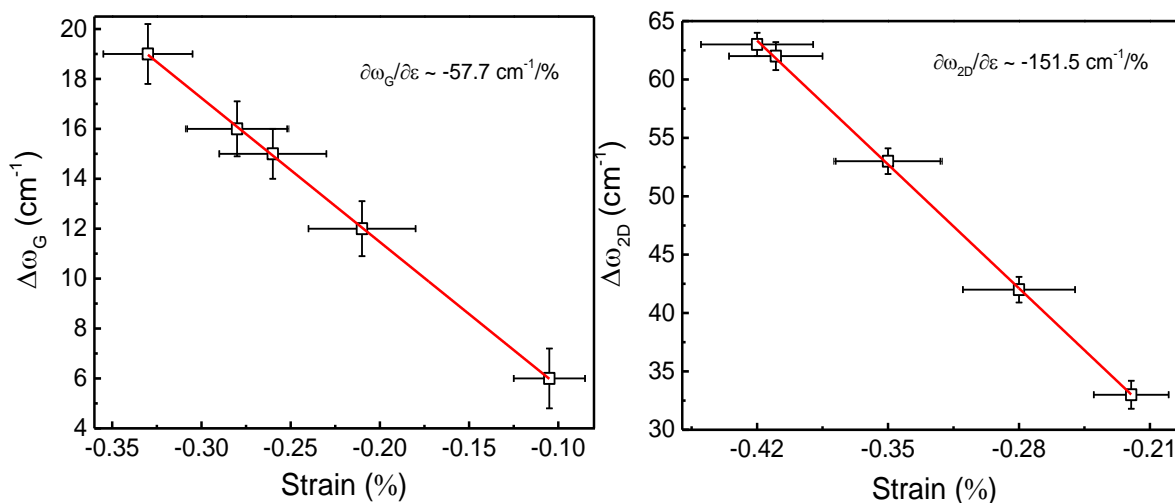


Figure 5.21: Relative shift of G (left) and 2D peak (right) positions as a function of induced strain by oxygen functional groups. Solid line indicates linear fits. The slopes of the fitting lines are also included.

coefficients give peak shift ratios of 2.64, which is also in good agreement with the reported biaxial strain values of 2.4–2.8 [280, 281].

Although strain plays a crucial role in these O-functionalised graphene films, it should be noted that strain alone cannot be responsible for the peak shifts observed here. This is because, applying or relaxing the strain in graphene should only shift the peak positions, reflecting the compression (phonon hardening) or elongation (phonon softening) of C-C bonds and is not expected to change the intensity of the 2D peak, which is sensitive to crystallinity and doping of the graphene film. The significant reduction of I_{2D} coupled with a profound increase in FWHM (2D) shown in Figure 5.17 suggests that the graphene is highly doped. Nevertheless, the substantial shift of 2D peak in comparison to the G peak also indicates that strain related variations takes place as a result of functionalisation. Therefore, the observed peak shifts here are a combination of both doping and strain.

For the 25 mTorr functionalised sample, doping plays a major role in peak shifting due to the absence of epoxy functional groups on the surface, which reduces the effect of strain relaxation in the graphene as indicated by the weak shift of ω_{2D} . As a result, the doping induced peak shift dominates the spectrum, which can be clearly seen in Figure 5.19. However, in the case of samples functionalised between 50 to 90 mTorr, the presence of epoxy oxygen atoms on the graphene sheet induces strain relaxation, which dominates the effect of carrier doping as indicated by the significant red shifts of ω_G and ω_{2D} . In other words, for the samples functionalised between 50–90 mTorr, oxygen induced doping changes in the Raman spectra were over shadowed by oxygen induced strain relaxation effects. These results show that, while graphene doping often manifests a shift of the G peak, such a shift is not always discernible, especially when analysing functionalised epitaxial graphene due to the presence of significant native compressive strain in as-grown films. Hence independent electrical measurements are necessary to confirm the presence of doping.

5.3.4 Hall measurements

Hall measurements were performed on all functionalised samples to analyse the effect of O-functionalisation on the electrical properties of graphene. As-grown films showed intrinsic n-type character with average sheet carrier densities of $7 \pm 2 \times 10^{12} \text{ cm}^{-2}$ due to the induced charge transfer from the underlying unsaturated Si-bonds near the SiC/graphene interface. The average sheet conductivities and mobilities of as-grown graphene films were measured as $10834 \pm 26 \text{ S/cm}$ and $850 \pm 80 \text{ cm}^2 \text{ V}^{-1} \text{ s}^{-1}$ respectively.

After functionalisation, the electronic properties of these graphene films changed considerably. For example, all functionalised samples showed p-type conduction, due to the electron withdrawing nature of oxygen, which changes the intrinsic n-type character of graphene by shifting the Fermi level (E_F) below the Dirac point (E_D) as depicted in Fig. 5.22. The hole density in these functionalised films increased linearly with increasing plasma pressure as shown in Figure 5.22 and reached $5 \times 10^{14} \text{ cm}^{-2}$ at 90 mTorr, which is more than one order of magnitude larger than previously reported values $\sim 4 \times 10^{13} \text{ cm}^{-2}$ for O, F or N-functionalised graphene [282-284]. The increase in carrier density with the increasing pressure is expected because, the charge transfer between the adsorbed molecule and the graphene can grow with the concentration of adsorbed molecules.

The increase in carrier density resulted in a considerable decrease in Hall mobility along with the decrease in sheet conductivity due to the presence of sp^3 scattering sites produced by oxygen functional groups. At 90 mTorr, mobility and conductivity were measured as $15 \text{ cm}^2 \text{ V}^{-1} \text{ s}^{-1}$ and 416 S/cm respectively. The decrease in conductivity with the plasma pressure is consistent with the increasing defect density observed in the Raman spectra (Figure 5.17). Nevertheless, the sheet conductivities measured here are significantly better than previously reported oxygen plasma functionalised graphene studies [48] and comparable/better than that of commonly reported values on highly reduced graphene oxide films (see Table 5.1). It should be noted that the reduction methods used for reducing GO films involve several hours of exposure to strong acids and/or multiple high temperature annealing cycles, which do not offer any degree of control over reduction in concentration of specific functional

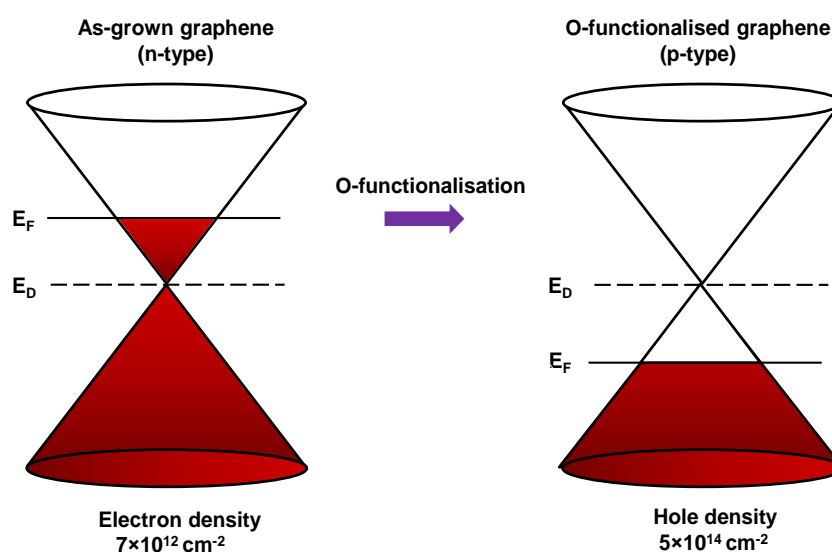


Figure 5.22: Schematic energy diagrams showing the effective hole doping of epitaxial graphene after O-functionalisation at 90 mTorr pressure.

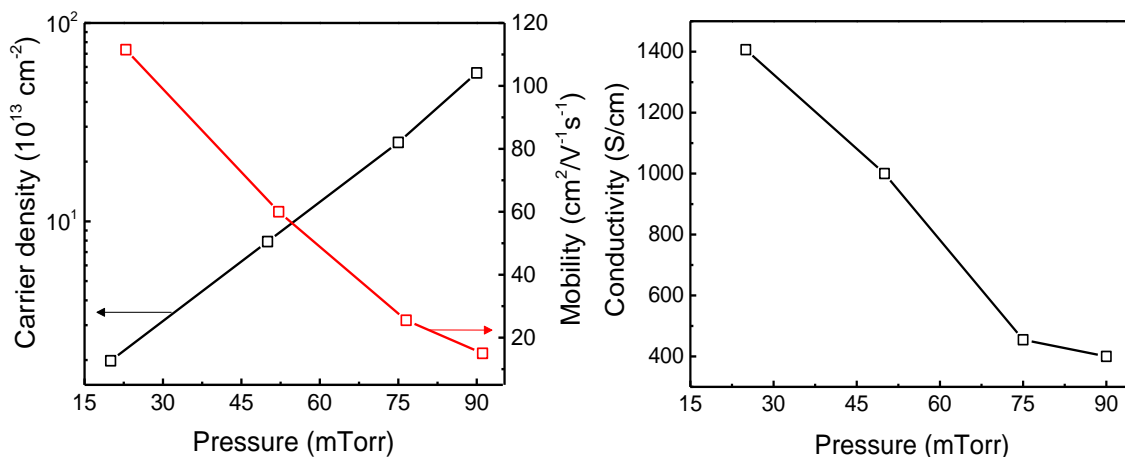


Figure 5.23: a) Plot showing the change in carrier density and mobility as a function of plasma pressure. b) Decrease in conductivity of functionalised epitaxial graphene films with the increasing functionalisation pressure

group(s). In contrast, e-beam plasma processing technique used here is relatively clean (no wet chemical or thermal processing required), extremely fast (less than concentration of functional groups on the graphene surface by controlling the plasma pressure).

Table 5.1: Comparison of conductivity values of rGO with the present work. Note, the thicknesses of the reported rGO films/flakes are usually from few layer to multi-layer.

Ref #	Conductivity (S/cm)	Treatment process
24	550	1100 °C in Ar and/or H ₂
48	100	Ar/O ₂ plasma
237	202	NaBH ₄ + H ₂ SO ₄ + 1100°C Ar/H ₂ anneal
249	550	N ₂ H ₄ and 1100 Ar/H ₂ anneal
This work	1406.5	Ar/O ₂ plasma [25 mTorr]
This work	1000.0	Ar/O ₂ plasma [50 mTorr]
This work	454.55	Ar/O ₂ plasma [75 mTorr]
This work	416.6	Ar/O ₂ plasma [90 mTorr]

5.4 Summary

In summary, controlled modification of epitaxial graphene films using e-beam generated Ar/O₂ plasmas has been demonstrated. The high resolution C1s and O1s core level spectra showed that selective incorporation of different concentrations of oxygen functional groups can be achieved by controlling the plasma pressure. At 25 mTorr, hydroxyl rich surface was created, whereas, almost an equal proportion of hydroxyl and epoxy functional groups has been realised at 50 mTorr. By increasing oxygen plasma pressure to 75 mTorr, an epoxy rich graphene surface was achieved, whilst as many as four different covalent functional groups (hydroxyl, epoxy, carbonyl and ether) can be generated at 90 mTorr with oxygen atoms located both on the graphene surface and in the lattice.

AFM topographic images showed no significant increase in the RMS surface roughness of these functionalised films, indicating that the functionalisation process does not have detrimental effect on the graphene film quality. Raman spectroscopy showed the change in planar sp^2 symmetry of graphene to distorted sp^3 hybridisation. In addition, Raman measurements also revealed that O-functionalisation results in strain relaxation, in which the intrinsic compressive strain present in epitaxial graphene films (-0.41% , ω_{2D}) decreases with the increasing oxygen concentration and reaches -0.21% , ω_{2D} at 90 mTorr. As a result, the Raman peak shifts were dominated by strain related variations, masking the doping related shifts caused by O-functional groups. These results show that, it is inappropriate to estimate the type of doping or the concentration of dopants on epitaxial graphene using Raman peak positions alone without considering the effects of strain. Hall measurements showed O-functional groups induces p-type doping on graphene with carrier densities as high as $5 \times 10^{14} \text{ cm}^{-2}$. The ability to selectively tailor the surface chemistry of graphene along with the control over doping and the capability to tune the local strain in graphene opens up the possibility of using O-functionalised graphene in a wide variety of applications ranging from developing next generation nanoelectronic devices ranging from graphene oxide based resistive switching memories to chemical and biological sensors.

Chapter 6

Effect of oxygen functionalisation on metal-graphene contact interfaces

6.1 Introduction

Surface functionalisation of graphene is being actively pursued in an effort to modify its intrinsic chemical, electronic, and optical properties using reactive species such as hydrogen, fluorine, oxygen and chlorine [140, 212, 215, 285]. In particular, oxygen functionalisation has been attracting enormous attention because of its rich and complex chemical reactions with graphene that results in the formation of multiple covalent carbon-oxygen chemical bonds, transforming its hydrophobic nature to more hydrophilic in character. Such oxygen functionalised graphene surfaces were shown to be highly promising for chemical and biological sensing [29, 136], non-volatile memories [286], and optoelectronic applications [118]. Nevertheless, the functionalisation process also significantly degrades the intrinsic properties of graphene due to the reactive nature of O-functional groups. For example, it was shown the O-functionalisation increases the graphene sheet resistance by several orders of magnitude, whilst the mobility decreases by three orders of magnitude even for mild functionalising conditions [118, 140]. Since, graphene based applications such as chemical sensors rely on the changes in electrical resistance introduced by adsorbed analyte molecules, maintaining low sheet resistances is crucial for maximising the sensor response. Hence,

identifying functionalisation techniques that can modify the surface chemistry of graphene without significantly sacrificing its intrinsic properties is critical for the development of functionalised graphene based electronic applications. Also of great interest is the effect of functionalisation on the electrical characteristics of metal/graphene interfaces. As the use of O-functionalised graphene films in electronic applications inevitably require metal contacts, it is critical to understand the electrical properties of metal/O-functionalised graphene interfaces. The performance of electronic devices greatly depends upon the nature and the quality of metal contact interfaces. Poor interface quality can result in high contact resistance, R_C and can degrade the performance of a device significantly. Therefore, understanding characteristics of metal/O-functionalised graphene interfaces is an important aspect of contact engineering for potential electronic applications. While there have been many studies on the interaction of metals with pristine graphene, a detailed study on the electrical characterisation of metal/O-functionalised graphene interfaces has not been reported.

In this chapter, a systematic study on the effect of O-functionalisation on the electrical characteristics of epitaxial graphene/metal contact interfaces is presented. Two functionalisation approaches were investigated here, where in, for the first approach, O-functionalisation was performed on as-grown blanket graphene film, followed by device fabrication (herein after referred to as method-A) and for the second approach, device fabrication was performed first, followed by O-functionalisation (herein after referred to as method-B). By employing such approaches, metal-graphene contact interfaces were created with oxygen atoms present primarily underneath the metal electrodes (method-A case) and at the metal contact edge sites (method-B case). In order to monitor the changes in chemical and structural properties of graphene, XPS and Raman spectroscopy were used, whilst electrical properties were analysed by transfer length method (TLM) and Hall measurements respectively. Low-frequency noise measurements were also performed to analyse the noise behaviour of these functionalised samples.

6.2 Experimental details

For the detailed description of sample preparation procedure, graphene growth morphology and the operation of plasma processing reactor, see chapter 3. Briefly, epitaxial graphene films were grown on three 8×8 mm² semi-insulating 6H-SiC (0001) substrates via sublimation of Si at 1540°C in an argon atmosphere for 30 min. All three substrates were diced from the same SiC wafer, underwent similar pre-cleaning procedures and were

synthesised in the same batch to minimise any substrate related or growth induced variations between samples. O-functionalisation was performed on two samples at room temperature using e-beam generated Ar/O₂ plasmas at 75 mTorr pressure, whilst no functionalisation has been performed on the third sample and was used as a reference. The total treatment time was 60 s and the plasma exposure time was 6 s. Note that both functionalised samples were processed under identical functionalisation conditions with variables such as functionalisation time, plasma power, temperature and the operating pressure kept constant. The primary difference that exists between these samples is the processing step at which the samples were functionalised (see Figure 6.1), i.e. one sample was functionalised immediately after growth and pre-cleaning procedure (exposing blanket graphene films to the O-plasma), whilst the second sample was fabricated first into two and four-terminal structures followed by O-functionalisation.

The surface chemistry of graphene films before and after functionalisation were analysed using XPS, by fitting the C1s and O1s spectra with mixed Gaussian-Lorentzian functions after performing Shirley background subtraction. The structural quality of these films was monitored by Raman spectroscopy using an excitation wavelength of 514.5 nm and a spot size of 700 nm. For the detailed description of instrumental settings and parameters used for XPS and Raman characterisation, see chapter 5.

For electrical measurements, an array of forty identical devices in Van-der-Pauw configuration and four sets of TLM test structures were fabricated on all three samples using standard photolithographic techniques as described in chapter 3. Ti/Au (10 nm/100 nm) metal films were deposited using e-beam evaporation followed by lift-off in acetone. The active channel area of van-der Pauw structures consists of 40×40 μm² channel cross, while each set of TLM test structures have contact dimensions of 150 μm wide (W) and 100 μm long (L) with channel lengths (L_{ch}) varying from 5 μm to 45 μm, in steps of 5 μm.

Hall measurements were performed at room temperature to measure the variation in parameters such as conductivity, mobility, carrier type and density. These measurements were performed on 40 μm×20 μm van-der Pauw structures with a magnetic field of 0.3 Tesla and a sample current of 100 μA. Low-frequency noise measurements were also performed to extract the noise magnitude and behaviour of these samples in two probe configuration between 1 Hz and 100 kHz and averaged over 15 times to minimise the noise magnitude span. All noise measurements were done at room temperature in a shielded Cascade Microtech probe station supported on an anti-vibration table.

6.3 Results and Discussion

Figure 6.1 shows the schematic illustration of process steps used for method-A and method-B samples respectively. For both methods, as-grown graphene films were pre-cleaned in HF solution (48%) for 2 min to remove any residual oxides from graphene surfaces. After this cleaning procedure, the sample used for method-A was immediately functionalised with Ar/O₂ plasma, exposing blanket graphene film to reactive oxygen species. This O-functionalised graphene sample was then lithographically patterned into mesa structures by reactive-ion-etching and subsequently metallised with Ti/Au to complete the device fabrication process. For the case of method-B sample, the blanket graphene film was first patterned into mesa structures, followed by metallisation and N₂/H₂ annealing at 400°C for

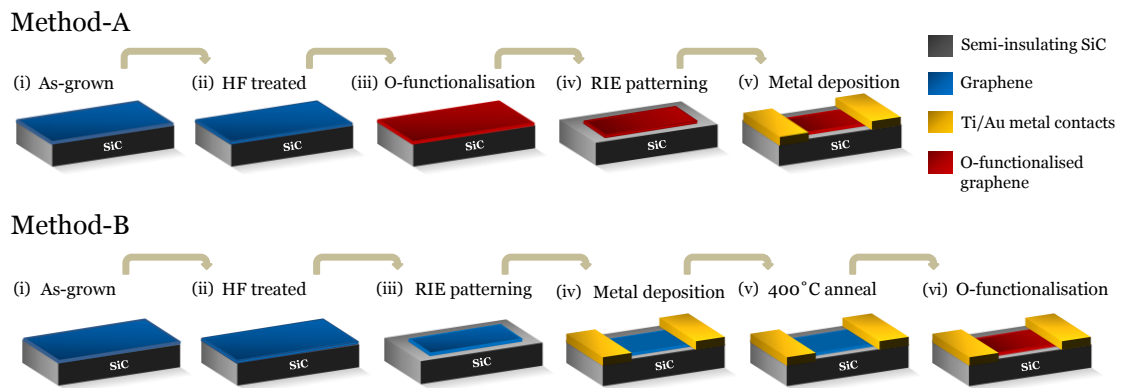


Figure 6.1: Schematic cross section of process steps followed for samples functionalised using method-A (top) and method-B (bottom) approaches.

30 min. Here, the annealing step was necessary to remove photo-resist residues from the graphene surface after lithography processing. Finally, this patterned graphene sample was functionalised with Ar/O₂ plasma. Note, apart from the additional annealing step used in method-B, similar device fabrication procedures and functionalisation conditions were followed for both methods.

6.3.1 XPS analysis

To characterise the surface chemical composition of these samples, XPS analysis was performed both before and after functionalisation. As the functionalisation was performed on blanket (method-A) and patterned graphene (method-B) films, the bonding mechanism of O-functional groups is expected to differ between these two methods due to the presence

of dangling bonds at the patterned graphene edges. Figure 6.2(a) shows the high resolution C1s spectra of method-A sample taken immediately after HF treatment and just before O-functionalisation, whilst Figure 6.2(c) shows the spectra of method-B sample taken after N₂/H₂ annealing and just before O-functionalisation. Fitting the C1s spectra with mixed Gaussian-Lorentzian functions revealed three characteristic peaks at ~283.1 eV, ~283.9 eV and ~284.6 eV for both samples, corresponding to SiC substrate, C-C (graphene) and the interfacial layer respectively. The relative concentration of these peaks correspond to 33.5%, 38.6% and 27.6% respectively. In addition to these peaks, a shoulder peak was observed at 285.2 eV (2.03%) in the C1s spectrum of the method-B sample, representing hydroxyl groups. The presence of this peak is consistent with previous studies, where it was shown that graphene attracts residual oxygen species from the ambient atmosphere after annealing. However, importantly, no peaks related to photoresist residues were observed, indicating clean graphene surfaces after the thermal treatment.

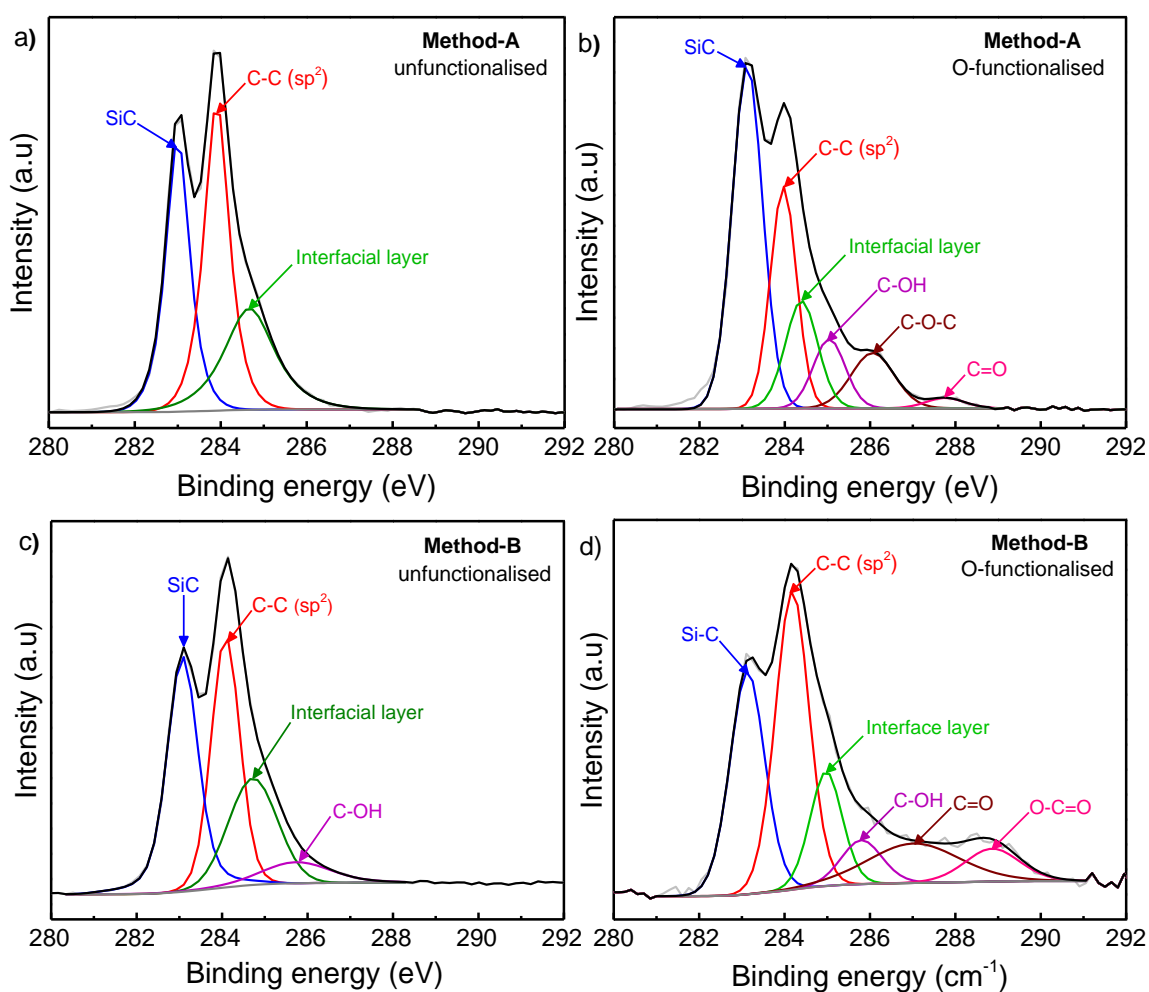


Fig. 6.2: High resolution XPS C1s spectra of epitaxial graphene taken before and after oxygen plasma functionalisation using methods A and B respectively.

Upon exposure to O-plasma, a clear change in the surface chemistry of both method-A and method-B samples was observed with increased full width half maximum (FWHM) of the C1s spectra along with shoulder peaks appearing at higher binding energies (Figure 6.2(b) and 6.2(d)), representing different carbon-oxygen functional groups. However, the extent of surface modification and the polarity of O-functional groups varied markedly between method-A and method-B samples. For example, as shown in Table 6.1, the concentration of sp^2 C-C bonds in the method-A sample reduced significantly from 38.6% to 25.8% after functionalisation, indicating substantial modification to the graphene film. In contrast, the method-B sample showed only a small reduction in concentration (34.95%) of sp^2 C-C bonds, implying minimal impact of O-plasma on the graphene lattice.

The deconvoluted C1s spectrum of method-A sample (Figure 6.2(b)) showed three O-functional peaks at 285.5 eV, 286.3 eV and 287.6 eV, attributed to C-OH (hydroxyl), C-O-C (epoxy) and C=O (carbonyl) groups respectively. The assignment procedure followed here is explained in detail in chapter 5. As shown by the data in Figure 6.2(b) and in Table 6.1, the most favourable configuration of these O-functional groups was found to be epoxy groups with 9.92% of the total oxygen coverage, followed by hydroxyls and carbonyls with 6.04% and 1.64% respectively. The chemical composition of the carbon-oxygen functional groups observed here is in agreement with previous studies, where, using nuclear magnetic resonance spectroscopy Lerf *et al.* [257] and Cai *et al.* [263] have demonstrated that the basal planes of oxidised graphene are predominantly decorated with epoxy and hydroxyl groups, whilst the edge sites or vacancies in the graphene film form exclusive adsorption sites for carbonyl and carboxyl species. The limited number of carbonyls and the absence of carboxyl functional groups in the C1s spectrum of method-A sample indicate negligible number of edge sites present in the as-grown blanket graphene film, thereby restricting the rise of carbonyl or carboxyl species and therefore results in an epoxy and hydroxyl rich graphene surface.

In contrast, for the method-B sample, the deconvoluted C1s spectrum (Figure 6.2(d)) showed three peaks representing C-OH, C=O and O-C=O (carboxyl) groups at 285.7 eV, 286.7 eV and 287.0 eV respectively. Table 6.1 shows the chemical state of the method-B sample surface, in which carbonyls constitute for the majority of oxygen functional groups present on the graphene surface with a relative concentration of 12.61%, whilst carboxyl and epoxy groups account for 7.33% and 5.15% each. The high concentration of carbonyl and carboxyl groups indicate the presence of edge sites, which is expected for patterned

Table 6.1: Differences in the relative concentration of O-functional groups present on the graphene surface after functionalisation at 75 mTorr pressure using method-A and method-B approaches.

Functional group	Method-A			Method-B		
	B.E (eV)	FWHM (eV)	Concentration (%)	B.E (eV)	FWHM (eV)	Concentration (%)
Si-C	283.10	0.84	42.25	283.13	0.96	27.14
C-C (sp^2)	284.02	0.73	25.84	284.18	0.92	34.95
IF layer	284.41	0.92	14.31	284.97	0.88	12.80
C-OH	285.05	0.79	6.04	285.79	1.12	5.42
C-O-C	286.08	1.20	9.92	N/A	N/A	N/A
C=O	287.79	1.06	1.64	287.02	2.53	12.61
O-C=O	N/A	N/A	N/A	288.86	1.50	7.08

graphene structures. It is well known that the edge sites of graphene with dangling bonds are more reactive than the basal planes, enabling the formation of double (C=O) or triple bonds (O-C=O) more favourable, in comparison to single bonds (C-OH or C-O-C) that are typically seen in homogeneous/blanket graphene films. Here, the presence of carboxyl groups is of particular interest because, they are commonly used as anchoring sites for attaching DNA and other bio-molecules for chemical and biological sensors [137], making method-B sample highly attractive for sensing applications.

In order to validate the distribution of carbon-oxygen functional groups observed here, the high resolution O1s core level spectral analysis was performed. For method-A sample, the O1s spectrum was fitted with six components (Figure. 6.3(a)), located at 530.1 eV, 530.8 eV, 531.7 eV, 532.5 eV and 533.0 eV. By reference to C1s peak shifts, these binding energies were assigned to carbonyl, epoxy, hydroxyl, silicon-oxycarbide and silicon-oxide bonds respectively. As it can be seen in the Figure 6.3(a), epoxy functional groups clearly dominate the O1s spectrum, which is in excellent agreement with the concentration of carbon-oxygen functional groups found in the C1s spectrum of method-A sample. Figure 6.3(b) shows the O1s spectrum of method-B sample, also fitted with six major peaks at 530.1 eV, 530.8 eV, 531.7 eV, 532.5 eV and 533.0 eV, corresponding to carboxyl, carbonyl, hydroxyl, silicon-oxycarbide and silicon-oxide bonds respectively. In addition to these peaks, a new component has been observed at 534.9 eV, which is assigned to residual H₂O bonds.

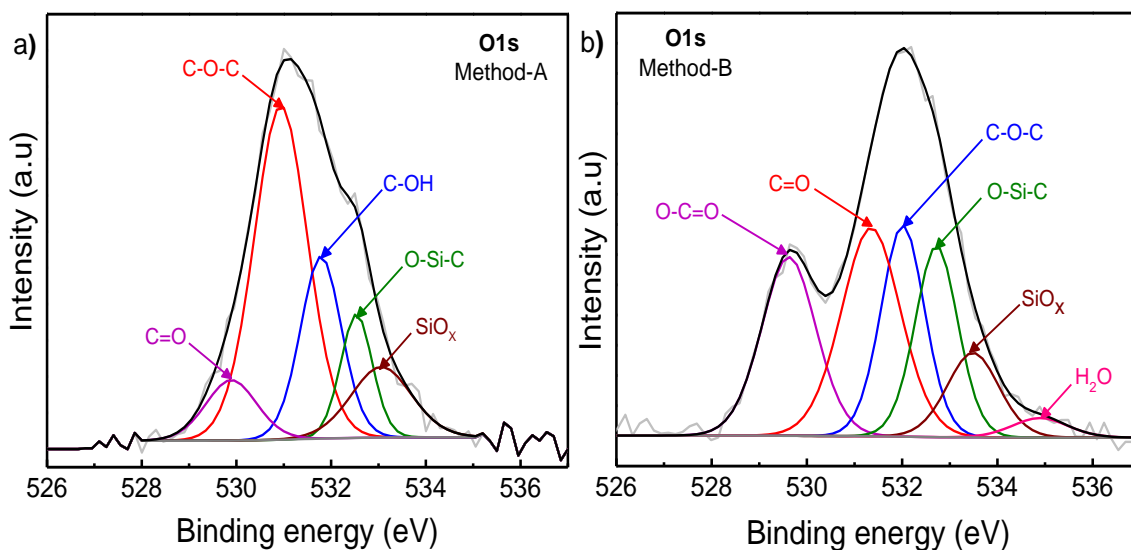


Figure 6.3: High resolution XPS O1s spectra of a) method-A and b) method-B sample.

Carboxyls were found to be dominant functional species followed by carboxyls and epoxy groups, consistent with the finding in the C1s spectrum of method-B sample shown above. This shows that the surface chemistry of graphene is greatly dependent upon the ordering of the functionalisation step during the device fabrication, in which, an epoxy rich surface can be created by functionalising graphene film immediately after growth and prior to device fabrication (method-A), whilst a carbonyl rich surface can be realised by functionalising graphene after the final device fabrication step (method-B).

6.3.2 Raman analysis

Raman spectroscopy was used to verify the effect of O-plasma treatment on the structural characteristics of epitaxial graphene. Figure 6.4 shows the typical Raman spectrum of an unfunctionalised graphene along with the spectra of method-A and method-B functionalised samples. The position and the full width at half maximum (FWHM) of G and 2D peaks taken before and after functionalisation are summarised in Table 6.2. The unfunctionalised graphene Raman spectrum showed G and 2D peaks at $\sim 1599\text{ cm}^{-1}$ and $\sim 2739\text{ cm}^{-1}$ respectively with no visible D peak, indicating high crystalline quality of graphene films. The FWHM of G peak was measured as 19 cm^{-1} , whilst it was recorded as 34 cm^{-1} for the 2D peak. Here, FWHM (2D) indicates that the thickness of the graphene film for the probed area is a single layer, which was further confirmed by fitting the 2D peak with a single Lorentzian function. The ratio of the intensity of 2D peak (I_{2D}) to the intensity of the G peak (I_G), i.e. I_{2D}/I_G was calculated as 1.15.

Upon exposure to O-plasma, significant changes to the G and 2D peaks were observed along with the presence of a new disorder induced D-peak in the Raman spectrum of both method-A and method-B functionalised samples, indicating structural modifications to the graphene film. The activation of D-peak is attributed to the covalent attachment of oxygen functional groups to the graphene surface, which structurally disrupts the planar sp^2 symmetry of graphene by forming out-of-plane chemical bonds and resulting in sp^3 hybridisation. Note that an additional peak has been observed at 1625 cm^{-1} as a shoulder to the G peak for both methods, representing another defect activated peak (D'). As discussed in chapters 3 and 5, this D' -peak is due to intravalley resonant Raman scattering events, where the defect provides the missing momentum in order to satisfy momentum conservation during the Raman scattering process []. Here, the extent of structural modification to the graphene film depends on the functionalisation method used. For example, functionalising graphene using method-A approach resulted in a significant increase in the intensity of the D peak (I_D). The I_D/I_G ratio, which is used as a footprint for measuring

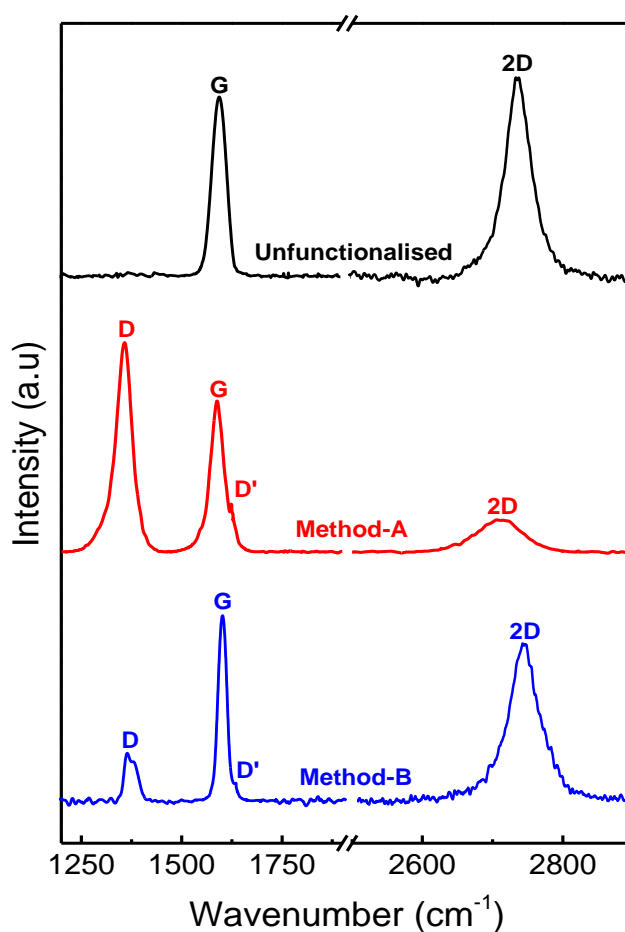


Figure 6.4: Raman spectra of unfunctionalised graphene and O-functionalised graphene using method-A and method-B approaches

the concentration of covalent defect sites in graphene, was calculated as 1.33. Interestingly, when the graphene was functionalised using method-B approach, only a small rise in I_D was observed with an I_D/I_G ratio of 0.27. From this ratio, the average distance between the defect sites, L_D can be calculated using the relation [154]:

$$L_D^2(\text{nm}^2) = (1.8 \pm 0.5) \times 10^{-9} \lambda_{laser}^4 \left(\frac{I_D}{I_G}\right)^{-1}$$

where λ is the excitation laser wavelength in nm. For method-A functionalised sample, L_D was measured as 10.2 nm, whilst for the method-B sample it was calculated as 27.5 nm. This shows that the concentration of O-functionalisation induced defects significantly vary depending on the functionalisation approach used. The average defect density, n_D in the graphene film can be estimated by using the expression [154]:

$$n_D (\text{cm}^{-2}) = \frac{(1.8 \pm 0.5) \times 10^{12}}{\lambda_{laser}^4} \left(\frac{I_D}{I_G}\right)$$

The resultant n_D for method-A sample was calculated as $1.5 \times 10^{11} \text{ cm}^{-2}$, while it was recorded as $4.3 \times 10^{11} \text{ cm}^{-2}$ for the method-B sample. Such a variation in the concentration of defect sites was also reflected on the intensity of the 2D peak, where a strong reduction in I_{2D} was observed for method-A sample, whilst only a moderate decrease in I_{2D} was seen for the method-B sample. It is known that the intensity of 2D peak is proportional to the electron/hole inelastic scattering rate. Since the O-functional groups adsorbed on to the graphene surface acts as defect sites as well as introduce doping, an increase in the probability of scattering events occur and therefore the intensity of the 2D peak decreases. As the intensity of G peak (I_G) shows negligible dependence on the doping related effects, the I_{2D}/I_G ratio can be used as a sensitive parameter to monitor doping in the graphene film, where I_{2D}/I_G ratio decreases with the increasing doping concentration, irrespective of the dopant type. Here, the average I_{2D}/I_G ratio for the unfunctionalised graphene was calculated as 1.15, which reduced significantly to 0.15 when functionalised with method-A approach, whereas it reduced only to 0.85 when functionalised using method-B technique. This shows that the magnitude of doping or the doping induced charge carrier scattering is substantially higher when the blanket graphene is functionalised, in comparison to patterned graphene film. The decrease in I_{2D}/I_G was followed by an increase in FWHM of the 2D-peak, where an increase from 34 cm^{-1} to 80 cm^{-1} was observed for method-A sample, whilst it was increased to 50

cm⁻¹ method-B sample respectively. Despite this increase, the 2D peak can still be fitted with a single Lorentzian function, implying the thickness of the graphene film has not been altered during the functionalisation process.

In addition to the change in peak intensity and FWHM, functionalisation also shifted the position of G (ω_G) and 2D (ω_{2D}) peaks as shown in Table 6.2. There are several origins for the shift of Raman peaks, including the effects of doping and strain as described in detail in chapter 5. Depending on the initial position of the Fermi level (E_F), ω_G either red shifts or blue shifts upon exposure to the O-plasma. For example, ω_G displays smallest energy value when the E_F of graphene is closer to the Dirac point, while it shifts to higher energies when E_F is far away from Dirac point due to either n or p doping [156]. In contrast, ω_{2D} does not show major changes for low doping levels, but it increases with the increasing hole doping concentration and decreases for the increasing electron concentration [156]. Nevertheless, the relative shift of G peak is usually greater than the relative shift of 2D peak, i.e. $\Delta\omega_G \gg \Delta\omega_{2D}$. Here, $\Delta\omega_{2D}$ and $\Delta\omega_G$ are relative shifts in peak positions with respect to ω_{2D} and ω_G of unfunctionalised graphene. Apart from doping induced shifts, ω_G and ω_{2D} are also strongly influenced by strain related variations [158].

Table 6.2: Raman data for method-A functionalised sample

Probed area	ω_D (cm ⁻¹)	ω_G (cm ⁻¹)	ω_{2D} (cm ⁻¹)	FWHM D (cm ⁻¹)	FWHM G (cm ⁻¹)	FWHM 2D (cm ⁻¹)	I_D/I_G
Basal plane (before functionalisation)	N/A	1599.1	2738.8	N/A	19.3	48.3	N/A
Basal plane (after functionalisation)	1356.1	1588.6	2709.6	41.9	38.6	75.7	1.40
Edge site (after functionalisation)	1357.3	1587.3	2707.3	45.3	36.2	79.6	1.47

For example, it was shown that both ω_G and ω_{2D} blue shifts when the graphene was subjected to compressive strain, whilst tensile strain results in their red shift [158]. It was found that for strain induced variations, the relative shift of G-peak is always lower than the relative shift of 2D-peak, i.e. $\Delta\omega_G \ll \Delta\omega_{2D}$.

Here, for the sample functionalised using method-A approach, ω_G red shifted from 1599 ± 1 cm⁻¹ to 1588 ± 1 cm⁻¹ ($\Delta\omega_G = 10 \pm 1$ cm⁻¹), whilst ω_{2D} also red shifted from 2739 ± 1 cm⁻¹

¹ to $2012 \pm 1 \text{ cm}^{-1}$ ($\Delta\omega_{2D} = 27 \pm 1 \text{ cm}^{-1}$). As can be seen, $\Delta\omega_{2D}$ is larger than $\Delta\omega_G$, implying that strain plays a major role in the shift of these Raman peaks, similar to that observed in chapter 5. Here, the red shift of G and 2D peaks can be understood on the basis of stretching/elongation of the C-C bonds, which weakens the bond strength and therefore lowers their vibrational frequency. For example, as O-functionalisation was performed on the blanket graphene film that has negligible amount of edge sites or vacancies, the resultant surface chemistry consists of a high concentration of epoxy and hydroxyl functional groups (see XPS data above), which induces significant distortion to the graphene lattice by pulling the carbon atoms out of the graphene basal plane [254]. In order to adapt to this tetrahedral sp^3 geometry, the stretching of C-C bonds occurs around the epoxy and hydroxyl defect sites. Since epitaxial graphene grown on SiC is already compressively strained (-0.42%) due to the variation in thermal expansion coefficients between SiC and graphene, this oxygen induced stretching of C-C bonds results in strain relaxation in the graphene lattice, thereby reducing the native compressive strain present in graphene to -0.26%. It should be noted that although O-functionalisation induces strain relaxation in epitaxial graphene, it also results in significant doping (as evidenced by the reduction in 2D-peak intensity). Nevertheless, strain related variations dominate the doping induced changes to the graphene film for method-A functionalised sample.

Similar to the method-A approach, functionalisation using method-B approach also resulted in the red shift of ω_G from $1599 \pm 1 \text{ cm}^{-1}$ to $1597 \pm 1 \text{ cm}^{-1}$ ($\Delta\omega_G = 4 \pm 1 \text{ cm}^{-1}$), whilst no noticeable change was observed for ω_{2D} ($\Delta\omega_{2D} = < 1 \text{ cm}^{-1}$), indicating doping is the main cause for the observed changes. Since O-functionalisation was performed on the patterned graphene film that contains edge sites or dangling bonds, the reactive nature of these unterminated bonds enable the formation of carbonyls and carboxyls more favourable than hydroxyl or epoxy species. It was shown before that both carbonyls and carboxyls maintain the planar sp^2 structure of graphene and does not have the same structural influence as hydroxyl or epoxy groups. This is because, unlike inner carbon atoms (i.e. basal planes) edge carbon atoms can adapt to tetrahedral configuration more freely without causing extra strain, making the doping induced changes more visible in the Raman peak shifts.

It is well known that the graphene grown on SiC (0001) is electron doped (n-type) due to the charge transfer from the SiC substrate with E_F located at around 0.35-0.4 eV above the Dirac point. The red shift in ω_G observed here after functionalisation implies that E_F is now located closer to the Dirac point due to the change in charge carrier density in the

graphene film. Interestingly, a higher reactivity was observed at the edges of graphene where the peak shift was more pronounced than the basal plane areas. For example, as shown in the Figure 6.5, $\Delta\omega_G$ was found to be 12 cm^{-1} when probed near the edge of the graphene, in comparison to 4 cm^{-1} observed at the central regions. Similarly, $\Delta\omega_{2D}$ showed 4 cm^{-1} change near the edge sites, in comparison to less than 1 cm^{-1} change seen at the basal plane areas. This clearly shows that the doping near the graphene edge sites is significantly higher than the basal plane regions. Moreover, after O-plasma treatment, the I_D/I_G ratio at the edge sites of graphene was calculated as 1.18, whereas it was only measured as ~ 0.35 at the graphene basal planes. The higher I_D/I_G ratio suggests higher reactivity of carbon atoms close to the edges than in the bulk plane. This indicates that functionalisation induced distortion to the graphene lattice can be significantly minimised by choosing patterned graphene films for functionalisation, where the reactive graphene edge sites with dangling bonds form exclusive adsorption sites for derivative O-functional groups, thereby reducing the structural impact on graphene lattice. Figure 6.6 and Table 6.3 further verifies the differences between edge sites and basal planes of the method-B functionalised sample.

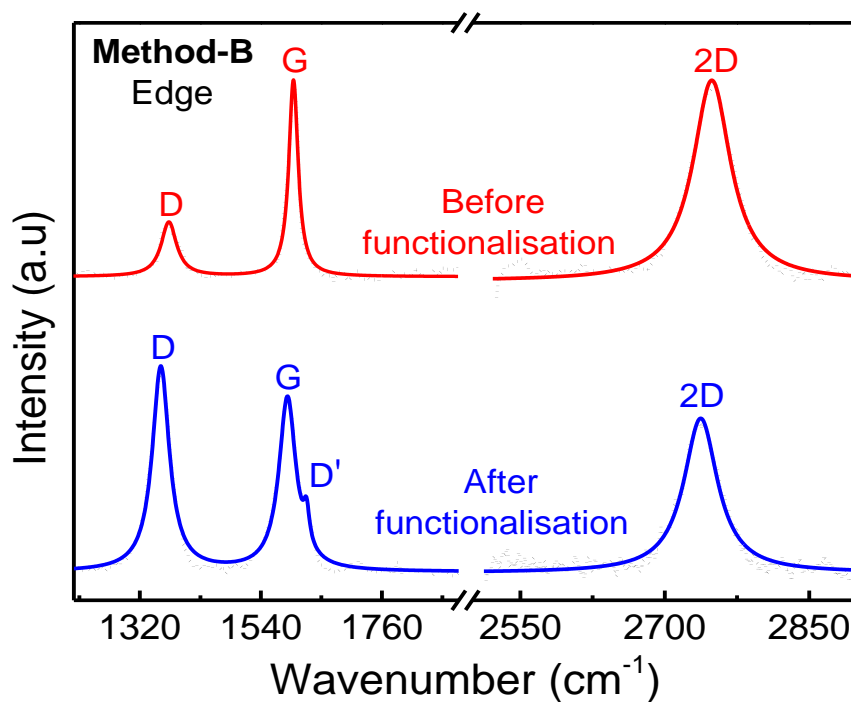


Figure 6.5: Raman spectra of method-B sample taken at patterned graphene edge before and after functionalisation, showing significant doping. Solid lines indicate Lorentzian fittings.

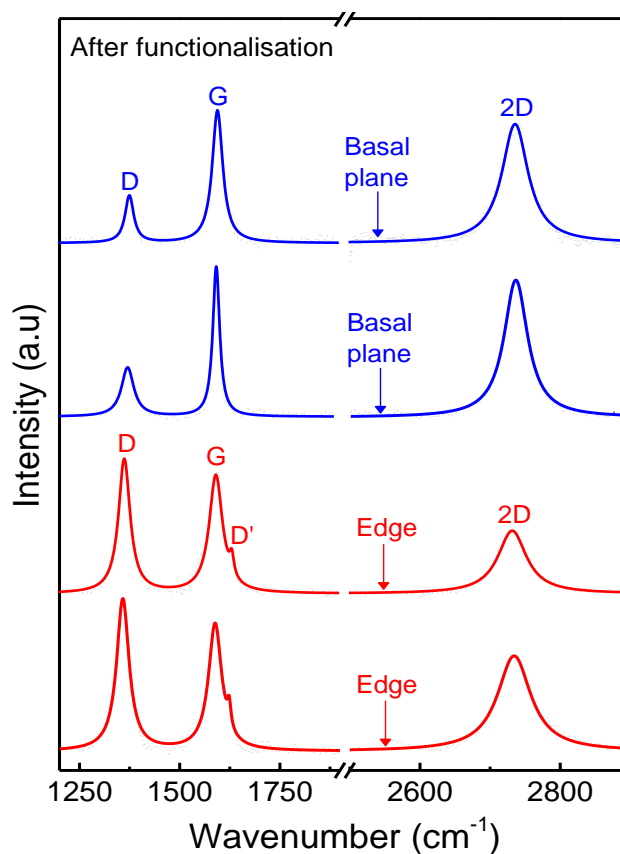


Figure 6.6: Raman spectra of method-B sample showing the magnitude of doping at basal plane areas and at patterned graphene edge sites. Solid lines indicate Lorentzian fittings.

Table 6.3: Raman data of method-B functionalised sample taken from different areas of the sample.

Probed area	ω_D (cm^{-1})	ω_G (cm^{-1})	ω_{2D} (cm^{-1})	FWHM D(cm^{-1})	FWHM G(cm^{-1})	FWHM 2D(cm^{-1})	I_D/I_G	I_{2D}/I_G
Basal plane (unfunctionalised)	N/A	1597.5	2738.4	N/A	34.7	47.2	N/A	0.97
Basal plane 1	1372.6	1597.7	2737.7	31.0	20.9	48.6	0.24	0.84
Basal plane 2	1376.5	1596.7	2737.6	26.1	28.7	45.5	0.35	0.89
Basal plane 3	1374.5	1597.9	2737.8	38.1	21.0	41.3	0.32	0.85
Edge site (unfunctionalised)	1373.7	1600.2	2739.5	34.0	20.3	50.0	0.27	1.16
Edge site 1	1358.0	1588.3	2733.2	37.4	37.4	44.2	1.18	0.62
Edge site 2	1362.3	1589.7	2732.4	34.8	40.3	51.9	1.14	0.53
Edge site 3	1358.0	1588.3	2734.3	37.4	39.8	57.6	1.19	0.65

6.3.3 Hall measurements

In addition to chemical and structural analysis, Hall measurements were also performed to verify the doping behaviour of these functionalised graphene samples and also to measure their transport properties. Table 6.4 displays the average sheet carrier density (n), Hall mobility (μ_H) and sheet resistivity (ρ_{sh}) extracted from thirty van-der Pauw devices fabricated on each of the unfunctionalised, method-A and method-B functionalised graphene samples. The unfunctionalised graphene showed intrinsic n-type character with an average sheet carrier density of $8.1 \times 10^{12} \text{ cm}^{-2}$, typical for epitaxial graphene films grown on Si-face of SiC. The Hall mobility and sheet resistivity was measured as $802 \text{ cm}^2 \text{ V}^{-1} \text{ s}^{-1}$ and $8.55 \times 10^{-5} \text{ } \Omega\text{-cm}$ respectively.

Table 6.4: Room temperature Hall measurements of unfunctionalised, method-A and method-B functionalised graphene samples.

Sample type	n (cm^{-2})	μ_H ($\text{cm}^2 \text{ V}^{-1} \text{ s}^{-1}$)	ρ_{sh} ($\Omega\text{-cm}$)	E_F (eV)
Unfunctionalised	-7×10^{12}	720	1.81×10^{-4}	-0.365
Method-A	$+5.41 \times 10^{13}$	15	8.31×10^{-4}	+0.960
Method-B	-5.6×10^{11}	1150	3.45×10^{-4}	-0.096

After functionalisation, the electronic properties of method-A and method-B samples changed considerably with significant differences between them. For example, method-A sample showed p-type conduction with a hole carrier density of $5.41 \times 10^{13} \text{ cm}^{-2}$, whilst, method-B sample still showed n-type behaviour albeit with more than one order of magnitude reduction in electron carrier density from $8.1 \times 10^{12} \text{ cm}^{-2}$ to $5.6 \times 10^{11} \text{ cm}^{-2}$. This change in electronic properties of graphene is expected due to the high electronegativity of oxygen (3.55), in comparison to carbon (2.44), which results in significant charge transfer from carbon atoms in the graphene film to chemisorbed oxygen atoms. However, the variation in carrier type and density observed here indicates that the magnitude of charge transfer from graphene to oxygen is very different for blanket (method-A) and patterned graphene (method-B) films. It is known that oxygen forms multiple covalent bonds such as C-OH, C-O-C, C=O and O-C=O when chemisorbed on to the graphene surface. However, it is not currently very well understood that which of these functional groups has maximum contribution to the charge transfer process. Nevertheless, the bonding mechanism of O-

functional groups suggests epoxides to have major impact on the doping of the graphene film. Since the epoxy oxygen atoms are bonded to two carbon atoms, in comparison to carbonyl, hydroxyl or carboxyl species, which are all bound to just one carbon atom, the magnitude of charge carrier extraction from the graphene film will be twice as much higher in the presence of epoxy species than otherwise. Using DFT calculations, Topsakal *et al* [253] recently estimated a charge transfer of 0.79 electrons from graphene to oxygen and identified that this charge was mainly transferred from two carbon atoms attached to oxygen in epoxy configuration, while other functional groups accounted for minor contribution. Based on these calculations, the observed p-type doping in the method-A sample can be attributed to the significant presence of epoxides on the graphene surface, which results in a strong charge transfer from graphene to adsorbed epoxy species, thereby shifting the graphene Fermi level (E_F) below the Dirac point. In contrast, the method-B sample with negligible concentration of epoxy groups resulted in moderate charge transfer, moving E_F only closer to the Dirac point, thereby retaining the intrinsic n-type character of epitaxial graphene. Here, the shift in E_F with the charge carrier density can be estimated using the expression [156]:

$$E_F = \hbar v_F (\sqrt{\pi n})$$

where $\hbar = 6.582 \times 10^{-16}$ eV.s, $v_F = 1.1 \times 10^6$ ms⁻¹ is the Fermi velocity. For unfunctionalised graphene, E_F was found to be located at 365 meV above the Dirac point, indicative of n-type doping. After functionalising graphene using method-A approach, E_F shifts from 0.365 eV to 0.943 eV below the Dirac point, making the graphene p-type. In contrast, for the

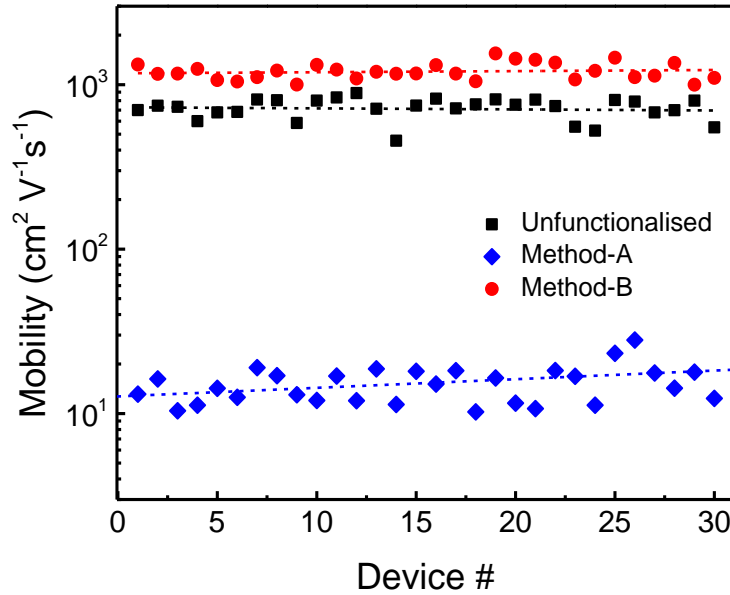


Figure 6.7: Change in carrier mobility of unfunctionalised graphene, method-A and method-B functionalised graphene samples. Dashed lines indicate guide to the eye only.

sample functionalised using method-B approach, the intrinsic n-type doping was still observed with E_F reducing from 0.365 eV to 0.096 eV just above the Dirac point.

In addition to the change in charge carrier type and density, functionalisation also had strong impact on the mobility and resistivity of these samples. Figure 6.7 shows the change in mobility of unfunctionalised and functionalised samples based on thirty measured van-der-Pauw devices. As can be seen, the Hall mobility of method-A sample decreased significantly from $\sim 802 \text{ cm}^2 \text{ V}^{-1} \text{ s}^{-1}$ to $\sim 15 \text{ cm}^2 \text{ V}^{-1} \text{ s}^{-1}$ after functionalisation, which is attributed to the increased charge carrier scattering due to the presence of O-functional groups on the basal planes of the graphene channel. In contrast, the mobility of method-B sample increased from $\sim 802 \text{ cm}^2 \text{ V}^{-1} \text{ s}^{-1}$ to as high as $\sim 1150 \text{ cm}^2 \text{ V}^{-1} \text{ s}^{-1}$, due to low carrier density and the presence of O-functional groups predominantly at the edge sites of the graphene channel, which results in reduced carrier scattering and therefore increase in mobility. In order to verify this behaviour, a plot of mobility as a function of carrier density was analysed. As shown in Figure 6.8, a strong correlation was observed, where, the Hall mobility decreased with the increasing carrier density irrespective of carrier type. This correlation is a signature of charge impurity scattering reported in graphene previously [287], where a charge carrier is scattered by Coulomb potential created by the adsorbed dopant.

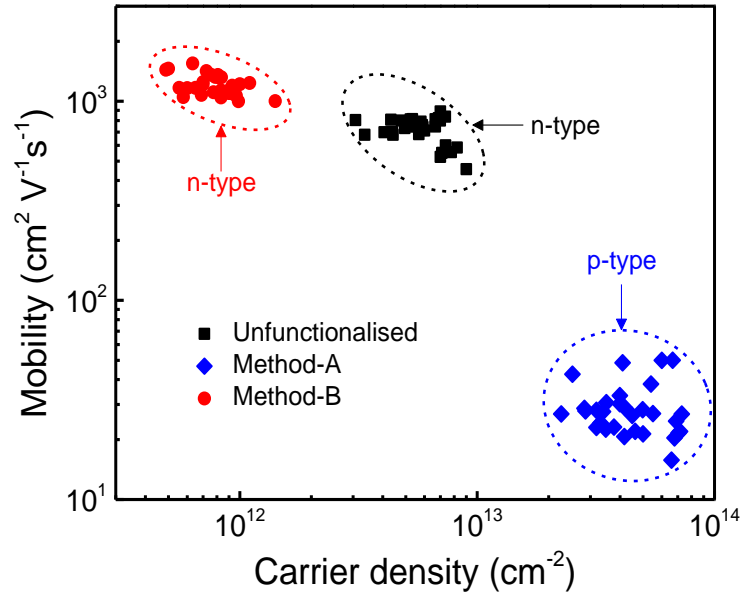


Figure 6.8: Dependence of carrier mobility on the sheet carrier density of unfunctionalised and functionalised graphene samples.

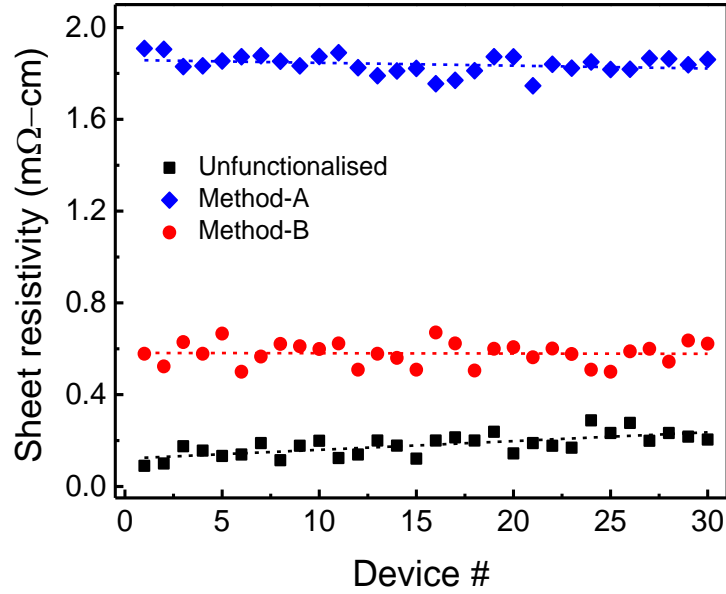


Figure 6.9: Change in sheet resistivity of graphene before functionalisation and after functionalising using method-A and method-B approaches. Dashed lines indicate guide to the eye only.

As shown in Figure 6.9, the charge impurity scattering also resulted in a 50% increase in sheet resistivity for method-A sample from $8.56 \times 10^{-5} \text{ } \Omega\text{-cm}$ to $1.81 \times 10^{-4} \text{ } \Omega\text{-cm}$ after functionalisation, whereas, method-B sample showed only 4% increase relative to unfunctionalised graphene. These results show that functionalising graphene before device fabrication (i.e method-A) results in significant degradation of intrinsic electronic properties of graphene, in comparison to functionalising after fabrication (method-B).

6.3.4 TLM measurements

The two-terminal measurements were performed to identify the differences in electrical properties between the two functionalisation methods. Figure 6.10(a) shows the linear I-V characteristics of method-A and method-B samples, indicating the ohmic nature of metal contacts. However, significant differences in the device electrical resistance were observed between these samples. The average two terminal resistance of forty devices measured on the sample functionalised using method-A was $150 \pm 9 \text{ k}\Omega$, whereas the average resistance measured (thirty eight devices) on the sample functionalised using method-B was recorded as $11 \pm 4 \text{ k}\Omega$. In order to understand these differences, TLM measurements were performed to extract the contact resistance, R_C and the sheet resistance, R_{sh} of these functionalised samples. Figure 6.10(b) shows the TLM plot of total resistance, R_T against the varying channel length, L_{ch} for both functionalised samples. The slope of this linear fit gives channel

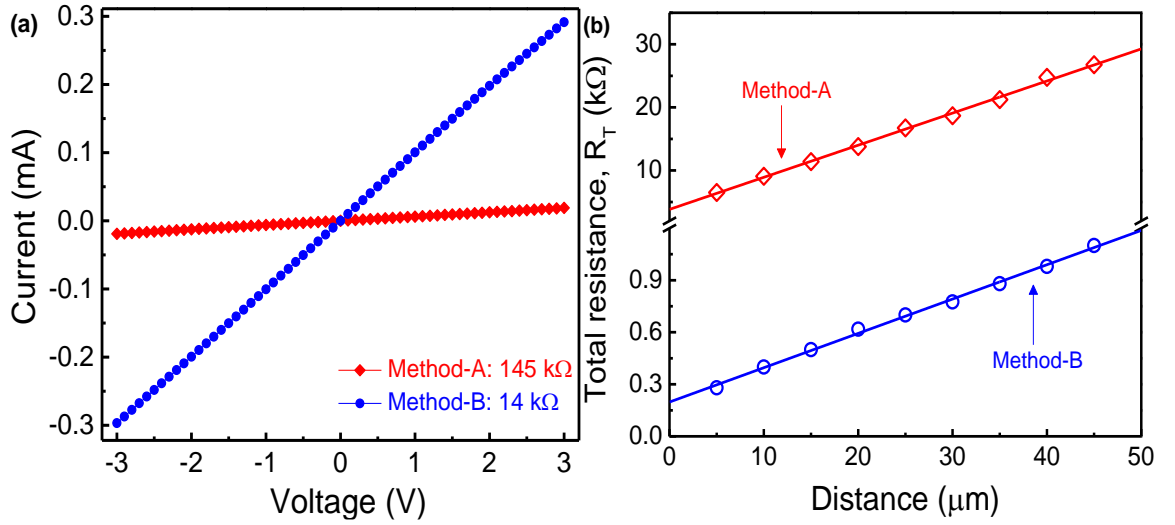


Figure 6.10: a) I-V characteristics of method-A and method-B functionalised sample b) TLM plot corresponding method-A and method-B sample. Solid lines in (b) indicates TLM linear fits.

width normalised value of graphene R_{sh} . The contact area independent term specific contact resistivity, ρ_c can be determined from the equation, $\rho_c = R_{sh}L_T^2$, where L_T is the transfer length. As shown in Figure 6.10(b), method-B sample exhibited substantially lower magnitude of resistance with the increasing TLM con-tact spacing in comparison to the method-A sample. The ohmic contact parameters of R_{sh} , R_C , ρ_C , and L_T extracted from four different sets of TLM structures on each sample are shown in Table 6.5.

The R_{sh} of for method-A sample was calculated as 76.33 k Ω /sq, whilst for the method-B sample it was recorded as 2.97 k Ω /sq, consistent with the differences highlighted by Hall measurements. The average R_C and ρ_C values for the method-A sample was calculated as 1.9 ± 0.3 k Ω , and 1×10^{-2} $\Omega\text{-cm}^2$ respectively, while it was recorded as 103 ± 14 Ω and 7×10^{-4} $\Omega\text{-cm}^2$ for the method-B sample. Such a large disparity in contact resistivity values with over an order of magnitude variation is attributed to the differences in bonding mechanism at the graphene-metal contact interface, where, the oxygen atoms are mainly present either underneath the metal contacts (method-A case) or situated at the contact edges (method-B case). It is well-known that the addition of O-functional groups greatly changes the surface wettability of graphene, causing it to become less hydrophobic and more hydrophilic. As a result, the surface energy of O-functionalised graphene also increases, leading to an enhanced adhesion of metal contacts to the functionalised graphene surface. This is mainly due to the electronic interaction of oxygen atoms with the graphene and the metal, where one electron from the oxygen $2p$ orbital is shared with the p_z orbital

Table 6.5: Electrical characteristics of metal-oxygen functionalised graphene interfaces extracted from TLM measurements

Functionalisation Method	R_c ($k\Omega \cdot \mu m$)	R_{sh} ($k\Omega/sq$)
Method-A	286.5	76.33
Method-B	15.4	2.97

of the carbon atom in graphene, leaving an additional electron to bond with the $3d$ orbital of a metal atom. Due to this strong interaction, significant bond strength exists between Ti and the graphene. Using XPS and theoretical calculations Felten *et al.* [288] showed the preference of Ti to form Ti–O bonds first, followed by Ti–C and finally Ti–Ti. This is because the presence of oxygen acts as strong trapping sites for Ti, where two oxygen atoms strongly bind to single Ti atom, resulting in significant weakening of Ti–C interaction. In the case of method-A, as the Ti metal film was deposited on top of oxygen functionalised graphene, the reactive nature of Ti atoms strongly interacts with the reservoir of oxygen atoms present on the graphene surface to form Ti–O bonds. However, the insulating nature of Ti–O bonds acts as an additional barrier for the efficient transmission of charge carriers across the interface, thereby leading to a high interfacial contact resistance as observed here.

In contrast, for the method-B sample, as metal films were directly deposited on top of the unfunctionalised graphene surface, Ti atoms chemisorb to the graphene with a high binding energy of 2.64 eV. It was shown that the high diffusion energy barrier (0.75 eV) of Ti atoms results in a continuous film formation on the graphene sheet [188]. As this sample was subjected to thermal annealing (at 400°C) prior to O-functionalisation, a strong chemical interaction between Ti $3d$ and graphene p_z orbitals takes place, leading to a formation of strong Ti–C bonds at the interface. Here, the electron donating behaviour of Ti dopes the graphene underneath the metal contacts n-type, shifting the E_F further away from the Dirac point. This observation is consistent with previous studies [288], where a high charge transfer occurs when Ti was bonded directly to carbon than in the presence of oxygen. For example, a strong net charge transfer from Ti to graphene was observed, resulting in a Ti charge of +0.98 e. This charge increased to +1.36 e upon addition of oxygen. However, the negative charge on oxygen atoms (-0.83 e per O) resulted in a much weaker net charge transfer in the opposite direction from graphene to Ti–O bonds of 0.29 e. Hence, the presence of oxygen at the Ti/graphene interface significantly reduces the charge transfer process. For method-B sample, as the graphene underneath the metal contacts is shielded from the exposure to

Ar/O₂ plasma, O-functional groups are mainly restricted to the edge of contacts, thereby increasing the transmission probability of charge carriers across the Ti/graphene contact interface. This enhanced transmission together with the negligible presence of Ti-O at the interface results in low ρ_c , in comparison to the method-A sample.

6.3.5 Low-frequency noise measurements

Low-frequency noise measurements were performed to gain further understanding on the observed variations between the two functionalisation methods. Considering that the change in noise is larger than that of the resistance, the noise spectral density will be more sensitive to defects than the resistance measurement [133]. Analysing the noise behaviour and magnitude is critical because, for applications such as chemical sensing, signal-to-noise ratio is the fundamental factor that determines the resolution and the minimum detection limit of a sensor [134]. In addition, noise measurements can also give great insights into defects and scattering mechanisms in graphene devices. Since functionalisation changes the intrinsic noise level of graphene due to the covalently bonded functional groups, this change in the noise magnitude can be used as a key parameter in determining the performance and the quality of a material or a device. In this study, the noise behaviour of graphene will be focused at lower frequencies (less than 1000 Hz), where the shot noise and Johnson-Nyquist noise are negligible and $1/f$ noise is the only dominant noise source.

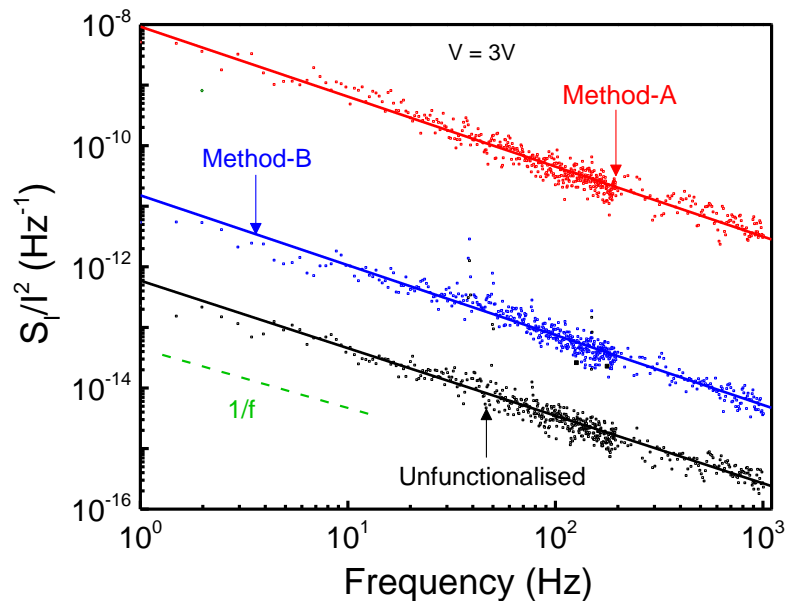


Figure 6.11: Low-frequency noise characteristics of unfunctionalised graphene, method-A and method-B functionalised graphene samples. Solid lines indicate logarithmic curve fittings.

Figure 6.11 shows the normalised current noise spectral density (S_I/I^2) of samples functionalised using methods A and B as a function of frequency. The spectrum of an unfunctionalised sample is also shown for reference. The normalised noise density on both functionalised samples varied with frequency, exhibiting clear $1/f$ dependence (dashed lines) similar to the unfunctionalised graphene. However, a large variation in noise magnitudes can be clearly seen between methods A and B, consistent with the differences highlighted by XPS, Raman and electrical measurements shown above. The mechanism behind the observed noise variations cannot be precisely determined, owing to the large prediction variability of available theories. The most commonly used and conventionally accepted theories to describe the $1/f$ noise behaviour are McWhorter and Hooge models [289, 290]. The primary difference between these two models is in describing the origin of noise sources. McWhorter model deals with surface or interface noise sources and considers the noise mechanism is due to the random trapping or de-trapping of charge carriers near the channel and the oxide interface (carrier number fluctuations, Δn). This model is typically used to describe the noise mechanism in metal-oxide semiconductor field-effect transistors (MOSFETs). In contrast, Hooge's model, which is generally used for describing the noise behaviour in metal films and semiconductors, deals with the distribution of noise sources in the bulk or volume of the material and argues that the noise mechanism is related to the carrier scattering by lattice vibrations (mobility fluctuations, $\Delta\mu$). However, both these models cannot be directly used in explaining the noise fluctuations observed here. For example, almost all previous noise studies on graphene have oxide layers serving as either top or bottom gate dielectrics [291, 292]. Reports based on McWhorter model assume that these oxide layers consists of finite density of traps or impurities and that the carriers in graphene channel tunnel into traps located in these oxide layers, become captivated and tunnel back into the graphene film, causing fluctuations in the current flow. Such fluctuations were assumed to create $1/f$ -like noise, which is a function of gate bias through a shift in the Fermi level of the graphene. However, as shown in the Figure 6.11, even without oxide layers (neither on top nor at bottom of the graphene channel), a clear $1/f$ -like dependency was observed for all devices investigated, implying that the trap sites in oxides does not necessarily act as noise sources and that McWhorter model's argument of trapping or de-trapping of charge carriers at the channel-oxide interface does not hold true for the devices investigated here.

Similarly, as Hooge's model is based on the bulk or volume of the material, it is not applicable to graphene films studied here. Recently, Liu *et al.* [293] demonstrated that $1/f$ noise in graphene is a surface phenomenon for the film thicknesses ranging from single layer to few-layers (less than 7 monolayers) and only becomes dominated by the volume when the thickness exceeds 7 atomic layers. Since the thickness of graphene used here is single layer (or bilayer at step edges), Hooge's model cannot be directly used to describe the noise mechanism in these graphene devices. Nevertheless, in order to analyse the performance of graphene based devices, previous studies have used the following expression [292] to quantitatively describe $1/f$ noise magnitude and the quality of graphene

$$\frac{S_I}{I^2} = \frac{A_N}{f^\lambda}$$

where f is the frequency, λ is the frequency scaling exponent with a value ≈ 1 and A_N is the $1/f$ noise amplitude. The amplitude A_N is the measure of $1/f$ noise level that generally reflects the quality of a material or a device and depends on the parameters such as the size of the device channel area, structural and chemical condition of the material and the fabrication methods employed. Higher the value of A_N , lower is the quality of a material or device. Figure 6.12(a) shows the area normalised ($W \times L$) $1/f$ noise amplitude extracted from the devices processed using methods A and B, along with the unfunctionalised graphene for reference. As can be seen in the data, unfunctionalised graphene exhibited extremely low noise magnitude (8.1×10^{-10}), which is an order of magnitude lower than previously reported noise amplitude values on exfoliated graphene flakes, demonstrating the superior crystal quality of epitaxial graphene films, in line with the Raman measurements shown above. Upon exposure to O-plasma, an increase in A_N was observed for both functionalisation methods albeit with a large variation in the magnitude between them. For example, at $f=10$ Hz, devices processed using method-A showed four orders of magnitude increase in noise from 5.6×10^{-10} to 5.8×10^{-6} , whilst less than an order of magnitude rise in A_N was recorded (1.2×10^{-9}) for the devices fabricated using method-B approach. This indicates that functionalisation of patterned graphene (i.e after device fabrication) yields much lower noise characteristics in comparison to functionalisation of blanket graphene films. Such a large variation in A_N is attributed to the differences in number of scattering sites present in the graphene channel. For example, in the method-A sample, the presence of high concentration of O-functional groups on the basal planes of graphene along with the high carrier density leads to significant increase in the carrier scattering rate in the conduction channel, leading to overall

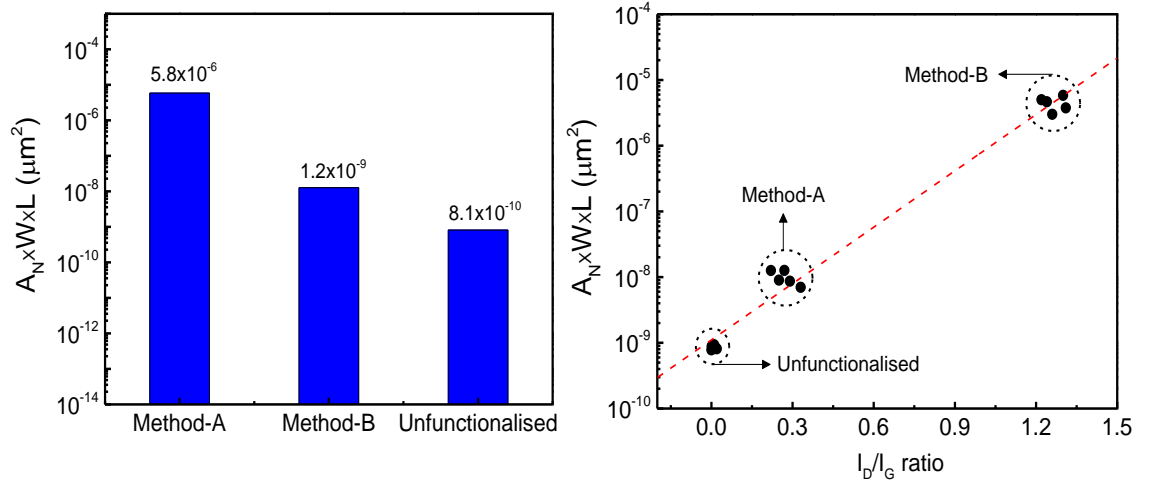


Figure 6.12: a) Normalised noise amplitude of unfunctionalised, method-A and method-B functionalised samples b) Correlation between noise amplitude and the I_D/I_G ratio.

enhancement of the $1/f$ noise magnitude. In contrast, for the method-B sample, the presence of O-functional groups on the edge sites of graphene channel together with low carrier density, results in reduced scattering probability and therefore reduces the noise amplitude. The differences in noise amplitude observed here is consistent with the structural changes highlighted by the Raman spectroscopy, in which, a strong correlation between A_N and I_D/I_G was observed as shown in Figure 6.12(b).

6.3.5.1 Role of metal contacts on $1/f$ noise behaviour

In order to identify the role of metal contacts in the observed $1/f$ noise behaviour, low-frequency noise measurements were performed on TLM structures with varying channel lengths. Here, the channel width is fixed ($W=100\ \mu\text{m}$) and only the channel length is varied from $L=5\ \mu\text{m}$ to $40\ \mu\text{m}$. If noise originates from the graphene channel (and not from the metal contacts), then A_N should scale with the graphene channel area. Previous studies on CNT films [27] have shown that A_N depends both on device dimensions and the resistivity of the film due to the percolative nature of the transport and any deviation in this behaviour was attributed to the influence of metal contacts on the $1/f$ noise characteristics. Figure 6.13 shows the measured values of noise amplitude normalised to resistance (A_N/R) versus TLM channel length (L). As can be seen, A_N/R showed strong dependence on the device channel length, indicating negligible influence of contacts on the noise characteristics. The reduction in noise amplitude with the channel length is consistent with the Hooge's law, where $1/f$ noise amplitude varies inversely with the number of carriers (N) in the device. Since $R \propto L$ and $N \propto L$, A_N/R is expected to scale as $A_N/R \propto L^{-2}$. The dashed line in Figure 6.13(a) is the

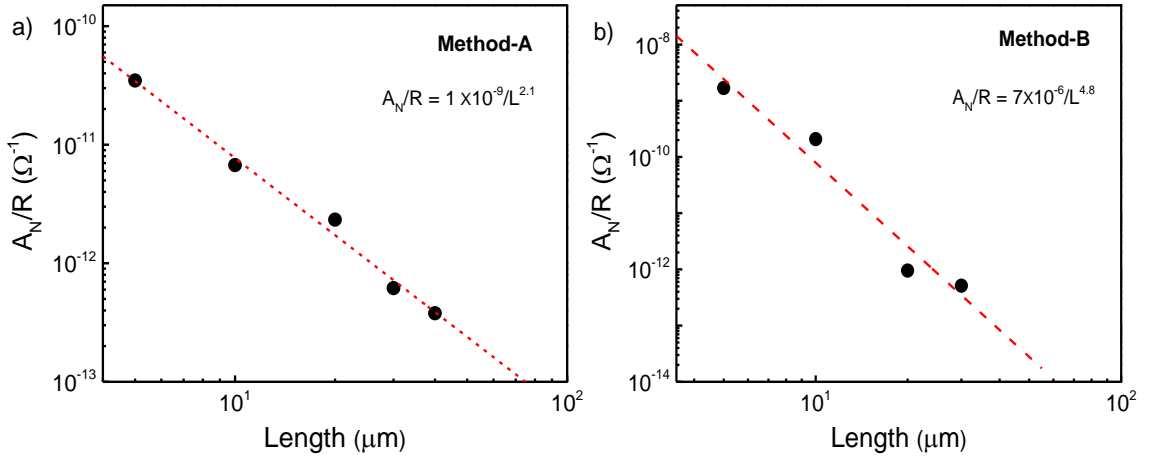


Figure 6.13: Log scale plot of the noise amplitude normalised by resistance as a function of device channel length for method-A and method-B samples. Dashed lines indicate power-law fits.

power-law fit to the experimental data, yielding $A_N/R \propto L^{-\beta}$ with a critical exponent, $\beta=2.0$, in excellent agreement with the expected $A_N/R \propto L^{-2}$ dependence. However, in the case of method-B, although noise amplitude scales down with the increasing channel length, the critical exponent extracted from the power law fit was calculated as 4.8, which deviates from the expected $1/L^2$ behaviour. Such deviation was observed previously in CNTs and was suggested that the critical exponent for the device length dependence of A_N/R is not a universal invariant, but rather depends strongly on parameters such as film uniformity and thickness [294]. Nevertheless, the epitaxial graphene synthesis process used here was designed to produce nominally one monolayer films on the terraces of the samples and the synthesis process has been demonstrated to be uniform and run-to-run reproducible. Hence, synthesis process cannot be the reason for this behaviour and there should be other competing mechanisms responsible.

To further elucidate the $1/f$ noise behaviour in these functionalised graphene samples, noise amplitude normalised to the device channel area ($A_N \times W \times L$) was plotted as a function of the graphene channel resistance. As can be seen from the Figure 6.14, a strong inverse correlation was observed for both methods, where the noise amplitude decreased with the increasing graphene channel resistance. Such behaviour is strikingly different from the behaviour reported for O-plasma functionalised multilayer exfoliated graphene flakes by Kim *et al* [30] where the noise amplitude was shown to increase with the increasing resistance. Similarly, Lin *et al* [295] and Liu *et al* [32] also reported increase in noise amplitude with resistance on unfunctionalised single layer and multilayer exfoliated graphene flakes respectively. The distinct inverse relationship between A_N and R observed in this study is

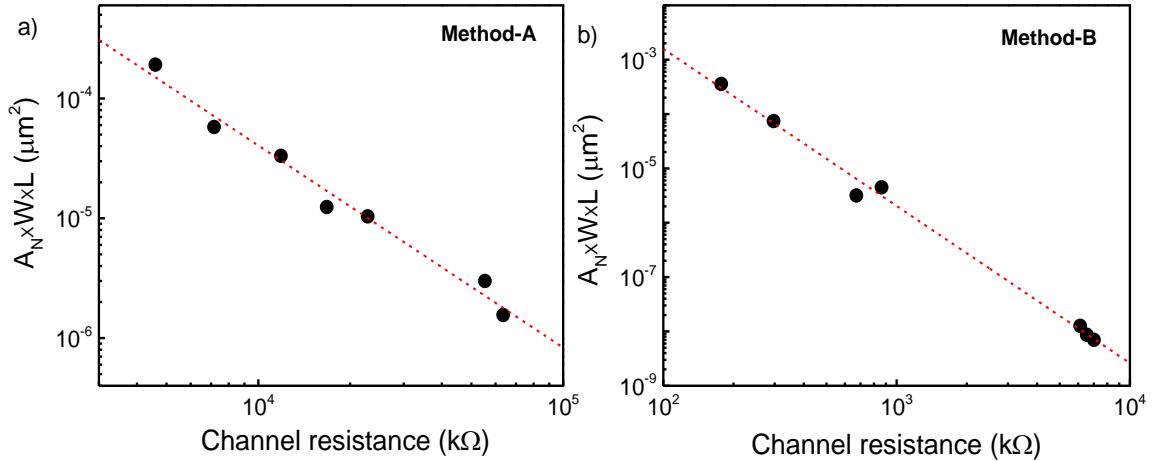


Figure 6.14: Log scale plot of the noise amplitude normalised to device channel area as a function of device channel resistance for method-A and method-B samples. Dashed lines are guide to the eye only.

also different from that of carbon nanotubes [294] and other semiconductors [296]. Such behaviour could be attributed to the unique nature of epitaxial graphene on SiC, where it was shown that the resistance increases at the junctions of monolayer (step terraces) and bi-layer (step edges) graphene regions, which in turn could affect the local noise properties of at these junctions [297]. Nonetheless, Raman, Hall, TLM and low-frequency noise characterisation demonstrate that functionalising graphene after device fabrication (i.e method-B) yields superior electrical properties with high mobility, low contact resistance, low sheet resistance and substantially lower noise characteristics without significantly degrading the structural characteristics of the graphene.

6.4 Summary

In summary, the effect of O-functionalisation on the electrical characteristics of metal-graphene interfaces has been investigated. Two functionalisation approaches were investigated here, where in, for the first approach, O-functionalisation was performed on as-grown blanket graphene film followed by device fabrication (method-A) and for the second approach, device fabrication was performed first followed by O-functionalisation (method-B). It was found that the surface chemistry of method-A processed graphene sample is very different from that of method-B fabricated one. Raman spectroscopy showed that the majority of O-functional groups on method-B functionalised sample were situated predominantly at the edge sites, in comparison their presence on the basal planes for method-

A functionalised sample. Hall, TLM and low-frequency noise characterisation demonstrate that functionalising graphene after device fabrication (i.e method-B) yields superior electrical properties with high mobility, low contact resistance, low sheet resistance and substantially lower noise characteristics without significantly degrading the structural characteristics of the graphene film.

Chapter 7

Epitaxial graphene chemiresistor sensors for polar chemical vapour detection

7.1 Introduction

Chemiresistors or chemically sensitive resistors are very attractive for sensing applications due to their simple device structure, potential for miniaturisation and low cost of manufacture [298]. Chemiresistors exhibit a change in electrical resistance (increase or decrease) upon exposure to analyte molecules. Increase or decrease in resistance depends on the nature of the sensor material (n-type or p-type) and the analyte. Several materials such as semiconducting metal oxides [122], conductive polymers [125], carbon black-polymer composites [124], nanowires [128] and carbon nanotubes [299, 300] have been utilised as chemiresistors, showing their surface sensitivity to different chemical species. However, the use of metal oxide based sensors in many applications is limited by their high power consumption, high operating temperatures ($> 200^{\circ}\text{C}$), and poor selectivity issues, while the poor environmental stability associated with conjugated polymers, and the high intrinsic noise of CNTs along with the complex growth procedures associated with the CNT films synthesis, limits their use in practical applications.

Graphene possesses exemplary physicochemical properties such as high specific surface area, high carrier mobility, and extremely low electrical noise characteristics, making it an

ideal material for sensing applications [301]. Chemiresistor vapour sensors based on graphene offers significant advantages over aforementioned materials, in terms of sensitivity, stability, low-power consumption, ease of synthesis and fabrication and room temperature operability. Given its two-dimensional structure, the electronic properties of graphene show a strong dependence towards surface adsorbates, which can alter the local charge carrier concentration leading to p-type or n-type doping of the film. There have been many studies in the past showing the sensing capability of different types of graphene to a variety of chemical species. For example, graphene prepared by mechanical exfoliation was shown to be highly sensitive to gases such as CO₂, NH₃, CO, NO₂, ethanol, and H₂O [28, 93], while pristine graphene grown by the CVD on Cu has demonstrated detection of O₂, SO₂, CO₂ and N₂O at parts-per-million or billion concentrations [302-305]. Furthermore, the sensing performance of rGO has also been widely studied for detecting chemically aggressive vapours such as Cl₂, 2,4-dinitrotoluene and trinitrotoluene [136, 264].

Graphene grown on SiC has been demonstrated as a viable route for practical applications because of the ability to produce high-quality wafer-size graphene films directly on semi-insulating SiC substrates [71] along with its compatibility with standard Si fabrication techniques. However, the chemical sensitivity of epitaxial graphene on SiC has been much less widely explored. The majority of sensing studies on epitaxial graphene were predominantly focused on inorganic gases [28] and pH-determination [306], whilst the detection of polar chemical vapours has been overlooked.

Polar chemicals have large intrinsic electric dipole moments and high dielectric constants due to the greater electronegativity differences between atoms of a molecule [307]. They can be classified into two categories based on their ability to form hydrogen bonding: polar protic and polar aprotic. Polar protic chemicals contain dissociable hydrogen atom attached to an electronegative oxygen or nitrogen (O-H or N-H), while these bonds are absent in polar aprotic chemicals. The real time detection and identification of these polar chemical vapours are critically important for environmental monitoring, homeland security and medical applications. Widely used in industries and chemical processing plants, many polar chemicals can be toxic or carcinogenic even at relatively low concentrations. Acute short-term exposure to highly polar chemicals such as dimethylformamide and acetic anhydride can cause severe damage to the human respiratory system and liver, while prolonged exposure to dimethylacetamide attacks the central nervous system in humans [307]. Similarly, high concentrations of hydrogen peroxide vapours are not only toxic to human health but are also used as an active agent in explosive devices [307]. Therefore, developing simple and reliable

sensors utilising the exceptional material properties of graphene is highly desirable for efficient monitoring of chemical vapours in the environment.

In addition, neither the sensing mechanism of graphene to polar protic and polar aprotic chemicals, nor the effects of their dipole moments on the sensor response have been explored to-date. As a result, the nature of interaction of these polar molecules with graphene and their impact on the electrical characteristics is currently unknown.

In this chapter, the chemical sensing behaviour of epitaxial graphene chemiresistors to a wide range of polar chemical vapours in the ambient atmosphere will be discussed. Specifically, the effect of chemical polarity and the significance of dipole moment on the chemical sensing characteristics of epitaxial graphene were studied using two-probe, Hall and low-frequency noise measurements. Section 7.3 of this chapter presents the chemical sensing responses of unfunctionalised epitaxial graphene, while section 7.4 details about the enhancement in sensing characteristics of graphene functionalised with oxygen species.

7.2 Experimental details

The epitaxial graphene films were grown on five different $8 \times 8 \text{ mm}^2$ semi-insulating 6H-SiC (0001) substrates by sublimation of Si at 1540°C in argon ambient. The sample preparation procedure and the graphene growth conditions are similar to those reported in chapter 3. For the fabrication of graphene chemiresistor sensors, two terminal structures with $40 \times 20 \mu\text{m}^2$ channel area (Figure 7.1, left) and Van-der-Pauw structures consisting of $40 \times 40 \mu\text{m}^2$ channel cross (Figure 7.1, right) were patterned on all five samples using conventional photolithographic techniques as described in chapter 3. Ti/Au (10 nm/100 nm) metal films were then deposited using e-beam evaporation followed by lift-off in warm acetone (45°C).

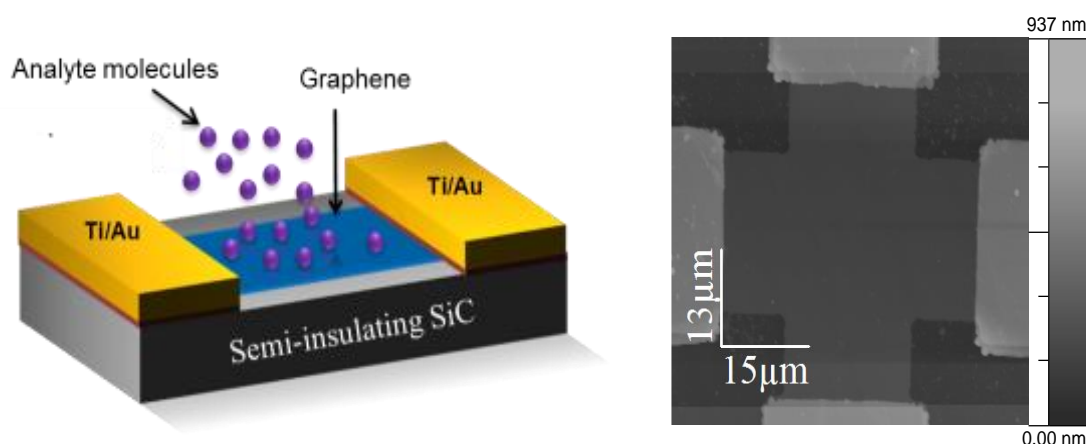


Figure 7.1: (Left) schematic cross section of a two-terminal chemiresistor device and (Right) AFM topographic images of a Van der Pauw device test structure.

After metallisation, samples were annealed in N_2/H_2 atmosphere at $400^\circ C$ for 60 min to minimise resist contamination and its possible impact on the electrical and sensing properties of graphene chemiresistor [36].

In order to evaluate the impact of functionalisation on the sensor response, two of these fabricated samples were functionalised with oxygen using e-beam generated plasmas at a total pressure of 75 mTorr. Note, apart from this additional functionalisation step, similar device processing procedures and annealing conditions were followed for fair comparison between the responses of unfunctionalised epitaxial graphene (UFEG) and oxygen functionalised epitaxial graphene (OFEG) chemiresistor sensors. The surface morphology and the chemical nature of fabricated graphene chemiresistors were analysed by AFM and XPS, respectively. Structural changes in graphene were observed by Raman spectroscopy with an excitation wavelength of 514.5 nm and laser spot size of $0.7 \mu m$.

For sensing experiments, the UFEG and OFEG chemiresistor devices were exposed to four *polar protic* chemicals: ethylene glycol (EG), hydrogen peroxide (H_2O_2), water (H_2O) and methanol (MeOH); and six polar aprotic chemicals: *n*-methyl-2-pyrrolidone (NMP), dimethylsulphoxide (DMSO), benzaldehyde (BZ), *n,n*-dimethylformamide (DMF), *n,n*-dimethylacetamide (DMAC), and acetic anhydride (AA). The graphene chemiresistor devices were exposed to a continuous flow of these chemical vapours generated at concentrations of less than 1% of the saturated vapour pressure, while simultaneously measuring the relative change in electrical resistance of the sensor during the exposure. To ensure reproducibility within sensing trials, experiments were repeated five times on twenty-eight UFEG sensor devices across three samples and thirty-one OFEG devices across two samples to obtain an averaged response for each analyte tested.

The low-frequency noise measurements were performed in a two-terminal configuration using a fast Fourier transform analyser (SR760) and a low noise current amplifier (SR560) between 1 Hz and 100 kHz and averaged over 15 times to minimise the noise magnitude span. The noise measurements were repeated nine times for each chemical tested with a time interval of approximately 20 min. All sensing measurements (resistance and noise) were performed under ambient conditions at $20^\circ C$ and a relative humidity of 40%-50%, using a Keithley 4200 semiconductor parameter analyser and a shielded Cascade Microtech probe station supported on an anti-vibration table.

7.3 Results and Discussion

Figure 7.2(a) depicts the AFM topographic image of a fabricated UFEG chemiresistor sensor after N_2/H_2 treatment at $400^\circ C$, showing no visible photoresist contamination on the surface. The RMS surface roughness was calculated as 2.31 nm. The high-resolution XPS C1s spectra (Figure 7.2(b)) showed four components at 283.6 eV, 284.5 eV, 285.2 eV and 286.3 eV, corresponding to Si-C, C-C (sp^3), interfacial layer and C-OH bonding respectively. No additional peaks representing carbonyl (287 eV) or carboxylate (288 eV) groups associated with the resist residues were present, further indicating relatively clean graphene surfaces after the N_2/H_2 treatment.

A typical Raman spectrum of epitaxial graphene with a G (1599 cm^{-1}) and a 2D peak (2725 cm^{-1}) is shown in Figure 7.3. The full width at half maximum (FWHM) of the 2D-peak is 34 cm^{-1} , indicating the average thickness of graphene film for the probed area is a single layer, which was further confirmed by peak fitting with a single Lorentzian function as shown in Figure 7.3. No D-peak was observed across several probed areas on all samples, demonstrating the high structural quality of graphene films.

Figure 7.4 shows the linear I-V characteristics of a chemiresistor sensor, where a 90% decrease in the device electrical resistance was observed after N_2/H_2 annealing. This indicates the reduction in contaminant concentration on the surface of the graphene channel and the improved adhesion of contacts by the formation of the TiC layer at the metal-graphene contact junctions [86]. Hall measurements showed n-type conduction as expected for

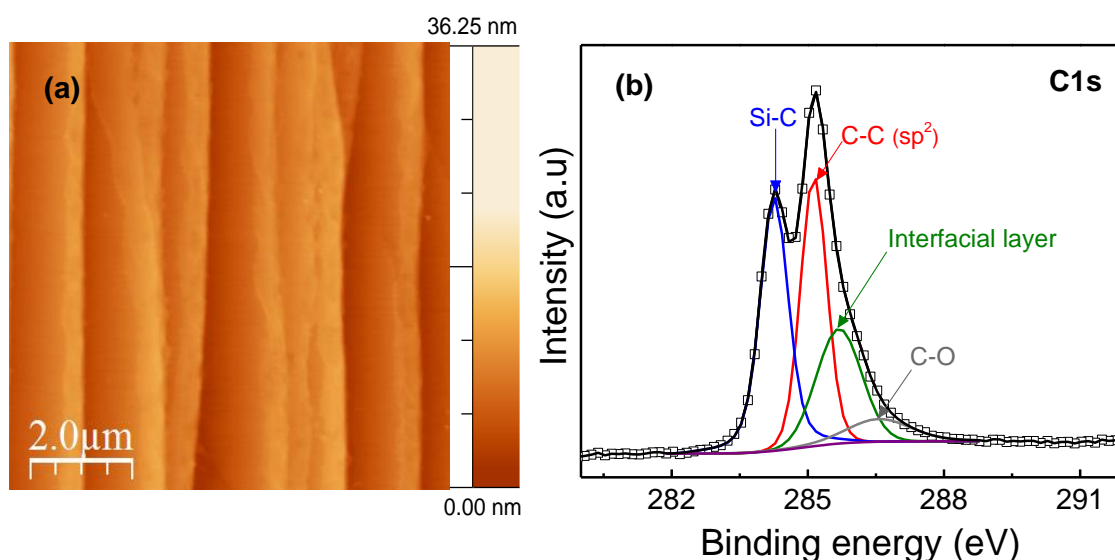


Figure 7.2: a) AFM topographic image and b) the XPS C1s spectrum of the graphene after N_2/H_2 annealing for 60 min.

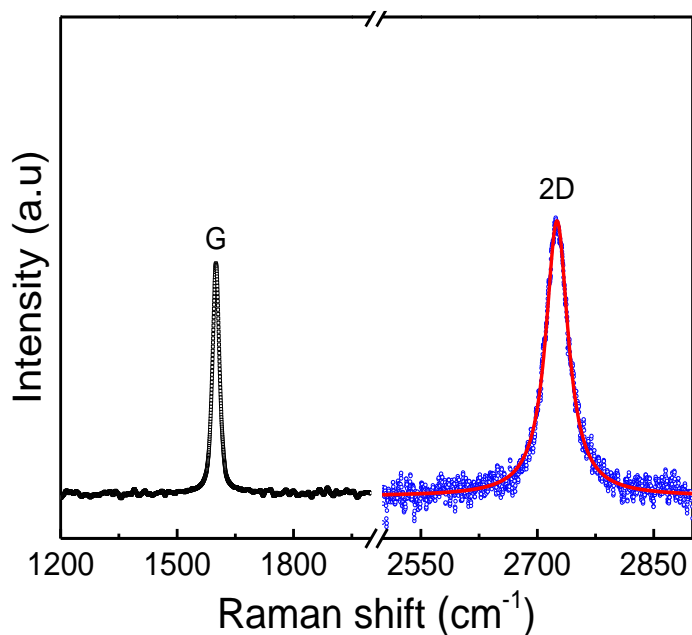


Figure 7.3: Raman spectrum of graphene showing G and 2D peaks. The 2D-peak was fitted (solid line) with a single Lorentzian function

epitaxial graphene on the Si-face of SiC. The average electron mobilities and carrier densities of eighty-four measured devices across all three UFEG samples were $1425 \pm 125 \text{ cm}^2 \text{ V}^{-1} \text{ s}^{-1}$ and $2.45 \pm 1.10 \text{ cm}^2 \text{ V}^{-1} \text{ s}^{-1}$ respectively. The list of polar chemicals used for the sensing experiments and their respective physiochemical properties are summarised in Table 7.1.

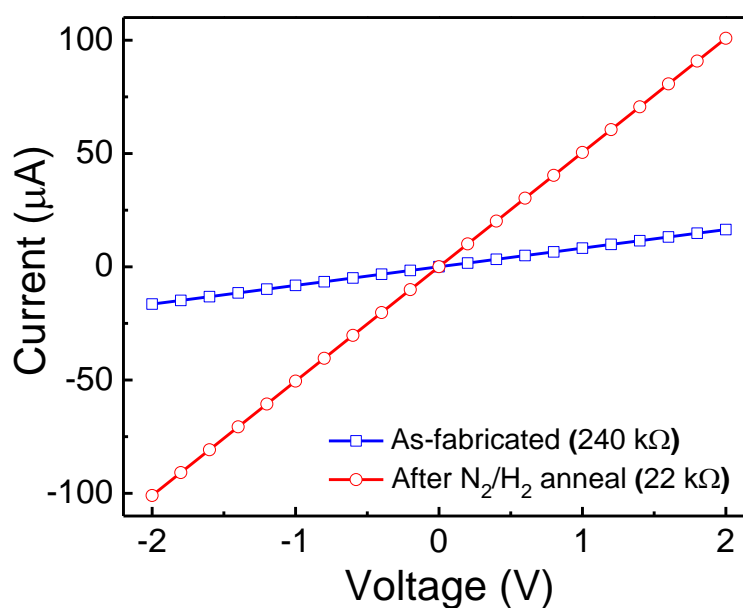


Figure 7.4: Typical I-V characteristics of a chemiresistor before and after N₂/H₂ anneal.

Table 7.1: List of polar analytes used in this study, their molecular properties [308] and relative resistance response.

Analyte	Polarity Type	Dipole moment	Dielectric constant	UFEG response (%)	OFEG response (%)
NMP	Polar aprotic	4.10	32.00	-27.14	-45.19
DMSO	Polar aprotic	3.96	47.24	-25.33	-43.50
DMF	Polar aprotic	3.82	38.25	-23.58	-42.03
DMAC	Polar aprotic	3.72	38.85	-22.38	-40.79
BZ	Polar aprotic	3.00	17.85	-19.19	-35.12
AA	Polar aprotic	2.72	22.45	-18.33	-33.31
EG	Polar protic	2.28	41.4	+17.13	+29.41
H ₂ O ₂	Polar protic	2.00	74.6	+16.53	+27.54
H ₂ O	Polar protic	1.85	80.10	+16.14	+25.77
MeOH	Polar protic	1.70	33.12	+15.96	+23.90

7.3.1 UFEG sensor response: I-V measurements

After chemical, electrical, structural, and surface analysis, the UFEG chemiresistor devices were exposed to several chemical vapours, while simultaneously measuring the relative change in the electrical resistance during the exposure. Figure 7.5 shows an example of the UFEG chemiresistor response to the individual vapours of NMP, DMF, AA, H₂O, and EG, as a function of time at 20°C. The data in the figure show large detectable changes in resistance occurred within 10 s of exposure to all chemicals. After the sensor response had reached equilibrium, the chemical exposure was discontinued and a mild annealing at 150°C in air was performed to fully recover the sensor base line (discussed in detail below). As can be observed from the data, different chemicals exhibited varying degrees of impact (sign and magnitude) on the sensor response. An increase in resistance was observed for polar protic chemicals, while the resistance decreased upon exposure to polar aprotic vapours. The observed responses are attributed to the surface charge transfer doping between adsorbed vapour molecules and the graphene [101]. Surface transfer doping does not usually disrupt the graphene band structure and in most cases this type of doping is reversible. Here, the direction of charge transfer and the magnitude of carrier injection depend on the electronic nature of the active graphene surface and the chemical nature of the analyte. As the majority

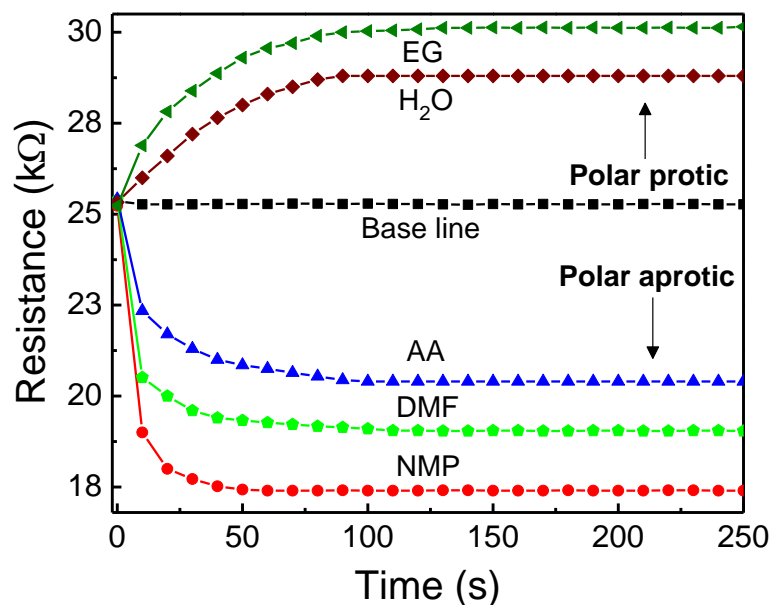


Figure 7.5: The chemical sensing behaviour of epitaxial graphene sensors to the saturated vapours of polar protic and polar aprotic chemicals in the ambient.

charge carriers in these graphene films are electrons, positively charged poles of analyte molecules are expected to strongly adsorb to the graphene surface.

This strong interaction leads to charge transfer between the physisorbed vapour molecules and graphene, which greatly alters the charge carrier concentration, depending on the chemical type. Hall measurements revealed that polar protic chemicals such as EG, H₂O, H₂O₂ and MeOH with hydroxyl groups (–OH) act as electron acceptors, thereby decreasing the electron density in the graphene channel. This reduction in electron concentration shifts the Fermi level closer to the Dirac point and leads to an increase in resistance [101]. In contrast, polar aprotic chemicals such as NMP, DMSO, DMF, DMAC, and AA with attached carbonyl (C=O) and sulphoxide (S=O) groups act as electron donors, increasing the electron concentration in the channel. The addition of electrons moves the Fermi energy further away from the Dirac point and thereby decreases the graphene resistance.

From Figure 7.5, it is evident that the response is very rapid initially, indicating the high adsorption rate of analyte molecules (within the first 20 sec) but slows down with time due to the increase in surface coverage by adsorbates [309]. Such an adsorption is best described by the Elovich equation [310], $d\theta/dt = a \times \exp(-b\theta)$, which has long been used to explain the kinetics of the adsorption of molecules on the surface of materials. Here, a and b are constants and $\theta(t)$ is the concentration of adsorbed analyte species on the graphene surface as a function of time. The constant a can be regarded as the initial adsorption rate since

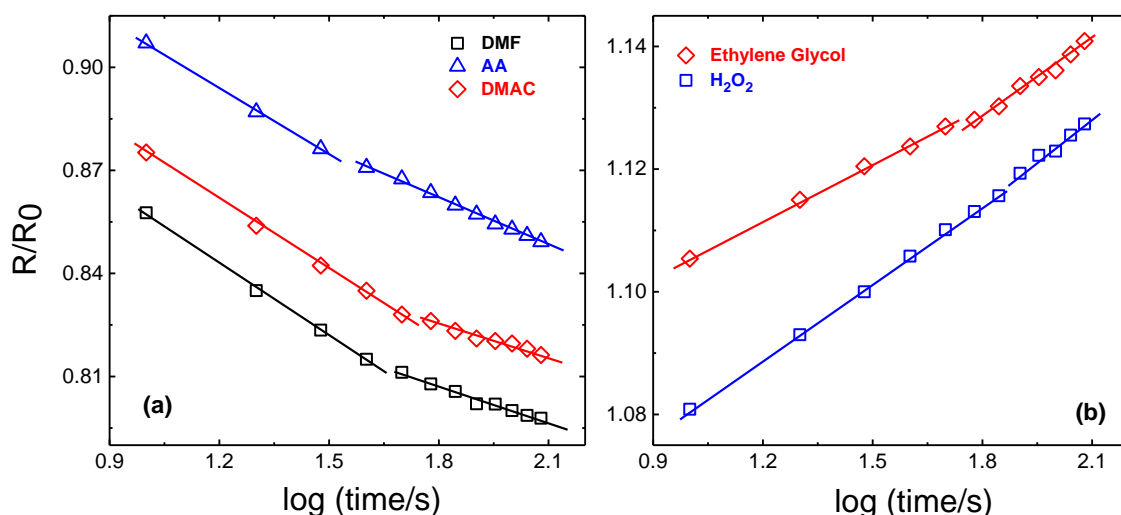


Figure 7.6: Elovich plots showing the relative resistance variation of the graphene sensor with linear fits to a) polar aprotic and b) polar protic vapour.

$d\theta/dt$ approaches a when θ approaches zero, while b is related to the nature of adsorption sites on the surface [311]. Integrating the Elovich equation with boundary condition $\theta(0) = 0$ reduces to, $\theta = (1/b) \ln(t/t_0 + 1)$, where $t_0 = (ab)^{-1}$. Assuming that the change in magnitude of the sensor resistance is proportional to the density of molecules (θ) adsorbed on the sensor surface upon exposure to analyte vapours, then a plot of resistance change against $\log(t)$ should exhibit a linear relationship [309]. The data shown in Figure 7.6 demonstrates a good linear agreement between the normalised resistance (R/R_0) change and $\log(t)$ for both protic and aprotic vapours at room temperature. However, as can be clearly seen in the data, the linear fits are separated into two parts, where the initial fit in the first few seconds correspond to the rapid change in resistance induced by the adsorbed vapour molecules upon immediate exposure to the graphene film, whilst the latter fit is related to the slow change in resistance after all the available adsorption sites in the graphene channel are filled up by analyte molecules and that the sensor has reached an equilibrium state. Notice that the slopes of both initial and final fits are different for each individual vapour tested here. Such a variation in slope could be used as an additional parameter in determining the chemical nature of the analyte species being tested, thereby improving the selectivity of the sensor significantly. Nevertheless, this confirms that the sensor response was driven by the adsorption of analyte molecules on the graphene surface and the adsorption increased with time due to an increase in analyte surface coverage and that these additional adsorption sites continued to contribute to the charge transfer.

Although a relatively fast response was observed for both protic and aprotic chemical vapours, the recovery rate of the sensor to reach its base line was slow with a recovery time of a few hours at room temperature. This is consistent with other reported studies on exfoliated flakes, CVD and epitaxial graphene based sensors, where the recovery times of a few tens of hours to a few days were reported to different chemical species [28, 93]. The recovery time is defined as the time it takes for the sensor to return to its baseline value upon discontinuing the chemical exposure. In order to recover the sensor base line, two different techniques were employed here: UV illumination and thermal annealing. The UV based surface cleaning process had been previously used in many studies to recover intrinsic CNT and graphene sensor properties after exposure to chemicals [304, 312, 313]. In the current study, when the graphene sensor device was illuminated with a UV light source of 5.0 mW/cm² intensity, a significant improvement in the sensory recovery was observed due to the photo-induced desorption of adsorbed vapour molecules. However, the extended exposure to UV light was found to irreversibly alter the graphene device characteristics and led to sensor degradation. This is mainly due to the use of high intensity UV light source, which led to the destruction of the graphene lattice structure by creating holes in the film. However, due to the limitation with the experimental set-up used here, the intensity of the UV light source could not be tuned to the desired power. Therefore, this method was not used in the sensing experiments reported in this thesis. Alternatively, low-temperature annealing was found to be a more reliable and reproducible, which did not significantly affect the UFEG properties. After discontinuing the vapour exposure, the UFEG sensor signal begins to recover slowly and this recovery process takes as long as three hours under the ambient conditions at 20°C. However, upon thermally annealing the sensor at 150°C, the recovery time was accelerated to approximately 10 min. The recovery of sensor baseline at such low-temperatures (150°C) indicates that the nature of interaction between graphene and vapour molecules is more likely to be physisorption rather than chemisorption. The improvement in the recovery time is attributed to the stimulated desorption rates of adsorbed vapour molecules at higher temperatures. The thermal treatment enhances the vaporisation rates of adsorbed molecules by providing them additional energy to overcome desorption energy barrier on the graphene surface. As a result, at elevated temperatures, the equilibrium concentration of adsorbed analyte molecules on the graphene surface will be reduced due to the faster desorption rates, resulting in faster recovery times. This annealing step was performed after each analyte exposure throughout the sensing experiments on UFEG

sensors to recover the initial undoped state of the sensor. Repeated exposure and thermal treatment cycles did not have any noticeable impact on the sensor performance or on the observed baseline.

7.3.1.1 Effect of dipole moment on the sensor response

In addition to discriminating between polar protic and aprotic chemicals, graphene also showed a striking difference in the magnitude of the response to these chemical vapours. The modulation in resistance is linked to the molecular dipole moment of chemicals, which arises due to the presence of attached functional groups and their asymmetrical molecular arrangement. Dipole moment, which is a crucial aspect for all chemicals can play a dominant role in device electrical characteristics and can heavily influence the resistance response of the graphene sensor. Figure 7.7 shows the magnitude of change in resistance to ten different chemical vapours as a function of dipole moment over the range of 1.70 D to 4.10 D [308]. Here the response of the sensor is determined by,

$$S (\%) = (R - R_0)/(R_0) \times 100$$

where R_0 and R , are resistances of the device before and after the chemical exposure, respectively. A strong correlation between the magnitude of the sensor response and the dipole moment of chemicals was observed, where the sensor exhibited an increase in response with the increasing dipole moment of the chemical. NMP with a high molecular dipole moment of 4.10 D showed the strongest response, whereas, methanol with a lower dipole moment of 1.70 D showed a relatively smaller response. This indicates that the

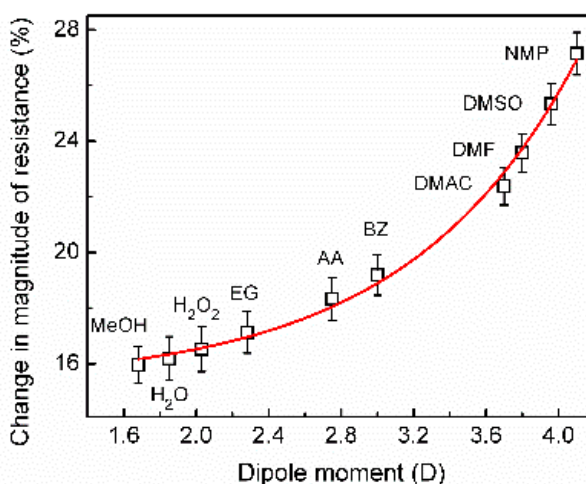


Figure 7.7: Relationship between the dipole moment of a chemical and the magnitude of UFEG sensor response.

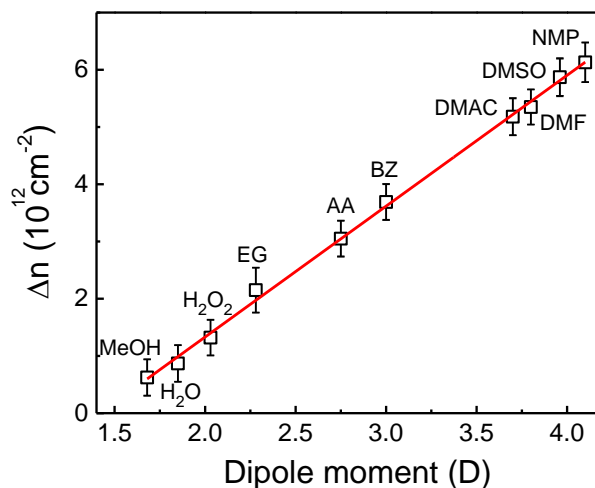


Figure 7.8: Change in adsorbate induced charge carrier density with the increasing dipole moment of a chemical.

magnitude of the resistance change is strongly modified by the surface interactions of the adsorbed vapour molecules. As mentioned above, molecules with higher dipole moments have large charge separation between the atoms and have strong polar character due to the greater electro-negativity difference. This results in a considerable charge transfer when they adsorb on to the graphene surface, affecting the magnitude of the response significantly. Hall measurements showed that highly polar chemicals such as NMP generate high concentrations of chemically induced charge carriers upon adsorption on to the graphene sheet, in comparison to less polar chemicals such as methanol, which produces relatively low concentration of additional charge carriers. As shown in the Figure 7.8, a linear increase in chemically induced carrier densities (Δn) with the dipole moment of the chemical was observed, indicating that the change in carrier concentration is the basic mechanism that governs the operation of epitaxial graphene sensor devices, similar to that reported on exfoliated graphene flakes [93].

7.3.2 UFEG sensor response: Low-frequency noise measurements

In order to gain further understanding about the observed chemical responses, $1/f$ noise measurements were performed to monitor the changes in the noise behaviour of graphene under vapour exposure. Since the $1/f$ noise in electronic device is more sensitive to external variations, in comparison to resistance changes, analysing the noise behaviour of the chemiresistor upon exposure to different analyte species can provide important information about the intrinsic sensing mechanism of the sensor [134, 314]. As graphene has very low

intrinsic noise [133], in comparison to carbon nanotubes, any changes produced by the surface adsorbates will have a significant impact on the $1/f$ noise spectrum. Rumyantsev *et al.* [134] recently reported that the $1/f$ noise of exfoliated graphene is highly sensitive to resistance fluctuations in the conducting channel, and can be used as an independent parameter in the analysis of the sensor response.

Figure 7.9 shows the normalised noise spectral density (NNPSD) of graphene measured as a function of frequency in air and during the exposure to H_2O_2 and EG vapours. The data shows an example of two overlapping spectra, corresponding to H_2O_2 and EG vapors, indicating good reproducibility of the noise measurements. After discontinuing the vapour exposure and mild annealing (150°C), the noise spectra returned to its baseline (two spectra shown in Figure 7.9 as ‘in air’), further demonstrating the excellent reversibility of UFEG sensors. As also can be seen in Figure 7.9, graphene exhibits a clear $1/f$ dependence (dashed lines) in air, similar to that observed previously in single layer graphene devices [291]. Upon exposure to chemical vapours, an apparent change in the noise was observed with no deviation from the $1/f$ behaviour for all chemicals tested over the measured frequency range. At 10 Hz, the NNPSD of graphene in air was $3.8 \times 10^{-9} \text{ Hz}^{-1}$, which increased to $2.3 \times 10^{-8} \text{ Hz}^{-1}$ and $1.1 \times 10^{-8} \text{ Hz}^{-1}$ after exposing to H_2O_2 and EG vapours, respectively. The change in noise is due to the fluctuations in carrier concentration in the active graphene channel associated with the adsorption of analyte molecules [134]. Figure 7.10 shows the strong dependence of the $1/f$ noise amplitude A_N , upon the dipole moment of a chemical, but unlike the resistance response observed above, the noise enhancement decreased with the increasing dipole moment. For example, H_2O_2 with a low dipole moment produced a high change in A_N , in comparison to a lower noise enhancement displayed by the highly polar chemical NMP. Such

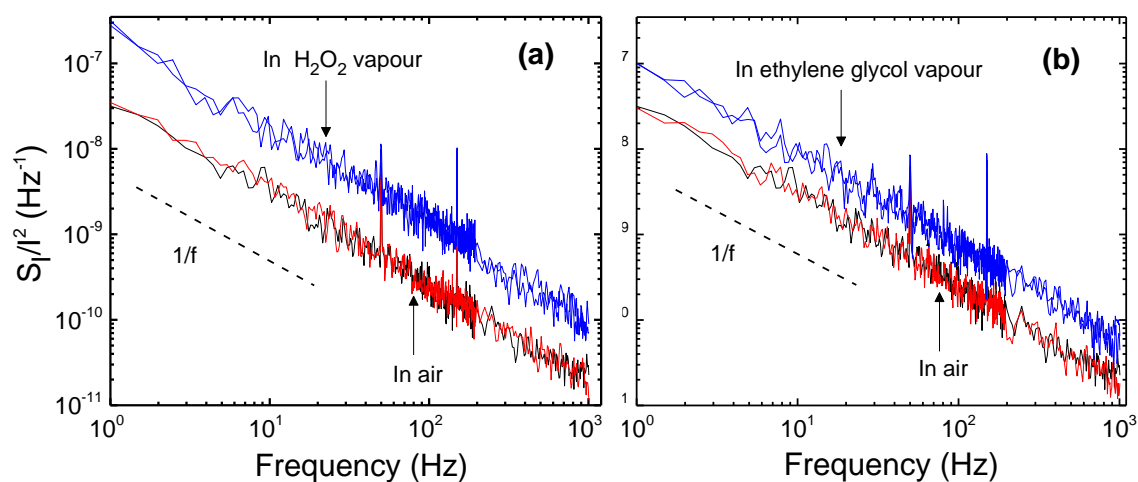


Figure 7.9: Low-frequency noise spectra of graphene in air and during exposure to a) H_2O_2 and b) ethylene glycol vapours.

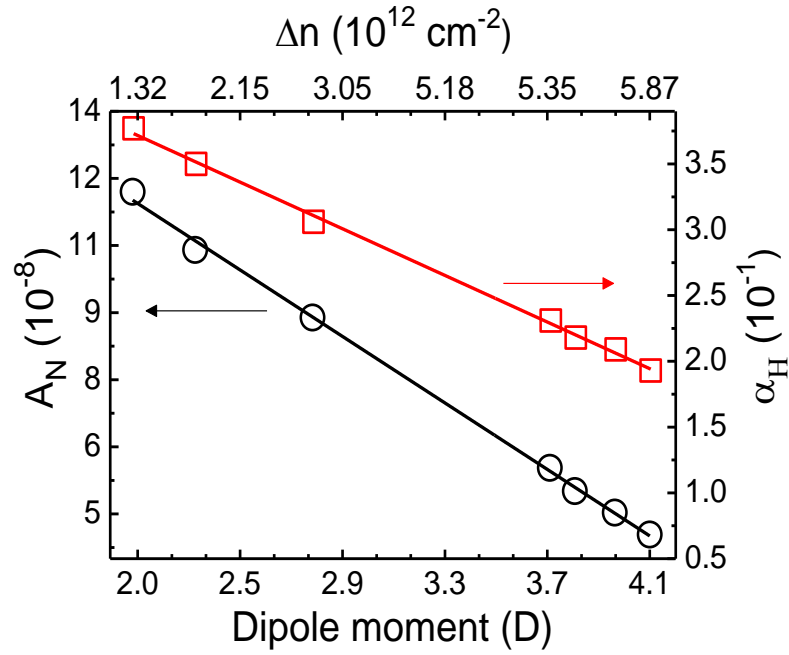


Figure 7.10: Change in noise amplitude and the Hooge parameter as a function of dipole moment of the chemical and the induced carrier density.

a behaviour can be described in terms of Hooge's model [49], which states that the noise amplitude varies inversely with the number of charge carriers, N in the channel, i.e. $A_N = \alpha_H/N$, where α_H is the Hooge parameter. However we observed that exposure to chemical vapours will not only change N but also change the value of α_H (Figure 7.10), which exhibited an inverse relationship with the carrier concentration, similar to that observed in diamond and AlGaIn/GaN based devices [315, 316]. It is important to note that α_H , while assumed to be constant for a given device or material, it is not an absolute constant and, instead depends upon scattering mechanisms such as charge impurity scattering, ripple scattering, or short-range disorder scattering [317] caused by adsorption of vapour molecules on the graphene surface. Here, H_2O_2 , with a low induced carrier concentration produced a large change in α_H , causing an overall increase in the noise amplitude. Conversely, NMP with a high density of induced charge carriers displayed a relatively small change in α_H , thereby resulting in minimal change in the $1/f$ noise amplitude. The contribution of both N and α_H to the noise enhancement may explain the behaviour observed previously [134], i.e. why some chemicals produce large changes in the electrical resistance, but with minimal or no change to the low-frequency noise spectra of graphene.

7.3.3 Sensing polar chemicals using OFEG sensors

Despite the fast response times and sensitivity to a wide range of chemicals, challenges still remain in using graphene sensors for practical applications. For example, as shown above, the desorption rate of vapour molecules on the UFEG surface was found to be slower than the adsorption rate, resulting in extremely long recovery times, ranging from tens of minutes to a few hours, limiting their use in situations where fast recovery times are required (eg. monitoring multiple leaks of toxic chemicals/explosives in short succession or in estimating the severity of chemical vapour dispersal etc.). Although the use of micro hot plates and UV-illumination would help accelerate the desorption process and recover the sensor base line [304, 313], integration of these additional elements with the sensor makes the final device bulky and complicated. Hence, identifying methods to accelerate desorption rates and recovery times without the need for these extra components is of great technological importance.

One of the proposed methods to overcome this is surface functionalisation. Recent studies have shown that chemical modification of graphene through surface functionalisation [110, 318], can not only control the electronic properties, but also modulate the binding energy of target molecules on graphene surface. Surface functionalisation creates chemical moieties, which serve as adsorption sites for analyte molecules and enables interaction with specific molecules thereby improving both the sensitivity and selectivity of the sensor

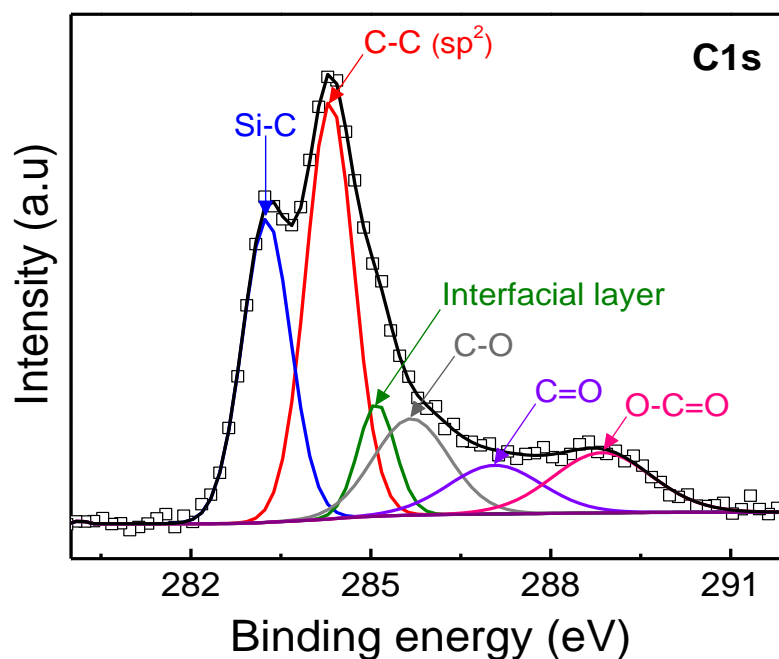


Figure 7.11: XPS C1s spectrum of oxygen functionalised graphene at 75 mTorr pressure.

dramatically. Such an improvement in sensor performance with a rapid recovery time was recently reported by Lu *et. al.* on chemically functionalised exfoliated graphene flakes using a self-assembled layer of single stranded DNA as a sensitising agent [31]. Similar enhancements in sensitivity, selectivity and recovery times were reported on functionalised CNTs [319] and rGO [136], highlighting the significance of functionalisation process in improving the sensor characteristics.

In order to investigate the impact of functionalisation, epitaxial graphene chemiresistors were functionalised with oxygen in this study and the sensor response was analysed using both resistance and low-frequency noise measurements, under similar experimental conditions that were used for UFEG sensing experiments. Figure 7.11 shows the high resolution XPS C1s spectra of OFEG exhibiting six major components at 283.8 eV, 284.7 eV, 285.4 eV, 285.6 eV, 287.1 eV, 288.8 eV corresponding to Si-C bond, C-C (sp^2) bond, interfacial layer, C-O, C=O and O-C=O bonds respectively. The addition of oxygen atoms changes the graphene sp^2 hybridization to sp^3 hybridization, which in-turn modifies the electronic and chemical properties. Analysis of the XPS spectra determined the surface coverage of oxygen atoms to be approximately 3.9 atomic %.

Figure 7.12 shows the Raman spectra of as-grown and oxygen functionalised graphene. The pristine as-grown graphene exhibited a G-peak at 1589 cm^{-1} and a 2D-peak at 2736 cm^{-1} , with no visible D-peak. After oxygen plasma treatment, a clear change in the Raman

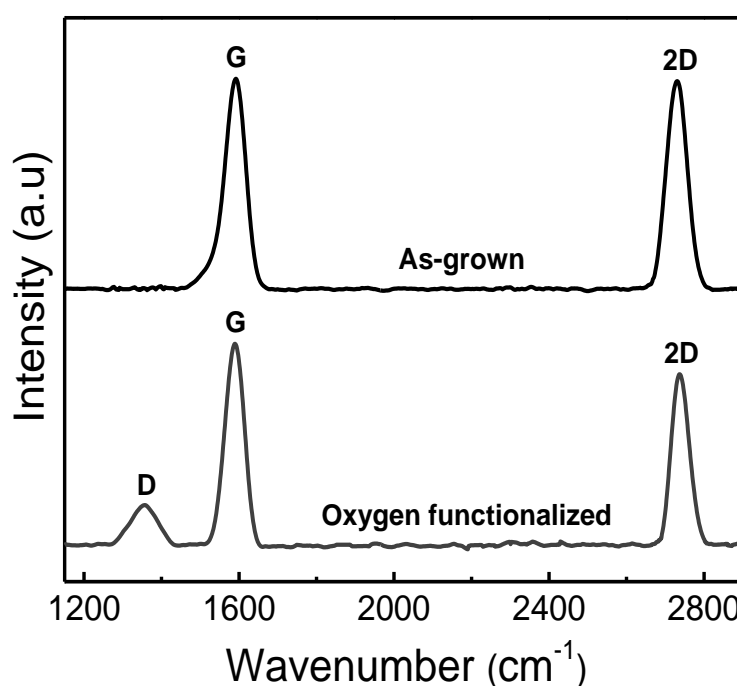


Figure 7.12: Raman spectra of graphene before and after O-functionalisation at 75 mTorr

spectrum can be seen, where the disorder induced D-peak at 1356 cm^{-1} was observed as a result of oxygen functionalisation. The addition of oxygen atoms increases the disorder in the graphene structure by forming out-of-plane chemical bonds. The disorder induced ratio (I_D/I_G) and the FWHM of D-peak were calculated as 0.30 and 80 cm^{-1} , respectively, demonstrating structural modifications to the graphene sp^2 character. From the I_D/I_G ratio, the average domain size, L_a was estimated to be 56 nm using Tunistra–Koenig relation [320] Hall measurements on forty OFEG devices showed the n-type conduction with average carrier density and electron mobilities of $1.6 \pm 1.9 \times 10^{12}\text{ cm}^{-2}$ and $1176 \pm 18\text{ cm}^2\text{ V}^{-1}\text{ s}^{-1}$ respectively.

7.3.4 OFEG sensor response: I-V measurements

Figure 7.13 shows the variation in I–V characteristics of an OFEG sensor, exhibiting linear behaviour when exposed to polar protic and aprotic vapours. The data also confirms the ohmic nature between the Ti/Au electrodes and the graphene. The measured baseline resistance of the chemiresistor after oxygen functionalisation was $6.5\text{ k}\Omega$, but varied upon exposure to different analyte vapours. Figure 7.14 shows the relative resistance response of an OFEG chemiresistor sensor to the individual vapours of NMP, DMAC and EG, as a function of time. As can be seen, different chemicals exhibited varying degrees of impact (sign and magnitude) on the sensor response. Similar to the UFEG sensor response, the electrical resistance of OFEG sensor increased when exposed to polar protic analytes, whilst

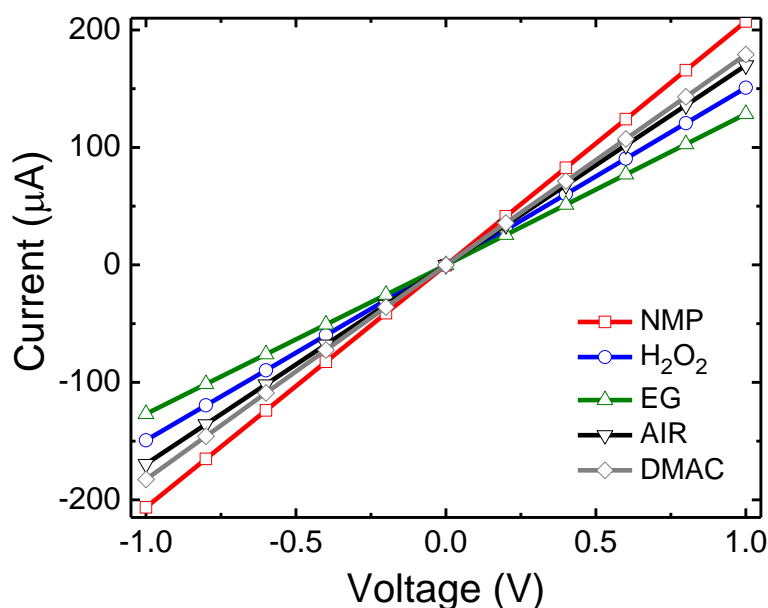


Figure 7.13: Change in I–V characteristics of an OFEG sensor exposed to polar protic and aprotic chemical vapours.

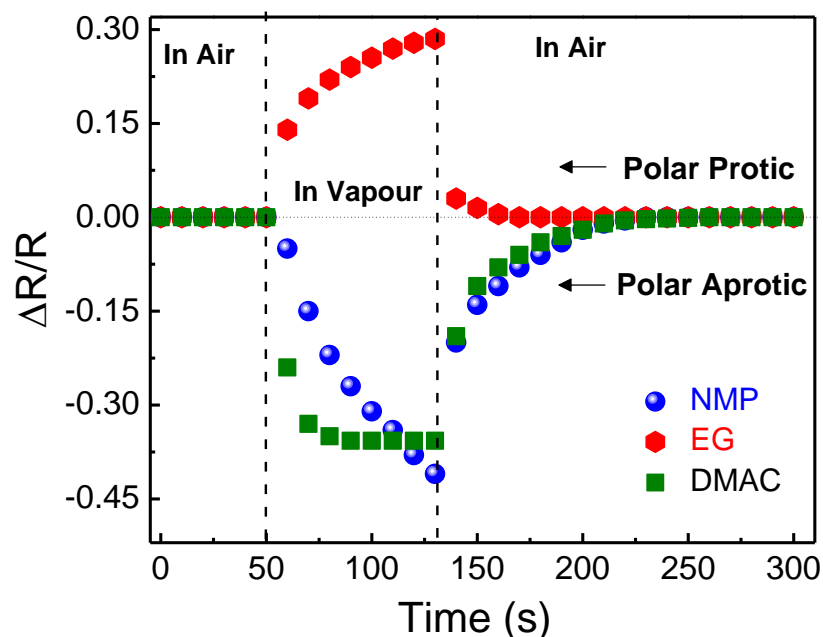


Figure 7.14: Sensing behaviour of an OFEG sensor to polar protic (EG) and polar aprotic (NMP and DMAC) chemical vapours.

the resistance decreased upon exposure to polar aprotic vapours. The chemical sensing mechanism is based on the change in local charge carrier concentrations due to electron donating and withdrawing behaviour of adsorbed analyte molecules [156]. Since the functionalisation was performed after the fabrication of chemiresistor device, the majority of functionalised oxygen species will be situated at the edge of the graphene channel due to the high chemical reactivity of the edge sites, in comparison to carbon atoms at the basal planes as described in the previous chapter. Here, the carbon-oxygen bond is a polar chemical bond, in which the re-distribution of electron charge in the bond leaves the oxygen atoms negatively charged and carbon atoms positively charged. As a result, the polar carbon-oxygen bonds with electro negative oxygen atoms are more chemically active to the surround environment than non-polar surfaces of the graphene. Therefore, when this reactive graphene surface is exposed to analyte vapours, the adsorption of analyte molecules takes place at these oxidised edges, resulting in significant charge transfer between carbon-oxygen bonds and the adsorbed analyte molecules. This leads to the variation in charge carrier density in graphene, which in turn influences the graphene sheet resistance drastically as observed here.

It is also evident from Figure 7.14 that, for DMAC vapours, the equilibrium state of the sensor was achieved within 30 s of analyte exposure. In contrast, the response to NMP and EG vapours were still changing even after 150 s of exposure, indicating either the slower

chemical kinetics of these analyte types or the slower saturation of adsorption sites, which continued to contribute to the resistance change. Upon discontinuing the vapour exposure, the sensor baseline was completely recovered. The average recovery time of the sensor to all analyte vapours studied was around 100 s. In comparison, the recovery time of UFEG sensors was in the range of a few hours. The observed short recovery times of OFEG sensors are attributed to the Van der Waal's like interaction between analyte molecules and the oxygenated graphene surface. Hence several minutes of high temperature annealing or the

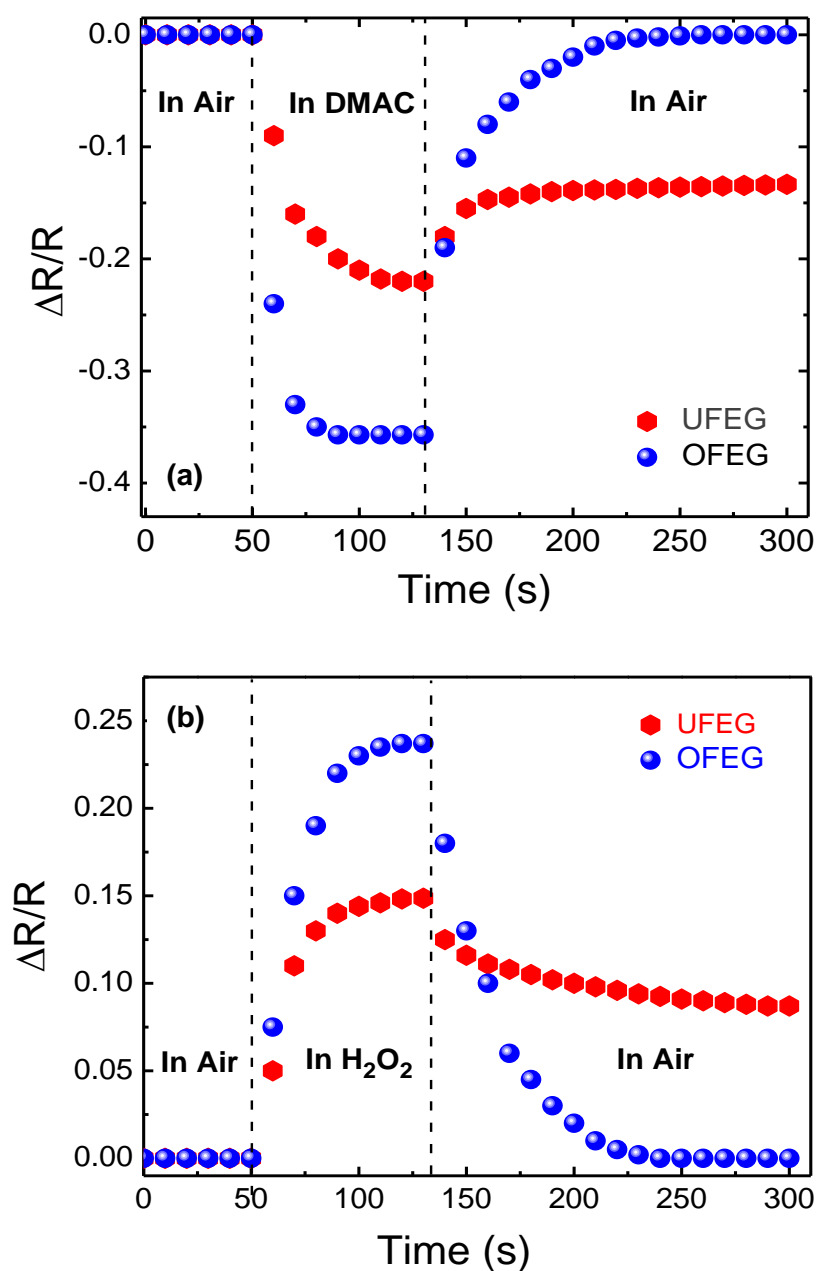


Figure 7.15: Comparison between UFEG and OFEG chemiresistor sensor responses upon exposure to the vapours of a) DMAC and b) H₂O₂.

use of UV illumination is not required to remove the adsorbed chemical species from the graphene surface.

Figure 7.15(a) and 7.15(b) shows the differences between UFEG and OFEG sensors when exposed to vapours of H_2O_2 and DMAC. For both chemicals, the UFEG chemiresistor sensor showed relatively weak response and extremely long recovery times in the range of ~ 1.5 to 2 hours. In contrast, OFEG sensors showed a considerable increase in sensitivity and an order of magnitude improvement in the recovery time over UFEG, illustrating the critical role of oxygen functionalisation on the sensor characteristics. Similar faster recovery rates were observed for all chemicals tested on OFEG sensors. This is consistent with other reported studies on rGO and functionalised CNT sensors [321], where the presence of oxygen change the wettability of graphene, causing the graphene to become less hydrophobic and more hydrophilic, which is suitable for adsorption of relatively low molecular weight and polar compounds. This results in a van der Waals like interaction between the surface adsorbates and the oxygen functional groups, leading to a rapid recovery of the OFEG sensor.

7.3.5 Effect of dipole moment on the sensor response

To further study the differences between OFEG and UFEG sensors, the changes in resistance vs. dipole moment were investigated. Figure 7.16 shows the percentage change in resistance to ten different analyte vapours as function of their respective dipole moments over a range from 1.70 D to 4.10 D. As can be seen, graphene exhibited a strong correlation between the magnitude of sensor response and the dipole moment of analyte vapors. A large

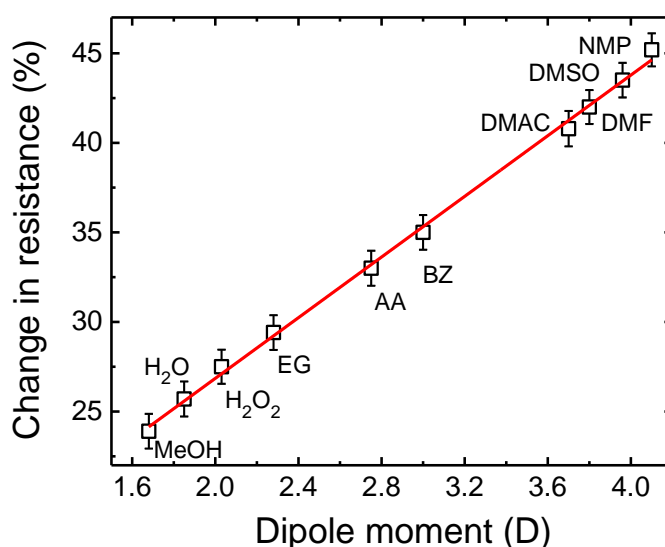


Figure 7.16: Change in resistance of OFEG chemiresistor sensors exposed to polar protic and aprotic chemical vapours.

linear increase in the magnitude of response for OFEG was observed in comparison to small non-linear change in resistance for UFEG, further demonstrating the superior performance of OFEG sensors. Functionalised graphene has a high density of surface adsorption sites [34], resulting in a higher adsorption capacity of vapour molecules. This leads to a significant change in the magnitude of the resistance due to the increased charge transfer between adsorbed molecules and graphene. Similar to that observed on UFEG sensors, Hall measurements showed a linear increase in induced carrier densities with the chemical dipole moment, demonstrating the mechanism of chemical sensing in OFEG sensors is due to the fluctuations in charge carrier densities after vapour exposure.

Figure 7.17(a) shows the deviation in resistance of thirty seven OFEG chemiresistor devices after exposure to different chemicals, followed by recovery. The variation of the

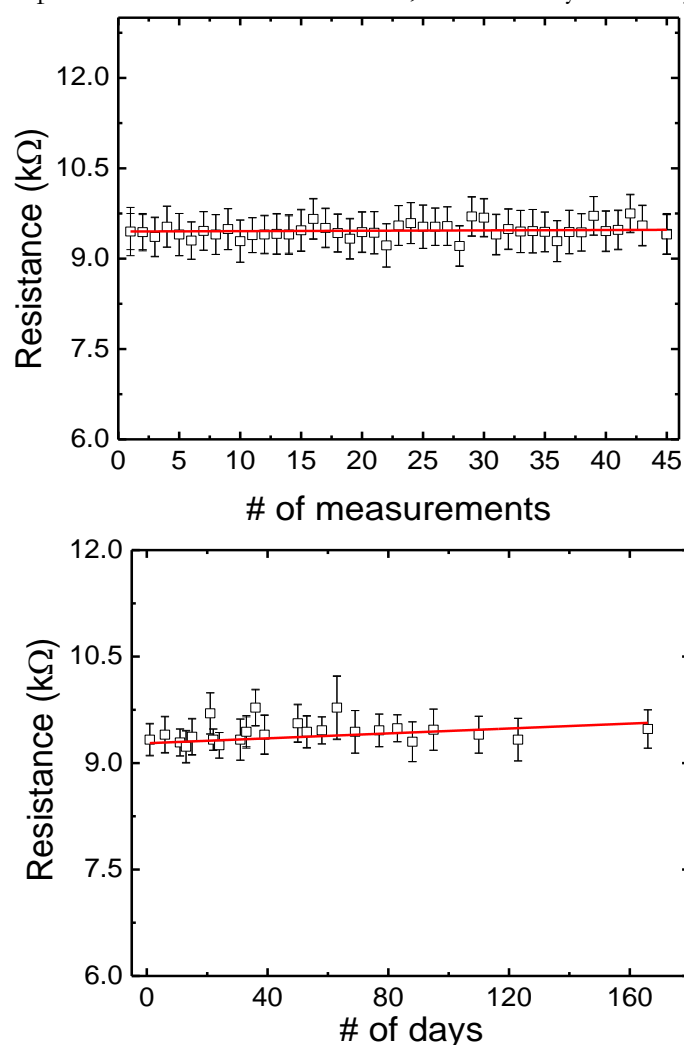


Figure 7.17: Repeatability and long-term stability of OFEG sensors. a) Variation in resistance of several chemiresistors after exposure to different chemical vapours followed by recovery. b) Resistance of chemiresistors over 160 days taken after recovery. Solid line is guide to the eye only.

resistance after recovery is within 2.3%, demonstrating the repeatability of these devices. In addition, the long term stability of OFEG chemiresistor devices was also analysed over time by monitoring the change in resistance after the chemical exposure and recovery, as shown in Figure 7.17(b). The resistance value varied by less than 3% over 169 days, showing highly stable behaviour of OFEG devices in the ambient atmosphere. Raman spectra was also obtained on several OFEG devices before and after the exposure to several chemical vapours, followed by the recovery, which showed no apparent change in the structural quality of graphene. This confirms negligible degradation of the OFEG device following multiple cycles of chemical exposure number of chemicals including, H_2O_2 and DMF molecules demonstrate the robustness of OFEG sensors and shows the ability of the sensor to maintain its properties when operated continuously for long durations, an important prerequisite for practical sensor applications.

7.3.6 OFEG sensor response: Low-frequency noise measurements

Noise analysis was also performed on OFEG sensors to monitor the changes in the behaviour of graphene during the vapour exposure. Figure 7.18 shows the noise spectral density of both UFEG and OFEG sensors as a function of frequency in air and during the exposure of DMF vapour. The noise spectra of both OFEG and UFEG sensors returned to their base lines upon discontinuing the vapour exposure, demonstrating the excellent reproducibility of the sensors. As shown in the Figure 7.18(a), UFEG exhibited identical $1/f$ dependence both before and after the vapour exposure, where λ is about 1.05. However, the noise spectral density has increased by an order of magnitude from $1 \times 10^{-18} A^2/Hz$ to $1 \times 10^{-17} A^2/Hz$ at 1 Hz. The noise increment is valid for the whole frequency range investigated here.

This increase in noise magnitude is associated with the fluctuation induced charge carrier concentration in the graphene channel upon adsorption of vapour molecules on the active graphene surface. In contrast, the OFEG noise spectrum produced a distinctive noise behavior in the low-frequency region (below 12 Hz). Such a deviation from the $1/f$ noise behaviour was previously observed [134], where the noise spectrum produced Lorentzian bulges upon exposure to different chemical vapours. This distinct behaviour of the noise spectrum over $1/f$ noise background is attributed to generation-recombination (G-R) processes that involve individual trapping and de-trapping of charge carriers via induced defects or trap centres [322] created during the oxygen functionalisation. The G-R noise is considered as a type of excess electrical noise due to fluctuations in the number of free carriers

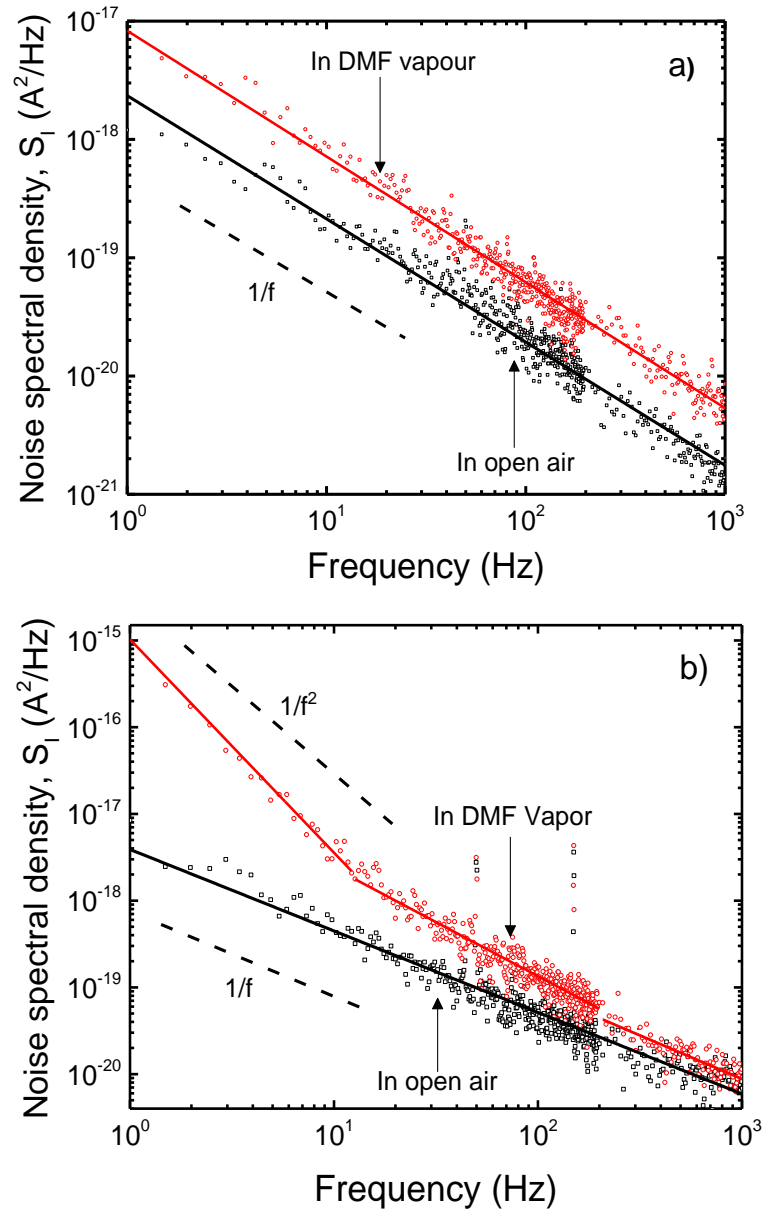


Figure 7.18: Low-frequency noise behaviour of a) unfunctionalised graphene and b) oxygen functionalised graphene in open air and under exposure to DMF vapour. Solid lines are logarithmic fits to the experimental data.

and is generally observed in semiconductors. The noise spectral density for G-R component is described by a Lorentzian spectrum:

$$S(\omega) \propto \frac{\tau}{1 + (\omega\tau)^2}$$

where τ is the time constant of the G-R process and $\omega = 2\pi f$ is the circular frequency. The noise spectrum after subtracting the $1/f$ noise component displayed $1/f^2$ type dependence at

a lower frequency range, indicating that traps with different energy levels were activated as the device was exposed to the chemical vapours. This illustrates that, in addition to having higher sensitivity and faster recovery time, OFEG sensors also embody a complex and unique noise spectrum, in comparison to UFEG and could be utilised to distinguish different chemical species that possess different characteristic frequencies.

In order to verify the effect of oxygen functional groups on the observed noise response, this O-functionalised sample was annealed in N_2/H_2 atmosphere at $400^\circ C$ for 60 min to intentionally remove the adsorbed O-functional groups from the graphene surface. XPS spectra showed the absence of $C=O$ and $O-C=O$ peaks as expected after the thermal treatment procedure. When the noise measurements were repeated on this sample under similar conditions as measured before, the characteristic $1/f^\beta$ dependence observed for previously functionalised graphene has now been disappeared as shown in Figure 7.19. Instead, the noise behavior was found to be similar to the spectrum observed for UFEG. This shows that the $1/f^\beta$ behaviour observed in oxygen functionalised graphene was mainly due to the presence of carbonyl and carboxyl groups and also signifies their crucial in the sensing mechanism of O-functionalised graphene sensor response.

However, a more in-depth analysis on the OFEG sensor noise with different analyte species is required to understand the underlying sensing mechanism associated with the sensor noise spectrum.

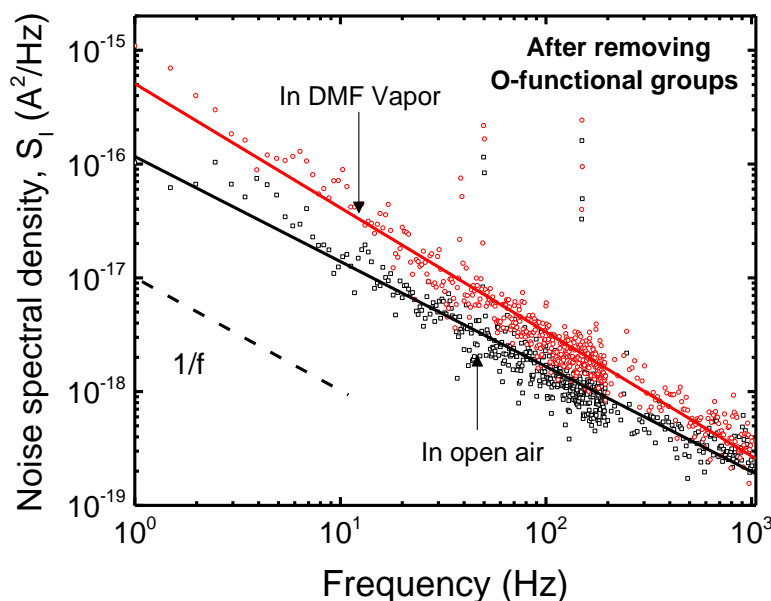


Figure 7.19: The noise spectra of O-functionalised graphene sample after de-oxygenation, i.e. removing O-functional groups from the graphene surface.

7.3.6.1 Influence of metal contacts on the UFEG and OFEG noise response

In order to identify the role of metal contacts in the observed responses, the noise amplitude of both UFEG and OFEG sensors were measured with the same channel dimensions as used above but with reduced metal contact sizes from $100 \times 150 \mu\text{m}^2$ to $100 \times 30 \mu\text{m}^2$. If the noise originates from the contacts, then the change in contact dimensions should also affect the noise amplitude. However, the noise spectra showed no significant change both the amplitude and the behaviour even after changing the contact sizes, demonstrating that contacts have a negligible influence on the noise and the sensing measurements. The negligible change shown in the Figure is within the experimental error of the system. Nevertheless, these results further demonstrate that the sensing mechanism in epitaxial graphene sensors is governed by the adsorbate induced carrier fluctuations in the channel and this fluctuation enhanced sensing of noise in combination with resistance measurements can provide complimentary capabilities of detecting chemical vapours that correspond distinctively in terms of these two sensing parameters.

7.4 Summary

In summary, the effectiveness of epitaxial graphene as a chemical sensor for detecting a wide range of polar chemical vapours in the ambient atmosphere has been demonstrated. The electrical responses of UFEG chemiresistors showed an increase in resistance to polar protic vapours, while the resistance decreased upon exposure to polar aprotic chemicals. It was

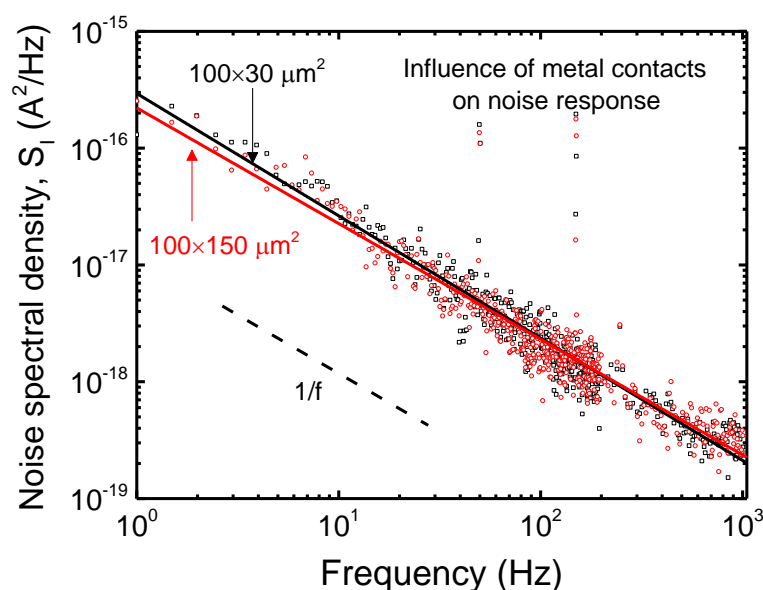


Figure 7.20: Influence of metal contacts on the $1/f$ noise response of graphene devices.

found that the magnitude of the sensor response has a strong dependence on the dipole moment of a chemical, in which the response increased with the increasing dipole moment. The low-frequency noise measurements, showed a contrasting behaviour, wherein the amplitude of the noise decreased with the increasing dipole moment of the chemical without otherwise affecting the $1/f$ spectrum. Despite the response to different chemical vapours, UFEG based sensors showed considerably weaker sensitivity and extremely slow recovery time in the range of ~ 1.5 to 2 hours.

By functionalising lithographically patterned graphene films with oxygen species, a highly sensitive and selective sensor was realised with high sensitivity and ultra-fast recovery times of around 100 s. Similar to the UFEG, the sensor responses of OFEG also showed a strong dependence on the analyte properties with increased resistance to polar protic analytes and decreased to polar aprotic analyte vapours. In addition, OFEG displayed a twofold increase in the sensor sensitivity over UFEG with the increasing dipole moment from 1.70 D to 4.1 D. For example, exposing OFEG to NMP vapours produced a 45% change in resistance, in comparison to a 27% resistance change displayed by UFEG sensors. The noise spectral density of UFEG showed a typical $1/f$ dependence upon exposure to dimethylformamide vapours but with a lower change in noise from $1 \times 10^{-18} \text{ A}^2/\text{Hz}$ to $1 \times 10^{-17} \text{ A}^2/\text{Hz}$ at 1 Hz. In contrast, OFEG showed a significant change to the sensor noise from $3 \times 10^{-18} \text{ A}^2/\text{Hz}$ to $2 \times 10^{-15} \text{ A}^2/\text{Hz}$ with unique $1/f^{\beta}$ dependence at the lower frequency range (1-10 Hz), which could be used for distinguishing different chemical species at their respective characteristic frequencies. The observed results were repeatable over many cycles of vapour exposures and several hours of continuous operation. The simple, reliable and robust performance of the epitaxial graphene sensors demonstrates the feasibility of using OFEG sensors for variety of applications, including, environmental monitoring, sensing in chemical processing plants, defense and homeland security.

Chapter 8

Summary and future outlook

The work presented in this thesis has mainly centred on investigating the issues related to performance limiting factors in graphene based electronic devices and sensors. Since graphene is extremely sensitive to its surrounding atmosphere, any materials that come in direct contact with the graphene can significantly alter its intrinsic properties. For instance, materials such as metal electrodes or photoresist polymers, which are commonly used in the graphene device fabrication will have irreversible impact on the electrical, chemical and structural properties of graphene and therefore indirectly affects the performance of the final fabricated graphene device. Hence, understanding and controlling these performance-limiting factors is critical for the development of graphene-based electronics.

The influence of metal contacts, the effect of photolithography processing and high-temperature annealing on the electrical characteristics of metal-graphene interfaces were investigated in chapter 4. In order to minimise lithography induced contamination, two methods were developed here, in which, for the first method, rapid thermal annealing of graphene devices was performed in N_2/H_2 atmosphere, whilst the second utilises a metal sacrificial layer to prevent graphene from coming into direct with photoresist during the lithography process. Chemical, electrical, structural and surface analysis showed that clean graphene surfaces could be achieved by both these methods, which allowed the intrinsic properties of graphene to be measured. However, the results obtained from Al sacrificial layer approach showed superior electrical properties, in comparison to that measured on

thermally annealed devices. TLM measurements showed that Ti with significant lattice (3.7%) mismatch along with its highly reactive nature can destroy the graphene lattice and leads to high contact resistance, whereas, Ni was found to produce lowest contact resistance among all the metals investigated due to its lowest lattice mismatch (1.2%) with the graphene film.

Although pristine graphene has many outstanding electronic properties, the lack of polar functional groups on its surfaces makes interfacing graphene with other chemical moieties extremely challenging, thereby limiting its use in chemical and biological sensing applications. Moreover, the highly hydrophobic and chemically inert nature of graphene surface inhibits uniform deposition of ultra-thin (2–10 nm) high-k dielectric layers, further impeding the development of graphene-based electronics for high frequency applications. Hence, surface functionalisation of graphene is essential to enhance its capabilities and promote chemical reactivity on its surfaces. Chapter 5 presents the investigation on the oxygen functionalised epitaxial graphene films using e-beam generated plasmas. XPS revealed the presence of different oxygen functional groups (e.g. hydroxyl, epoxy, carbonyl and ether) on the graphene surface, whilst Raman spectroscopy showed the transformation of planar sp^2 symmetry of graphene to distorted sp^3 hybridisation as a result of plasma treatment. In addition, it was found that oxygen plasma treatment results in strain relaxation, in which the intrinsic compressive strain present in epitaxial graphene film decreases progressively with the increasing plasma pressure. Hall measurements showed p-type doping of oxygen functionalised graphene films with maximum induced carrier densities of $5 \times 10^{14} \text{ cm}^{-2}$ obtained at the highest oxidation pressure (90 mTorr).

However, since the use of functionalised graphene films in device applications inevitably require metal contacts, it is important to understand the influence of oxygen presence at metal-graphene interfaces on the device electrical characteristics. Hence, a systematic study on the effect of oxygen functionalisation on the electrical characteristics of epitaxial graphene-metal contact interfaces is presented in Chapter 6. Two functionalisation approaches were investigated, wherein, for the first approach, oxygen functionalisation was performed on as-grown blanket graphene films, followed by device fabrication (method-A) and for the second approach, device fabrication was performed first, followed by oxygen functionalisation (method-B). Hall, TLM and low-frequency noise characterisation demonstrated that functionalising graphene after device fabrication (i.e method-B) yields superior electrical properties with high mobility, low contact resistance, low sheet resistance

and substantially lower noise characteristics without significantly degrading the structural characteristics of graphene. Such superior performance obtained from method-B functionalised devices were attributed to preserving the intrinsic properties of graphene, in which, majority of oxygen functional groups were attached to the edge of the conduction channel without inducing significant stress to the graphene lattice.

The effectiveness of such functionalised epitaxial graphene devices as a chemical sensor for detecting a wide range of polar chemical vapours in the ambient atmosphere has been demonstrated in chapter 7. Specifically, the effect of chemical polarity and the significance of dipole moment on the sensing properties of graphene were studied using two-probe, Hall and $1/f$ noise measurements. First, the experiments performed on unfunctionalised graphene chemiresistors showed an increase in resistance to polar protic vapours, while the resistance decreased upon exposure to polar aprotic chemicals. It was found that the magnitude of the sensor response has a strong dependence on the dipole moment of a chemical, in which the response increased with the increasing dipole moment. Despite the response to different chemical vapours, graphene based sensors showed considerably weaker sensitivity and extremely slow recovery time in the range of ~ 1.5 to 2 hours.

However, these issues were overcome by functionalising graphene devices with oxygen species, which resulted in a two-fold increase in the sensor sensitivity, along with ultra-fast recovery times of around 40 s to 150 s. The low-frequency noise measurements of oxygen functionalised graphene showed unique $1/f^2$ dependence at the lower frequency range (1-10 Hz), in comparison to typical $1/f$ noise observed in unfunctionalised graphene sensors. Such distinct $1/f^2$ dependence could be used for distinguishing different chemical species at their respective characteristic frequencies. The observed results were repeatable over many cycles of vapour exposures and several hours of continuous operation. The simple, reliable and robust performance of the epitaxial graphene sensors demonstrates the feasibility of using oxygen functionalised graphene sensors for variety of applications, including, environmental monitoring, sensing in chemical processing plants, defense applications.

8.1 Future outlook

The work presented in chapter 7 demonstrated the chemical sensing capability of graphene to a wide range of analyte vapours. In particular, it was shown that by functionalising epitaxial graphene devices with oxygen species (at 75 mTorr), both the sensitivity, selectivity and the response times of the sensor can be significantly improved. However, by selectively

functionalising different graphene devices with different functionalisation pressures, a variety of functional groups can be attached to the graphene surface. For instance, devices with hydroxyl rich, epoxy rich and carboxyl rich surfaces can be created on a same sample when functionalised at 25 mTorr, 50 mTorr and 90 mTorr functionalisation pressures. Such graphene devices with different surface chemistries could enhance the selectivity of graphene-based sensors, because the interaction of different chemicals or gases will vary depending on the functional species present on the surface.

Furthermore, functionalising graphene with both oxygen and fluorine species on a single graphene sample will create regions with hydrophilic and hydrophobic surfaces. Such a change in surface wettability will significantly impact the adsorption energies of different analyte species, which therefore also affects the graphene sensing responses.

Apart from graphene, other two-dimensional materials, such as MoS₂, WS₂ and their heterostructure combinations are currently gaining more attention and are currently under investigation to uncover their chemical sensing properties. By combining graphene with these exotic materials, different sensor devices sensitive to targeted chemical species can potentially be fabricated.

References

- [1] H. O. Peierls, *Handbook of carbon, graphite, diamond and fullerenes*. New Jersey: Noyes Publications, 1993.
 - [2] E. H. Falcao and F. Wudl, "Carbon allotropes: beyond graphite and diamond," *J. Chem. Technol. Biotechnol.*, vol. 82, pp. 524-531, 2007.
 - [3] G. B. Neighbour, *Management of ageing processes in graphite reactor cores*. Cambridge: RSC Publishing, 2007.
 - [4] A. K. Padhi, K. Nanjundaswamy, and J. B. d. Goodenough, "Phospho-olivines as positive-electrode materials for rechargeable lithium batteries," *J. Electrochem. Soc.*, vol. 144, pp. 1188-1194, 1997.
 - [5] R. E. Smalley, H. Kroto, and J. Heath, "C60: Buckminsterfullerene," *Nature*, vol. 318, pp. 162-163, 1985.
 - [6] (28th March 2014). *The Nobel Prize in Chemistry 1996*. Available: http://www.nobelprize.org/nobel_prizes/chemistry/laureates/1996/
 - [7] S. Iijima, "Helical microtubules of graphitic carbon," *Nature*, vol. 354, pp. 56-58, 1991.
 - [8] S. V. N. T. Kuchibhatla, A. S. Karakoti, D. Bera, and S. Seal, "One dimensional nanostructured materials," *Prog. Mater. Sci.*, vol. 52, pp. 699-913, 7// 2007.
 - [9] C. Riedl, "Epitaxial Graphene on Silicon Carbide Surfaces: Growth, Characterization, Doping and Hydrogen Intercalation," PhD thesis, Der Naturwissenschaftlichen Fakultät der Friedrich-Alexander-Universität Erlangen-Nürnberg, 2010.
 - [10] K. S. Novoselov, A. K. Geim, S. Morozov, D. Jiang, Y. Zhang, S. Dubonos, *et al.*, "Electric field effect in atomically thin carbon films," *Science*, vol. 306, pp. 666-669, 2004.
 - [11] A. K. Geim and K. S. Novoselov, "The rise of graphene," *Nature Mater.*, vol. 6, pp. 183-191, 2007.
 - [12] R. Peierls, "Quelques propriétés typiques des corps solides," in *Ann. l. H. Poincaré*, 1935, pp. 177-222.
 - [13] L. Landau, "Zur Theorie der phasenumwandlungen II," *Phys. Z. Sowjetunion*, vol. 11, pp. 26-35, 1937.
 - [14] N. D. Mermin, "Crystalline order in two dimensions," *Physical Review*, vol. 176, p. 250, 1968.
-

REFERENCES

- [15] J. Venables, G. Spiller, and M. Hanbucken, "Nucleation and growth of thin films," *Rep. Prog. Phys.*, vol. 47, p. 399, 1984.
- [16] J. Evans, P. Thiel, and M. Bartelt, "Morphological evolution during epitaxial thin film growth: Formation of 2D islands and 3D mounds," *Surf. Sci. Rep.*, vol. 61, pp. 1-128, 2006.
- [17] J. C. Meyer, A. K. Geim, M. Katsnelson, K. Novoselov, T. Booth, and S. Roth, "The structure of suspended graphene sheets," *Nature*, vol. 446, pp. 60-63, 2007.
- [18] (28th March 2014). *The Nobel Prize in Physics 2010*. Available: http://www.nobelprize.org/nobel_prizes/physics/laureates/2010/
- [19] Q. H. Wang, K. Kalantar-Zadeh, A. Kis, J. N. Coleman, and M. S. Strano, "Electronics and optoelectronics of two-dimensional transition metal dichalcogenides," *Nature Nanotech.*, vol. 7, pp. 699-712, 2012.
- [20] A. K. Geim, "Graphene: status and prospects," *Science*, vol. 324, pp. 1530-1534, 2009.
- [21] C. Berger, Z. Song, T. Li, X. Li, A. Y. Ogbazghi, R. Feng, *et al.*, "Ultrathin epitaxial graphite: 2D electron gas properties and a route toward graphene-based nanoelectronics," *J. Phys. Chem. B*, vol. 108, pp. 19912-19916, 2004.
- [22] X. Li, W. Cai, L. Colombo, and R. S. Ruoff, "Evolution of graphene growth on Ni and Cu by carbon isotope labeling," *Nano Lett.*, vol. 9, pp. 4268-4272, 2009.
- [23] S. Bae, H. Kim, Y. Lee, X. Xu, J.-S. Park, Y. Zheng, *et al.*, "Roll-to-roll production of 30-inch graphene films for transparent electrodes," *Nature Nanotech.*, vol. 5, pp. 574-578, 2010.
- [24] X. Wang, L. Zhi, and K. Müllen, "Transparent, conductive graphene electrodes for dye-sensitized solar cells," *Nano Lett.*, vol. 8, pp. 323-327, 2008.
- [25] Y. Ji, S. Lee, B. Cho, S. Song, and T. Lee, "Flexible organic memory devices with multilayer graphene electrodes," *ACS Nano*, vol. 5, pp. 5995-6000, 2011.
- [26] P. Blake, P. D. Brimicombe, R. R. Nair, T. J. Booth, D. Jiang, F. Schedin, *et al.*, "Graphene-based liquid crystal device," *Nano Lett.*, vol. 8, pp. 1704-1708, 2008.
- [27] Y. Wu, K. A. Jenkins, A. Valdes-Garcia, D. B. Farmer, Y. Zhu, A. A. Bol, *et al.*, "State-of-the-Art Graphene High-Frequency Electronics," *Nano Lett.*, vol. 12, pp. 3062-3067, 2012/06/13 2012.
- [28] R. Pearce, T. Iakimov, M. Andersson, L. Hultman, A. L. Spetz, and R. Yakimova, "Epitaxially grown graphene based gas sensors for ultra sensitive NO₂ detection," *Sensors and Actuators B: Chemical*, vol. 155, pp. 451-455, 2011.

REFERENCES

- [29] O. J. Guy, A. Castaing, Z. Tehrani, and S. H. Doak, "Fabrication of ultrasensitive graphene nanobiosensors," in *Sensors, 2010 IEEE*, 2010, pp. 907-912.
- [30] F. Bonaccorso, Z. Sun, T. Hasan, and A. Ferrari, "Graphene photonics and optoelectronics," *Nature Photon.*, vol. 4, pp. 611-622, 2010.
- [31] Y. Lu, B. R. Goldsmith, N. J. Kybert, and A. C. Johnson, "DNA-decorated graphene chemical sensors," *Appl. Phys. Lett.*, vol. 97, p. 083107, 2010.
- [32] Y. Wang, Z. Li, J. Wang, J. Li, and Y. Lin, "Graphene and graphene oxide: biofunctionalization and applications in biotechnology," *Trends Biotechnol.*, vol. 29, pp. 205-212, 2011.
- [33] K. S. Novoselov, V. Fal, L. Colombo, P. Gellert, M. Schwab, and K. Kim, "A roadmap for graphene," *Nature*, vol. 490, pp. 192-200, 2012.
- [34] S. Santavirta, M. Takagi, L. Nordsletten, A. Anttila, R. Lappalainen, and Y. T. Konttinen, "Biocompatibility of silicon carbide in colony formation test in vitro," *Archives of orthopaedic and trauma surgery*, vol. 118, pp. 89-91, 1998.
- [35] F. Xia, V. Perebeinos, Y.-m. Lin, Y. Wu, and P. Avouris, "The origins and limits of metal-graphene junction resistance," *Nature Nanotech.*, vol. 6, pp. 179-184, 2011.
- [36] Y. Dan, Y. Lu, N. J. Kybert, Z. Luo, and A. C. Johnson, "Intrinsic response of graphene vapor sensors," *Nano Lett.*, vol. 9, pp. 1472-1475, 2009.
- [37] M. Ishigami, J. Chen, W. Cullen, M. Fuhrer, and E. Williams, "Atomic structure of graphene on SiO₂," *Nano Lett.*, vol. 7, pp. 1643-1648, 2007.
- [38] A. Bianco, H.-M. Cheng, T. Enoki, Y. Gogotsi, R. H. Hurt, N. Koratkar, *et al.*, "All in the graphene family—A recommended nomenclature for two-dimensional carbon materials," *Carbon*, vol. 65, pp. 1-6, 2013.
- [39] Q. H. Wang, Z. Jin, K. K. Kim, A. J. Hilmer, G. L. Paulus, C.-J. Shih, *et al.*, "Understanding and controlling the substrate effect on graphene electron-transfer chemistry via reactivity imprint lithography," *Nature Chem.*, vol. 4, pp. 724-732, 2012.
- [40] Y. Yang, K. Brenner, and R. Murali, "The influence of atmosphere on electrical transport in graphene," *Carbon*, vol. 50, pp. 1727-1733, 2012.
- [41] C. Lee, X. Wei, J. W. Kysar, and J. Hone, "Measurement of the elastic properties and intrinsic strength of monolayer graphene," *Science*, vol. 321, pp. 385-388, 2008.
- [42] R. Nair, P. Blake, A. Grigorenko, K. Novoselov, T. Booth, T. Stauber, *et al.*, "Fine structure constant defines visual transparency of graphene," *Science*, vol. 320, pp. 1308-1308, 2008.

REFERENCES

- [43] J. S. Bunch, S. S. Verbridge, J. S. Alden, A. M. van der Zande, J. M. Parpia, H. G. Craighead, *et al.*, "Impermeable atomic membranes from graphene sheets," *Nano Lett.*, vol. 8, pp. 2458-2462, 2008.
- [44] A. Peigney, C. Laurent, E. Flahaut, R. Bacsa, and A. Rousset, "Specific surface area of carbon nanotubes and bundles of carbon nanotubes," *Carbon*, vol. 39, pp. 507-514, 2001.
- [45] A. A. Balandin, S. Ghosh, W. Bao, I. Calizo, D. Teweldebrhan, F. Miao, *et al.*, "Superior thermal conductivity of single-layer graphene," *Nano Lett.*, vol. 8, pp. 902-907, 2008.
- [46] J.-H. Chen, C. Jang, S. Xiao, M. Ishigami, and M. S. Fuhrer, "Intrinsic and extrinsic performance limits of graphene devices on SiO₂," *Nature Nanotech.*, vol. 3, pp. 206-209, 2008.
- [47] A. Tzalenchuk, S. Lara-Avila, A. Kalaboukhov, S. Paolillo, M. Syväjärvi, R. Yakimova, *et al.*, "Towards a quantum resistance standard based on epitaxial graphene," *Nature Nanotech.*, vol. 5, pp. 186-189, 2010.
- [48] S. V. Morozov, K. S. Novoselov, M. I. Katsnelson, F. Schedin, D. C. Elias, J. A. Jaszczak, *et al.*, "Giant Intrinsic Carrier Mobilities in Graphene and Its Bilayer," *Phys. Rev. Lett.*, vol. 100, p. 016602, 01/07/ 2008.
- [49] K. I. Bolotin, K. Sikes, Z. Jiang, M. Klima, G. Fudenberg, J. Hone, *et al.*, "Ultra-high electron mobility in suspended graphene," *Solid State Commun.*, vol. 146, pp. 351-355, 2008.
- [50] P. R. Wallace, "The band theory of graphite," *Physical Review*, vol. 71, p. 622, 1947.
- [51] A. C. Neto, F. Guinea, N. Peres, K. S. Novoselov, and A. K. Geim, "The electronic properties of graphene," *Rev. Mod. Phys.*, vol. 81, p. 109, 2009.
- [52] A. Bostwick, T. Ohta, J. L. McChesney, K. V. Emtsev, T. Seyller, K. Horn, *et al.*, "Symmetry breaking in few layer graphene films," *New J. Phys.*, vol. 9, p. 385, 2007.
- [53] F. Bonaccorso, A. Lombardo, T. Hasan, Z. Sun, L. Colombo, and A. C. Ferrari, "Production and processing of graphene and 2d crystals," *Mater. Today*, vol. 15, pp. 564-589, 2012.
- [54] R. Van Noorden, "Production: Beyond sticky tape," *Nature*, vol. 483, pp. S32-S33, 03/15/print 2012.

REFERENCES

- [55] S. Chen, H. Ji, H. Chou, Q. Li, H. Li, J. W. Suk, *et al.*, "Millimeter-Size Single-Crystal Graphene by Suppressing Evaporative Loss of Cu During Low Pressure Chemical Vapor Deposition," *Adv. Mater.*, vol. 25, pp. 2062-2065, 2013.
- [56] W. Zhu, V. Perebeinos, M. Freitag, and P. Avouris, "Carrier scattering, mobilities, and electrostatic potential in monolayer, bilayer, and trilayer graphene," *Phys. Rev. B*, vol. 80, p. 235402, 12/02/ 2009.
- [57] R. Muñoz and C. Gómez-Aleixandre, "Review of CVD Synthesis of Graphene," *Chem. Vap. Deposition*, vol. 19, pp. 297-322, 2013.
- [58] Y. Zhang, L. Zhang, and C. Zhou, "Review of chemical vapor deposition of graphene and related applications," *Acc. Chem. Res.*, vol. 46, pp. 2329-2339, 2013.
- [59] X. Li, C. W. Magnuson, A. Venugopal, J. An, J. W. Suk, B. Han, *et al.*, "Graphene Films with Large Domain Size by a Two-Step Chemical Vapor Deposition Process," *Nano Lett.*, vol. 10, pp. 4328-4334, 2010/11/10 2010.
- [60] X. Li, W. Cai, J. An, S. Kim, J. Nah, D. Yang, *et al.*, "Large-area synthesis of high-quality and uniform graphene films on copper foils," *Science*, vol. 324, pp. 1312-1314, 2009.
- [61] P. Y. Huang, C. S. Ruiz-Vargas, A. M. van der Zande, W. S. Whitney, M. P. Levendorf, J. W. Kevek, *et al.*, "Grains and grain boundaries in single-layer graphene atomic patchwork quilts," *Nature*, vol. 469, pp. 389-392, 2011.
- [62] Z. Cheng, Q. Zhou, C. Wang, Q. Li, C. Wang, and Y. Fang, "Toward intrinsic graphene surfaces: a systematic study on thermal annealing and wet-chemical treatment of SiO₂-supported graphene devices," *Nano Lett.*, vol. 11, pp. 767-771, 2011.
- [63] J. Casady and R. W. Johnson, "Status of silicon carbide (SiC) as a wide-bandgap semiconductor for high-temperature applications: a review," *Solid-State Electron.*, vol. 39, pp. 1409-1422, 1996.
- [64] J. Zolper, "A review of junction field effect transistors for high-temperature and high-power electronics," *Solid-State Electron.*, vol. 42, pp. 2153-2156, 1998.
- [65] T. Funaki, J. C. Balda, J. Junghans, A. S. Kashyap, H. A. Mantooth, F. Barlow, *et al.*, "Power conversion with SiC devices at extremely high ambient temperatures," *Power Electronics, IEEE Transactions on*, vol. 22, pp. 1321-1329, 2007.

REFERENCES

- [66] P. Schlotter, R. Schmidt, and J. Schneider, "Luminescence conversion of blue light emitting diodes," *Applied Physics A: Materials Science & Processing*, vol. 64, pp. 417-418, 1997.
- [67] A. I. a. H. Matsunami, "Single crystal growth of SiC and electronic devices," *CRC Critical Rev. Solid state and Mater. Sci.*, vol. 22, p. 111, 1997.
- [68] C. Berger, Z. Song, X. Li, X. Wu, N. Brown, C. Naud, *et al.*, "Electronic confinement and coherence in patterned epitaxial graphene," *Science*, vol. 312, pp. 1191-1196, 2006.
- [69] W. Norimatsu and M. Kusunoki, "Structural features of epitaxial graphene on SiC {0 0 0 1} surfaces," *J. Phys. D: Appl. Phys.*, vol. 47, p. 094017, 2014.
- [70] C. Riedl, C. Coletti, and U. Starke, "Structural and electronic properties of epitaxial graphene on SiC (0 0 0 1): a review of growth, characterization, transfer doping and hydrogen intercalation," *J. Phys. D: Appl. Phys.*, vol. 43, p. 374009, 2010.
- [71] K. V. Emtsev, A. Bostwick, K. Horn, J. Jobst, G. L. Kellogg, L. Ley, *et al.*, "Towards wafer-size graphene layers by atmospheric pressure graphitization of silicon carbide," *Nature Mater.*, vol. 8, pp. 203-207, 2009.
- [72] C. Virojanadara, M. Syväjärvi, R. Yakimova, L. Johansson, A. Zakharov, and T. Balasubramanian, "Homogeneous large-area graphene layer growth on 6 H-SiC (0001)," *Phys. Rev. B*, vol. 78, p. 245403, 2008.
- [73] J.-S. Moon and D. K. Gaskill, "Graphene: Its fundamentals to future applications," *Microwave Theory and Techniques, IEEE Transactions on*, vol. 59, pp. 2702-2708, 2011.
- [74] U. Starke and C. Riedl, "Epitaxial graphene on SiC (0001) and $\overline{\text{SiC}}(000\bar{1})$: from surface reconstructions to carbon electronics," *J. Phys.: Condens. Matter*, vol. 21, p. 134016, 2009.
- [75] Y.-M. Lin, C. Dimitrakopoulos, D. B. Farmer, S.-J. Han, Y. Wu, W. Zhu, *et al.*, "Multicarrier transport in epitaxial multilayer graphene," *Appl. Phys. Lett.*, vol. 97, pp. -, 2010.
- [76] G. R. Yazdi, R. Vasiliauskas, T. Iakimov, A. Zakharov, M. Syväjärvi, and R. Yakimova, "Growth of large area monolayer graphene on 3C-SiC and a comparison with other SiC polytypes," *Carbon*, vol. 57, pp. 477-484, 2013.
- [77] R. Yakimova, T. Iakimov, G. Yazdi, C. Bouhafs, J. Eriksson, A. Zakharov, *et al.*, "Morphological and electronic properties of epitaxial graphene on SiC," *Physica B: Condensed Matter*, 2014.

REFERENCES

- [78] W. Strupinski, K. Grodecki, A. Wyszomolek, R. Stepniewski, T. Szkopek, P. Gaskell, *et al.*, "Graphene epitaxy by chemical vapor deposition on SiC," *Nano Lett.*, vol. 11, pp. 1786-1791, 2011.
- [79] J. Park, W. C. Mitchel, L. Grazulis, H. E. Smith, K. G. Eyink, J. J. Boeckl, *et al.*, "Epitaxial Graphene Growth by Carbon Molecular Beam Epitaxy (CMBE)," *Adv. Mater.*, vol. 22, pp. 4140-4145, 2010.
- [80] K. Nagashio and A. Toriumi, "Density-of-states limited contact resistance in graphene field-effect transistors," *Jpn. J. Appl. Phys.*, vol. 50, p. 0108, 2011.
- [81] G. Giovannetti, P. Khomyakov, G. Brocks, V. Karpan, J. Van den Brink, and P. Kelly, "Doping graphene with metal contacts," *Phys. Rev. Lett.*, vol. 101, p. 026803, 2008.
- [82] P. Khomyakov, G. Giovannetti, P. Rusu, G. Brocks, J. Van den Brink, and P. Kelly, "First-principles study of the interaction and charge transfer between graphene and metals," *Phys. Rev. B*, vol. 79, p. 195425, 2009.
- [83] Y. Ren, S. Chen, W. Cai, Y. Zhu, C. Zhu, and R. S. Ruoff, "Controlling the electrical transport properties of graphene by in situ metal deposition," *Appl. Phys. Lett.*, vol. 97, p. 053107, 2010.
- [84] K. Pi, K. McCreary, W. Bao, W. Han, Y. Chiang, Y. Li, *et al.*, "Electronic doping and scattering by transition metals on graphene," *Phys. Rev. B*, vol. 80, p. 075406, 2009.
- [85] C. Gong, S. McDonnell, X. Qin, A. Azcatl, H. Dong, Y. J. Chabal, *et al.*, "Realistic Metal-Graphene Contact Structures," *ACS Nano*, 2013.
- [86] V. Nagareddy, I. Nikitina, D. Gaskill, J. Tedesco, R. Myers-Ward, C. Eddy, *et al.*, "High temperature measurements of metal contacts on epitaxial graphene," *Appl. Phys. Lett.*, vol. 99, p. 073506, 2011.
- [87] J. Wintterlin and M. L. Bocquet, "Graphene on metal surfaces," *Surf. Sci.*, vol. 603, pp. 1841-1852, 6/1/ 2009.
- [88] P. Merino, M. Švec, A. L. Pinardi, G. Otero, and J. A. Martín-Gago, "Strain-driven moiré superstructures of epitaxial graphene on transition metal surfaces," *ACS Nano*, vol. 5, pp. 5627-5634, 2011.
- [89] J. Moon, D. Curtis, M. Hu, D. Wong, C. McGuire, P. Campbell, *et al.*, "Epitaxial-graphene RF field-effect transistors on Si-face 6H-SiC substrates," *IEEE Electron Device Lett.*, vol. 30, pp. 650-652, 2009.

REFERENCES

- [90] Y.-M. Lin, K. A. Jenkins, A. Valdes-Garcia, J. P. Small, D. B. Farmer, and P. Avouris, "Operation of graphene transistors at gigahertz frequencies," *Nano Lett.*, vol. 9, pp. 422-426, 2008.
- [91] J. Kedzierski, H. Pei-Lan, P. Healey, P. W. Wyatt, C. L. Keast, M. Sprinkle, *et al.*, "Epitaxial Graphene Transistors on SiC Substrates," *IEEE Trans. Electron Devices*, vol. 55, pp. 2078-2085, 2008.
- [92] Y. J. Shin, Y. Wang, H. Huang, G. Kalon, A. T. S. Wee, Z. Shen, *et al.*, "Surface-energy engineering of graphene," *Langmuir*, vol. 26, pp. 3798-3802, 2010.
- [93] F. Schedin, A. Geim, S. Morozov, E. Hill, P. Blake, M. Katsnelson, *et al.*, "Detection of individual gas molecules adsorbed on graphene," *Nature Mater.*, vol. 6, pp. 652-655, 2007.
- [94] J. E. Johns and M. C. Hersam, "Atomic covalent functionalization of graphene," *Acc. Chem. Res.*, vol. 46, pp. 77-86, 2012.
- [95] V. Georgakilas, M. Otyepka, A. B. Bourlinos, V. Chandra, N. Kim, K. C. Kemp, *et al.*, "Functionalization of graphene: covalent and non-covalent approaches, derivatives and applications," *Chem. Rev.*, vol. 112, pp. 6156-6214, 2012.
- [96] J. M. Englert, C. Dotzer, G. Yang, M. Schmid, C. Papp, J. M. Gottfried, *et al.*, "Covalent bulk functionalization of graphene," *Nature Chem.*, vol. 3, pp. 279-286, 2011.
- [97] D. Boukhvalov and M. Katsnelson, "Chemical functionalization of graphene," *J. Phys.: Condens. Matter*, vol. 21, p. 344205, 2009.
- [98] H. Bai, Y. Xu, L. Zhao, C. Li, and G. Shi, "Non-covalent functionalization of graphene sheets by sulfonated polyaniline," *Chem. Commun.*, pp. 1667-1669, 2009.
- [99] T. Kuila, S. Bose, A. K. Mishra, P. Khanra, N. H. Kim, and J. H. Lee, "Chemical functionalization of graphene and its applications," *Prog. Mater. Sci.*, vol. 57, pp. 1061-1105, 2012.
- [100] P.-G. Nanocomposites, "Graphene Functionalization: A Review," 2012.
- [101] H. Liu, Y. Liu, and D. Zhu, "Chemical doping of graphene," *J. Mater. Chem.*, vol. 21, pp. 3335-3345, 2011.
- [102] J. Liu, J. Tang, and J. J. Gooding, "Strategies for chemical modification of graphene and applications of chemically modified graphene," *J. Mater. Chem.*, vol. 22, pp. 12435-12452, 2012.

REFERENCES

- [103] F. e. Karlický, K. Kumara Ramanatha Datta, M. Otyepka, and R. Zbořil, "Halogenated Graphenes: Rapidly Growing Family of Graphene Derivatives," *ACS Nano*, vol. 7, pp. 6434-6464, 2013.
- [104] L. Yan, Y. B. Zheng, F. Zhao, S. Li, X. Gao, B. Xu, *et al.*, "Chemistry and physics of a single atomic layer: strategies and challenges for functionalization of graphene and graphene-based materials," *Chem. Soc. Rev.*, vol. 41, pp. 97-114, 2012.
- [105] T. Sreepasad and V. Berry, "How do the electrical properties of graphene change with its functionalization?," *Small*, vol. 9, pp. 341-350, 2013.
- [106] R. Balog, B. Jørgensen, L. Nilsson, M. Andersen, E. Rienks, M. Bianchi, *et al.*, "Bandgap opening in graphene induced by patterned hydrogen adsorption," *Nature Mater.*, vol. 9, pp. 315-319, 2010.
- [107] K.-J. Jeon, Z. Lee, E. Pollak, L. Moreschini, A. Bostwick, C.-M. Park, *et al.*, "Fluorographene: a wide bandgap semiconductor with ultraviolet luminescence," *ACS Nano*, vol. 5, pp. 1042-1046, 2011.
- [108] T. Gokus, R. Nair, A. Bonetti, M. Bohmler, A. Lombardo, K. Novoselov, *et al.*, "Making graphene luminescent by oxygen plasma treatment," *ACS Nano*, vol. 3, pp. 3963-3968, 2009.
- [109] A. Nourbakhsh, M. Cantoro, A. V. Klekachev, G. Pourtois, T. Vosch, J. Hofkens, *et al.*, "Single layer vs bilayer graphene: a comparative study of the effects of oxygen plasma treatment on their electronic and optical properties," *J. Phys. Chem. C*, vol. 115, pp. 16619-16624, 2011.
- [110] A. Nourbakhsh, M. Cantoro, T. Vosch, G. Pourtois, F. Clemente, M. H. van der Veen, *et al.*, "Bandgap opening in oxygen plasma-treated graphene," *Nanotechnology*, vol. 21, p. 435203, 2010.
- [111] P. E. Hopkins, M. Baraket, E. V. Barnat, T. E. Beechem, S. P. Kearney, J. C. Duda, *et al.*, "Manipulating thermal conductance at metal-graphene contacts via chemical functionalization," *Nano Lett.*, vol. 12, pp. 590-595, 2012.
- [112] D. R. Dreyer, S. Park, C. W. Bielawski, and R. S. Ruoff, "The chemistry of graphene oxide," *Chem. Soc. Rev.*, vol. 39, pp. 228-240, 2010.
- [113] S. Park and R. S. Ruoff, "Chemical methods for the production of graphenes," *Nature Nanotech.*, vol. 4, pp. 217-224, 2009.

REFERENCES

- [114] N. Xiao, X. Dong, L. Song, D. Liu, Y. Tay, S. Wu, *et al.*, "Enhanced Thermopower of Graphene Films with Oxygen Plasma Treatment," *ACS Nano*, vol. 5, pp. 2749-2755, 2011/04/26 2011.
- [115] A. Ganguly, S. Sharma, P. Papakonstantinou, and J. Hamilton, "Probing the thermal deoxygenation of graphene oxide using high-resolution in situ X-ray-based spectroscopies," *J. Phys. Chem. C*, vol. 115, pp. 17009-17019, 2011.
- [116] A. Bagri, C. Mattevi, M. Acik, Y. J. Chabal, M. Chhowalla, and V. B. Shenoy, "Structural evolution during the reduction of chemically derived graphene oxide," *Nature Chem.*, vol. 2, pp. 581-587, 2010.
- [117] A. Felten, A. Eckmann, J. Pireaux, R. Krupke, and C. Casiraghi, "Controlled modification of mono-and bilayer graphene in O₂, H₂ and CF₄ plasmas," *Nanotechnology*, vol. 24, p. 355705, 2013.
- [118] A. Felten, B. S. Flavel, L. Britnell, A. Eckmann, P. Louette, J. J. Pireaux, *et al.*, "Single- and Double-Sided Chemical Functionalization of Bilayer Graphene," *Small*, vol. 9, pp. 631-639, 2013.
- [119] M. Z. Hossain, J. E. Johns, K. H. Bevan, H. J. Karmel, Y. T. Liang, S. Yoshimoto, *et al.*, "Chemically homogeneous and thermally reversible oxidation of epitaxial graphene," *Nature Chem.*, vol. 4, pp. 305-309, 2012.
- [120] J. Janata, "Chemical sensors," *Anal. Chem.*, vol. 64, pp. 196R-219R, 1992.
- [121] A. Orsini and A. D'Amico, "CHEMICAL SENSORS AND CHEMICAL SENSOR SYSTEMS: FUNDAMENTALS LIMITATIONS AND NEW TRENDS," in *Advances in Sensing with Security Applications*. vol. 2, J. Byrnes and G. Ostheimer, Eds., ed: Springer Netherlands, 2006, pp. 69-94.
- [122] K. Wetchakun, T. Samerjai, N. Tamaekong, C. Liewhiran, C. Siriwong, V. Kruefu, *et al.*, "Semiconducting metal oxides as sensors for environmentally hazardous gases," *Sensors and Actuators B: Chemical*, vol. 160, pp. 580-591, 2011.
- [123] B. Li and D. N. Lambeth, "Chemical sensing using nanostructured polythiophene transistors," *Nano Lett.*, vol. 8, pp. 3563-3567, 2008.
- [124] F. Zee and J. W. Judy, "Micromachined polymer-based chemical gas sensor array," *Sensors and Actuators B: Chemical*, vol. 72, pp. 120-128, 2001.
- [125] B. Li, G. Sauvé, M. C. Iovu, M. Jeffries-El, R. Zhang, J. Cooper, *et al.*, "Volatile organic compound detection using nanostructured copolymers," *Nano Lett.*, vol. 6, pp. 1598-1602, 2006.

REFERENCES

- [126] X.-J. Huang and Y.-K. Choi, "Chemical sensors based on nanostructured materials," *Sensors and Actuators B: Chemical*, vol. 122, pp. 659-671, 2007.
- [127] W. Chen, L. Duan, and D. Zhu, "Adsorption of polar and nonpolar organic chemicals to carbon nanotubes," *Environ. Sci. Technol.*, vol. 41, pp. 8295-8300, 2007.
- [128] A. Kolmakov, Y. Zhang, G. Cheng, and M. Moskovits, "Detection of CO and O₂ using tin oxide nanowire sensors," *Adv. Mater.*, vol. 15, pp. 997-1000, 2003.
- [129] S. Iijima, "Growth of carbon nanotubes," *Materials Science and Engineering: B*, vol. 19, pp. 172-180, 1993.
- [130] N. Wang, Y. Cai, and R. Zhang, "Growth of nanowires," *Materials Science and Engineering: R: Reports*, vol. 60, pp. 1-51, 2008.
- [131] Z. Zhang, B. Wei, G. Ramanath, and P. Ajayan, "Substrate-site selective growth of aligned carbon nanotubes," *Appl. Phys. Lett.*, vol. 77, pp. 3764-3766, 2000.
- [132] S. Vitusevich and F. Gasparyan, "Low-Frequency Noise Spectroscopy at Nanoscale: Carbon Nanotube Materials and Devices," *Carbon Nanotubes Applications on Electron Devices*, InTech publisher, pp. 257-298, 2011.
- [133] A. A. Balandin, "Low-frequency 1/f noise in graphene devices," *Nature Nanotech.*, vol. 8, pp. 549-555, 2013.
- [134] S. Rumyantsev, G. Liu, M. S. Shur, R. A. Potyrailo, and A. A. Balandin, "Selective gas sensing with a single pristine graphene transistor," *Nano Lett.*, vol. 12, pp. 2294-2298, 2012.
- [135] M. G. Chung, D. H. Kim, H. M. Lee, T. Kim, J. H. Choi, J.-B. Yoo, *et al.*, "Highly sensitive NO₂ gas sensor based on ozone treated graphene," *Sens. Actuators B*, vol. 166, pp. 172-176, 2012.
- [136] J. T. Robinson, F. K. Perkins, E. S. Snow, Z. Wei, and P. E. Sheehan, "Reduced graphene oxide molecular sensors," *Nano Lett.*, vol. 8, pp. 3137-3140, 2008.
- [137] R. L. M.-W. Brenda L. VanMil, Joseph L. Tedesco, Charles R. Eddy, Jr., Glenn G. Jernigan, James C. Culbertson, Paul M. Campbell, Joseph M. McCrate, Stephen A. Kitt and D. Kurt Gaskill, "Graphene formation on SiC substrates," *Mater. Sci. Forum*, vol. 615-617, p. 211 2009.
- [138] G. G. J. D. Kurt Gaskill, Paul M. Campbell, Joseph L. Tedesco, James C. Culbertson, Brenda L. VanMil, Rachael L. Myers-Ward, Charles R. Eddy, Jr., Jeong Moon, D. Curtis, M. Hu, D. Wong, C. McGuire, Joshua A. Robinson, Mark A. Fanton, Joseph

REFERENCES

- P. Stitt, Thomas Stitt, David Snyder, Xiaojun Weng, and Eric Frantz, "Epitaxial Graphene Growth on SiC Wafers," *ECS Trans.*, vol. 19, p. 117, 2009.
- [139] M. Eliáš, Z. Kučerová, O. Jašek, L. Zajíčková, V. Buršíková, H. Maršíková, *et al.*, "FUNCTIONALIZATION OF CARBON NANOTUBES IN LOW PRESSURE CAPACITIVE COUPLED RF DISCHARGE," 2008.
- [140] D. C. Kim, D.-Y. Jeon, H.-J. Chung, Y. Woo, J. K. Shin, and S. Seo, "The structural and electrical evolution of graphene by oxygen plasma-induced disorder," *Nanotechnology*, vol. 20, p. 375703, 2009.
- [141] A. Felten, C. Bittencourt, J. J. Pireaux, G. Van Lier, and J. C. Charlier, "Radio-frequency plasma functionalization of carbon nanotubes surface O₂, NH₃, and CF₄ treatments," *J. Appl. Phys.*, vol. 98, pp. -, 2005.
- [142] A. Kumar, A. Voevodin, R. Paul, I. Altfeder, D. Zemlyanov, D. N. Zakharov, *et al.*, "Nitrogen-doped graphene by microwave plasma chemical vapor deposition," *Thin Solid Films*, vol. 528, pp. 269-273, 2013.
- [143] C. Shen, G. Huang, Y. Cheng, R. Cao, F. Ding, U. Schwingenschlögl, *et al.*, "Thinning and functionalization of few-layer graphene sheets by CF₄ plasma treatment," *Nanoscale Res. Lett.*, vol. 7, pp. 1-8, 2012.
- [144] M. Baraket, S. Walton, E. Lock, J. Robinson, and F. Perkins, "The functionalization of graphene using electron-beam generated plasmas," *Appl. Phys. Lett.*, vol. 96, p. 1501, 2010.
- [145] S. C. Hernandez, C. J. Bennett, C. E. Junkermeier, S. D. Tsoi, F. J. Bezares, R. Stine, *et al.*, "Chemical Gradients on Graphene To Drive Droplet Motion," *ACS Nano*, vol. 7, pp. 4746-4755, 2013.
- [146] G. M. P. D R Boris, E H Lock, Tz B Petrova, R F Fernsler and S G Walton, "Controlling the electron energy distribution function of electron beam generated plasmas with molecular gas concentration: I. Experimental results," *Plasma Sources Sci. Technol.*, vol. 22, p. 065004, 2013.
- [147] M. Baraket, R. Stine, W. K. Lee, J. T. Robinson, C. R. Tamanaha, P. E. Sheehan, *et al.*, "Aminated graphene for DNA attachment produced via plasma functionalization," *Appl. Phys. Lett.*, vol. 100, p. 233123, 2012.
- [148] D. Leonhardt, S. G. Walton, and R. F. Fernsler, "Fundamentals and applications of a plasma-processing system based on electron-beam ionization), " *Physics of Plasmas (1994-present)*, vol. 14, pp. -, 2007.

REFERENCES

- [149] R. Williams, *Modern GaAs processing methods*: Artech house Boston and London, 1990.
- [150] V. Wheeler, N. Garces, L. Nyakiti, R. Myers-Ward, G. Jernigan, J. Culbertson, *et al.*, "Fluorine functionalization of epitaxial graphene for uniform deposition of thin high- κ dielectrics," *Carbon*, vol. 50, pp. 2307-2314, 2012.
- [151] L. Malard, M. Pimenta, G. Dresselhaus, and M. Dresselhaus, "Raman spectroscopy in graphene," *Phys. Rep.*, vol. 473, pp. 51-87, 2009.
- [152] A. Ferrari, J. Meyer, V. Scardaci, C. Casiraghi, M. Lazzeri, F. Mauri, *et al.*, "Raman spectrum of graphene and graphene layers," *Phys. Rev. Lett.*, vol. 97, p. 187401, 2006.
- [153] K. S. N. J. Lee, and H. S. Shin, "Interaction between metal and graphene-dependence of layer number of graphene," *ACS Nano*, vol. 5, pp. 608-612, 2011.
- [154] L. G. Cançado, A. Jorio, E. M. Ferreira, F. Stavale, C. Achete, R. Capaz, *et al.*, "Quantifying defects in graphene via Raman spectroscopy at different excitation energies," *Nano Lett.*, vol. 11, pp. 3190-3196, 2011.
- [155] M. M. Lucchese, F. Stavale, E. Ferreira, C. Vilani, M. Moutinho, R. B. Capaz, *et al.*, "Quantifying ion-induced defects and Raman relaxation length in graphene," *Carbon*, vol. 48, pp. 1592-1597, 2010.
- [156] A. Das, S. Pisana, B. Chakraborty, S. Piscanec, S. Saha, U. Waghmare, *et al.*, "Monitoring dopants by Raman scattering in an electrochemically top-gated graphene transistor," *Nature Nanotech.*, vol. 3, pp. 210-215, 2008.
- [157] C. Casiraghi, "Doping dependence of the Raman peaks intensity of graphene close to the Dirac point," *Phys. Rev. B*, vol. 80, p. 233407, 12/23/ 2009.
- [158] T. Mohiuddin, A. Lombardo, R. Nair, A. Bonetti, G. Savini, R. Jalil, *et al.*, "Uniaxial strain in graphene by Raman spectroscopy: G peak splitting, Grüneisen parameters, and sample orientation," *Phys. Rev. B*, vol. 79, p. 205433, 2009.
- [159] S. Shivaraman, R. A. Barton, X. Yu, J. Alden, L. Herman, M. Chandrashekar, *et al.*, "Free-standing epitaxial graphene," *Nano Lett.*, vol. 9, pp. 3100-3105, 2009.
- [160] N. Ferralis, R. Maboudian, and C. Carraro, "Evidence of structural strain in epitaxial graphene layers on 6H-SiC (0001)," *Phys. Rev. Lett.*, vol. 101, p. 156801, 2008.
- [161] D. K. Schroder, "Semiconductor material and device characterization," 2006.
- [162] P. Dutta and P. Horn, "Low-frequency fluctuations in solids: $1/f$ noise," *Rev. Mod. Phys.*, vol. 53, 1981.
- [163] L. Liao, Y.-C. Lin, M. Bao, R. Cheng, J. Bai, Y. Liu, *et al.*, "High-speed graphene transistors with a self-aligned nanowire gate," *Nature*, vol. 467, pp. 305-308, 2010.

REFERENCES

- [164] B. Fu, Y. Hua, X. Xiao, H. Zhu, Z. Sun, and C. Yang, "Broadband Graphene Saturable Absorber for Pulsed Fiber Lasers at 1, 1.5 and 2 μm ."
- [165] S. Das and J. Appenzeller, "An all-graphene radio frequency low noise amplifier," in *Radio Frequency Integrated Circuits Symposium (RFIC), 2011 IEEE*, 2011, pp. 1-4.
- [166] H. Wang, A. Hsu, J. Wu, J. Kong, and T. Palacios, "Graphene-based ambipolar RF mixers," *IEEE Electron Device Lett.*, vol. 31, pp. 906-908, 2010.
- [167] B. Sensale-Rodriguez, T. Fang, R. Yan, M. M. Kelly, D. Jena, L. Liu, *et al.*, "Unique prospects for graphene-based terahertz modulators," *Appl. Phys. Lett.*, vol. 99, p. 113104, 2011.
- [168] B. Sensale-Rodriguez, R. Yan, M. M. Kelly, T. Fang, K. Tahy, W. S. Hwang, *et al.*, "Broadband graphene terahertz modulators enabled by intraband transitions," *Nat. Commun.*, vol. 3, p. 780, 2012.
- [169] Y.-C. Lin, C.-C. Lu, C.-H. Yeh, C. Jin, K. Suenaga, and P.-W. Chiu, "Graphene annealing: how clean can it be?," *Nano Lett.*, vol. 12, pp. 414-419, 2011.
- [170] Y. Ahn, H. Kim, Y.-H. Kim, Y. Yi, and S.-I. Kim, "Procedure of removing polymer residues and its influences on electronic and structural characteristics of graphene," *Appl. Phys. Lett.*, vol. 102, p. 091602, 2013.
- [171] K. N. Parrish and D. Akinwande, "Impact of contact resistance on the transconductance and linearity of graphene transistors," *Appl. Phys. Lett.*, vol. 98, p. 183505, 2011.
- [172] A. Hsu, H. Wang, K. K. Kim, J. Kong, and T. Palacios, "Impact of graphene interface quality on contact resistance and RF device performance," *IEEE Electron Device Lett.*, vol. 32, pp. 1008-1010, 2011.
- [173] A. Pirkle, J. Chan, A. Venugopal, D. Hinojos, C. Magnuson, S. McDonnell, *et al.*, "The effect of chemical residues on the physical and electrical properties of chemical vapor deposited graphene transferred to SiO₂," *Appl. Phys. Lett.*, vol. 99, p. 122108, 2011.
- [174] "The National Technology Roadmap for Semiconductors, Semiconductor Industry Association," ed, 2010.
- [175] A. Venugopal, L. Colombo, and E. Vogel, "Contact resistance in few and multilayer graphene devices," *Appl. Phys. Lett.*, vol. 96, p. 013512, 2010.

REFERENCES

- [176] S. Russo, M. Craciun, M. Yamamoto, A. Morpurgo, and S. Tarucha, "Contact resistance in graphene-based devices," *Physica E: Low-dimensional Systems and Nanostructures*, vol. 42, pp. 677-679, 2010.
- [177] K. Nagashio, T. Nishimura, K. Kita, and A. Toriumi, "Contact resistivity and current flow path at metal/graphene contact," *Appl. Phys. Lett.*, vol. 97, p. 143514, 2010.
- [178] W. Li, Y. Liang, D. Yu, L. Peng, K. P. Pernstich, T. Shen, *et al.*, "Ultraviolet/ozone treatment to reduce metal-graphene contact resistance," *Appl. Phys. Lett.*, vol. 102, p. 183110, 2013.
- [179] S. M. Song, J. K. Park, O. J. Sul, and B. J. Cho, "Determination of work function of graphene under a metal electrode and its role in contact resistance," *Nano Lett.*, vol. 12, pp. 3887-3892, 2012.
- [180] R. Nouchi, T. Saito, and K. Tanigaki, "Observation of negative contact resistances in graphene field-effect transistors," *J. Appl. Phys.*, vol. 111, pp. -, 2012.
- [181] J. T. Smith, A. D. Franklin, D. B. Farmer, and C. D. Dimitrakopoulos, "Reducing Contact Resistance in Graphene Devices through Contact Area Patterning," *ACS Nano*, vol. 7, pp. 3661-3667, 2013.
- [182] O. Balci and C. Kocabas, "Rapid thermal annealing of graphene-metal contact," *Appl. Phys. Lett.*, vol. 101, pp. -, 2012.
- [183] X. P. Qiu, Y. J. Shin, J. Niu, N. Kulothungasagaran, G. Kalon, C. Qiu, *et al.*, "Disorder-free sputtering method on graphene," *AIP Adv.*, vol. 2, p. 032121, 2012.
- [184] W. Liu, H. Yu, J. Wei, and M. Li, "Impact of process induced defects on the contact characteristics of ti/graphene devices," *Electrochem. Solid-State Lett.*, vol. 14, pp. K67-K69, 2011.
- [185] J. A. Robinson, M. LaBella, M. Zhu, M. Hollander, R. Kasarda, Z. Hughes, *et al.*, "Contacting graphene," *Appl. Phys. Lett.*, vol. 98, pp. 053103-053103-3, 2011.
- [186] J. Fan, J. Michalik, L. Casado, S. Roddaro, M. Ibarra, and J. De Teresa, "Investigation of the influence on graphene by using electron-beam and photo-lithography," *Solid State Commun.*, vol. 151, pp. 1574-1578, 2011.
- [187] H. Sevinçli, M. Topsakal, E. Durgun, and S. Ciraci, "Electronic and magnetic properties of 3 d transition-metal atom adsorbed graphene and graphene nanoribbons," *Phys. Rev. B*, vol. 77, p. 195434, 2008.

REFERENCES

- [188] H. Valencia, A. Gil, and G. Frapper, "Trends in the adsorption of 3d transition metal atoms onto graphene and nanotube surfaces: a DFT study and molecular orbital analysis," *J. Phys. Chem. C*, vol. 114, pp. 14141-14153, 2010.
- [189] W. S. Kim, S. Y. Moon, J. H. Lee, S. Y. Bang, B. G. Choi, H. Ham, *et al.*, "Fabrication of single-phase titanium carbide layers from MWCNTs using high DC pulse," *Nanotechnology*, vol. 21, p. 055608, 2010.
- [190] J. Roth, H. Graupner, S. P. Withrow, D. Zehner, and R. A. Zuhr, "Chemical interaction of Si, Ti, and Mo with graphite surfaces," *J. Appl. Phys.*, vol. 79, pp. 7695-7702, 1996.
- [191] T. Tachibana, B. E. Williams, and J. T. Glass, "Correlation of the electrical properties of metal contacts on diamond films with the chemical nature of the metal-diamond interface. I. Gold contacts: A non-carbide-forming metal," *Phys. Rev. B*, vol. 45, pp. 11968-11974, 05/15/ 1992.
- [192] C. A. Fyfe, M. S. McKinnon, A. Rudin, and W. J. Tchir, "Investigation of the mechanism of the thermal decomposition of cured phenolic resins by high-resolution carbon-13 CP/MAS solid-state NMR spectroscopy," *Macromolecules*, vol. 16, pp. 1216-1219, 1983/07/01 1983.
- [193] A. Goossens, V. Calado, A. Barreiro, K. Watanabe, T. Taniguchi, and L. Vandersypen, "Mechanical cleaning of graphene," *Appl. Phys. Lett.*, vol. 100, p. 073110, 2012.
- [194] C. W. Chen, F. Ren, G.-C. Chi, S.-C. Hung, Y. Huang, J. Kim, *et al.*, "UV ozone treatment for improving contact resistance on graphene," *Journal of Vacuum Science & Technology B*, vol. 30, p. 060604, 2012.
- [195] M. S. Choi, S. H. Lee, and W. J. Yoo, "Plasma treatments to improve metal contacts in graphene field effect transistor," *J. Appl. Phys.*, vol. 110, p. 073305, 2011.
- [196] W. S. Leong, H. Gong, and J. T. Thong, "Low-Contact-Resistance Graphene Devices with Nickel-Etched-Graphene Contacts," *ACS Nano*, 2013.
- [197] S.-W. Lee, M. Muoth, T. Helbling, M. Mattmann, and C. Hierold, "Suppression of resist contamination during photolithography on carbon nanomaterials by a sacrificial layer," *Carbon*, vol. 66, pp. 295-301, 2014.
- [198] T. Mueller, F. Xia, M. Freitag, J. Tsang, and P. Avouris, "Role of contacts in graphene transistors: A scanning photocurrent study," *Phys. Rev. B*, vol. 79, p. 245430, 2009.

REFERENCES

- [199] C. Malec, B. Elkus, and D. Davidović, "Vacuum-annealed Cu contacts for graphene electronics," *Solid State Commun.*, vol. 151, pp. 1791-1793, 2011.
- [200] A. D. Franklin, S.-J. Han, A. A. Bol, and V. Perebeinos, "Double contacts for improved performance of graphene transistors," *IEEE Electron Device Lett.*, vol. 33, pp. 17-19, 2012.
- [201] E. Watanabe, A. Conwill, D. Tsuya, and Y. Koide, "Low contact resistance metals for graphene based devices," *Diamond Relat. Mater.*, vol. 24, pp. 171-174, 2012.
- [202] R. Murali, K. Brenner, Y. Yang, T. Beck, and J. D. Meindl, "Resistivity of graphene nanoribbon interconnects," *IEEE Electron Device Lett.*, vol. 30, pp. 611-613, 2009.
- [203] X. Chen, D. Akinwande, K.-J. Lee, G. F. Close, S. Yasuda, B. C. Paul, *et al.*, "Fully integrated graphene and carbon nanotube interconnects for gigahertz high-speed CMOS electronics," *IEEE Trans. Electron Devices*, vol. 57, pp. 3137-3143, 2010.
- [204] S. Ghosh, I. Calizo, D. Teweldebrhan, E. Pokatilov, D. Nika, A. Balandin, *et al.*, "Extremely high thermal conductivity of graphene: Prospects for thermal management applications in nanoelectronic circuits," *Appl. Phys. Lett.*, vol. 92, pp. 151911-151911-3, 2008.
- [205] F. Xia, T. Mueller, Y.-m. Lin, A. Valdes-Garcia, and P. Avouris, "Ultrafast graphene photodetector," *Nature Nanotech.*, vol. 4, pp. 839-843, 2009.
- [206] T. Mueller, F. Xia, and P. Avouris, "Graphene photodetectors for high-speed optical communications," *Nature Photon.*, vol. 4, pp. 297-301, 2010.
- [207] G. Jo, M. Choe, S. Lee, W. Park, Y. H. Kahng, and T. Lee, "The application of graphene as electrodes in electrical and optical devices," *Nanotechnology*, vol. 23, p. 112001, 2012.
- [208] V. Nagareddy, H. Chan, S. Hernandez, V. Wheeler, R. Myers-Ward, L. Nyakiti, *et al.*, "Detection of polar chemical vapors using epitaxial graphene grown on SiC (0001)," *Appl. Phys. Lett.*, vol. 102, p. 173103, 2013.
- [209] X. Wang, S. M. Tabakman, and H. Dai, "Atomic layer deposition of metal oxides on pristine and functionalized graphene," *J. Am. Chem. Soc.*, vol. 130, pp. 8152-8153, 2008.
- [210] S. M. Song and B. J. Cho, "Investigation of interaction between graphene and dielectrics," *Nanotechnology*, vol. 21, p. 335706, 2010.

REFERENCES

- [211] N. Lu, Z. Li, and J. Yang, "Electronic structure engineering via on-plane chemical functionalization: a comparison study on two-dimensional polysilane and graphane," *The Journal of Physical Chemistry C*, vol. 113, pp. 16741-16746, 2009.
- [212] J. T. Robinson, J. S. Burgess, C. E. Junkermeier, S. C. Badescu, T. L. Reinecke, F. K. Perkins, *et al.*, "Properties of fluorinated graphene films," *Nano Lett.*, vol. 10, pp. 3001-3005, 2010.
- [213] S. Ryu, M. Y. Han, J. Maultzsch, T. F. Heinz, P. Kim, M. L. Steigerwald, *et al.*, "Reversible basal plane hydrogenation of graphene," *Nano Lett.*, vol. 8, pp. 4597-4602, 2008.
- [214] H. Yang, M. Chen, H. Zhou, C. Qiu, L. Hu, F. Yu, *et al.*, "Preferential and reversible fluorination of monolayer graphene," *J. Phys. Chem. C*, vol. 115, pp. 16844-16848, 2011.
- [215] B. Li, L. Zhou, D. Wu, H. Peng, K. Yan, Y. Zhou, *et al.*, "Photochemical chlorination of graphene," *ACS Nano*, vol. 5, pp. 5957-5961, 2011.
- [216] X. Zhang, A. Hsu, H. Wang, Y. Song, J. Kong, M. S. Dresselhaus, *et al.*, "Impact of Chlorine Functionalization on High-Mobility Chemical Vapor Deposition Grown Graphene," *ACS Nano*, vol. 7, pp. 7262-7270, 2013.
- [217] J. Choi, K.-j. Kim, B. Kim, H. Lee, and S. Kim, "Covalent functionalization of epitaxial graphene by azidotrimethylsilane," *J. Phys. Chem. C*, vol. 113, pp. 9433-9435, 2009.
- [218] E. Bekyarova, M. E. Itkis, P. Ramesh, C. Berger, M. Sprinkle, W. A. de Heer, *et al.*, "Chemical modification of epitaxial graphene: spontaneous grafting of aryl groups," *J. Am. Chem. Soc.*, vol. 131, pp. 1336-1337, 2009.
- [219] S.-H. Cheng, K. Zou, F. Okino, H. R. Gutierrez, A. Gupta, N. Shen, *et al.*, "Reversible fluorination of graphene: Evidence of a two-dimensional wide bandgap semiconductor," *Phys. Rev. B*, vol. 81, p. 205435, 2010.
- [220] B. R. Matis, J. S. Burgess, F. A. Bulat, A. L. Friedman, B. H. Houston, and J. W. Baldwin, "Surface doping and band gap tunability in hydrogenated graphene," *ACS Nano*, vol. 6, pp. 17-22, 2012.
- [221] J. Wei, J. Qiu, L. Li, L. Ren, X. Zhang, J. Chaudhuri, *et al.*, "A reduced graphene oxide based electrochemical biosensor for tyrosine detection," *Nanotechnology*, vol. 23, p. 335707, 2012.

REFERENCES

- [222] Y. Liu, D. Yu, C. Zeng, Z. Miao, and L. Dai, "Biocompatible graphene oxide-based glucose biosensors," *Langmuir*, vol. 26, pp. 6158-6160, 2010.
- [223] J. H. Jung, D. S. Cheon, F. Liu, K. B. Lee, and T. S. Seo, "A Graphene Oxide Based Immuno-biosensor for Pathogen Detection," *Angew. Chem. Int. Ed.*, vol. 49, pp. 5708-5711, 2010.
- [224] V. Nagareddy, H. Chan, S. Hernandez, V. D. Wheeler, L. Nyakiti, R. Myers-Ward, *et al.*, "Improved Chemical Detection and Ultra-Fast Recovery Using Oxygen Functionalized Epitaxial Graphene Sensors," *IEEE Sens. J.*, vol. 13, pp. 2810 - 2817, 2013.
- [225] J. D. Fowler, M. J. Allen, V. C. Tung, Y. Yang, R. B. Kaner, and B. H. Weiller, "Practical chemical sensors from chemically derived graphene," *ACS Nano*, vol. 3, pp. 301-306, 2009.
- [226] S. Wang, Y. Zhang, N. Abidi, and L. Cabrales, "Wettability and surface free energy of graphene films," *Langmuir*, vol. 25, pp. 11078-11081, 2009.
- [227] S. Kumar, N. Peltekis, K. Lee, H.-Y. Kim, and G. S. Duesberg, "Reliable processing of graphene using metal etchmasks," *Nanoscale research letters*, vol. 6, pp. 1-4, 2011.
- [228] J. Yuan, L.-P. Ma, S. Pei, J. Du, Y. Su, W. Ren, *et al.*, "Tuning the Electrical and Optical Properties of Graphene by Ozone Treatment for Patterning Monolithic Transparent Electrodes," *ACS Nano*, vol. 7, pp. 4233-4241, 2013.
- [229] F. Alzina, H. Tao, J. Moser, Y. Garcia, A. Bachtold, and C. Sotomayor-Torres, "Probing the electron-phonon coupling in ozone-doped graphene by Raman spectroscopy," *Phys. Rev. B*, vol. 82, p. 075422, 2010.
- [230] K. Krishnamoorthy, M. Veerapandian, K. Yun, and S.-J. Kim, "The chemical and structural analysis of graphene oxide with different degrees of oxidation," *Carbon*, vol. 53, pp. 38-49, 2013.
- [231] A. Dimiev, D. V. Kosynkin, L. B. Alemany, P. Chaguine, and J. M. Tour, "Pristine graphite oxide," *J. Am. Chem. Soc.*, vol. 134, pp. 2815-2822, 2012.
- [232] T. Szabó, O. Berkesi, P. Forgó, K. Josepovits, Y. Sanakis, D. Petridis, *et al.*, "Evolution of surface functional groups in a series of progressively oxidized graphite oxides," *Chem. Mater.*, vol. 18, pp. 2740-2749, 2006.
- [233] H. A. Becerril, J. Mao, Z. Liu, R. M. Stoltenberg, Z. Bao, and Y. Chen, "Evaluation of solution-processed reduced graphene oxide films as transparent conductors," *ACS Nano*, vol. 2, pp. 463-470, 2008.

REFERENCES

- [234] N. McEvoy, H. Nolan, N. Ashok Kumar, T. Hallam, and G. S. Duesberg, "Functionalisation of graphene surfaces with downstream plasma treatments," *Carbon*, vol. 54, pp. 283-290, 2013.
- [235] S. Zhao, S. P. Surwade, Z. Li, and H. Liu, "Photochemical oxidation of CVD-grown single layer graphene," *Nanotechnology*, vol. 23, p. 355703, 2012.
- [236] N. Mitoma, R. Nouchi, and K. Tanigaki, "Photo-oxidation of Graphene in the Presence of Water," *The Journal of Physical Chemistry C*, vol. 117, pp. 1453-1456, 2013.
- [237] S. Pei and H.-M. Cheng, "The reduction of graphene oxide," *Carbon*, vol. 50, pp. 3210-3228, 2012.
- [238] G. Eda, G. Fanchini, and M. Chhowalla, "Large-area ultrathin films of reduced graphene oxide as a transparent and flexible electronic material," *Nature Nanotech.*, vol. 3, pp. 270-274, 2008.
- [239] W. Gao, L. B. Alemany, L. Ci, and P. M. Ajayan, "New insights into the structure and reduction of graphite oxide," *Nature Chem.*, vol. 1, pp. 403-408, 2009.
- [240] C. Gómez-Navarro, J. C. Meyer, R. S. Sundaram, A. Chuvilin, S. Kurasch, M. Burghard, *et al.*, "Atomic structure of reduced graphene oxide," *Nano Lett.*, vol. 10, pp. 1144-1148, 2010.
- [241] K. Ostrikov, E. Neyts, and M. Meyyappan, "Plasma nanoscience: from nano-solids in plasmas to nano-plasmas in solids," *Advances in Physics*, vol. 62, pp. 113-224, 2013.
- [242] A. Avila, I. Montero, L. Galan, J. M. Ripalda, and R. Levy, "Behavior of oxygen doped SiC thin films: An x-ray photoelectron spectroscopy study," *J. Appl. Phys.*, vol. 89, pp. 212-216, 2001.
- [243] C. Öneby and C. Pantano, "Silicon oxycarbide formation on SiC surfaces and at the SiC/SiO₂ interface," *Journal of Vacuum Science & Technology A*, vol. 15, pp. 1597-1602, 1997.
- [244] J. Park, W. C. Mitchel, S. Elhamri, and T. C. Back, "Effect of in-situ oxygen on the electronic properties of graphene grown by carbon molecular beam epitaxy," *Appl. Phys. Lett.*, vol. 100, pp. -, 2012.
- [245] W. Lu, R. Barbosa, E. Clarke, K. Eyink, L. Grazulis, W. C. Mitchel, *et al.*, "Interface Oxidative Structural Transitions in Graphene Growth on SiC (0001)," *The Journal of Physical Chemistry C*, vol. 116, pp. 15342-15347, 2012.
- [246] P. Shemella and S. K. Nayak, "Electronic structure and band-gap modulation of graphene via substrate surface chemistry," *Appl. Phys. Lett.*, vol. 94, p. 032101, 2009.

REFERENCES

- [247] S. Zhou, G.-H. Gweon, A. Fedorov, P. First, W. De Heer, D.-H. Lee, *et al.*, "Substrate-induced bandgap opening in epitaxial graphene," *Nature Mater.*, vol. 6, pp. 770-775, 2007.
- [248] X. Peng and R. Ahuja, "Symmetry breaking induced bandgap in epitaxial graphene layers on SiC," *Nano Lett.*, vol. 8, pp. 4464-4468, 2008.
- [249] R. Larciprete, S. Gardonio, L. Petaccia, and S. Lizzit, "Atomic oxygen functionalization of double walled C nanotubes," *Carbon*, vol. 47, pp. 2579-2589, 2009.
- [250] R. Larciprete, P. Lacovig, S. Gardonio, A. Baraldi, and S. Lizzit, "Atomic oxygen on graphite: chemical characterization and thermal reduction," *The Journal of Physical Chemistry C*, vol. 116, pp. 9900-9908, 2012.
- [251] C. Mattevi, G. Eda, S. Agnoli, S. Miller, K. A. Mkhoyan, O. Celik, *et al.*, "Evolution of electrical, chemical, and structural properties of transparent and conducting chemically derived graphene thin films," *Adv. Funct. Mater.*, vol. 19, pp. 2577-2583, 2009.
- [252] Y. Zhu, X. Li, Q. Cai, Z. Sun, G. Casillas, M. Jose-Yacamán, *et al.*, "Quantitative analysis of structure and bandgap changes in graphene oxide nanoribbons during thermal annealing," *J. Am. Chem. Soc.*, vol. 134, pp. 11774-11780, 2012.
- [253] M. Topsakal and S. Ciraci, "Domain formation on oxidized graphene," *Phys. Rev. B*, vol. 86, p. 205402, 2012.
- [254] D. W. Boukhvalov and M. I. Katsnelson, "Modeling of graphite oxide," *J. Am. Chem. Soc.*, vol. 130, pp. 10697-10701, 2008.
- [255] J.-A. Yan and M. Chou, "Oxidation functional groups on graphene: Structural and electronic properties," *Phys. Rev. B*, vol. 82, p. 125403, 2010.
- [256] N. Vinogradov, K. Schulte, M. L. Ng, A. Mikkelsen, E. Lundgren, N. Martensson, *et al.*, "Impact of atomic oxygen on the structure of graphene formed on Ir (111) and Pt (111)," *The Journal of Physical Chemistry C*, vol. 115, pp. 9568-9577, 2011.
- [257] A. Lerf, H. He, M. Forster, and J. Klinowski, "Structure of graphite oxide revisited," *The Journal of Physical Chemistry B*, vol. 102, pp. 4477-4482, 1998.
- [258] H. He, J. Klinowski, M. Forster, and A. Lerf, "A new structural model for graphite oxide," *Chem. Phys. Lett.*, vol. 287, pp. 53-56, 1998.

REFERENCES

- [259] H.-K. Jeong, Y. P. Lee, R. J. Lahaye, M.-H. Park, K. H. An, I. J. Kim, *et al.*, "Evidence of graphitic AB stacking order of graphite oxides," *J. Am. Chem. Soc.*, vol. 130, pp. 1362-1366, 2008.
- [260] D. Pacilé, J. Meyer, A. Fraile Rodríguez, M. Papagno, C. Gomez-Navarro, R. Sundaram, *et al.*, "Electronic properties and atomic structure of graphene oxide membranes," *Carbon*, vol. 49, pp. 966-972, 2011.
- [261] S. Zhou, S. Kim, and A. Bongiorno, "Chemical Structure of Oxidized Multilayer Epitaxial Graphene: A Density Functional Theory Study," *The Journal of Physical Chemistry C*, vol. 117, pp. 6267-6274, 2013.
- [262] Y. Si and E. T. Samulski, "Synthesis of water soluble graphene," *Nano Lett.*, vol. 8, pp. 1679-1682, 2008.
- [263] W. Cai, R. D. Piner, F. J. Stadermann, S. Park, M. A. Shaibat, Y. Ishii, *et al.*, "Synthesis and solid-state NMR structural characterization of ¹³C-labeled graphite oxide," *Science*, vol. 321, pp. 1815-1817, 2008.
- [264] V. Dua, S. P. Surwade, S. Ammu, S. R. Agnihotra, S. Jain, K. E. Roberts, *et al.*, "All-Organic Vapor Sensor Using Inkjet-Printed Reduced Graphene Oxide," *Angew. Chem. Int. Ed.*, vol. 49, pp. 2154-2157, 2010.
- [265] E. C. Mattson, K. Pande, M. Unger, S. Cui, G. Lu, M. Gajdardziska-Josifovska, *et al.*, "Exploring adsorption and reactivity of NH₃ on reduced graphene oxide," *The Journal of Physical Chemistry C*, vol. 117, pp. 10698-10707, 2013.
- [266] S. Berciaud, S. Ryu, L. E. Brus, and T. F. Heinz, "Probing the intrinsic properties of exfoliated graphene: Raman spectroscopy of free-standing monolayers," *Nano Lett.*, vol. 9, pp. 346-352, 2008.
- [267] D. Graf, F. Molitor, K. Ensslin, C. Stampfer, A. Jungen, C. Hierold, *et al.*, "Spatially resolved Raman spectroscopy of single- and few-layer graphene," *Nano Lett.*, vol. 7, pp. 238-242, 2007.
- [268] E. M. Ferreira, M. V. Moutinho, F. Stavale, M. Lucchese, R. B. Capaz, C. Achete, *et al.*, "Evolution of the Raman spectra from single-, few-, and many-layer graphene with increasing disorder," *Phys. Rev. B*, vol. 82, p. 125429, 2010.
- [269] L. Cancado, K. Takai, T. Enoki, M. Endo, Y. Kim, H. Mizusaki, *et al.*, "General equation for the determination of the crystallite size L_a of nanographite by Raman spectroscopy," *Appl. Phys. Lett.*, vol. 88, pp. 163106-163106-3, 2006.

REFERENCES

- [270] F. Tuinstra and J. L. Koenig, "Raman spectrum of graphite," *J. Chem. Phys.*, vol. 53, pp. 1126-1130, 1970.
- [271] A. Eckmann, A. Felten, I. Verzhbitskiy, R. Davey, and C. Casiraghi, "Raman study on defective graphene: Effect of the excitation energy, type, and amount of defects," *Phys. Rev. B*, vol. 88, p. 035426, 07/15/ 2013.
- [272] M. Kalbac, A. Reina-Cecco, H. Farhat, J. Kong, L. Kavan, and M. S. Dresselhaus, "The influence of strong electron and hole doping on the Raman intensity of chemical vapor-deposition graphene," *ACS Nano*, vol. 4, pp. 6055-6063, 2010.
- [273] C. Casiraghi, S. Pisana, K. Novoselov, A. Geim, and A. Ferrari, "Raman fingerprint of charged impurities in graphene," *Appl. Phys. Lett.*, vol. 91, p. 233108, 2007.
- [274] K. Subrahmanyam, R. Voggu, A. Govindaraj, and C. Rao, "A comparative Raman study of the interaction of electron donor and acceptor molecules with graphene prepared by different methods," *Chem. Phys. Lett.*, vol. 472, pp. 96-98, 2009.
- [275] L. Liu, S. Ryu, M. R. Tomasik, E. Stolyarova, N. Jung, M. S. Hybertsen, *et al.*, "Graphene oxidation: thickness-dependent etching and strong chemical doping," *Nano Lett.*, vol. 8, pp. 1965-1970, 2008.
- [276] G. Tsoukleri, J. Parthenios, K. Papagelis, R. Jalil, A. C. Ferrari, A. K. Geim, *et al.*, "Subjecting a graphene monolayer to tension and compression," *Small*, vol. 5, pp. 2397-2402, 2009.
- [277] A. Strudwick, G. Creeth, N. Johansson, and C. Marrows, "Probing residual strain in epitaxial graphene layers on 4H-SiC (0001) with Raman spectroscopy," *Appl. Phys. Lett.*, vol. 98, p. 051910, 2011.
- [278] J. A. Robinson, C. P. Puls, N. E. Staley, J. P. Stitt, M. A. Fanton, K. V. Emtsev, *et al.*, "Raman topography and strain uniformity of large-area epitaxial graphene," *Nano Lett.*, vol. 9, pp. 964-968, 2009.
- [279] D. A. Schmidt, T. Ohta, and T. E. Beechem, "Strain and charge carrier coupling in epitaxial graphene," *Phys. Rev. B*, vol. 84, p. 235422, 2011.
- [280] J. Zabel, R. R. Nair, A. Ott, T. Georgiou, A. K. Geim, K. S. Novoselov, *et al.*, "Raman spectroscopy of graphene and bilayer under biaxial strain: bubbles and balloons," *Nano Lett.*, vol. 12, pp. 617-621, 2012.
- [281] C. Metzger, S. Rémi, M. Liu, S. V. Kusminskiy, A. H. Castro Neto, A. K. Swan, *et al.*, "Biaxial strain in graphene adhered to shallow depressions," *Nano Lett.*, vol. 10, pp. 6-10, 2009.

REFERENCES

- [282] Y.-C. Lin, C.-Y. Lin, and P.-W. Chiu, "Controllable graphene N-doping with ammonia plasma," *Appl. Phys. Lett.*, vol. 96, pp. 133110-133110-3, 2010.
- [283] I. Childres, L. A. Jauregui, J. Tian, and Y. P. Chen, "Effect of oxygen plasma etching on graphene studied using Raman spectroscopy and electronic transport measurements," *New Journal of Physics*, vol. 13, p. 025008, 2011.
- [284] A. L. Walter, K.-J. Jeon, A. Bostwick, F. Speck, M. Ostler, T. Seyller, *et al.*, "Highly p-doped epitaxial graphene obtained by fluorine intercalation," *Appl. Phys. Lett.*, vol. 98, p. 184102, 2011.
- [285] D. Elias, R. Nair, T. Mohiuddin, S. Morozov, P. Blake, M. Halsall, *et al.*, "Control of graphene's properties by reversible hydrogenation: evidence for graphane," *Science*, vol. 323, pp. 610-613, 2009.
- [286] H. Y. Jeong, J. Y. Kim, J. W. Kim, J. O. Hwang, J.-E. Kim, J. Y. Lee, *et al.*, "Graphene oxide thin films for flexible nonvolatile memory applications," *Nano Lett.*, vol. 10, pp. 4381-4386, 2010.
- [287] J.-H. Chen, C. Jang, S. Adam, M. Fuhrer, E. Williams, and M. Ishigami, "Charged-impurity scattering in graphene," *Nature Phys.*, vol. 4, pp. 377-381, 2008.
- [288] A. Felten, I. Suarez-Martinez, X. Ke, G. Van Tendeloo, J. Ghijsen, J. J. Pireaux, *et al.*, "The role of oxygen at the interface between titanium and carbon nanotubes," *ChemPhysChem*, vol. 10, pp. 1799-1804, 2009.
- [289] C. Ciofi and B. Neri, "Low-frequency noise measurements as a characterization tool for degradation phenomena in solid-state devices," *J. Phys. D: Appl. Phys.*, vol. 33, p. R199, 2000.
- [290] F. Hooge, T. Kleinpenning, and L. Vandamme, "Experimental studies on $1/f$ noise," *Rep. Prog. Phys.*, vol. 44, p. 479, 1981.
- [291] G. Liu, W. Stillman, S. Romyantsev, Q. Shao, M. Shur, and A. Balandin, "Low-frequency electronic noise in the double-gate single-layer graphene transistors," *Appl. Phys. Lett.*, vol. 95, p. 033103, 2009.
- [292] Q. Shao, G. Liu, D. Teweldebrhan, A. A. Balandin, S. Romyantsev, M. S. Shur, *et al.*, "Flicker noise in bilayer graphene transistors," *Electron Device Letters, IEEE*, vol. 30, pp. 288-290, 2009.
- [293] G. Liu, S. Romyantsev, M. S. Shur, and A. A. Balandin, "Origin of $1/f$ noise in graphene multilayers: Surface vs. volume," *Appl. Phys. Lett.*, vol. 102, p. 093111, 2013.

REFERENCES

- [294] A. Behnam, G. Bosman, and A. Ural, "Percolation scaling of $1/f$ noise in single-walled carbon nanotube films," *Phys. Rev. B*, vol. 78, p. 085431, 2008.
- [295] Y.-M. Lin and P. Avouris, "Strong suppression of electrical noise in bilayer graphene nanodevices," *Nano Lett.*, vol. 8, pp. 2119-2125, 2008.
- [296] A. Tarasov, W. Fu, O. Knopfmacher, J. Brunner, M. Calame, and C. Schonenberger, "Signal-to-noise ratio in dual-gated silicon nanoribbon field-effect sensors," *Appl. Phys. Lett.*, vol. 98, pp. 012114-012114-3, 2011.
- [297] F. Giannazzo, I. Deretzis, A. La Magna, F. Roccaforte, and R. Yakimova, "Electronic transport at monolayer-bilayer junctions in epitaxial graphene on SiC," *Phys. Rev. B*, vol. 86, p. 235422, 2012.
- [298] D. K. Aswal and S. K. Gupta, *Science and technology of chemiresistor gas sensors*: Nova Publishers, 2007.
- [299] F. Wang, H. Gu, and T. M. Swager, "Carbon nanotube/polythiophene chemiresistive sensors for chemical warfare agents," *J. Am. Chem. Soc.*, vol. 130, pp. 5392-5393, 2008.
- [300] A. Salehi-Khojin, F. Khalili-Araghi, M. A. Kuroda, K. Y. Lin, J.-P. Leburton, and R. I. Masel, "On the sensing mechanism in carbon nanotube chemiresistors," *ACS Nano*, vol. 5, pp. 153-158, 2010.
- [301] F. Yavari and N. Koratkar, "Graphene-based chemical sensors," *J. Phys. Chem. Lett.*, vol. 3, pp. 1746-1753, 2012.
- [302] C. W. Chen, S. C. Hung, M. D. Yang, C. W. Yeh, C. H. Wu, G. C. Chi, *et al.*, "Oxygen sensors made by monolayer graphene under room temperature," *Appl. Phys. Lett.*, vol. 99, pp. -, 2011.
- [303] H. J. Yoon, D. H. Jun, J. H. Yang, Z. Zhou, S. S. Yang, and M. M.-C. Cheng, "Carbon dioxide gas sensor using a graphene sheet," *Sensors and Actuators B: Chemical*, vol. 157, pp. 310-313, 2011.
- [304] G. Chen, T. M. Paronyan, and A. R. Harutyunyan, "Sub-ppt gas detection with pristine graphene," *Appl. Phys. Lett.*, vol. 101, p. 053119, 2012.
- [305] Y. Ren, C. Zhu, W. Cai, H. Li, H. Ji, I. Kholmanov, *et al.*, "Detection of sulfur dioxide gas with graphene field effect transistor," *Appl. Phys. Lett.*, vol. 100, pp. -, 2012.
- [306] P. K. Ang, W. Chen, A. T. S. Wee, and K. P. Loh, "Solution-gated epitaxial graphene as pH sensor," *J. Am. Chem. Soc.*, vol. 130, pp. 14392-14393, 2008.
- [307] R. P. Pohanish, *Handbook of Toxic and Hazardous Chemicals and Carcinogens*, 4th ed. ed. New Jersey: Noyes Publications, 2002.

REFERENCES

- [308] D. R. Lide, *CRC Handbook of Chemistry and Physics*, 87th ed. ed. Florida: Taylor & Francis, 2006.
- [309] S. Capone, S. Mongelli, R. Rella, P. Siciliano, and L. Valli, "Gas sensitivity measurements on NO₂ sensors based on copper (II) tetrakis (n-butylaminocarbonyl) phthalocyanine LB films," *Langmuir*, vol. 15, pp. 1748-1753, 1999.
- [310] C. W. Cheung, J. F. Porter, and G. McKay, "Elovich equation and modified second-order equation for sorption of cadmium ions onto bone char," *J. Chem. Technol. Biotechnol.*, vol. 75, pp. 963-970, 2000.
- [311] M. Low, "Kinetics of Chemisorption of Gases on Solids," *Chem. Rev.*, vol. 60, pp. 267-312, 1960.
- [312] C. Chen, S. Hung, M. Yang, C. Yeh, C. Wu, G. Chi, *et al.*, "Oxygen sensors made by monolayer graphene under room temperature," *Appl. Phys. Lett.*, vol. 99, p. 243502, 2011.
- [313] Y. Ren, C. Zhu, W. Cai, H. Li, H. Ji, I. Kholmanov, *et al.*, "Detection of sulfur dioxide gas with graphene field effect transistor," *Appl. Phys. Lett.*, vol. 100, p. 163114, 2012.
- [314] E. S. Snow, F. Perkins, and J. A. Robinson, "Chemical vapor detection using single-walled carbon nanotubes," *Chem. Soc. Rev.*, vol. 35, pp. 790-798, 2006.
- [315] H. Rao and G. Bosman, "Simultaneous low-frequency noise characterization of gate and drain currents in AlGaN/GaN high electron mobility transistors," *J. Appl. Phys.*, vol. 106, pp. -, 2009.
- [316] M. V. Hauf, L. H. Hess, J. Howgate, M. Dankerl, M. Stutzmann, and J. A. Garrido, "Low-frequency noise in diamond solution-gated field effect transistors," *Appl. Phys. Lett.*, vol. 97, pp. -, 2010.
- [317] Y. Zhang, E. E. Mendez, and X. Du, "Mobility-Dependent Low-Frequency Noise in Graphene Field-Effect Transistors," *ACS Nano*, vol. 5, pp. 8124-8130, 2011/10/25 2011.
- [318] J. Ito, J. Nakamura, and A. Natori, "Semiconducting nature of the oxygen-adsorbed graphene sheet," *J. Appl. Phys.*, vol. 103, pp. -, 2008.
- [319] S. Dhall, N. Jaggi, and R. Nathawat, "Functionalized multiwalled carbon nanotubes based hydrogen gas sensor," *Sensors and Actuators A: Physical*, vol. 201, pp. 321-327, 10/15/ 2013.
- [320] F. Tuinstra and J. L. Koenig, "Raman Spectrum of Graphite," *The Journal of Chemical Physics*, vol. 53, pp. 1126-1130, 1970.

REFERENCES

- [321] B. Pan and B. Xing, "Adsorption mechanisms of organic chemicals on carbon nanotubes," *Environmental Science & Technology*, vol. 42, pp. 9005-9013, 2008.
- [322] V. Sokolov, V. Kochelap, and K. Kim, "Generation-recombination noise in bipolar graphene," *J. Appl. Phys.*, vol. 110, p. 044327, 2011.